Shaping Anisotropy
3D-printing of Liquid Crystal Polymers

Important note
To cite this publication, please use the final published version (if applicable).
Please check the document version above.

Shaping Anisotropy

3D-printing of Liquid Crystal Polymers

Caroline Houriet

Shaping Anisotropy

3D-printing of Liquid Crystal Polymers

Shaping Anisotropy

3D-printing of Liquid Crystal Polymers
Dissertation

for the purpose of obtaining the degree of doctor

at Delft University of Technology

by the authority of the Rector Magnificus, prof. dr. ir. T.H.J.J. van der Hagen,

chair of the Board for Doctorates

to be defended publicly on

Monday 11 November 2024 at 10:00

by

Caroline Colette Marcelle Christiane Annie Germaine Philomène HOURIET

Master of Science in Aerospace Engineering,
Delft University of Technology, the Netherlands

Ingénieure,
ENSTA Paris, Institut Polytechnique de Paris, France

born in Calais, France.

This dissertation has been approved by the promotors.

Composition of the doctoral committee:

Rector Magnificus,	chairperson
Dr. K. Masania,	Delft University of Technology, *promotor*
Prof. C. A. Dransfeld,	Delft University of Technology, *promotor*

Independent members:

Prof. dr. ir. J.W.G. van de Kuilen	
	Delft University of Technology
Prof. dr. S.J. Picken	Delft University of Technology
Prof. dr. J. Morlier	ISAE Supaero, France
Dr. F. Libonati	University of Genoa, Italy

Other members:

Dr. U. Lafont,	European Space Agency

An electronic copy of this dissertation is available at
https://resolver.tudelft.nl/uuid:d59312f1-7ae2-4eb2-914c-ec830a065dc7.

Summary

The cellular, hierarchical nature of living materials such as wood or bone, enables their mechanical properties to vary locally. This variability grants them multi-functionality and high mechanical performance with low resource consumption. To obtain such desirable features with man-made structures, many manufacturing restrictions need to be overcome. Currently, the most common structural anisotropic materials are fibre-reinforced composites, which allow limited control over material placement, orientation, and directional strength.

In this thesis, we explore how the additive manufacturing of Liquid Crystal Polymers (LCP) can unlock our ability to control these parameters and, therefore, expand the design space to optimize structural performance while limiting material use. To achieve this, we leveraged the alignment of nematic domains in LCPs, induced by shear and elongational flow during extrusion through the 3D printer nozzle. By modulating the pressure inside the nozzle to change line width, we observed an axial stiffness range between 3 GPa and 30 GPa, associated with a failure mode shift from ductile to brittle. Demonstrating our ability to print with variable toolpath widths and sharp curvatures, we created 3D patterns inspired by fluid dynamics. This combination of shaping freedom and anisotropy control enabled the design of functional objects with embedded crack mitigation strategies, or improved buckling performance.

Anisotropy gradients are also present in the structure of trees. Inspired by the seamless transition of wood fibres from parallel to interlocked at the branch junctions, we manufactured sinusoidal and helical patterns with LCP. The introduction of local waviness decreased axial tensile stiffness, but significantly enhanced toughness. Tensile and interlocking performance were driven by two critical parameters: angle of maximum deviation to the axial direction, and pattern size. Moreover, the resistance to normal stresses was improved, as shown by the 88% increase in load-bearing capacity compared to a non-reinforced configuration in a two-strut junction. This opens the possibility to integrate localized interlocking patterns in multi-axis loaded regions of anisotropic parts.

Manufacturing methods which utilize as little material and energy as possible are needed for future space exploration missions. To assess whether the strategies mentioned previously are applicable to this context, 3D-printed LCPs were subjected to four different space environments. High-energy electron radiations created colour-centres, leading to a bright green coloration in the bulk of the specimen. However, no significant decrease in static mechanical properties was observed, with unidirectional stiffness remaining close to 30 GPa even after intense electron irradiation and thermal cycling. These results indicate that LCPs are a promising alternative to engineering polymers like PEEK or PEI for space applications.

Future research into topology-optimization methods integrating both asymmetry between tension and compression, and mechanical property gradients, will enable to further explore the design space opened by the tunable anisotropy of LCPs.

Sammenvatting

De cellulaire, hiërarchische aard van levende materialen zoals hout of bot zorgt ervoor dat hun mechanische eigenschappen lokaal kunnen variëren. Deze variabiliteit geeft ze multifunctionaliteit en hoge mechanische prestaties met een laag gebruik van grondstoffen. Om zulke wenselijke eigenschappen te verkrijgen in door de mens gemaakte structuren moeten veel limitaties in het productieproces worden overwonnen. Momenteel zijn de meest voorkomende structurele anisotrope materialen vezelversterkte composieten, die beperkte controle mogelijk maken over de plaatsing, oriëntatie en richtingssterkte van het materiaal. In dit proefschrift onderzoeken we hoe de additieve productie van vloeibare kristalpolymeren (VKP) ons de mogelijkheid geeft om deze parameters te beheersen en zo de ontwerpruimte kunnen vergroten om de structurele prestaties te optimaliseren en tegelijkertijd het materiaalgebruik te beperken.

Om dit te bereiken maken we gebruik van de uitlijning van nematische domeinen in VKP'en, veroorzaakt door schuif- en rekstroming tijdens extrusie door de spuitkop van de 3D-printer. Door de druk in de spuitkop te moduleren om de lijnbreedte te veranderen, hebben we een axiale stijfheidsbereik tussen 3 GPa en 30 GPa waargenomen, geassocieerd met een verschuiving van de faalmodus van ductiel naar bros. Om ons vermogen om te printen met variabele gereedschapspadbreedtes en scherpe krommingen te demonstreren, creëerden we 3D-patronen geïnspireerd op de vloeistofdynamica. Deze combinatie van vormvrijheid en anisotropiecontrole maakte het ontwerp mogelijk van functionele objecten met ingebedde strategieën voor scheurvermindering of verbeterde knikprestaties.

Anisotrope gradiënten zijn ook aanwezig in bomen. Geïnspireerd door de naadloze overgang van houtvezels van evenwijdig naar in elkaar grijpend bij de aftakkingen, vervaardigden we sinusoïdale en spiraalvormige patronen met VKP. De introductie van lokale golving verminderde de axiale trekstijfheid, maar verbeterde de taaiheid aanzienlijk. De trek- en in elkaar grijpende prestaties werden bepaald door twee kritische parameters: de hoek van de maximale afwijking ten opzichte van de axiale richting en de patroongrootte. Bovendien werd de weerstand tegen normale spanningen verbeterd, zoals blijkt uit de 88% toename van het draagvermogen vergeleken met een niet-versterkte configuratie in een verbinding met twee stutten. Dit geeft de mogelijkheid om gelokaliseerde in elkaar grijpende patronen te integreren in meerassige belaste gebieden van anisotrope onderdelen.

Voor toekomstige ruimteverkenningsmissies zijn productiemethoden nodig die zo min mogelijk materiaal en energie gebruiken. Om te beoordelen of de eerder genoemde strategieën toepasbaar zijn in deze context, werden 3D-geprinte VKP'en onderworpen aan vier verschillende ruimteomgevingen. Door elektronenstraling met hoge energie ontstonden er kleurcentra, wat leidde tot een heldergroene kleur in het grootste deel van het monster.

Er werd echter geen significante afname van de statische mechanische eigenschappen waargenomen, waarbij de unidirectionele stijfheid dicht bij 30 GPa bleef, zelfs na intensieve elektronenbestraling en thermische cycli. Deze resultaten geven aan dat VKP'en een veelbelovend alternatief zijn voor technische polymeren zoals PEEK of PEI voor ruimte-toepassingen.

Toekomstig onderzoek naar topologie-optimalisatiemethoden die zowel asymmetrie tussen spanning en compressie integreren, als mechanische eigenschapsgradiënten, zal het mogelijk maken om de ontwerpruimte die mogelijk wordt gemaakt door de afstembare anisotropie van VKP'en verder te verkennen.

Contents

Chapter 1

Introduction

To imagine structures which more closely resemble living materials in sustainability, multi-functionality, and adaptation to their environment, manufacturing approaches that enlarge design freedom need to be developed.

1.1. Motivation: anisotropy and shaping freedom

Anisotropy is defined by the directional dependence of a material to a physical property. In this work, anisotropy is always implied to refer to mechanical properties such as stiffness and strength. The prevalence and diversity of anisotropic bio-materials are associated with evolutionary advantages such as the optimization of mechanical properties based on scarce resources, additional resilience, or other functionalities that are useful to the living organism. These advantages essentially strive to meet the same goal: making the most of finite resources.
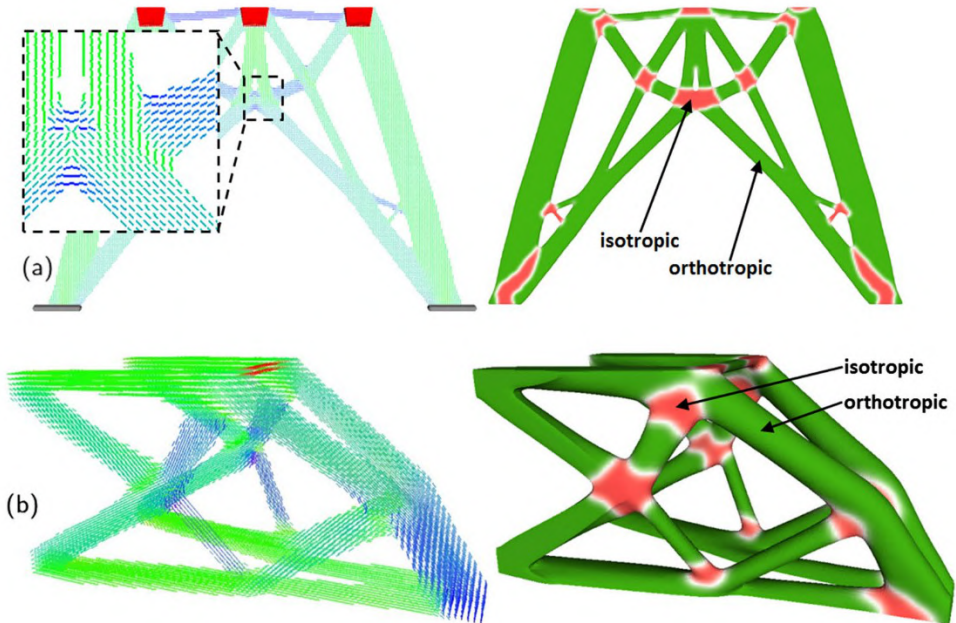
Figure 1.1 – Designs optimized for stiffness with spatially varying ratios of anisotropy for (a) a 2D bridge and (b) a 3D cantilever design. On the left, material orientation is indicated, and on the right, the field of ratio of anisotropy is shown, with orthotropic materials in green and isotropic materials in red. Reproduced from [1] with permission from Springer.

The lightweight structures of today are still a long way from being as light as a bird's bone, as adapted as the fibres in a tree that flow around a branch, or as well-architected as nacre shells.

Yet, an algorithm [1] can be asked, given a limited quantity of material, to optimize the stiffness of a structure while deciding where to place this material, but also whether it should be locally isotropic or anisotropic and if so, in which direction. The algorithm outputs a configuration shown in Figure 1.1. The topology is made of anisotropic struts of different angles joined together, while in these intersection zones, isotropy is preferred.
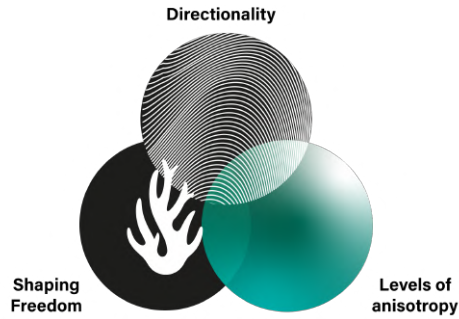
Figure 1.2 – In this thesis, a manufacturing route is developed that strives to control three parameters: the shape of the part, and within this part, the directionality of any given point and its level of anisotropy, just like a vector for which is known location, direction and norm. This "trinity" also resonates with the well-known structure-material-processing relationship of material science.

To make these mechanically optimized structures become a tangible reality beyond the digital realm, a manufacturing route should be explored, that enables control of three crucial components:

- Shape: the topological domain in which the material is deposited

- Directionality: the material can be steered along a set orientation coinciding with higher properties along one axis (1), compared to the others (2,3)

- Levels of anisotropy: material properties can seamlessly be changed spatially, creating gradients for instance between isotropic ($E_1 = E_2 = E_3$) and anisotropic ($E_1 > E_2 > E_3$) mechanical behaviour. This level can be quantified by a ratio of anisotropy E_1/E_3 or E_1/E_2.

Humans have strived to control these three components simultaneously with great processing efforts, and often only two at a time. Two broad categories of manufacturing routes have been envisioned: blending dissimilar materials, or selecting one and tailoring its mechanical properties locally. In both cases, many experimental challenges emerge. In contrast, living organisms as common as trees can achieve this very elegantly, through a bottom-up, hierarchical self-assembly.

Therefore, the following question arises: *"Does a manufacturing method that can control the directionality of a material and locally tune its level of anisotropy, improve structural performance?"*

1

1.2. Outline of thesis

Inspired by the frugality and crafted anisotropy of living materials, this thesis aims to develop a manufacturing method that controls these three components for human-made engineering components, i.e. create complex shapes, control directionality, and locally tune anisotropy levels, using Liquid Crystal Polymers (LCP). This manufacturing method, based on Fused Filament Fabrication (FFF) with a desktop 3D-printer, also strives to keep the polymer recyclable.

In Chapter 2, an overview of biological and synthetic materials showing anisotropy variations is proposed. The state of the art on the existing manufacturing routes to tune the parameters illustrated in Figure 1.2 is presented. A general description of the thermotropic Liquid Crystal Polymers (LCP) used in this thesis is given, with a focus on the origin of its complex hierarchical fibrillar microstructure and on thermal and rheological characteristics that are central to any processing route, including 3D-printing. A brief review of the traditional processing routes of this LCP is proposed, as well as a summary of the most important findings of the recent works in which it was 3D-printed.

Chapter 3 examines the approach of changing the line width of the print on-the-fly to tune tensile properties in 2D. The Young's modulus obtained by this method, ranging from 3 GPa to 30 GPa, is found to be strongly influenced by the directionality of the nematic flow. By determining a relationship between stiffness, nozzle diameter and line width, we identify a suitable design space where shaping and mechanical performance can be combined. Patterns inspired by fluid dynamics are successfully manufactured with steep curvature variations. The versatility of LCPs combined with this freedom of directionality allows to 3D-print objects with gradients of stiffness and curvature, offering applications in lightweight functional structures embedding crack-mitigation strategies.

In Chapter 4, a bio-inspired strategy using wavy patterns is studied to tune anisotropy. Different patterns are assessed in tension, short-beam shear, interlaminar crack resistance and curved-beam bending. Planar and non-planar interlocking geometries are studied, showing a strong trade-off between short-beam shear and tensile properties along the fibre direction. In contrast, fracture tests indicate that wavy patterns can reinforce interfaces in Mode I as they trigger extrinsic toughening mechanisms. Finally, local normal tensile stresses are introduced via bending moments in curved-beam samples. The behaviour of samples with and without a helical pattern at the junction of the two beams are compared. The samples without the helical pattern show early failure by delamination, while the reinforced samples can sustain a 88 % larger load and fail elsewhere than at the junction.

Chapter 5 evaluates the potential of this 3D-printed material for space applications. 3D-printed parts are subjected to thermal cycling under vacuum, atomic oxygen, UV and high-energy electron irradiation. Their changes in optical or mechanical performance are studied. Furthermore, their performance in unidirectional tension is evaluated in the longitudinal axis and normal to the layer plane across different printing temperatures, to illustrate the impact of this processing parameter on anisotropy levels.

1

Finally, in Chapter 6, a consolidation of the findings from the research topics presented in this thesis is established. Possible future research directions in the field of tunable anisotropy with liquid crystal polymers are also outlined.

References

1. Schmidt, M. P., Couret, L., Gout, C. & Pedersen, C. B. Structural topology optimization with smoothly varying fiber orientations. *Structural and Multidisciplinary Optimization* **62,** 3105–3126. ISSN: 16151488 (Dec. 2020).

2

Chapter 2

State of the Art

This chapter is divided into four main parts, articulated around Figure 1.2. First, the state of the art on tunable anisotropy is presented, focusing on gradients and patterns in biological materials. In the second part, the stakes and challenges in simultaneous control of shape and directionality are discussed. The third part summarizes the different approaches in literature where tunable anisotropy is manufactured in combination with controlled directionality. Finally, an overview of the characteristics of the polymer used in this thesis is provided, as well as the state of the art in its applications in Additive Manufacturing (AM) and key-processing parameters.

2.1. Anisotropy gradients

2.1.1. Anisotropy in nature

Anisotropy is omnipresent in natural materials. This includes both bio-materials and mineral solids. To illustrate this, the reader is invited to find natural materials that are isotropic. Looking at abiotic materials first, one may have difficulty finding true isotropy at the microscale: some crystals[1] and gems, some mineraloids like opals [2] and inorganic glasses like obsidian, formed during the rapid solidification of lava. At mesoscale when crystalline anisotropy is homogenized, isotropy is easier to find with metals, even though finding metals in their native state, like gold, is rather rare. Furthermore, even when mesoscale properties are indeed isotropic, a mechanical anisotropic response can

---

[1] Even with cubic crystals, the properties in the direction 001, 010, 100 are the same, but they differ from those in the diagonal direction 111. As such, nearly all crystals are anisotropic mechanically, with tungsten, diamond or aluminium as notable exceptions [1]. However, many materials are encountered in a polycrystalline state, and thus can be considered isotropic at the macro-scale.

Anisotropic   Isotropic   Anisotropic
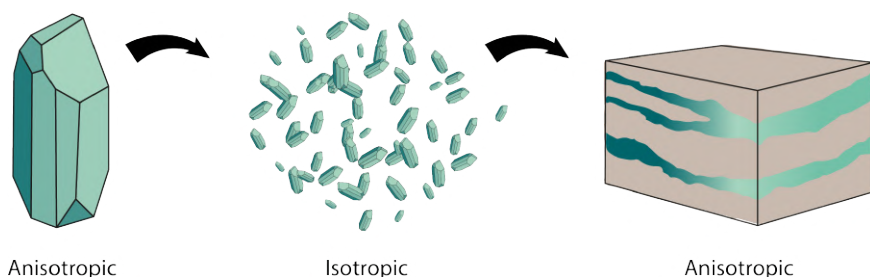
Figure 2.1 – Anisotropy also depends on scale. At the molecular scale, the material may form an anisotropic crystalline structure. However, this anisotropy can be averaged out at the mesoscale by the presence of multiple crystals. If the material is homogeneous, the bulk will remain isotropic. However, there can also be heterogeneity at the macroscale (interfaces, inclusions, defects) that still make the whole structural response anisotropic.

still be observed at the macroscale if the material is heterogeneous, which may for instance happen if an uneven distribution of defects such as voids or inclusions is found locally [3]. This is illustrated in Figure 2.1. As such, Earth's complex tectonic history produced a variety of anisotropic materials. Natural science museums are full of metamorphic rocks whose anisotropy stems from no other cause than the gigantic energy of the crust deployed over time. Directionality is dictated by tectonic motions, which create pressure and temperature gradients [4].

As life emerged, so did the materials carrying it. To produce these bio-materials, evolutionary driving principles tend to favour efficiency, i.e. making the most out of available resources, which essentially are carbon, oxygen and nitrogen. Most of the structural natural materials are anisotropic composites. Cell walls of plants are composites made of cellulose, lignin, pectin and proteins. For animal tissues, collagen, hydroxyapatite, elastin, chitin and some minerals like calcium and silica are needed. A remarkable array of structured composites are produced from this small number of building blocks [5]. High structural efficiency at the macro-scale is achieved by a hierarchical structure, organised with directionality. Many different routes lead to anisotropy, such as variations in composition, distribution of constituents, porosity, or density, as illustrated by Figure 2.2 [6].

Wood is a prime example of a structural anisotropic bio-material with weak building blocks and a hierarchical, directional structure [5]. It is also an example of a material which is both anisotropic and heterogeneous (see Figure 2.1). Its Young's modulus depends strongly on loading conditions, as shown in Figure 2.3b. The modulus of cellulose compares with that of Polyamide-6, while the matrix of lignin-hemicellulose in which the cellulose fibres are embedded compares to epoxy [5]. The arrangement into a hierarchical structure is beneficial for fracture resistance: a potential crack is led to follow a zig-zag pattern between the cell walls, and the fibrils spanning across it blunt its tip and slow its growth, as illustrated in Figure 2.3c and Figure 2.3d [7, 8]. Furthermore, wood can adapt its growth based on the loading conditions experienced by the tree, creating a structure that optimizes over time [9, 10]. As a substantial benefit to humanity, it also sequesters about 1 tonne of CO_2 per tonne (wet) [11].
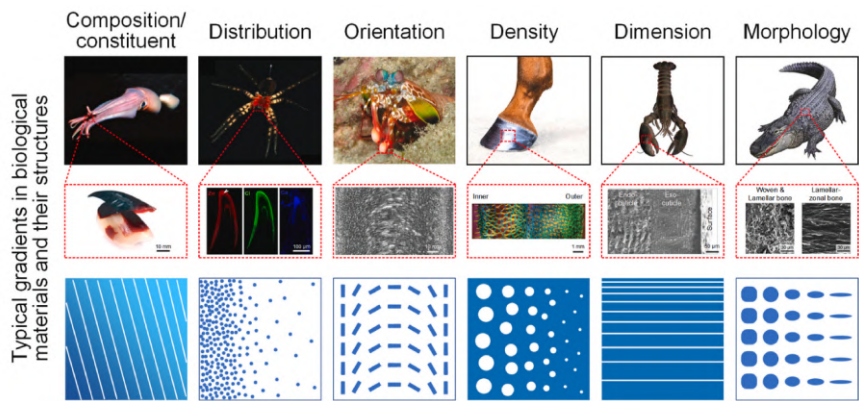
Figure 2.2 – Biological materials may display different configurations of anisotropy which provide different functionalities. These may be impact resistance, wear resistance, damage tolerance, or shape-shifting capabilities. Reproduced from Ren *et al.* [6] with permission from Elsevier.

2.1.2. Anisotropy in engineering

Humans have learnt to harness the anisotropy of natural materials to their benefit: the first toolbox of humanity consists of flint, wood and bone, and tendon strings or plant-based fibres as binding media. Their anisotropy has then been shaped in more complex ways. Evidence indicates that by the time of Ancient Egyptians, advanced wood-forming methods for ship-building were already mastered [14].

The use of composites for engineering applications has mainly increased after the Second World War [15]. Its use in aviation has enabled the reduction of the mass of aircraft, contributing to their increasing efficiency. The A350 is for instance made of more than 50 % of composites in weight [16]. The different possibilities for controlling directionality with composite materials are detailed in the following section.

2
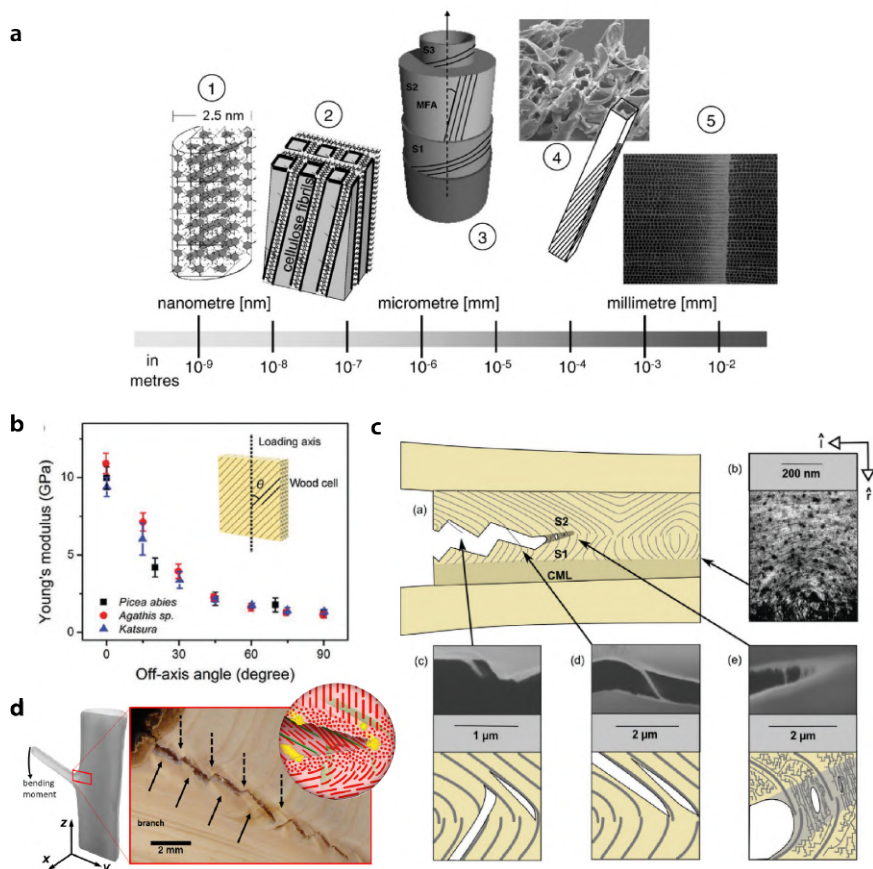
Figure 2.3 – **A.** The hierarchical structure of wood, with the crystalline lattice of a cellulose microfibril (1). These fibrils are embedded inside a matrix of hemicellulose reinforced by lignin within the S2-layer (2). The tracheids in softwoods are structured with the S1, S2 and S3 layers. (3) The cellulose fibres spiral around the schematically drawn wood cell with a direction to the longitudinal axis known as the microfibril angle (MFA). (4) The wood cells are stacked in a sequence of early wood/late wood with a variation from low to high density within an annual ring. (5) Reproduced from [12] with permission from Elsevier. **B.** This hierarchical structure leads to an anisotropic mechanical behaviour. Reproduced from [13] with permission from Wiley. **C.** The multi-level fibrillar hierarchy enables a relatively high fracture toughness. The crack is deflected in a zig-zag around the S2/S1 interface. Microfibril aggregates spanning the crack contribute to blunt its tip and slow down its propagation. Reproduced from [7] with permission from Wiley. **D.** Photograph of the crack zig-zag deflection when a bending moment is applied. Resin ducts in yellow provide anti-microbial and hydrophobic protection. Reproduced from [8] with permission from Nature.

2.2. Shape and directionality

Several manufacturing and computing challenges arise with anisotropy. For structural applications, four main approaches are presented in this section: composite lay-up, fibre steering techniques such as Automated Fibre Placement, Tailored Fibre Placement and finally continuous carbon-fibre 3D-printing. In all these cases, anisotropy stems from a top-down approach to create a composite material: fibres, which convey anisotropy, are placed within a isotropic matrix for load transfer. A schematics of each method as well as some manufacturing limitations can be found in Figure 2.4.

In traditional composite manufacturing, different layers of unidirectional or woven fibre fabrics are cut, stacked into a specific order by hand, impregnated in resin, and then polymerized using heat and/or pressure inside a mould or a vacuum bag. This is ideal for laminates with simple, two-dimensional geometries, and for simple lay-ups. Structures as big as wind turbine blades can be manufactured in this manner. However, it is difficult to control precisely the layup orientation, which is fixed within one ply.

When the performance-to-mass ratio needs to be maximized in large-scale components, for instance aircraft fuselage and wings, a better control of the fibre directionality is achieved with Automated Fibre Placement (AFP). AFP uses a robotic arm or a gantry to deposit tows of pre-impregnated carbon or glass fibres in a pre-determined orientation onto the mould or the underlying layer with heat and pressure. This can also take place on curved surfaces [17]. Variable stiffness laminates can thus be manufactured [18–20]. Several manufacturing constraints need to be integrated: limiting steering curvatures to avoid wrinkling of the fibre tows [21, 22] or having a minimal cutting length [23]. Another issue related to the width of the tow is the presence of gaps and overlaps. This can be remediated with continuous tow shearing, where width variations can be obtained by shearing the tow, essentially making it thicker [24]. The level of anisotropy can also not be tuned: the fibre volume ratio is determined by the prepreg.

Tailored Fibre Placement (TFP) offers larger freedom in the placement of fibres. Bundles of dry fibre tows are laid down and stitched onto a base material to form a dry preform of the fibre pattern, akin to embroidery [25]. Because the tow is dried, i.e. no resin is attached to it, it is more easily bent or sheared, like a thread. Layers of preforms can be turned into 3D shapes and infused with resin at a later stage. Indeed, while AFP has a minimum radius of curvature between 400 mm and 1000 mm [18, 26, 27], for TFP this is approximately 5 mm [28]. Thanks to the larger shaping freedom and the use of high-performance fibres, high structural properties can be achieved [29]. Some manufacturing considerations should be integrated in design: cross-stitches are used to keep the dried tows in place before infusion, however they cause local fibre wrinkles at high curvature locations. Furthermore, the tension applied on the tow by the embroidery machine tends to offset its path toward lower curvatures [30]. Paths can only be interrupted by cutting the tow, when enough length has already been deposited. Due to the higher risk of defects at tow ends, trajectories tend to minimize fibre path interruption via U-turns bridging parallel paths [31]. Again here, the presence of anisotropy is binary: at any point, there may either be a highly anisotropic fibre bundle or isotropic resin.

Finally, different 3D-printing techniques have also been developed for composite materials, using either short fibres for greater processability, or continuous fibre for strength. The most common technique used for composite materials is Fused Filament Fabrication (FFF), which uses a continuous filament that gets heated, molten and extruded to form a shape layer by layer. While the fibre volume ratio for AFP and TFP can be on the order of 60 % [32], this value is closer to 20 % for short-fibre reinforced composite filament, and 35.4 % for Markforged pre-impregnated CF-FR-50 filament [33].

Mechanical properties reported in longitudinal and transverse directions for the continuous carbon-fibre reinforced Polyamide (PA) material from Markforged are shown in Table 2.1 based on twelve studies compiled by Le Duigou *et al.* [34] The large range between 16 GPa and 75 GPa for Young's modulus indicates the large variability in printing quality between different experimenters and printers. However, most of the studies achieve a Young's modulus above 60 GPa.

Shaping freedom with continuous-fibre 3D-printing is restricted by a few considerations. Fibres are reported to break below radii of curvatures of 4 mm [35]. Within a part, fibre volume fraction can be tuned by changing the number of fibre layers, printed with a separate nozzle, as opposed to those printed only with the "matrix material" which can also itself be reinforced with short fibres. Due to the need for adhesion between fibre paths, up to 55 % of the deposited volume can be filled by the reinforcement material, which is itself made of 35.4 % continuous fibres [36].

Other methods of controlling the directionality of fibres with a 3D-printer include rotational devices to shear-align short-carbon fibres into patterns [37] or using a two-step process with a deposition step and a consolidation step using heat and temperature [38]. An extensive review of the diversity of techniques used to obtain 3D-printed anisotropy can be found in [39].

Taking into account the manufacturing constraints described above, computational efforts have been made to find the best possible fibre orientation for a given load case. Variable stiffness laminates have notably been optimized using lamination parameters, with AFP as manufacturing method [21, 40]. With 3D-printing, an improvement of 60 % can for instance be observed on the specific bearing strength of a lug by aligning the fibres along the principal stress directions compared to a conventional laminate with straight fibre orientation [41]. The shape of the part, which is readily controlled with 3D-printing, can also be optimized to achieve additional improvements in structural performance. A popular approach is to synchronously optimize the part design and the fibre layout by aligning fibre paths with principal stress directions. With this approach, Fang *et al.* [33] have recently obtained a 6.4-fold increase in failure load in a bracket by optimizing the fibre path in three dimensions, compared to a part where the fibres are aligned within planar printing layers. This illustrates the strong synergy that can be fostered between shaping freedom and control of the fibre directionality.
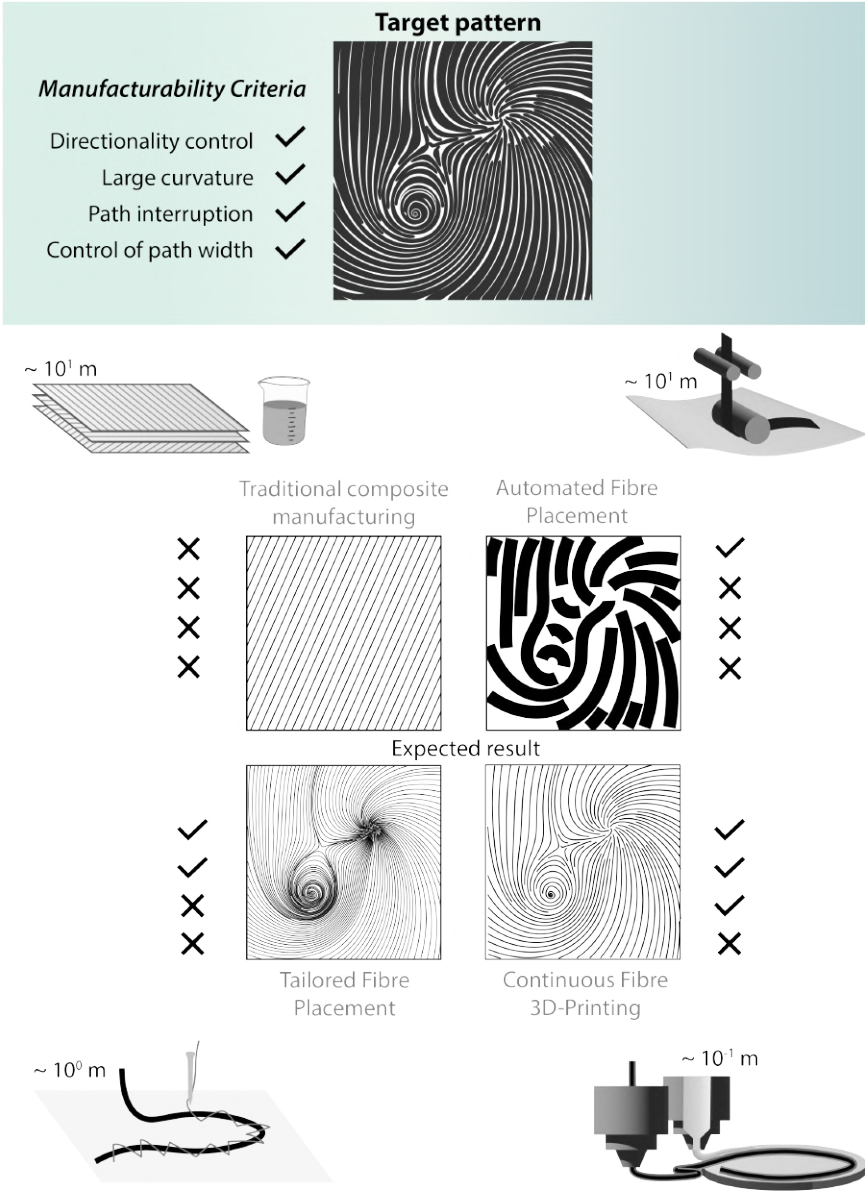
Figure 2.4 – Illustration of a target pattern with two-dimensional complexity. Its manufacturing necessitates local control of the angle direction (directionality). The vortex zone needs small curvature radii, and the sink feature requires facile path interruption. In order to create a fully dense fill of the space without gaps or overlaps for such large gradients in curvature, a path of varying width is also desired. For illustration purposes, the pattern is further transformed by the manufacturing constraints of four manufacturing methods, whose working principle is schematically added, along with the order of magnitude of the size of parts that can be manufactured by each method.

2.3. Simultaneous tailoring of shape, directionality and anisotropy levels

Several manufacturing approaches can control shape and directionality to obtain improved structural performance. Less widely encountered are approaches that allow simultaneous tailoring of shape, directionality and anisotropy levels. They can be divided into two main categories: those focusing on microstructure optimization, and those using fibre-like materials.

Isotropic materials can create anisotropic structures with tunable anisotropic levels by shaping them into spatially varying "microstructures". The term microstructure does not refer to the microscopic scale here, but to the idea that repeated unit-cells, of the smallest dimension allowed by the manufacturing technique, create a bulk "structural material" with tuned properties, in the spirit of metamaterials. In [42], control over anisotropy is obtained in an isotropic material by a unit-cell, optimized to the load case. Both the orientation of this unit-cell, and the macroscopic shape are also optimized simultaneously. Furthermore, varying unit cells with varying geometry and effective density result in different responses in compliance. Building onto this, topology-optimized shapes with structural anisotropy and varying anisotropy levels have been created by combining several well-connected unit cells into a structure [43, 44]. An example of an L-shaped beam is shown in Figure 2.5a. Another such bracket using reaction-diffusion as a driving force for the growth of lattice-like microstructures is shown in Figure 2.5b. These works remain computational and the resulting shapes have not been experimentally manufactured and tested.

Tailored anisotropic spinodal structures also recently emerged [45]. Again, the inverse design problem is of interest, namely: "What would the meta-material resemble, given a desired set of properties ?" [46]. Like in the previously mentioned approaches, microstructural optimization is achieved with isotropic materials, and porosity is here as well the key driver of the mechanical anisotropic behaviour. The difference lies in the lack of a unit-cell, facilitating the possibility to integrate them into complex shapes with smooth gradients of properties. Four different spinodoid structures joined in a seamless transition are illustrated in Figure 2.5c. Locally varying anisotropy levels can thus be created and manufactured with isotropic materials, for instance with two-photon lithography [47].

The structural properties of these metamaterials are capped by those of the bulk material. However, varying levels of anisotropy have also been envisioned with fibre-filled materials.

Schmidt et al. [49], have developed an algorithm capable of optimizing topology and simultaneously choosing the orientation and material properties between stiffness bounds of $E_1 : E_2 = 50 : 10$ (orthotropic) and $E_1 : E_2 = 18 : 18$ (isotropic). The resulting geometry, shown in Figure 1.1, displays orthotropy at strut locations. At junctions between these struts, isotropy is considered more favourable for stiffness. One can also expect it to be more robust to the multi-axial stress state at these locations, and also to simplify manufacturing, especially for three-dimensional parts. In Jung *et al.* [50] a homogenization-based multiscale approach is used to optimize spatially-varying fibre size and orientation as
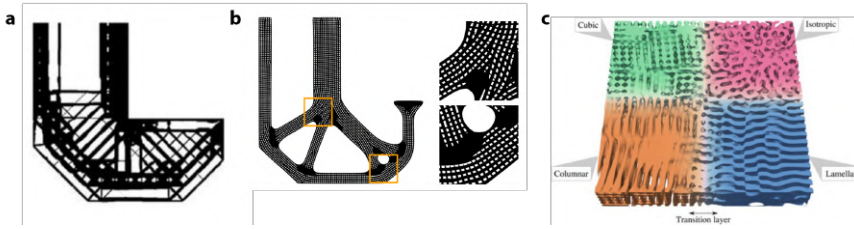
Figure 2.5 – **A.** L-shaped bracket obtained via multiscale topology optimization. Unit-cells of varying geometry and density give directionality with varying anisotropy levels to the topology-optimized shape. Reproduced with permission from [44]. **B.** The same L-shaped bracket load case optimized to reduce peak-load is obtained with a reaction-diffusion system guided by an orthotropic diffusion tensor. The porosity decreases at junction locations where several struts meet. Reproduced from [48] with permission from Springer-Verlag. **C.** Spinodoid metamaterials can show also three-dimensional elastic anisotropy response. A smooth transition between different topologies can be made. Reproduced from [46] with permission from Springer.

well as topology. A 20.8 % decrease in compliance is obtained by using spatially varying fibre size compared to a configuration with a fixed fibre-volume ratio. More recently, Vertonghen *et al.* [51] have developed a gradient-based framework capable of handling larger bounds of anisotropy with a polar formalism.

A topology optimization framework for wet fibre placement has also been developed. Stronger, bi-axial fibre orientation at junctions can be obtained by overlapping wet rovings [52]. The strength anisotropy induced by the many interfaces between print lines has also been taken into account in topology optimization frameworks, by locally selecting discrete infill orientations accordingly [53, 54].

Despite these recent advances, the interest in this field has been mostly limited to numerical frameworks by the practical difficulties of smoothly tuning levels of anisotropy on-the-fly within sufficiently large stiffness bounds with additive manufacturing.

2.4. Thermotropic Liquid Crystal Polymers
2.4.1. General description of HBA:HNA
To tailor shape, directionality and anisotropy levels simultaneously, and to overcome some of the obstacles faced by top-down approaches mentioned previously, using a bottom-up approach may be beneficial.

The thermotropic liquid crystal polymer studied in the scope of this thesis is a random co-polymer of hydroxybenzoic acid (HBA) and hydroxynaphtoic acid (HNA), with a ratio 73 : 27. It is also commercialized under the tradename Vectra A950 and Vectran in its fibre-form. Many of its properties derive from its liquid crystalline properties in the molten state, therefore the concept of liquid crystallinity is briefly introduced. We then describe the microstructure and morphology of this polymer with thermal and rheological properties that are relevant for its use in 3D-printing. Traditional manufacturing routes and applications are summarized, and the recent works in 3D-printing thermotropic LCP are presented.

2

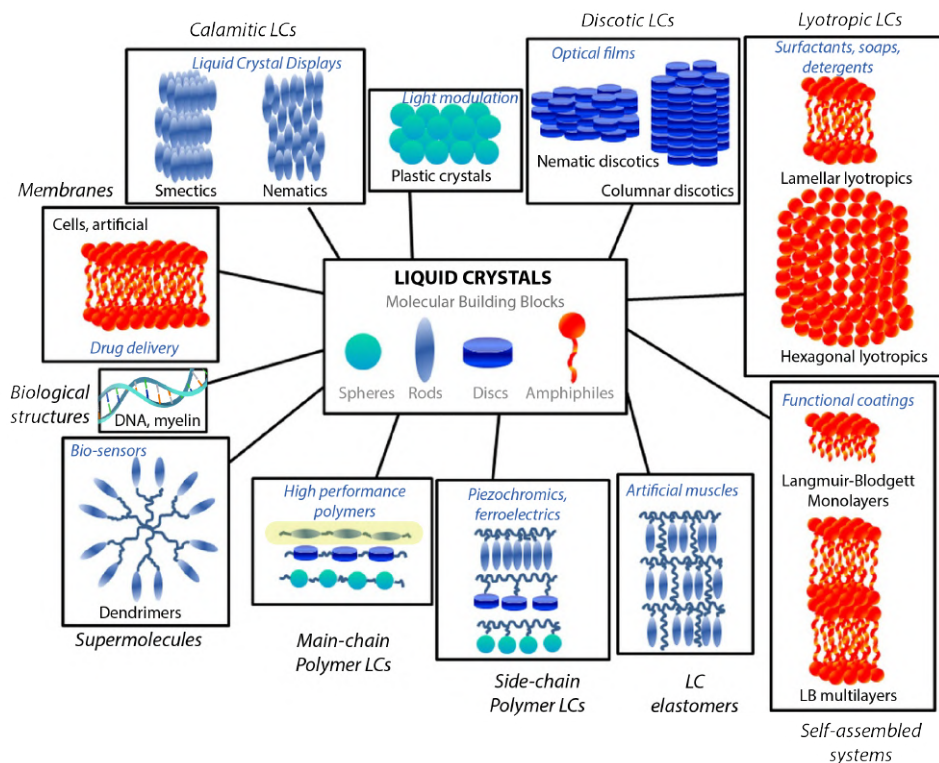Figure 2.6 – Classes of liquid crystals and their applications. Reproduced and adapted from [55]. The class of LC used in the scope of this thesis, rod-like main-chain polymeric LCs, is highlighted in yellow.

Liquid crystallinity

Liquid crystallinity (LC) refers to a state of matter (or meso-phase) where the material can flow like a liquid but displays a level of order like a crystalline solid. As a shortcut, liquid crystals also refer to the materials that can display a liquid crystalline phase.

The discovery of liquid crystals is attributed to Austrian botanist Friedrich Reinitzer in 1888 with cholesterol benzoate extracted from plants. As summarized in Figure 2.6, a very large diversity of molecular structures can display LC properties, from membranes to polymers, and from synthetic or biological origin. Some common occurrences include DNA [56], soap [57], and liquid crystal displays [58]. The majority of LCs structures create self-organising soft matter. The structural materials displaying a LC phase are called LC polymers (LCPs). They are distinguished by their molecular weight being orders of magnitude larger than conventional LC materials.

The first LCPs were invented in the late 1960s. They were lyotropic, meaning that the LC phase is triggered by dissolving the molecules under acidic conditions. Aramids such as Kevlar are successful commercial products stemming from this class of LCP [59]. Their need to be spun in strong acid solvents presents environmental and safety challenges [60]. To overcome these, the first thermotropic LCP was invented in 1976 by Eastmann-Kodak and commercialized under the name X7G [61]. "Thermotropic" refers to the ability of the polymer to display an LC phase with heat rather than through dissolving means. Soon after, Celanese and Dupont developed families of polymers aiming to maintain melt-processability while increasing their service temperature. In particular, a patent application by Calundann from Celanese in 1979 marks the first use of the wholly aromatic thermotropic LCP made from HNA (2-hydroxy-6-naphthoic acid) and HBA (4-hydroxy-benzoic acid) which is studied in this thesis, hereafter referred to as HBA:HNA [60, 62].

Hierarchical description of HBA:HNA

HBA:HNA is a highly hierarchical material, with features that drive properties at different scales. In this introduction, we divide them into two main scales: molecular morphology ($< 1\,\mu m$) at the level of polymeric chains, and microstructure ($> 1\,\mu m$) with flow-induced orientation of nematic domains and corresponding textures, and resulting fibrillar morphologies induced by flow.

Molecular morphology

The macro- and micromorphological behaviour of main-chain LCPs is dictated to a large extent by molecular morphology. Because of this, the crystallinity of HBA:HNA and other main-chain LCPs has been largely studied [65]. The hierarchical complexity of the distribution of chains is summarized in Figure 2.7. Typically, in semi-crystalline polymers, crystallites consist of neatly-packed and folded chains, surrounded by amorphous zones where chains are loosely entangled with no order. In contrast, crystallinity in LCP is very different. Three main characteristics of the HBA:HNA co-polymer chains render periodic packing difficult: first, the arrangement of the monomer units, shown in Figure 2.7a and Figure 2.7b, has been shown in X-ray diffraction to be random [68], which significantly lowers the possibility of long-range register between two chains. Second, as illustrated in

2
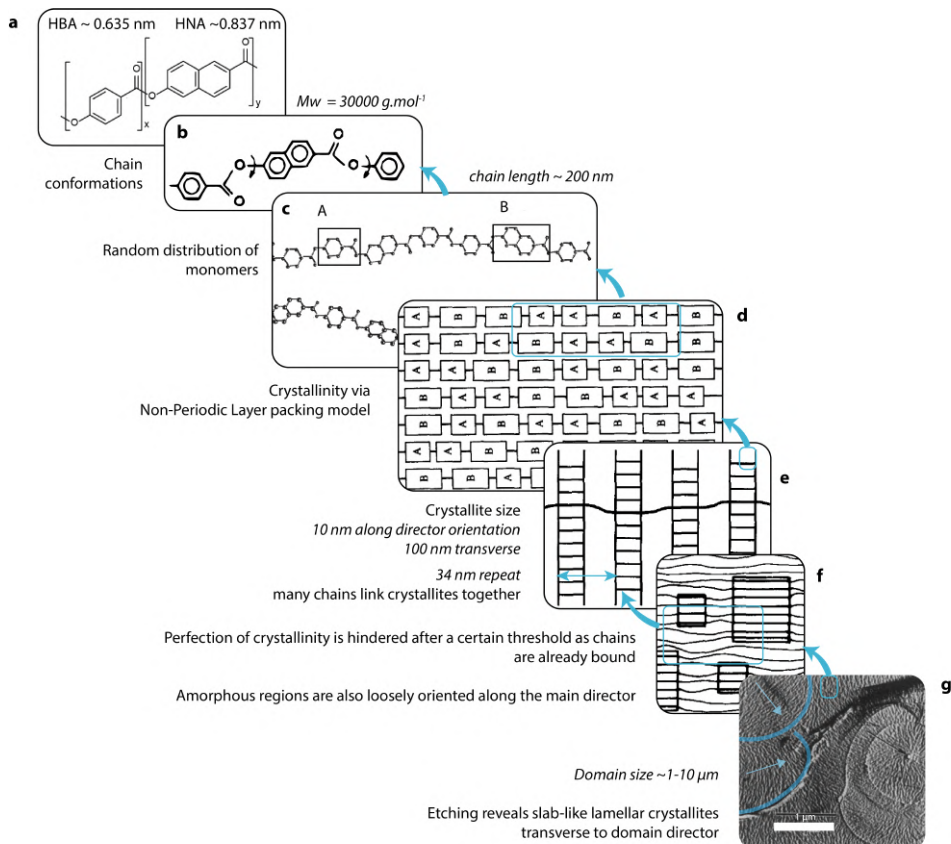
Figure 2.7 – **A.** Chemical backbone of HBA:HNA **B.** Possible chain rotations between the monomers. Reproduced from Acierno *et al.* [63] with permission from Elsevier. **C.** A random distribution of the monomers, identified as A and B, renders traditional regular crystallinity packing difficult. Reproduced from Karacan [64] with permission from Wiley. **D.** The Non-Periodic Layer model suggests a different packing system with a longer-range sequence registry. Reproduced from Langelaan *et al.* [65] with permission from Elsevier. **E.** Experimental evidence suggests that crystalline zones are rather large in the direction transverse to the main chain axis, and are approximately periodic with 34 nm period. Reproduced from Hudson & Lovinger [66] with permission from Elsevier. **F.** Because the chains are on average 200 nm long, one chain is thought to be involved with multiple crystallites. The amorphous zones consist of more loosely oriented chains. Reproduced from Butzbach *et al.* [67] with permission from Elsevier. **G.** An etched sample is shown in Transmission Electron Microscopy (TEM). The crystallites are oriented perpendicular to the average chain direction known as the nematic director, represented by a blue arrow. Reproduced from Hudson & Lovinger [66] with permission from Elsevier.

2

Figure 2.7c [64], the naphthalene monomer and its kink make the chain geometry rigid and tortuous, restricting the possibility of chain folds [69]. Finally, packing is also frustrated by a mismatch in length, with a ratio close to 3:4, between HBA with 6.35 Å and HNA with about 8.37 Å [66].

Despite these obstacles, a degree of crystallinity is still achieved via a larger-scale correlation between HBA and HNA monomers. This can happen via the "Non-Periodic Layer" model, shown in Figure 2.7d, developed initially by Windle and coworkers [70–72]. Inter-chain correlation can occur between sequences of similar length, in spite of the aperiodicity within segments. Hudson & Lovinger have used diffraction and etching to visualize the slab-like crystallites formed from these matched sequences [66]. Dimensions of 10 nm in thickness, and 100 nm laterally have been derived for these slabs, spaced together by 34 nm. This small repeat, contrasting with the average molecular length of 200 nm, combined to the impossibility of tight folds for such a rigid chain, implies that the average chain has segments incorporated in multiple lamellar crystals, as shown in Figure 2.7e. While the ordered region appears to impart rigidity to the polymer in a similar fashion to conventional semi-crystalline polymers, the level of crystallinity ranges typically for HBA:HNA 73 : 27 from 10 %-20 % in a pristine sample, up to 30 % for an annealed one [73]. The crystallites therefore account for a small proportion of the material.

A large difference to semi-crystalline polymers is the amorphous phase: unlike the typical entangled flexible chain conformation seen for these, a main-chain LCP like HBA:HNA displays overall an aligned nematic configuration, as shown in Figure 2.7f [67]. Two consequences arise from this relatively similar aligned conformation between crystalline and amorphous zones: a low enthalpy of fusion compared to other polymers (from 0.45 J/g as extruded to 10.5 J/g when annealed for 5 h [73]) and a coefficient of thermal expansion that is low and negative when the polymer is melt-spun [74].

Microstructure of HBA:HNA

As shown in Figure 2.7g and schematically represented in Figure 2.8a, the chains are oriented in an almost parallel manner along a nematic director within a domain of size 1 μm to 10 μm [66, 79, 80]. Texture refers to the distribution of local orientations within a poly-domain sample. The flow behaviour during melt heavily influences the size, shape and orientation of these domains [75, 80]. While elongational flow is the most effective at aligning domains and even merging them [75], shear flow can also act to impart a global orientation. However, a tumbling motion can take place instead of flow-alignment [77], as shown schematically in Figure 2.8c. This depends on the backbone and molecular weight of the polymer and the chain stiffness, as illustrated in Figure 2.8d [78]. In HBA:HNA, interestingly, the tumbling parameter λ is always reported very close to unity, but some studies assume a shear-tumbling nature to correlate to experimental measurements [81, 82] while others propose a shear-aligning behaviour [76, 83, 84]. In spite of these discussions, a three-dimensional approach to predict the director field has recently been developed by Sullivan *et al.* [76] which has successfully reproduced skin-core regions in injection-moulded plaques.
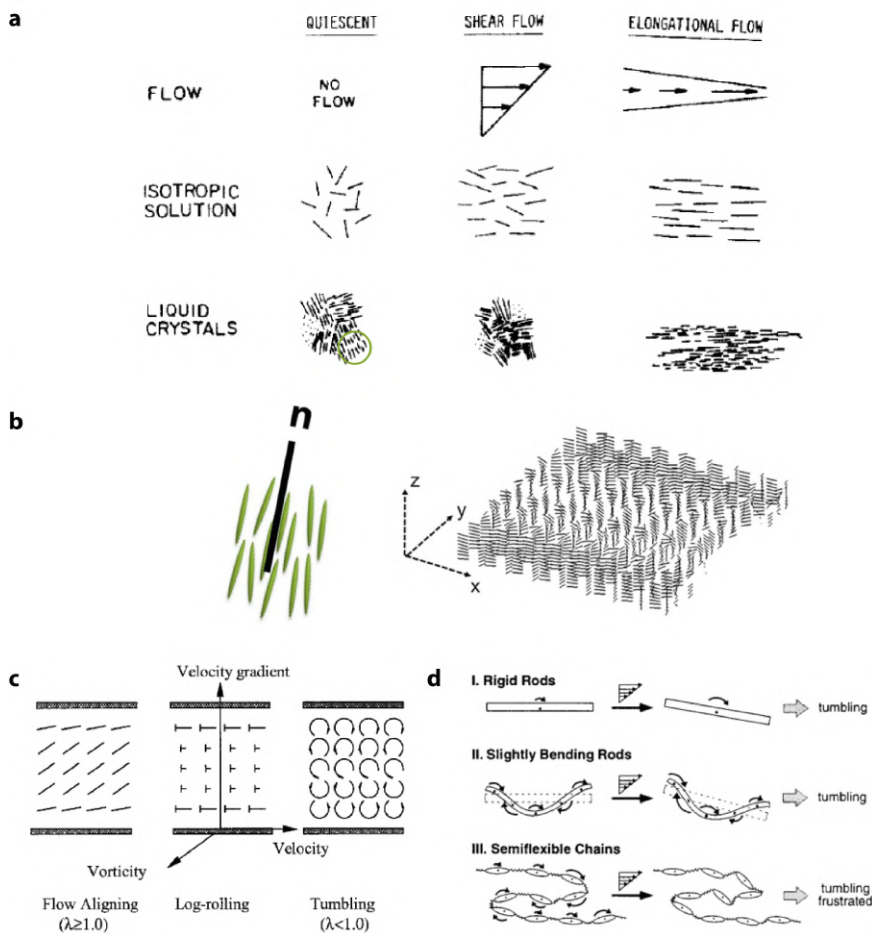
Figure 2.8 – Effect of nature of the flow on molecular orientation. **A.** Schematic representation of flow-induced orientation of rod-like molecules. Reproduced from [75] with permission from Wiley. **B.** The same nematic order is heavily influenced by complex flows, leading to a potentially complex distribution of directors. Together, they make the mesoscopic texture of the bulk polymer. Reproduced from [76] with permission from Sage. **C.** Under shear flow, main-chain LCPs may tend to tumble instead of flow-aligning. A middle behaviour is log-rolling, which has been observed for HBA:HNA at low molecular weights. Reproduced from [77] with permission from Taylor & Francis. **D.** If the polymer is of the tumbling nature, molecular flexibility can still influence its behaviour during tumbling. For instance, tumbling motion can be suppressed by the semi-flexible nature of the chain compared to a perfect rigid rod. Reproduced from [78] with permission from ACS.
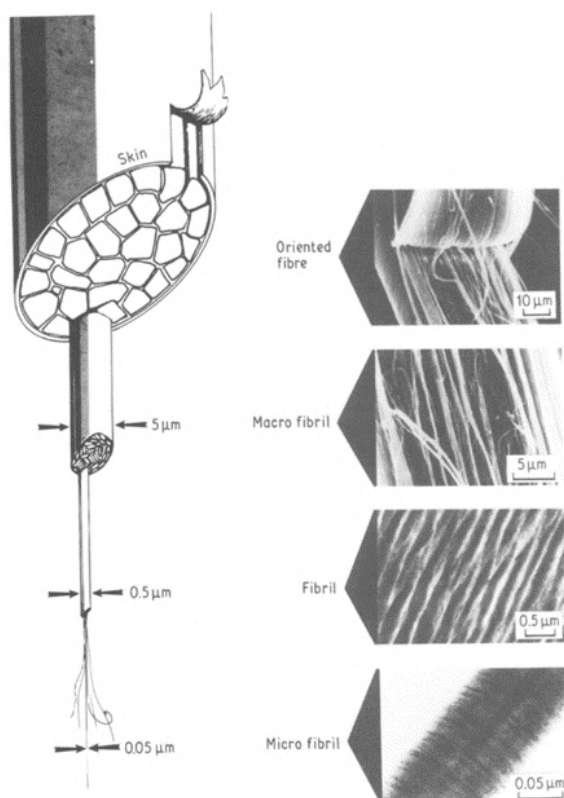
Figure 2.9 – The hierarchical fibrillar microstructure of LCP is shown with its main features: an aligned skin and lesser-aligned core displaying a multi-scale fibrillar structure. Micrographs of oriented extrudates at different scales also show experimental evidence. An example of a banded texture is seen in the bottom micrographs. Reprinted from Sawyer et Jaffe [80] with permission from Chapman and Hall.

Accurate simulation of the flow behaviour of HBA:HNA is still in development, but can also be indicated in aligned samples by banded textures, which have been observed both in thermotropic and lyotropic LCP [85–87]. These patterns, consisting of dark and light bands visible under polarized light, are periodically arranged and oriented parallel to the flow. The bands have been linked to a relaxation phenomenon or 'recoil' after cessation of shear [88]. The resulting sinusoidal-like, periodic spatial modulation of the orientation due to the recoil, leads to local variations of the effective birefringence that can be observed with polarized light [89].

The capability of HBA:HNA, like other thermotropic co-polyesters, to align in flow, results in a highly fibrillar microstructure. Sawyer & Jaffe have described this hierarchical microstructure, reproduced in Figure 2.9. This fibrillar model involves three scales of fibres. Macro-fibrils are about 5 µm in diameter. They can be peeled into fibrils of size 0.5 µm, which can then be noticed to split further into microfibrils of size 5 nm [80]. These fibres are observed both for extrudates and injection-moulded parts.

Physical properties of HBA:HNA
Thermal range

High-performance applications often require materials that maintain their characteristics throughout a large temperature range. In this section, the main thermal properties of HBA:HNA are summarized. As an upper value, the degradation of the polymer without heat treatment does not start before 400 °C, with a 3 % mass-loss measured between 400 °C and 480 °C. The onset of thermal decomposition starts at 484 °C [90]. However, as for many polymers, relaxation processes such as a glass transition take place and reduce its stiffness, effectively restricting its service temperature to lower values.

When measuring the dynamic stiffness of HBA:HNA over different temperatures, three different molecular processes have been identified: at −50 °C a relaxation is associated to local motions of the hydroxybenzoic moiety. For the hydroxy-naphthalene moiety, this relaxation takes place at ca. 60 °C. A last relaxation akin to a glass transition occurs at around 110 °C, related to the cooperative motions of the two units [73, 91]. However, Saw *et al.* [92] observe that this "glass-transition" does not correspond to a long-range segmental motion as in typical amorphous or semi-crystalline polymers, as no loss of orientation is shown to occur in fibres of HBA:HNA. They attribute the relaxation to rotations of polar structures along the chains.

By increasing the temperature further on a specimen without thermal history, the melting point is reached at around 282 °C [90]. In a similar manner to semi-crystalline polymers, the solidification temperature can be lower due to the super-cooling (or undercooling) effect, related to nucleation of crystallites [93]. For a cooling rate of 10 °C.min^{-1}, a solidification point at 240 °C is reported in [90].

Various thermal treatments have been studied to increase the melting point of HBA:HNA, up to 350 °C [92, 94, 95]. Annealing is used to perfect crystallinity [73], and step-annealing can also create cross-links involving interchain transesterification reactions [94, 96–98]. When these occur, however, the recyclability of the polymer is greatly undermined [99]. It follows naturally that service temperature highly depends on the heat treatments applied.

As a result, the upper bound of the thermal range of Vectran, measured by the 50 % strength retention temperature, is around 150 °C [100] whereas it is between 230 °C and 400 °C for aramids (standard and high modulus Kevlar). For PEEK, this value is around 240 °C [100]. Its lower bound is below −200 °C, as Vectran fabric sees a strength increase of 20 % at cryogenic temperatures [101]. As a result, it can be used in anti-sloshing devices in liquified natural gas tankers, exposed to −162 °C [102].

Rheological considerations

Together with thermal characteristics, the rheological properties of HBA:HNA can be useful to understand phenomena at play during processing. The viscosity of this polymer is plotted in Figure 2.10a against the apparent shear rate through a 3D-printer nozzle. The apparent shear rate can be approximated [106] by

$$\dot{\gamma} = \frac{4Q}{\pi R^3},$$

with $R = 0.2$ mm as the nozzle radius. The volumetric flow rate Q is given by $Q = whV_p$ where h, w, V_p are the layer height, width and print speed respectively. The viscosity η can be approximated by a power law behaviour with $\eta = K\dot{\gamma}^{n-1}$ for shear-thinning fluids. The material parameters $k = 5000$ Pa.s^n and $n = 0.375$ were extrapolated from viscosity-shear rate curves of the LCP at 290 °C [103]. At a layer height of 0.10 mm, the viscosity of HBA:HNA at a printing speed of 30 mm/s is ca. 160 Pa.s while for ABS, it is around 650 Pa.s. The shear-thinning behaviour combined with lower viscosity is an advantage for injection-moulding, as cavities as thin as 0.2 mm can be filled at low injection pressures [107].

Whether the ultimate goal of the processing route is to maintain or avoid anisotropy, knowledge of the orders of magnitude of time needed for the anisotropic features of the flow to relax back to a global isotropic state can be enlightening. Figure 2.10b,c,d extracted from [105] highlights relaxation time scales for HBA:HNA after a shear force has been applied, measured with different methods. As measured by a rheometer, the stress exerted by the melt is shown in Figure 2.10b. At 310 °C, it is seen to decay after about 7 s. Observation with polarized light also shows that the texture returns to an isotropic state after the occurrence of shear bands within 6 s. In contrast, Wide-Angle X-ray Scattering (WAXS), which provides information at the molecular scale, shows that an appreciable degree of alignment can still be found after 1300 s. As stated in [105], this indicates that the texture relaxation and the molecular orientation relaxation are distinct processes with their own time scales. These relatively large durations before full relaxation takes place can be useful to adapt manufacturing processes to the level of anisotropy desired.
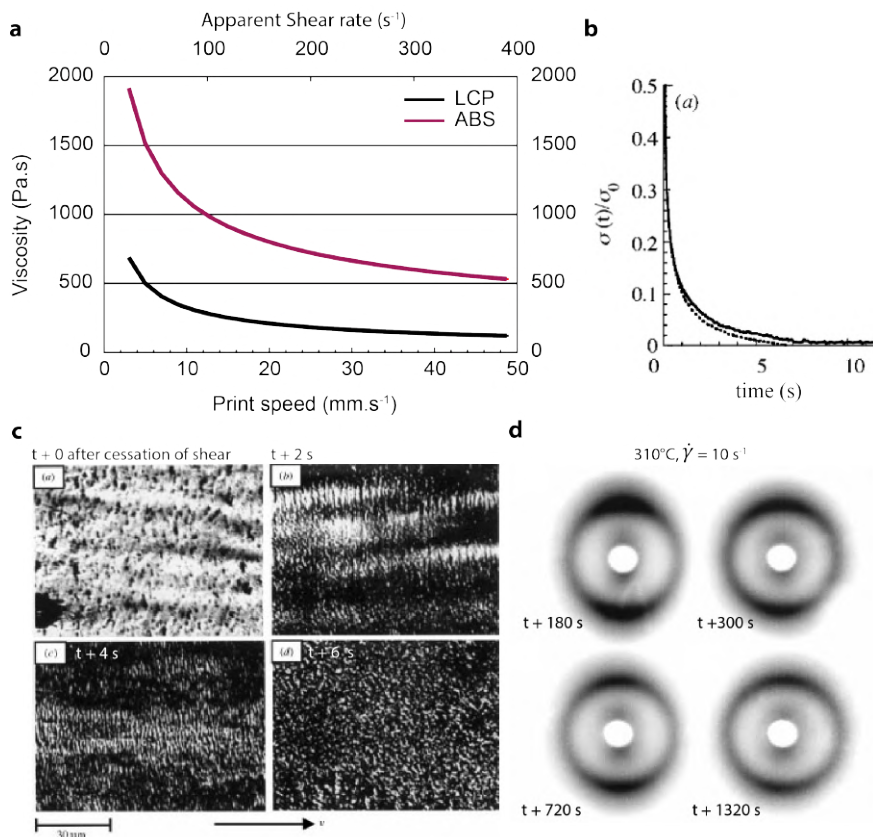
Figure 2.10 – Some rheological characteristics of HBA:HNA. **A.** Viscosity of LCP, like other polymers such as ABS, shows a shear-thinning behaviour plotted for different shear rates and equivalent 3D-printing speeds. Data from [103] for HBA:HNA and [104] for ABS. **B.** Stress-relaxation of HBA:HNA measured by a strain-controlled rheometer after cessation of shear $\dot{\gamma} = 10\,\mathrm{s}^{-1}$ shows a complete relaxation after 7 s. **C.** Likewise, optical observation shows a relaxation of the texture within the same time frame. **D.** In contrast, Wide-Angle X-ray Scattering (WAXS) indicates that after 1300 s some molecular alignment can still be found, indicating two relevant time scales for relaxation for molecular orientation and texture. Images of **B,C,D**, reproduced from [105] with permission from Royal Society.

2.4.2. Applications of LCPs, available processing routes and resulting performances

Applications

The different scales of applications of HBA:HNA are shown in Figure 2.11. Injection-moulded and melt-spun forms can be found, either to create ropes or larger structures with fabric. A diode-receptacle is shown with injection-moulding. Anti-puncture strips can be embedded in bicycle tyres [108]. Its high tensile strength and relatively low moisture regain (<0.1%) have led it to be used for marine applications, both for ropes and sail cloth [109].

Like many polymeric fibres, it retains only 10-20% of its tensile properties in compression, compared to 60-80% for carbon and glass fibres. This is one of the limitations to its use as composite reinforcement for primary structural loads [110]. In contrast to carbon fibres which can take compression because its graphene sheets are folded and interlocked [111], the highly fibrillar microstructure of Vectran tends to split or defibrillate when exposed to compressive loads. Instead, the compression force are accommodated by widely distributed kink bands, and create little damage to the load-bearing fibres. This enables the fabrics and fibres to sustain many bending/folding cycles with minimal loss of tensile properties [101, 112]. As a result, it has been used in flexible composites for inflatable structures, for instance as structural layer of air beams for military emergency shelters, as shown in Figure 2.11d. Larger structures, for instance air-supported composite radomes are also developed by ILC Dover, shown in Figure 2.11e [112].

These properties are also particularly attractive for space applications, leading it to be used in fabric form in previous missions, for instance as astronaut gloves, and to be also investigated as a restraint layer for future inflatable habitats [113]. Notably, its strength increase at $-62\,^{\circ}$C has led it to be selected for the 1997 Mars Pathfinder mission as airbag material and external assembly tendons as illustrated in Figure 2.12 [114]. A more detailed review of these space applications is available in Chapter 5.

2
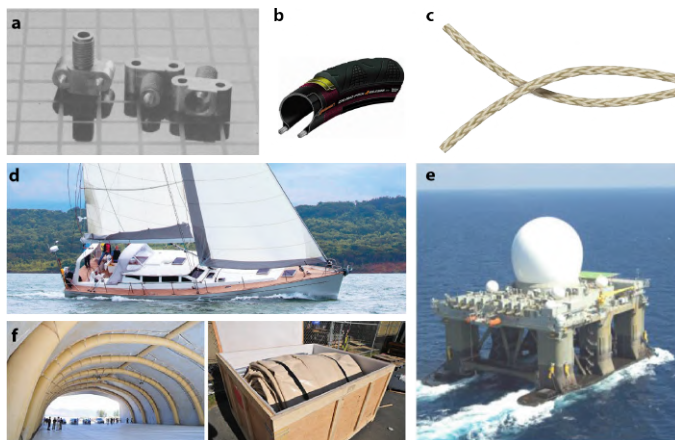
Figure 2.11 – Examples of technical applications for Vectra and Vectran. **A.** Injection-moulded diode holder. Reproduced from [63] with permission from Springer. **B.** Cross-section of bicycle tyre with Vectran puncture strip in yellow [108]. **C.** Marine ropes and **D.** sail cloth can be made from Vectran [109]. Large flexible composite structures are also developed, for **E.** air-supported radome or **F.** fast-deployment of emergency shelters in difficult zones [115].
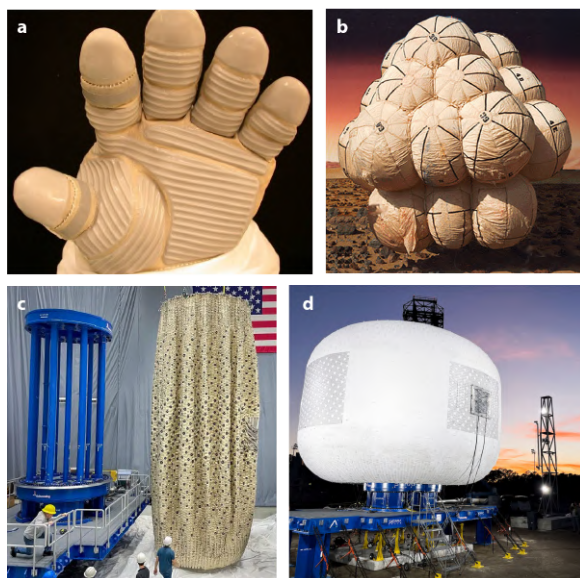
Figure 2.12 – Examples of different space applications for Vectran. **A.** Vectran is utilized inside the glove palm of astronaut gloves [116]. **B.** Artist rendering of the Mars Pathfinder airbag setup which successfully protected the payload upon landing [114]. **C.** Inflatable structure made with a restraint layer with woven straps of Vectran, before inflating and **D.** full-size model of the future space habitat before burst-test. Image courtesy of Sierra Space [113].

2

Injection-moulding

During injection-moulding, the material advances through the mould channel in a fountain-type flow [117], resulting in high extensional forces on the surface and weaker shear forces in the centre. This process forms a highly aligned skin and a lesser-aligned core with complex layer-like microstructures [118]. To avoid weld lines, anisotropy must be reduced. Different methods have been used such as push-pull moulding with two gates to switch flow directions [119], or the addition of fillers such as glass fibres. The skin-core effect is effectively reduced while the material is still able to fill very thin sections [107]. A review of different applications can be found in [120], and an example of an injection-moulded precision part is shown in Figure 2.11a.

Extrusion

Extruded LCPs also exhibit a hierarchical fibrillar core-shell microstructure [80] as shown in Figure 2.9. Decreasing the diameter increases the proportion of highly aligned skin and therefore increases the mechanical properties. As a result, HBA:HNA is used to produce high-performance fibres with moduli ranging from 100 GPa to 200 GPa and strengths up to 2 GPa [101]. In particular, Kuraray Co. Ltd commercializes two grades of melt-spun HBA:HNA fibres, under the tradenames Vectran UM (improved modulus) and Vectran HT (improved heat-treatment). The properties of Vectran HT are similar to Kevlar 29 aramid fibres. Vectran UM has a melting point of 350 °C and for Vectran HT, no melting point is reported [121]. Proprietary heat treatments to obtain such high melting points are patented [122]. These fibres also demonstrate excellent resistance to high temperatures and creep [123].

Thin-films

Thermotropic LCPs can be also extruded in sheet form via "foil spin-trusion" [124, 125]. These tightly packed molecular films also exhibit excellent gas barrier properties [126]. Parts can be manufactured from the films by stacking them and heat-pressing them just below the melting temperature to allow a solid-state polycondensation reaction to fuse the individual layers, like prepregs [125]. This method produces monolithic composites with moduli of 65 GPa and strengths of 1.7 GPa. However, the need to stack individual unidirectional sheets manually significantly limits the accessible geometries.

Three-dimensional printing

Since the control of the direction of the nematic domains is key to ensuring high performance, 3D-printing is an attractive processing route for thermotropic LCPs. Early efforts in the 1990s have focused on "in-situ composites" with LCPs. In these systems, small amounts of LCP are blended with other thermoplastic materials with lower melting temperatures. The material is extruded at high elongational flow rates above the LCP melt point, forming elongated fibre-like LCP particles along the extrusion direction [137, 138]. This approach has had limited success due to low fibre content and discontinuous reinforcement [139, 140]. Newer methods have employed optimized mixing units to form nearly continuous LCP fibres, and achieve relatively high mechanical properties without the drawbacks of traditional fibre-reinforced 3D printing approaches [141, 142].

Instead of compounding, Gantenbein *et al.* [99] have used FFF to extrude HBA:HNA directly without fillers or thermoplastic matrices. Figure 2.14a shows the schematic influ-
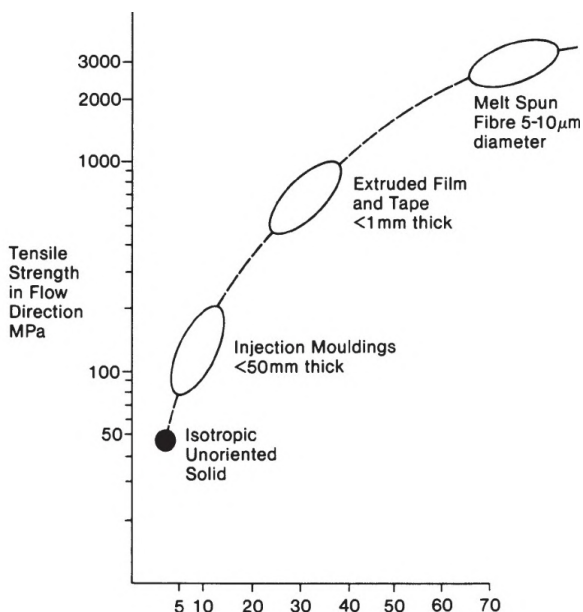
Figure 2.13 – Tensile strength of main-chain LCP versus stiffness according to the manufacturing route employed. Reproduced from [79] with permission from Springer.

	Name	Characteristics	Density (g.cm^{-3})	Young's modulus (GPa) E_L	E_T	Tensile Strength (MPa) S_L	S_T	Source
Unfilled polymers	LCP	Spun-fibre (Vectran)	1.4	55-103	NA	2900-3200	NA	[100, 101]
		Injection moulded		15-15.4	*	120-127	*	[100]
		3D-printed		15.4-17.9	2.0-2.6	363-426	27.4-44.1	[99]
	PLA	Injection moulded	1.25	3.07-3.7	*	49.5-55	*	[127, 128]
		3D-printed		3.0-4.0	2.5-4.0	51.1-63.9	34.7-59.1	[127–129]
	Polyamide	Injection moulded	1.06	2.15	*	42.1	*	[127]
		3DP		1.29-1.34	1.14-1.24	24.6-45.3	19.5-43	[127, 130]
	PC	Injection moulded	1.2	2.31	*	33.9	*	[127]
		3DP		2.0-2.1	1.5-1.6	37.9-51.7	19.9-23.1	[127, 130]
	PEEK	Injection moulded	1.3	4	*	98	*	[131]
		3DP		3.8-4.7	3.0-4.7	82.3-127.8	29.7-85.4	[132–134]
Wood	Oak	Hardwood	0.9	20.6-25.2	5	133-162	8	[100]
	Douglas Fir	Softwood	0.5	12.3-16.3	1	71.5-87.4	2.3	[100]
Metals	Steel	AerMet 100	7.85	200	*	2000	*	[100]
	Aluminium	7055-T7751	2.87	69	*	607	*	[100]
Composites	CF/Epoxy	UD CF/Epoxy prepreg	1.56	129-164	8.5	1740-2170	49.8-56.7	[135]
	PA-12-CF	3DP + compaction, 9TLabs	1.46	130	6.5	1820	39	[38, 136]
	CCF/CF-PA	3DP, Markforged	1.4	16-75	0.2-6.3	450-1050	10-50	[34]

Table 2.1 – Overview of transverse and longitudinal performance in stiffness and ultimate tensile strength of HBA:HNA, processed through different routes, and a selection of other materials.

ence of 3D-printing on molecular orientation. In the melt at rest, the directors within nematic domains are randomly oriented. The pressure of the non-molten filament onto the melt results in the movement of the molten domains through the contraction die of the nozzle, with a combination of elongational and shear flow. The resulting alignment of domains is partially conserved as the material is exposed to ambient temperatures upon exit. The typical skin-core microstructure shown in Figure 2.9 is also observed with an increasing proportion of lesser-oriented core as layer height increases.

The monolithic LCP structures, which can take complex shapes thanks to 3D-printing, reach tensile properties in between injection-moulded components and spun-fibres, as seen in Table 2.1. In Table 2.1, properties of HBA:HNA processed with different routes are compared to un-reinforced 3D-printed polymers and other materials such as wood, metals and 3D-printed continuous composites.

As shown in Figure 2.14b, unidirectional laminates manufactured with this method follow Classical Laminate Theory [143, 144] according to the following relation:

$$\frac{1}{E_x} = \frac{\cos^4\theta}{E_{11}} + \frac{\sin^4\theta}{E_{22}} + \left(\frac{1}{G_{12}} - \frac{2v_{12}}{E_{11}}\right)\cos^2\theta\sin^2\theta,$$

where E_{11}, E_{22}, G_{12}, v_{12} are measured experimentally for each layer height, and θ is the angle between the loading direction and the reinforcement direction. Due to the highly oriented fibrillar nature of LCPs, their tensile strength is also highly influenced by the loading angle. It ranges from 363-426 MPa in the longitudinal direction, to 27.4-44.1 MPa in the transverse direction. This range depends on layer height, with larger properties obtained for the smallest layer height, 0.05 mm. The combination of this anisotropic material as well as shaping freedom imparted by 3D-printing opens the possibility to lay down material properties according to the load case envisioned. This is illustrated in Figure 2.14c, by the example of a hole in tension. The curvilinear fibre path, which follows the stress lines developing around the hole, almost doubles the maximum strength in tension compared to a simple unidirectional path. Compared to a hot-pressed isotropic LCP, an almost ten-fold increase is observed. However, in the same study, annealing the 3D-printed parts at 270 °C has been shown to trigger cross-links, rendering the material untractable. In contrast, non-annealed 3D-printed parts retain a high melt-flow index, indicating that they can be re-processed into filaments and show a potential for recyclability.

2
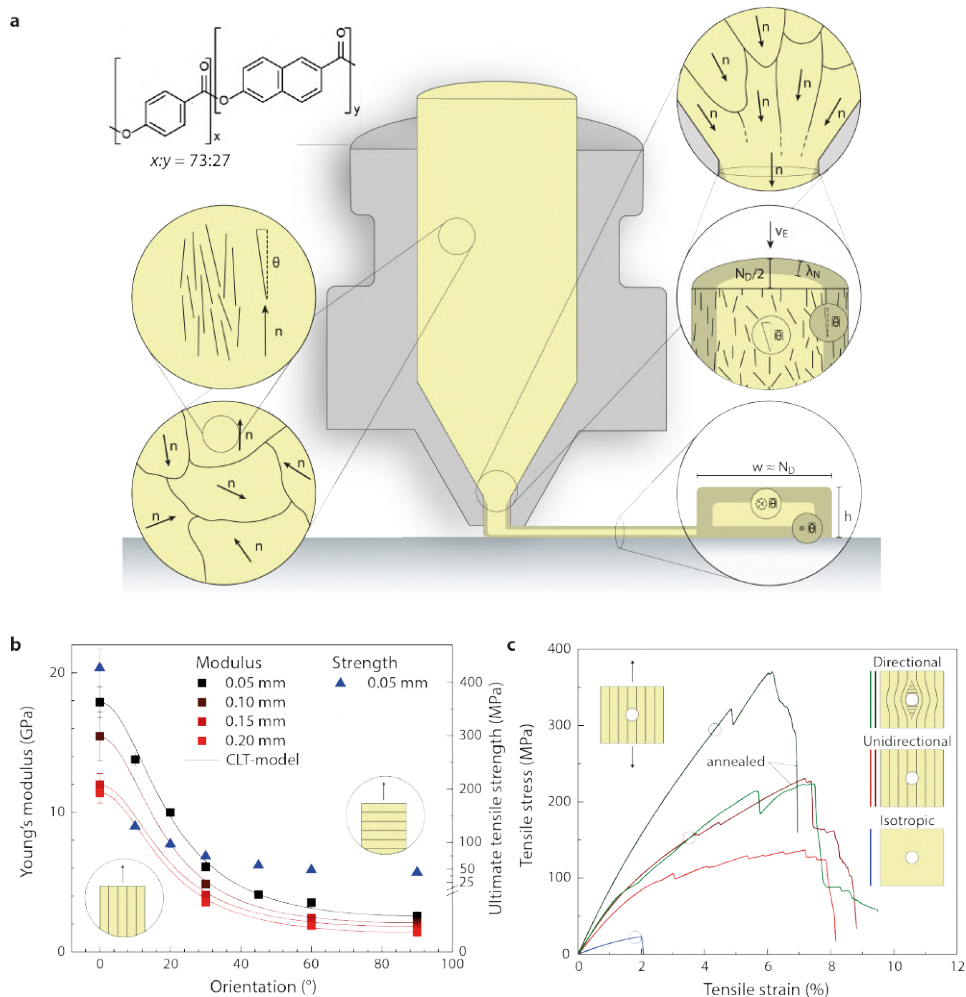
Figure 2.14 – Three-dimensional printing of HBA:HNA. **A.** Inside the 3D-printer nozzle heated to a minimum value of 295 °C, the LCP melt is in the nematic phase. Molecules are oriented along nematic directors within domains. Globally, the melt is isotropic. Upon extrusion, elongational and shear flow create a longer-range alignment of the domains, which is partially frozen in place as the extrudate solidifies, exposed to the ambient temperatures. A skin-core microstructure emerges from this method depending on the layer height. **B.** The resulting mechanical properties at part level follow Classical Laminate Theory. **C.** An Open-hole tension test is performed with different layer geometries, with and without annealing, revealing the advantage of 3D-printing at steering the printed lines according to the load case.
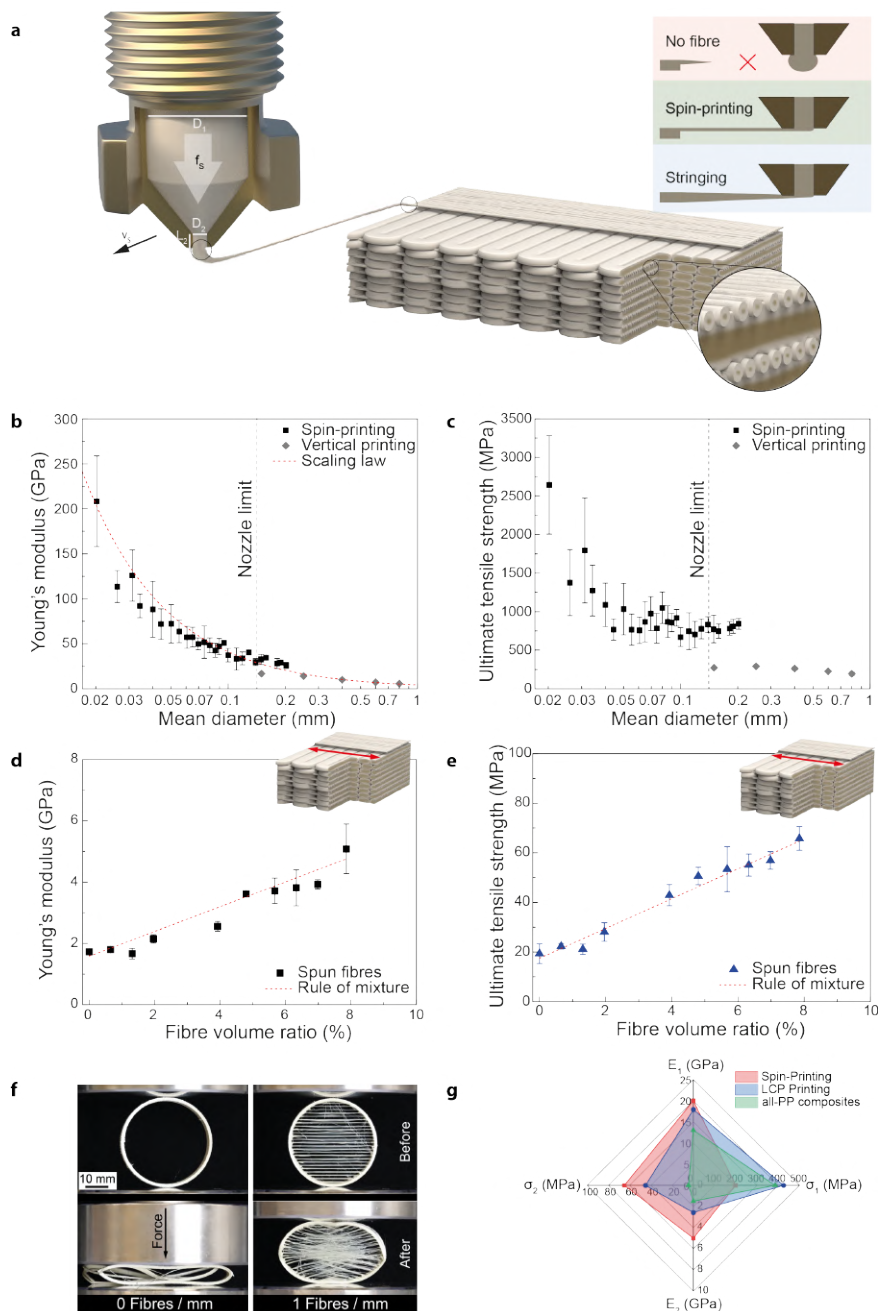
Figure 2.15 – **A.** HBA:HNA can also be spun by the 3D-printer nozzle by a process called "spin-printing". Constant diameter spun-lines of high mechanical properties can be embedded into a matrix of the same polymer. **B.** The stiffness of these 3D-printed fibres attain the range of Vectran fibres. **C.** While their strength is lower, it is still comparable to values of aluminium. **D.** The largest improvement in part stiffness and **E.** strength is obtained when the fibres reinforce the weaker 90° direction of the print. **F.** The fibres can also be incorporated as reinforcement spanning holes inside parts, like bamboo [145]. **G.** The spin-printing method is compared to LCP-printing and all-polypropylene structures produced by hot compaction of co-extruded tapes [146].

2
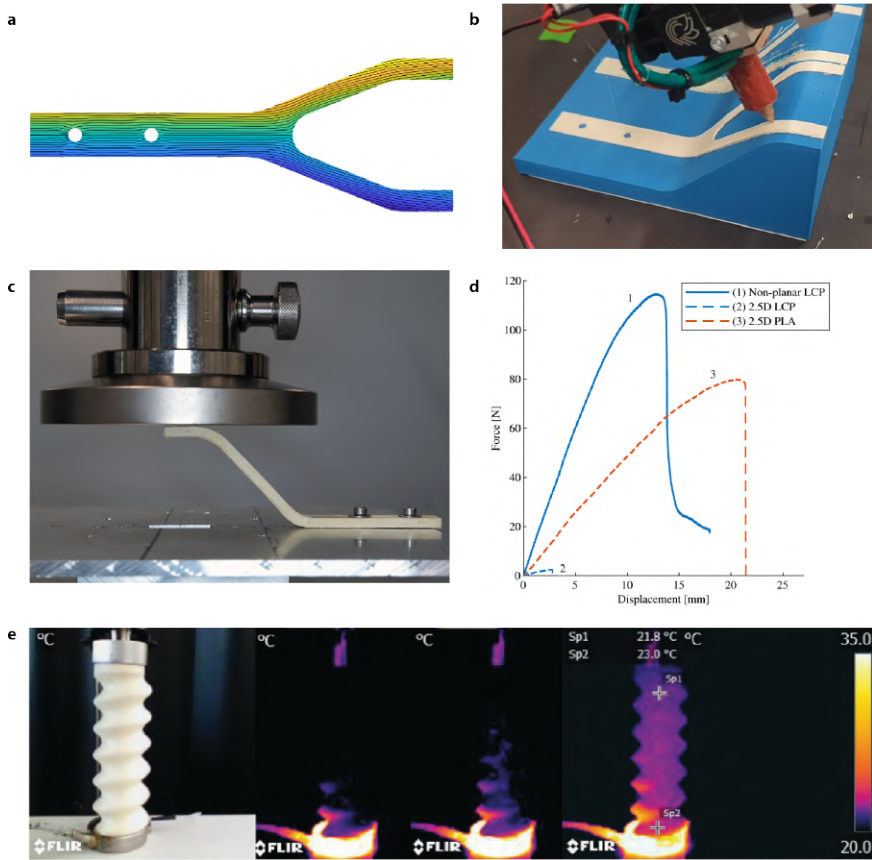
Figure 2.16 – **A.** A three-dimensional trajectory-generating scalar field is computed from the maximum principal stresses given by the load case. Isolines in this field will determine the toolpath. **B.** The part is manufactured on supports with a 5-axis 3D-printer, and **C.** compressed until failure. **D.** The mechanical performance of this part is compared to the same geometry printed with planar layers and Polylactic Acid (PLA). Reproduced from [147] with permission from Elsevier. **E.** 3D-printing of LCP can also make use of their other properties, such as low permeability in this case with a thermosyphon. Reproduced from [148] with permission from Wiley.

Building upon this work, the "spin-printing" technique, shown in Figure 2.15 has been developed to reinforce the 3D-printed parts with highly-aligned fibres, that can be created by melt-spinning fibres with the 3D-printer nozzle. As shown in Figure 2.15b, careful control of the fibre diameter down to 20 μm with draw ratios of up to 200 has been achieved, leading to tensile Young's modulus comparable to those of Vectran fibres. Strength values from 550 MPa to 2500 MPa are also reported in Figure 2.15c, which is one to two orders of magnitude larger than the unreinforced 3D-printing polymers typically printed by desktop 3D printers. These fibres can be embedded inside the 3D-printed polymer on the fly without a change of hardware. If embedded parallel to the printed lines, they do not stiffen the parts and even reduce their strength according to Griffith's law ($1/d^{1/2}$) where d is the defect size, i.e. fibre diameter. Transverse to the printed lines however, they can multiply stiffness and strength by 3 and 3.4 with just an 8 % fibre volume ratio,

as shown in Figure 2.15d and Figure 2.15e. In Figure 2.15f, the shaping freedom of combining 3D-printing and spin-printing is illustrated. Cylinders are compressed with and without fibres spanning across their diameter. The load-bearing capacity of the cylinders increases proportionally to the density of fibres printed at a negligible mass increase. Figure 2.15 shows a comparison between all-polypropylene composites [146] and all-LCP composites prepared with the spin-printing method. Spin-printing allows the manufacturing of a material whose transverse properties can be improved wherever the load case requests it.

The anisotropy and shaping freedom of LCP have been also harnessed in [147] with 5-axis 3D-printing to align print paths with 3D stress lines, as shown in Figure 2.16a. Parts are printed on pre-existing supports along the optimized toolpath in Figure 2.16b. They are subsequently tested in compression (Figure 2.16c) and compared to 2.5-D parts (i.e. printed with planar 3D-printing) made with LCP and PLA in Figure 2.16d. Because of the high anisotropy of LCPs contrasting with the high adhesion of PLA between 3D-printed layers [129], the 2.5D LCP fails very early compared to the 2.5D PLA. However, the load reached by the non-planar LCP is more than twice larger than the one reached by 2.5D PLA. This is another example of the synergy between anisotropy and shaping freedom that can be harnessed by 3D-printing LCP.

In other directions, some works on HBA:HNA 3D-printing have focused on the tuning of different parameters to achieve higher reliability and understanding of the processes at play during printing, by studying force exerted on the filament driving gears [149]. Correlating external parameters such as surface roughness to printing parameters and mechanical properties has also been of interest [150]. Other works with 3D-printing of HBA:HNA have focused on utilizing different properties of LCPs that can also benefit from shaping freedom, such as low gas permeability in [148] to create thermosyphons, as shown in Figure 2.16e.

Table 2.2 summarizes key printing parameters and trends emerging from research on 3D-printing HBA:HNA. It also provides an overview of the parameters selected in the upcoming chapters of this thesis, in light of the current state of knowledge.

Table 2.2 – Key-parameters for LCP 3D-printing

Parameter	Values selected in the-sis	Trend and reasoning	Investigated in
Bed temperature	90°C	A glue that activates above 90°C (Dimafix) gives reliable adhesion between LCP and bed.	[99]
Enclosure	23-30°C	A passive enclosure is used. An active enclosure at high temperature will help layer adhesion only if it is high enough to significantly slow down the solidification of LCP (240°C), but greatly reduces printing accuracy.	NematX R&D
Nozzle temperature	330°C (Chapter 3) 295°C, 330°C (Chapter 4) 295°C-340°C (Chapter 5)	A desktop 3D-printer can handle up to 340°C with extruder parts changes. For larger temperatures, industrial printers are needed. Larger temperatures enhance layer adhesion but decrease tensile properties. (See Figure 5.7). 295°C shows the best tensile results, but can be practically challenging for tall objects, prone to delaminate during printing due to thermal stresses.	Chapter 5, [99, 151]
Layer height	0.05 - 0.1 mm	The majority of prints shown in the thesis are with 0.1 mm layer height, which is considered a good trade-off between printing speed and performance. In [99], E_{11} is 17.9 GPa for 0.05 mm and 15.40 GPa for 0.1 mm, with the print completion twice as rapid.	[99]
Line width	0.1-2 mm (Chapter 3) 0.35 mm	A full discussion is available in Chapter 3, with Figure 3.2. Elsewhere, 0.35 mm is used.	Chapter 3
Extrusion multiplier	0.98	Over-extrusion is very harmful to tensile properties, creating wavy stochastic patterns that self propagate within the structure and create defects [152]. To avoid this, a slight under-extrusion can be set. It has been shown to improve Young's modulus and UTS [150].	[150, 152], NematX R&D

Parameter	Values selected in the-sis	Trend and reasoning	Investigated in
Nozzle diameter	0.15–0.8 mm (Chapter 3) 0.4 mm	A 0.4 mm nozzle is most common for desktop 3D-printers, as it shows a good balance between printing resolution and print completion time. Larger nozzle diameters tend to reduce Young's modulus [99]. The influence of nozzle diameter and linewidth on Young's modulus is further investigated in Chapter 3, Figure 3.2.	[99], Chapter 3
Printing speed	60 mm.s^{-1} (Chapter 3) 35 mm.s^{-1}	Increasing printing speed tends to improve tensile and adhesion properties unless the printer creates artifacts like vibrations (patent submitted by NematX). For desktop printers, a speed of 35 mm.s^{-1} was chosen as baseline as in the works of Gantenbein et al. [99, 153] considering the hardware stiffness. 60 mm.s^{-1} was also used to reduce printing time for larger prints (eg. Figure 3.5a).	[151], NematX R&D
Annealing	None	In [99], annealing at 270°C greatly reduced re-processability (drop in Melt Flow index). In [151], annealing under certain conditions (260°C, >24h) shows improvements in the mechanical performance of parts, increases their melting point and their density, which may indicate that recycling is still possible even with annealing.	[99, 151]
Fan speed	0%	LCP cools down very fast, no sagging is noted even without a fan. Accelerating cooling tends to cuase print failure by delamination.	NematX R&D

2.5. Conclusion

2.5.1. Scope and Research gaps

As research on HBA:HNA gathered in previous sections shows, the link between material, process and structure is especially strong with this highly anisotropic polymer. In contrast to other 3D-printable polymers cited for engineering applications such as PEI or PEEK, HBA:HNA has the potential to be simultaneously architected at microscopic scale (skin-core ratio, level of molecular alignment, crystallinity) and at macroscopic-scale, via shaping its anisotropy without typical manufacturing constraints associated, shown in Figure 2.4.

In this thesis, we therefore aim to explore the unique combination of anisotropy and shaping freedom provided by this material, and to investigate how this combination can improve mechanical performance.

To investigate such levels of shaping freedom, the important step of path-planning is missing in literature, as typical slicers adapted to 3D-printers are restricted to simple, periodic infills. An approach to create complex patterns inspired by analytical singularity functions in fluid mechanics, and which can also work with any angle field is therefore proposed in Chapter 3 to fill this gap.

As described in Section 2.3, there also remain challenges in translating some of the computational results in topology- and anisotropy-optimization into manufacturable parts. Such parts can only start to materialize when gradients of mechanical properties can be manufactured with large shaping freedom. Two different techniques to obtain these gradients should therefore be investigated: one by tailoring the microstructure of HBA:HNA, in Chapter 3; and the other by tailoring its macrostructure with toolpaths, in Chapter 4.

In the scope of this thesis, HBA:HNA is processed with a desktop 3D-printer shown in Figure 2.17, and without hindering its recyclability potential via annealing or compounding. This decision stems from a will to minimize the use of resources, which simultaneously aligns with global sustainability challenges and respects the context of a space-exploration mission. Indeed, another question arising from the literature is whether this material can, like its woven counterpart Vectran, be used for space missions. Indeed, the applicability of such highly-optimized structures is especially relevant in this environment, where mass-savings are crucial. Therefore, a thorough study of the space-worthiness of 3D-printed HBA:HNA via different exposure sources is also proposed in Chapter 5.
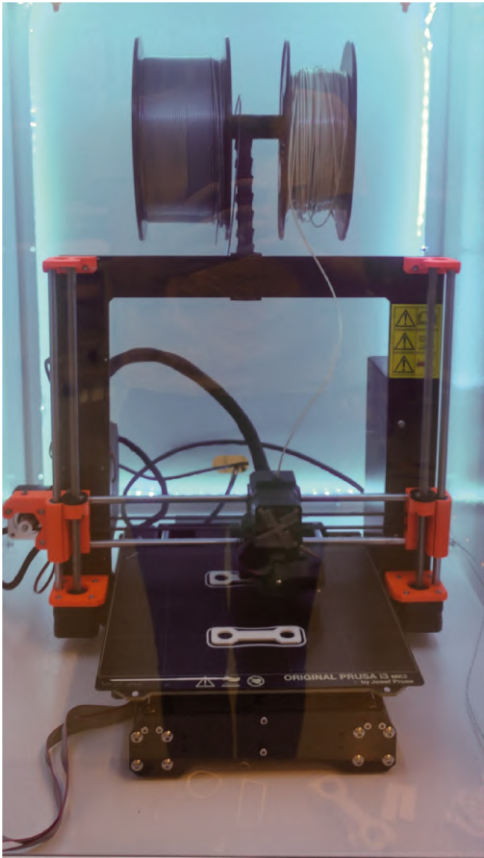
Figure 2.17 – Desktop 3D-printer (Prusa MK3S+ *Moebius*) inside a passive, insulated enclosure used in this thesis.

2.5.2. Concluding remarks

In this chapter, a broad review of different approaches proposed in literature to shape materials while controlling their directionality and their level of anisotropy has been given. The liquid crystal polymer used in this thesis, HBA:HNA, has also been presented, with a special focus on its microstructure, and the influence of processing on its orientability. The latest developments in 3D-printing of HBA:HNA have also been summarized. In the next chapter, an approach to tune mechanical properties and manufacture complex infills with this polymer will be presented.

References

1. Leibfried, G. Elastic Green's function for anisotropic cubic crystals. *Physical Review* **188,** 1175–1183. ISSN: 0031899X (1969).

2. Jones, J., Sanders, J. & Segnit, E. Structure of Opal. *Nature* **204,** 990–991 (1964).

3. Caselle, C., Bonetto, S. M. R., Costanzo, D. & Alonso, E. E. Effect of Microstructure and Relative Humidity on Strength and Creep of Gypsum. *Rock Mechanics and Rock Engineering* **54,** 4121–4145. ISSN: 1434453X (2021).

4. Earle, S. *Physical Geology - 2nd Edition* BC Campus. ISBN: 9781774200285 (Victoria, 2019).

5. Ashby, M. F. The mechanical efficiency of natural materials. *Philosophical Magazine* **84,** 2167–2186. ISSN: 14786435 (2004).

6. Ren, L. *et al.* Graded biological materials and additive manufacturing technologies for producing bioinspired graded materials: An overview. *Composites Part B: Engineering* **242,** 110086. ISSN: 13598368 (2022).

7. Maaß, M. C., Saleh, S., Militz, H. & Volkert, C. A. The Structural Origins of Wood Cell Wall Toughness. *Advanced Materials* **32.** ISSN: 15214095 (2020).

8. Müller, U., Gindl-Altmutter, W., Konnerth, J., Maier, G. A. & Keckes, J. Synergy of multi-scale toughening and protective mechanisms at hierarchical branch-stem interfaces. *Scientific Reports* **5,** 1–9. ISSN: 20452322 (2015).

9. Jaffe, M. J. & Forbes, S. Thigmomorphogenesis: the effect of mechanical perturbation on plants. *Plant Growth Regulation* **12,** 313–324 (1993).

10. Mattheck, C. *Design in Nature : Learning from Trees* ISBN: 978-3-540-62937-5 (Springer, Berlin, 1998).

11. Hausmann, H. Wood Vault: remove atmospheric CO2 with trees, store wood for carbon sequestration for now and as biomass, bioenergy and carbon reserve for the future. *Carbon Balance and Management* **17,** 1–29. ISSN: 17500680 (2022).

12. Weinkamer, R. & Fratzl, P. Mechanical adaptation of biological materials - The examples of bone and wood. *Materials Science and Engineering C* **31,** 1164–1173. ISSN: 09284931 (2011).

13. Liu, Z., Zhang, Z. & Ritchie, R. O. Structural Orientation and Anisotropy in Biological Materials: Functional Designs and Mechanics. *Advanced Functional Materials* **30,** 1–17. ISSN: 16163028 (2020).

14. Creasman, P. P. Reflections of a timber economy: the interpretation of Middle Kingdom ship and boat timbers. *Göttinger Miszellen* **240,** 19–36 (2014).

15. Haka, T. *Engineered Stability: The History of Composite Materials in the 19th and 20th Centuries* ISBN: 978-3-658-41407-8 (Springer Nature, 2023).

16. Vijayachandran, A. A. & Waas, A. M. Steered fiber paths for improved in-plane compressive response of aerostructural panels : Experimental studies and numerical modeling. *Composite Structures* **289,** 115426. ISSN: 0263-8223 (2022).

2

17. Prusty, B. G., Compston, P. & Rajan, G. Automated fibre placement based composite structures: Review on the defects, impacts and inspections techniques. *Composite Structures* **224,** 110987. ISSN: 02638223 (2019).

18. Lopes, C. S., Gürdal, Z. & Camanho, P. P. Variable-stiffness composite panels: Buckling and first-ply failure improvements over straight-fibre laminates. *Computers and Structures* **86,** 897–907. ISSN: 00457949 (2008).

19. Peeters, D. M. J., van Baalen, D. & Abdallah, M. Combining topology and lamination parameter optimisation. *Structural and Multidisciplinary Optimization* **52,** 105–120. ISSN: 16151488 (2015).

20. Setoodeh, S., Abdalla, M. M. & Gürdal, Z. Design of variable – stiffness laminates using lamination parameters. *Composites Part B: Engineering* **37,** 301–309 (2006).

21. Peeters, D. M. J., Irisarri, F.-X., Groenendijk, C. & Růžek, R. Optimal design, manufacturing and testing of non-conventional laminates. *Composite Structures* **210,** 29–40 (2019).

22. Peeters, D. M., Lozano, G. G. & Abdalla, M. M. Effect of steering limit constraints on the performance of variable stiffness laminates. *Computers & Structures* **196,** 94–111. ISSN: 0045-7949 (Feb. 2018).

23. Blom, A. W., Stickler, P. B. & Gürdal, Z. *Design and manufacture of a variable-stiffness cylindrical shell* in *Proceedings of the SAMPE Europe 30th international conference* (2009), 1–8.

24. Rautmann, M. & Kim, B. C. Continuous tow shearing for the automated manufacture of defect-free complex 3D geometry composite parts. *Composites Part A: Applied Science and Manufacturing* **183,** 108212. ISSN: 1359835X (2024).

25. Crothers, P. J., Drechsler, K., Feltin, D., Herszberg, I. & Kruckenberg, T. Tailored fibre placement to minimise stress concentrations. *Composites Part A: Applied Science and Manufacturing* **28,** 619–625. ISSN: 1359835X (1997).

26. Lozano, G. G., Tiwari, A., Turner, C. & Astwood, S. A review on design for manufacture of variable stiffness composite laminates. *Proceedings of the Institution of Mechanical Engineers, Part B: Journal of Engineering Manufacture* **230,** 981–992. ISSN: 20412975 (2016).

27. Nagendra, S., Kodiyalam, S., Davis, J. E. & Parthasarathy, N. *Optimization of tow fiber paths for composite design* in *36th Structures, Structural Dynamics and Materials Conference* (1995), 1275.

28. Almeida, J. H. S., Bittrich, L., Jansen, E., Tita, V. & Spickenheuer, A. Buckling optimization of composite cylinders for axial compression: A design methodology considering a variable-axial fiber layout. *Composite Structures* **222.** ISSN: 02638223 (2019).

29. Huelskamp, S. R., Tanner, C., Rapking, D. & Ricchi, R. D. Application of tailored fiber placement to fabricate automotive composite components with complex geometries. *Composite Structures* **313,** 116855. ISSN: 02638223 (2023).

30. Kim, B. B., Hazra, K., Weaver, P. & Potter, K. *Limitations of fibre placement techniques for variable angle tow composites and their process-induced defects* in *Proceedings of the 18th international conference on composite materials (ICMM18), Jeju, Korea* (Jeju, 2011), 21–26.

31. Simon, J., Hamila, N., Binetruy, C., Comas-Cardona, S. & Masseteau, B. Design and numerical modelling strategy to form Tailored Fibre Placement preforms: Application to the tetrahedral part with orthotropic final configuration. *Composites Part A: Applied Science and Manufacturing* **158,** 106952. ISSN: 1359835X (2022).

32. Oromiehie, E., Prusty, B. G., Compston, P. & Rajan, G. *The influence of consolidation force on the performance of AFP manufactured laminates* in *ICCM International Conferences on Composite Materials* (2017), 1–11.

33. Fang, G. *et al.* Exceptional mechanical performance by spatial printing with continuous fiber: Curved slicing, toolpath generation and physical verification. *Additive Manufacturing* **82,** 104048. ISSN: 22148604 (2024).

34. Le Duigou, A. *et al.* Thermomechanical performance of continuous carbon fibre composite materials produced by a modified 3D printer. *Heliyon* **9.** ISSN: 24058440 (2023).

35. Matsuzaki, R. *et al.* Effects of Set Curvature and Fiber Bundle Size on the Printed Radius of Curvature by a Continuous Carbon Fiber Composite 3D Printer (2018).

36. Hetrick, D. R., Sanei, S. H. R., Bakis, C. E. & Ashour, O. Evaluating the effect of variable fiber content on mechanical properties of additively manufactured continuous carbon fiber composites. *Journal of Reinforced Plastics and Composites* **40,** 365–377. ISSN: 15307964 (2021).

37. Raney, J. R. *et al.* Rotational 3D printing of damage-tolerant composites with programmable mechanics. *Proceedings of the National Academy of Sciences of the United States of America* **115,** 1198–1203. ISSN: 10916490 (2018).

38. Grieder, S. *et al.* Consolidation of Additive Manufactured Continuous Carbon Fiber Reinforced Polyamide 12 Composites and the Development of Process-Related Numerical Simulation Methods. *Polymers* **14.** ISSN: 20734360 (2022).

39. Chen, J. *et al.* 3D-Printed Anisotropic Polymer Materials for Functional Applications. *Advanced Materials* **34,** 1–33. ISSN: 15214095 (2022).

40. Groh, R. M. & Weaver, P. M. *Mass optimization of variable angle tow, variable thickness panels with static failure and buckling constraints* in *56th AIAA/ASCE/AHS/ASC Structures, Structural Dynamics, and Materials Conference* (2015), 5–9. ISBN: 9781624103421.

41. Sugiyama, K. *et al.* 3D printing of optimized composites with variable fiber volume fraction and stiffness using continuous fiber. *Composites Science and Technology* **186,** 107905. ISSN: 02663538 (2020).

42. Lu, Y. & Tong, L. Concurrent topology optimization of cellular structures and anisotropic materials. *Computers and Structures* **255.** ISSN: 00457949 (2021).

2

2

43. Duriez, E., Morlier, J., Charlotte, M. & Azzaro-Pantel, C. A well connected, locally-oriented and efficient multi-scale topology optimization (EMTO) strategy. *Structural and Multidisciplinary Optimization* **64,** 3705–3728. ISSN: 16151488 (2021).

44. Di Rienzo, A., Duriez, E., Charlotte, M. & Morlier, J. Lightweighting structures using an explicit microarchitectured material framework. *Mechanics and Industry* **25.** ISSN: 22577750 (2024).

45. Kumar, S., Tan, S., Zheng, L. & Kochmann, D. M. Inverse-designed spinodoid metamaterials. *npj Computational Materials* **6,** 1–10. ISSN: 20573960 (2020).

46. Kumar, S. & Kochmann, D. M. in *Current Trends and Open Problems in Computational Mechanics* 275–285 (Springer, 2022).

47. Portela, C. M. *et al.* Extreme mechanical resilience of self-assembled nanolabyrinthine materials. *Proceedings of the National Academy of Sciences of the United States of America* **117,** 5686–5693. ISSN: 10916490 (2020).

48. Garnier, D. H., Schmidt, M. P. & Rohmer, D. Growth of oriented orthotropic structures with reaction/diffusion. *Structural and Multidisciplinary Optimization* **65.** ISSN: 16151488 (2022).

49. Schmidt, M. P., Couret, L., Gout, C. & Pedersen, C. B. Structural topology optimization with smoothly varying fiber orientations. *Structural and Multidisciplinary Optimization* **62,** 3105–3126. ISSN: 16151488 (Dec. 2020).

50. Jung, T., Lee, J., Nomura, T. & Dede, E. M. Inverse design of three-dimensional fiber reinforced composites with spatially-varying fiber size and orientation using multiscale topology optimization. *Composite Structures* **279.** ISSN: 02638223 (2022).

51. Vertonghen, L., Irisarri, F. X., Bettebghor, D. & Desmorat, B. Gradient-based concurrent topology and anisotropy optimization for mechanical structures. *Computer Methods in Applied Mechanics and Engineering* **412,** 116069. ISSN: 00457825 (2023).

52. Eckrich, M., Arrabiyeh, P. A., Dlugaj, A. M. & May, D. An anisotropic topology optimization procedure for continuous fiber reinforced polymer structures with biaxial fiber layout for improved intersection point design. *Composite Structures* **337,** 118064. ISSN: 02638223 (2024).

53. Kundu, R. D. & Zhang, X. S. Stress-based topology optimization for fiber composites with improved stiffness and strength: Integrating anisotropic and isotropic materials. *Composite Structures* **320,** 117041. ISSN: 02638223 (2023).

54. Kundu, R. D. & Zhang, X. S. Additive manufacturing of stiff and strong structures by leveraging printing-induced strength anisotropy in topology optimization. *Additive Manufacturing* **75,** 103730. ISSN: 22148604 (2023).

55. Garbovskiy, Y. A. & Glushchenko, A. V. in (eds Camley, R. E. & Stamps, R. L.) 1–74 (Academic Press, 2010).

56. Bellini, T. & Todisco, M. Liquid Crystal Ordering in DNA Double Helices with Backbone Discontinuities. *Macromolecules* **55,** 5946–5953. ISSN: 15205835 (2022).

57. Charvolin, J. & Keller, P. Disorder of lipid chains as a function of their lateral packing in lyotropic liquid crystals. *Chemistry and Physics of Lipids* **15,** 161–173. ISSN: 00093084 (1975).

58. Castellano, J. A. *Liquid Gold: The Story of Liquid Crystal Displays and the Creation of an Industry* ISBN: 9789812389565 (World Scientific, 2005).

59. Morgan, P. W., Schaefgen, J. R. & Gulrich, L. W. Synthesis, Anisotropic Solutions, and Fibers of Poly(1,4-benzamide). *Macromolecules* **10,** 1390–1396 (1977).

60. The Recent Developments of Thermotropic Liquid Crystalline Polymers. *Polymer Engineering and Science* **26,** 901–918. ISSN: 15213900 (1985).

61. Jackson, W. J. & Kuhfuss, H. F. Liquid crystal polymers, I. Preparation and properties of p-hydroxybenzoic acid copolyesters. *Journal of Polymer Science* **14,** 3031–3046. ISSN: 0887624X (1976).

62. Calundann, G. W. *Industrial Development of Thermotropic Polyesters* in *High Performance Polymers: Their Origin and Development* (Springer, 1986), 235–249.

63. Brostow, W. & Collyer, A. A. *Liquid Crystal Polymers: From Structures to Applications* ISBN: 1851667970 (1993).

64. Karacan, I. A comparative study of structure-property relationships in highly oriented thermoplastic and thermotropic polyesters with different chemical structures. *Journal of Applied Polymer Science* **100,** 142–160. ISSN: 00218995 (2006).

65. Langelaan, H. C. & Posthuma De Boer, A. Crystallization of thermotropic liquid crystalline HBA/HNA copolymers. *Polymer* **37,** 5667–5680. ISSN: 00323861 (Jan. 1996).

66. Hudson, S. D. & Lovinger, A. J. Transmission electron microscopic investigation of the morphology of a poly(hydroxybenzoate-co-hydroxynaphthoate) liquid crystal polymer. *Polymer* **34,** 1123–1129. ISSN: 00323861 (1993).

67. Butzbach, G. D., Wendorff, J. H. & Zimmermann, H. J. Structure and structure formation of a main chain thermotropic polymer. *Polymer* **27,** 1337–1344. ISSN: 00323861 (1986).

68. Blackwell, J., Gutierrez, G. A. & Chivers, R. A. Diffraction by Aperiodic Polymer Chains: The Structure of Liquid Crystalline Copolyesters. *Macromolecules* **17,** 1219–1224. ISSN: 15205835 (1984).

69. Blackwell, J. & Biswas, A. in *Developments in Oriented Polymers—2* 153–197 (Springer, 1987).

70. Lemmon, T. J., Spontak, R. J. & Windle, A. H. Dimensions of crystallites in a thermotropic random copolyester. *Polymer* **33,** 3–10. ISSN: 00323861 (1992).

71. Hanna, S. & Windle, A. H. Geometrical limits to order in liquid crystalline random copolymers. *Polymer* **29,** 207–223 (1988).

72. Windle, A. H. Electron microscopy of NPL crystallites in a thermotropic random copoly(ester-amide). *Polymer* **31,** 1395–1400. ISSN: 00323861 (1990).

2

73. Romo-Uribe, A., Reyes-Mayer, A., Calixto Rodriguez, M. & Sarmiento-Bustos, E. On the influence of thermal annealing on molecular relaxations and structure in thermotropic liquid crystalline polymer. *Polymer* **240,** 124506. ISSN: 00323861 (2022).

74. Kenner, W. S., Jones, T. C. & Le Boffe, V. M. *Controlled Environmental Effects on Creep Test Data of Woven Fabric Webbings for Inflatable Space Modules (NASA/TM2020-220561)* tech. rep. (NASA, 2020).

75. Ide, Y. & Ophir, Z. Orientation development in thermotropic liquid crystal polymers. *Polymer Engineering & Science* **23,** 261–265. ISSN: 15482634 (1983).

76. Sullivan, A., Saigal, A. & Zimmerman, M. A. Structure-property-processing relationships in extruded liquid crystal polymer film. *Polymers and Polymer Composites* **29,** S450–S463. ISSN: 14782391 (2021).

77. Goldbeck-Wood, G. & Windle, A. H. Simulation of texture evolution for nematic liquid crystalline polymers under shear flow. *Liquid Crystals* **29,** 335–345. ISSN: 02678292 (2002).

78. Kornfield, J. A. & Burghardt, W. R. Shear aligning properties of a main-chain thermotropic liquid crystalline polymer. *Macromolecules* **34,** 3654–3660. ISSN: 00249297 (2001).

79. McDonald, W. in *Liquid crystal polymers: from structures to applications* Springer, 407–446 (Dordrecht, 1992).

80. Sawyer, L. C. & Jaffe, M. The structure of thermotropic copolyesters. *Journal of Materials Science* **21,** 1897–1913 (1986).

81. Fang, J., Burghardt, W. R. & Bubeck, R. A. Molecular Orientation Distributions During Injection Molding of Liquid Crystalline Polymers: Ex Situ Investigation of Partially Filled Moldings. *Polymer Engineering and Science* **52,** 774–786 (2012).

82. Fang, J., Burghardt, W. R., Bubeck, R. A., Burgard, S. M. & Fischer, D. A. Bulk and Surface Molecular Orientation Distribution in Injection-Molded Liquid Crystalline Polymers: Experiment and Simulation. *Polymer Engineering & Science* **50,** 1864–1877 (2010).

83. Goldbeck-Wood, G. *et al.* Modelling of Liquid Crystal Polymers at Different Length Scales. *Molecular Simulation* **21,** 143–160. ISSN: 1029-0435 (1998).

84. Romo-Uribe, A. Smectic-like order in the log-rolling flow of thermotropic random copolymers. A time-resolved wide-angle x-ray scattering study. *Proceedings of the Royal Society A: Mathematical, Physical and Engineering Sciences* **457,** 1327–1342. ISSN: 13645021 (2001).

85. Donald, A. M., Viney, C. & Windle, A. H. Banded structures in oriented thermotropic polymers. *Polymer* **24,** 155–159. ISSN: 00323861 (1983).

86. Vermant, J., Moldenaers, P., Mewis, J. & Picken, S. J. Band formation upon cessation of flow in liquid-crystalline polymers. *Journal of Rheology* **38,** 1571–1589. ISSN: 0148-6055 (1994).

87. Viney, C. & Windle, A. H. On understanding the optical extinction behaviour of uniaxially sheared liquid crystalline polymers. *Philosophical Magazine A: Physics of Condensed Matter, Structure, Defects and Mechanical Properties* **55,** 463–480. ISSN: 01418610 (1987).

88. Ding, J., Feng, J. & Yang, Y. A preliminary morphological evidence for the existence of back-flow effect associated with the formation of band texture after cessation of shear for a polymeric liquid crystal. *Polymer Bulletin* **36,** 773–778 (1996).

89. Rey, A. D. & Denn, M. M. in *Annual Review of Fluid Mechanics* 1, 233–266 (2002).

90. Reyes-Mayer, A., Alvarado-Tenorio, B., Romo-Uribe, A. & Jaffe, M. SALS, WAXS and mechanical properties of heat-treated thermotropic polymers. *Polymers for Advanced Technologies* **24,** 1029–1039. ISSN: 10427147 (2013).

91. Troughton, M. J., Davies, G. R. & Ward, I. M. Dynamic mechanical properties of random copolyesters of 4-hydroxybenzoic acid and 2-hydroxy 6-naphthoic acid. *Polymer* **30,** 58–62. ISSN: 00323861 (1989).

92. Saw, C. K., Collins, G., Menczel, J. & Jaffe, M. Thermally induced reorganization in LCP fibers: Molecular origin of mechanical strength. *Journal of Thermal Analysis and Calorimetry* **93,** 175–182. ISSN: 13886150 (2008).

93. Schick, C. in *Polymer Crystallization I. Advances in Polymer Science, vol 276* (eds Auriemma, F., Alfonso, G. & de Rosa, C.) 257–289 (Springer, Cham, 2015). ISBN: 978-3-319-49203-2.

94. Kim, Y. C. & Economy, J. The mechanical properties of thermally treated 73/27 HBA/HNA copolyester. *Polymers for Advanced Technologies* **10,** 493–500. ISSN: 10427147 (1999).

95. Wiberg, G., Hillborg, H. & Gedde, U. W. Assessment of development and relaxation of orientation in a sheared thermotropic liquid crystalline copolyester. *Polymer Engineering and Science* **38,** 1278–1285. ISSN: 00323888 (1998).

96. Economy, J., Schneggenburger, L. A. & Frich, D. in *Transreactions in Condensation Polymers* 195–217 (2007).

97. Frich, D., Hall, A. & Economy, J. Nature of adhesive bonding via interchain transesterification reactions (ITR). *Macromolecular Chemistry and Physics* **199,** 913–921. ISSN: 1022-1352 (May 1998).

98. Kim, Y. C. & Economy, J. Degradation process observed during step annealing of 73/27 HBA/HNA copolyester. *Macromolecules* **32,** 2855–2860. ISSN: 00249297 (1999).

99. Gantenbein, S. *et al.* Three-dimensional printing of hierarchical liquid-crystal-polymer structures. *Nature* **561,** 226–230. ISSN: 0028-0836 (Sept. 2018).

100. ANSYS Inc. *Ansys Granta EduPack Database* www.ansys.com/materials (2024).

101. Sloan, F. in *Structure and Properties of High-Performance Fibers* 113–140 (Elsevier Ltd, 2017). ISBN: 9780081005514.

102. BASF Press Release. *Blanket made of foam blocks prevents sloshing of liquefied gas* https://www.basf.com/ru/ru/media/news-releases/2013/07/p-13-306.html (2024).

103. Magagnini, P. L., Paci, M., La Mantia, F. P., Surkova, I. N. & Vasnev, V. A. Morphology and rheology of polysulfone/Vectra-A950 blends. *Journal of Applied Polymer Science* **55,** 461–480. ISSN: 00218995 (Jan. 1995).

104. Anderegg, D. A. *et al.* In-situ monitoring of polymer flow temperature and pressure in extrusion based additive manufacturing. *Additive Manufacturing* **26,** 76–83. ISSN: 22148604 (Mar. 2019).

105. Romo-Uribe, A. & Windle, A. H. A rheo-optical and dynamic X-ray-scattering study of flow-induced textures in main-chain thermotropic liquid-crystalline polymers: the influence of molecular weight. *Proceedings of the Royal Society A: Mathematical, Physical and Engineering Sciences* **455,** 1175–1201. ISSN: 13645021 (1999).

106. Dealy, J. M. & Wang, J. Melt Rheology and its Applications in the Plastics Industry. *Melt Rheology and its Applications in the Plastics Industry,* 19–47. ISSN: 1619-0181 (2013).

107. Campus Plastics - Celanese. *Vectra A950 LCP Datasheet* https://www.campusplastics.com/material/pdf/190204/VECTRAA950?sLg=en (2024).

108. Continental. *Grand Prix 4-Season* https://www.continental-tires.com/products/b2c/bicycle/tires/grand-prix-4-season/ (2024).

109. Contender Sailcloth. *Vectran reinforced for extra performance* https://contendersailcloth.com/en/7p/fiberconsupregsup-pro-vectran.aspx (2024).

110. Iannucci, L., Greenhalgh, E. S. & Ahmad, Z. A Plane-Stress Damage Model for Vectran Laminated Composite. *Applied Composite Materials* **28,** 1255–1276. ISSN: 15734897 (2021).

111. Park, S. & Lee, S. in *Carbon Fibers* (Springer, 2014). ISBN: 978-94-017-9478-7.

112. Hoshiro, H., Endo, R. & Sloan, F. E. in *High-Performance and Specialty Fibers: Concepts, Technology and Modern Applications of Man-Made Fibers for the Future* 171–190 (2016).

113. Sierra Space. *Sierra Space Sets the Stage for Pioneering Full-Scale "Burst Test" of Expandable Space Station Module* https://www.sierraspace.com/newsroom/press-releases/sierra-space-sets-the-stage-for-pioneering-full-scale-burst-test-of-expandable-space-station-module/ (2024).

114. Cadogan, D., Sandy, C. & Grahne, M. Development and Evaluation of the Mars Pathfinder Inflatable Airbag Landing System. *Acta Astronautica* **50,** 633–640 (2002).

115. *Rapidly Deployable Structures in Collective Protection Systems* (2006).

116. Mousavi, M. M. S. *et al. Spacesuits and EVA gloves evolution and future trends of extravehicular activity gloves* in *41st International Conference on Environmental Systems 2011, ICES 2011* (2011), 1–10. ISBN: 9781600869488.

117. Plummer, C. J., Zülle, B., Demarmels, A. & Kausch, H. The structure of filled and unfilled thermotropic liquid crystalline polymer injection moldings. *Journal of Applied Polymer Science* **48,** 751–766. ISSN: 10974628 (1993).

118. Weng, T., Hiltner, A. & Baer, E. Hierarchical structure in a thermotropic liquid-crystalline copolyester. *Journal of Materials Science* **21,** 744–750. ISSN: 00222461 (1986).

119. Meddad, A., Fisa, B. & Favis, B. D. Weldlines in injection-molded parts: A review. *Advances in Polymer Technology* **14,** 169–195. ISSN: 10982329 (1995).

120. Luise, R. R. *Applications of high temperature polymers* (CRC press, 2018).

121. Kuraray. *Vectran: Liquid crystal polymer fiber technology* https://www.kuraray.eu/fileadmin/product_ranges/vectran/downloads/2017_VECTRAN_Product_Brochure.pdf (2024).

122. Nakagawa, Yamamoto, Kishino, Saneto & Sugita. *Heat treatment of thermotropic fiber* Patent no. JPH03119110A, 1989.

123. Fette, R. B. & Sovinski, M. F. *Vectran Fiber Time-Dependent Behavior and Additional Static Loading Properties (NASA/TM—2004-212773)* tech. rep. (NASA, 2004).

124. Lefèvre, J. *et al.* "Foil spintrusion" of high-performance polymer films. *Journal of Polymer Science, Part B: Polymer Physics* **50,** 1713–1727 (Dec. 2012).

125. Peijs, T. & Tervoort, T. A. High-performance liquid-crystalline polymer films for monolithic "composites". *Composites Part A: Applied Science and Manufacturing* **81,** 296–304. ISSN: 1359835X (2016).

126. Hedenqvist, M. S. & Gedde, U. W. Barrier Properties of injection Molded Blends of Liquid Crystalline Polyesters (Vectra) and High-Density Polyethylene. *Polymer Engineering & Science* **43,** 1044–1057 (2004).

127. Zhang, G. *et al.* A systematic investigation on the minimum tensile strengths and size effects of 3D printing polymers. *Polymer Testing* **117,** 107845. ISSN: 01429418 (2023).

128. Song, Y. *et al.* Measurements of the mechanical response of unidirectional 3D-printed PLA. *Materials and Design* **123,** 154–164. ISSN: 18734197 (2017).

129. Allum, J., Moetazedian, A., Gleadall, A. & Silberschmidt, V. V. Interlayer bonding has bulk-material strength in extrusion additive manufacturing: New understanding of anisotropy. *Additive Manufacturing* **34,** 101297. ISSN: 22148604 (2020).

130. Nelson, J. W. *et al.* Generalized models for unidirectional anisotropic properties of 3D printed polymers. *Rapid Prototyping Journal* **26,** 1453–1462. ISSN: 13552546 (2020).

131. Victrex. *Victrex PEEK Polymer 450G Datasheet* https://www.victrex.com/-/media/downloads/datasheets/victrex_tds_450g.pdf (2024).

132. Xu, Q. *et al.* Enhanced interlayer strength in 3D printed poly (ether ether ketone) parts. *Additive Manufacturing* **55.** ISSN: 22148604 (2022).

2

133. Arif, M. F., Kumar, S., Varadarajan, K. M. & Cantwell, W. J. Performance of biocompatible PEEK processed by fused deposition additive manufacturing. *Materials and Design* **146,** 249–259. ISSN: 18734197 (2018).

134. Vindokurov, I., Pirogova, Y., Tashkinov, M. & Silberschmidt, V. V. Effect of Heat Treatment on Elastic Properties and Fracture Toughness of Fused Filament Fabricated PEEK for Biomedical Applications. *Polymers* **14,** 1–19. ISSN: 20734360 (2022).

135. Reja, R. & Månson, J. A. *Comprehensive Composite Materials Vol 2: Polymer Matrix Composites.* ISBN: 9780081005330 (Elsevier, 2000).

136. 9TLabs. *Material Datasheet CF/PA12 v1.0* https://www.9tlabs.com/ (2024).

137. Handlos, A. A. & Baird, D. G. Processing and Associated Properties of In Situ Composites Based on Thermotropic Liquid Crystalline Polymers and Thermoplastics. *Journal of Macromolecular Science, Part C* **35,** 183–238. ISSN: 15205746 (1995).

138. Kohli, A., Chung, N. & Weiss, R. A. Effect of deformation history on the morphology of blends of polycarbonate and a thermotropic liquid crystalline polymer. *Polymer Engineering & Science* **29,** 573–580. ISSN: 07334192 (1989).

139. Gray, R. W., Baird, D. G. & Bøhn, J. H. Effects of processing conditions on short TLCP fiber reinforced FDM parts. *Rapid Prototyping Journal* **4,** 14–25 (1998).

140. Gray, R. W., Baird, D. G. & Bøhn, J. Thermoplastic Composites Reinforced With Long Fiber Thermotropic Liquid Crystalline Polymers for Fused Deposition Modeling. *Polymer Composites* **19,** 383–394 (1998).

141. Ansari, M. Q., Redmann, A., Osswald, T. A., Bortner, M. J. & Baird, D. G. Application of thermotropic liquid crystalline polymer reinforced acrylonitrile butadiene styrene in fused filament fabrication. *Additive Manufacturing* **29,** 100813. ISSN: 22148604 (2019).

142. Chen, T. *et al.* Thermotropic liquid crystalline polymer reinforced polyamide composite for fused filament fabrication. *Additive Manufacturing* **40,** 101931. ISSN: 22148604 (2021).

143. Noack, D. & von Roth, W. On the theory of elasticity of the orthotropic material wood. *Wood Science and Technology* **10,** 97–110 (1976).

144. Gürdal, Z., Haftka, R. T. & Hajela, P. *Design and optimization of laminated composite materials* (John Wiley & Sons, 1999).

145. Kappel, R., Mattheck, C., Bethge, K. & Tesari, I. *Bamboo as a composite structure and its mechanical failure behaviour* in *Design and Nature II* (WIT Press, 2004). ISBN: 1853127213.

146. Cabrera, N. O., Barkoula, N. M., Loos, J. & Peijs, T. The mechanical properties of unidirectional all-polypropylene composites. *Composites Part A: Applied Science and Manufacturing* **37,** 716–726. ISSN: 1359835X (2006).

147. Guidetti, X. *et al.* Data-Driven Process Optimization of Fused Filament Fabrication based on In Situ Measurements. *22nd IFAC World Congress Proceedings* **56,** 4713–4718. ISSN: 24058963 (2023).

148. Seshadri, B., Hischier, I., Masania, K. & Schlueter, A. 3D Printed Liquid Crystal Polymer Thermosiphon for Heat Transfer under Vacuum. *Advanced Materials Technologies* **2300403,** 1–10. ISSN: 2365709X (2023).

149. Guidetti, X. *et al.* Force Controlled Printing for Material Extrusion Additive Manufacturing. *arXiv pre-print,* 1–23 (2024).

150. Guidetti, X. *et al.* Stress flow guided non-planar print trajectory optimization for additive manufacturing of anisotropic polymers. *Additive Manufacturing* **72,** 103628. ISSN: 22148604 (2023).

151. Johann, K. S., Wolf, A. & Bonten, C. Mechanical Properties of 3D-Printed Liquid Crystalline Polymers with Low and High Melting Temperatures. *Materials* **17.** ISSN: 19961944 (2024).

152. Houriet, C. *Additive Manufacturing of Liquid Crystal Polymers* Master's Thesis (Delft University of Technology, 2019).

153. Gantenbein, S. *et al.* Spin-Printing of Liquid Crystal Polymer into Recyclable and Strong All-Fiber Materials. *Advanced Functional Materials,* 2104574. ISSN: 1616-3028 (Sept. 2021).

2

Chapter 3

3D Printing of Flow-inspired Anisotropic Patterns with LCP

ABSTRACT

Anisotropic materials formed by living organisms possess remarkable mechanical properties due to their intricate microstructure and directional freedom. In contrast, human-made materials face challenges in achieving similar levels of directionality due to material constraints and manufacturability. To overcome these limitations, we present an approach using 3D printing of self-assembling thermotropic LCP. The remarkably high stiffness of the LCP is granted by the alignment of nematic domains within the polymer during extrusion. The Young's modulus ranging from 3 GPa to 30 GPa is found to be strongly influenced by the directionality of the nematic flow. By determining a relationship between stiffness, nozzle diameter and line width, we identify a suitable design space where shaping and mechanical performance can be combined. We demonstrate the ability to print LCPs with on-the-fly width changes to accommodate arbitrary spatially varying directions. This enables us to manufacture exquisite patterns inspired by fluid dynamics with steep curvature variations. The versatility of LCP combined with this approach allows to 3D-print functional objects with gradients of stiffness and curvatures, offering potential applications in lightweight functional structures embedding crack-mitigation strategies. This method also opens avenues for studying and replicating intricate patterns observed in nature, such as wood or turbulent flow using extrusion 3D printing.

3

3.1. Introduction

Anisotropic materials can be formed by living organisms such as the cellulose fibres in wood grains [1] and fibre bundles in osteons of bone [2]. Their microstructures are shaped with spatially tunable stiffness gradients and sharp orientation changes [3] in order to accommodate stresses and morphogenesis of the living organism in an efficient manner [4]. This freedom enables remarkable mechanical properties while keeping energy consumption low and using weak building blocks [5]. In contrast, despite the larger processing energy and stronger base materials used, human-made materials such as composites cannot be shaped with similar levels of anisotropy and directionality freedom [6]. While the latter can be achieved with 3D printing such as FFF, or via automated composite tape laying [7], compatible anisotropic materials are typically fibre-filled [8]. Paradoxically, these fibres restrict directional freedom due to their intrinsic stiffness and relatively large size. Problems such as wrinkling or fibre breakage have been reported [9] and often result in the need to predetermine curvature constraints in the design space [6].

To remove these constraints, one could shape polymer chains that self-assemble into ordered liquid crystalline domains in the melt [10]. In LCPs, the direction of the molecules in each domain was found to align with the direction of extrusion by the nozzle of the FFF 3D printer [10]. Because alignment is strongly influenced by elongational flow, melt-spun LCP fibres with remarkably high mechanical performance were spun and integrated into recyclable and strong all-fibre lightweight materials [11]. Despite attaining high properties in printed objects, the need for the LCP fibres to undergo stretching has limited their integration to unidirectional straight-line patterns. Reconciling these properties in tailored printed objects that closely resemble the exquisite microstructure of natural materials remains a challenge.

To achieve this goal, the printed lines should follow a spatially varying directional field while avoiding gaps or overlaps. One way to enable manufacturing could be to allow line width to vary by changing extrusion rate [12–14]. However, increasing the line width negatively affects the stiffness [15] and failure mode [16] of polymers because of a loss of alignment [17, 18]. As a result, the path-planning method should carefully control the spacing between printed lines to balance manufacturability and desired performance. We hypothesize that streamlines, which are commonly used in fluid mechanics to visualize flow, could accurately generate toolpaths describing complex 3D-printed microstructures with LCP. The characteristic of this approach, beyond its mathematical elegance, is to produce multiple smooth individual paths instead of one tortuous cyclic path that is generally shown for single continuous motion approaches [19–25]. Recently, evenly distributed streamlines [26] were generated for printed paths of fixed width following principal stress directions. Studies using streamlines have mainly focused on computing toolpath location for fibres flowing around a hole based on the potential flow functions describing flow around a cylinder [27–29], akin to the microstructure of wood around a knot.

To fully exploit the unusual combination of anisotropy and directionality freedom of LCP, we extend the streamline approach to path-planning for 3D printing aiming for dense filling of any pattern. By ensuring a distribution of streamlines such that all gaps can
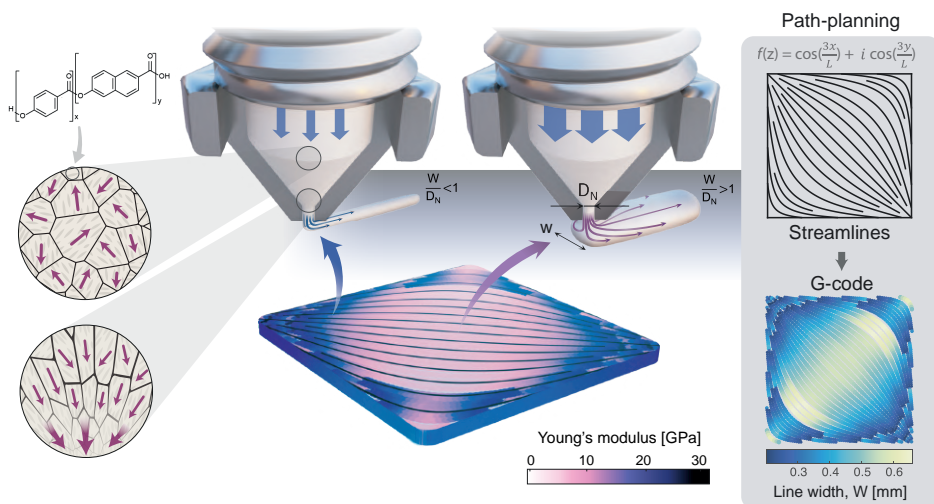
Figure 3.1 – **Overview of the printing of liquid crystal polymer patterns with line width variation.** The nematic domains of an aromatic co-polyester are subjected to shear and extensional flow during extrusion via the 3D-printer nozzle, which promotes their homogeneous alignment. By varying the extrusion rate, the flow behavior upon exit can be controlled. The distribution of nematic domains remains parallel to the travel (longitudinal) direction when the ratio of line width W to nozzle diameter D_N is below unity. In contrast, above unity, a transverse component of the flow leads a portion of the domains to solidify at an angle to the longitudinal direction. A controlled gradient of stiffness can be printed within one line by varying line width. Axial stiffness of each print path can be predicted from line width and printing nozzle diameter by utilizing a scaling law. A path-planning algorithm mindful of user-input bounds of line width allows to generate complex patterns that make use of this feature.

effectively be filled by the flowing material, we show that the LCPs can be 3D-printed into complex shapes with steep curvature variations by tuning the width of a line during the printing process. To explore the potential of such curvature changes, we generate angle fields via analytical functions traditionally describing potential flows in fluid dynamics. This enables us to easily superimpose local and global flow features. This path-planning approach, combined with the anisotropy and directionality freedom of LCP, allows for the first time to manufacture patterns such as vortices with FFF, showing significant mechanical benefits.

3.2. Results & Discussion

3.2.1. Printing strategy

To combine high anisotropy with full directionality freedom, a thermotropic liquid crystal polymer displaying a self-aligning behavior is deposited via extrusion 3D printing [10, 11, 30] . In the melt at rest, the polydomain structure of the aromatic co-polyester shown in Figure 3.1 is macroscopically unoriented, while the liquid crystalline orientational order is preserved within the nematic domains [31]. Above its melting point, its rigid molecular segments self-assemble into nematic domains of a few micrometers in size [32]. Anisotropy is generated in the melt by shear and extensional flow arising

during extrusion through the converging nozzle of the 3D printer. As the polymer exits the nozzle and is exposed to ambient temperature, rapid cooling enables the co-polymer to solidify and preserve alignment before the nematic order can relax into its macroscopically unoriented configuration [10]. When a print line is deposited by the moving nozzle onto the heated bed with a fixed height $h = 100\,\mu m$, changing the amount of material pushed into the nozzle results in a proportional change in the line width W, due to conservation of volume. When the ratio between line width W and nozzle diameter D_N is close to or below unity, the flow orientation aligns with the nozzle travel direction [33]. However, when the volumetric flow rate is increased, the polymer chains may partially adopt a transverse component. The line width change causing a gradient of stiffness represents a remarkably simple method to modulate mechanical performance, due to the capability of producing both stiff-strong, and soft-ductile lines, with an order of magnitude difference in stiffness, from a single material system. The low viscosity of the polymer enables us to utilize this line width variation to create fully dense parts with large curvature changes. Once the angle fields describing a pattern have been generated, the path planning algorithm generates corresponding streamlines as toolpath, such that each streamline is placed at a fillable distance to its neighbours.

3.2.2. Dependence of extruded line width on mechanical properties

The influence of varying line width on the tensile and microstructural properties of single printed lines of LCP was investigated. The layer height h, print temperature T_{print} and speed V_{print} were kept constant at 0.1 mm, 330 °C, and 60 mm.s^{-1} respectively. The volumetric flow rate was calculated as $Q = V_{print} h W$ where W is the target line width. Single printed lines were tested in tension. For a single nozzle diameter D_N of 0.4 mm, stress-strain curves in Figure 3.2a show a notable change in failure behavior from brittle to ductile with increasing line width. Imaging of the specimen after failure reveals that either behavior is also linked to significant differences in the micro- and macroscopic morphologies.

The lines printed with a width smaller than the nozzle diameter (0.4 mm) demonstrated a high mechanical performance. For the best-performing sample, we obtained a modulus of 27.6 GPa and an ultimate tensile strength of 847 MPa corresponding to a 4 % failure strain. The fibres were found to fail in a quasi-brittle manner. Such a failure behavior has been widely documented for highly aligned LCP such as melt-spun or extruded filaments with high draw-ratios displaying a fibrillar structure [33, 34]. Scanning Electron Microscopy (SEM) revealed a typical fibrillar microstructure in these samples as well, with fibrils of $\approx 0.1\,\mu m$ bridging broken ends. The axial cracks indicate that the polymer chains are so highly aligned that a shear fracture is more likely to take place. The chain modulus of the LCP is reported much larger at 122 GPa than the molecular shear modulus of 1.7 GPa. The weak van der Waals forces holding together the oriented fibrils of LCP explain the prevalence of chain slippage over chain stretching [33]. In hardwoods and softwoods loaded in tension parallel to the grain, a similar slippage between microfibrils occurs and creates a fibrillar fracture surface with an unraveling of the S2 layer from the S1 layer [35]. Moreover, the toughening mechanism of wood involves microfibril ligaments bridging the crack and crack-tip blunting [36]. In our case, the presence of these
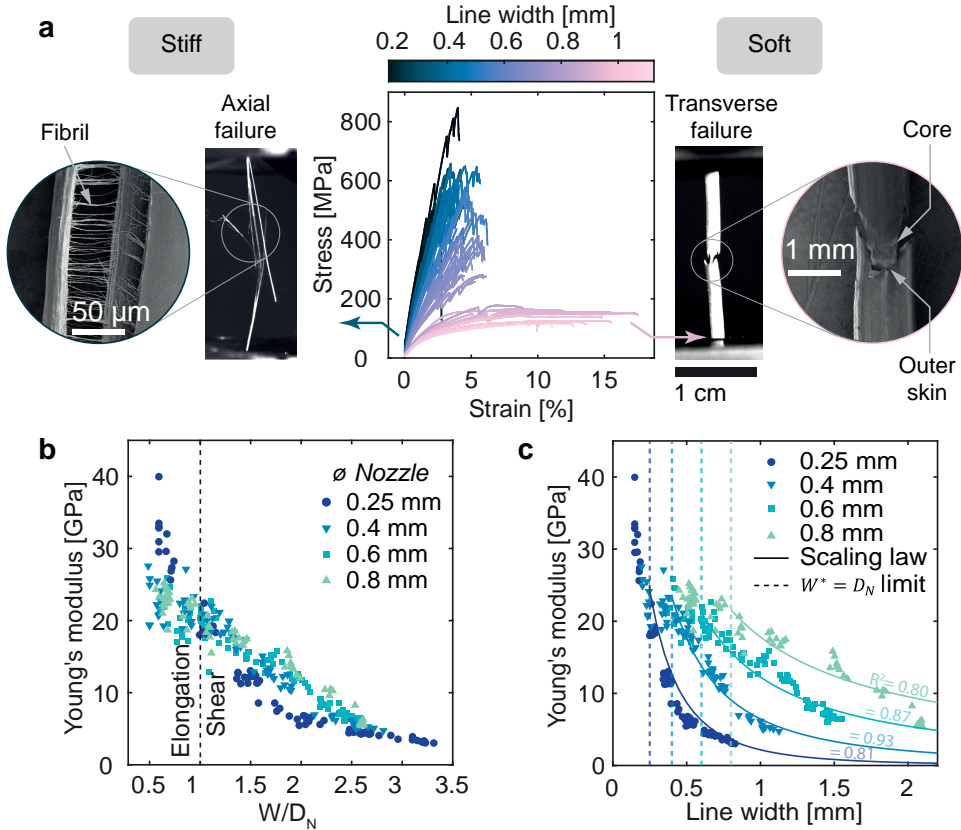
Figure 3.2 – **Line width influences the microstructure and mechanical response of the 3D-printed liquid crystal polymer**. **A.** The tensile behavior of printed lines transitions from brittle to ductile with increasing line width due to the increasing contribution of transverse flow from the nozzle. In the stiff samples, a fibrillar failure is identified in SEM while in the softer samples, a skin and core structure is observed. **B.** Increasing the ratio of printed line width W to nozzle diameter D_N leads to a decrease in Young's modulus for the four different nozzle diameters that were tested. **C.** The Young's modulus scales with line width by a power law of exponent $-\pi/(4D_N)$ beyond a threshold where shear flow dominates over elongational flow.

Figure 3.3 – **A.** Transmitted-light dark-field microscopy of constant line width samples printed with four different nozzle diameters demonstrate texturing. **B.** Shear bands, typical of aligned nematic polymers, decrease in intensity with increasing nozzle diameter and decreasing shear rate. Their wavelength follows a reciprocal square-root shear scaling.

fibrils effectively allows the printed lines to stay connected after fracture. In contrast, the specimens printed with line widths larger than the nozzle diameter sho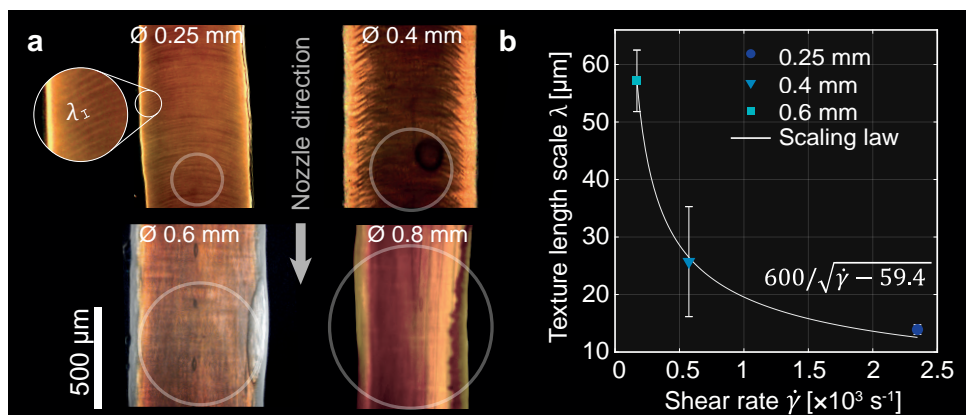w a ductile fracture, with a skin/core behavior [10]. The stiffer skin fails first while the more compliant core remains embedded, revealing a conical fracture surface shown in the SEM image. We obtained a modulus of 4.7 GPa and a strength of 115 MPa corresponding to a 10 % failure strain for the specimen with the largest line width.

To further elucidate the effect of nozzle diameter, measurements of the tensile response were conducted for four nozzle diameters and different values of W/D_N as shown in Figures 3.2b and 3.2c. The elastic modulus was observed to vary widely with W/D_N for all nozzle sizes that were studied, both for single lines and unidirectional tensile samples, shown in Figure SI 3.3. For example, the 0.25 mm nozzle shows the widest property variation, Young's modulus ranges from 3 GPa for the widest lines to 40 GPa for the thinnest line. The strength variation also covers one order of magnitude up to a value of 1.28 GPa (Figure SI 3.1a). A decrease in mechanical properties with increasing line width was reported in the work of Yan *et al.* [15] for CF-PLA, CF-ABS and CF-PA. However, the span of this variation was far narrower, with Young's moduli ranging from 2.8 GPa to 4.2 GPa for respective line widths between 0.48 and 0.72 mm, as shown in Figure SI 3.2. This has been associated with a wider distribution of fibre orientations with increasing widths of short-fibre composites [15]. A transverse flow component was identified using numerical simulations of the 3D flow during extrusion [17, 18]. For narrow extruded lines, fibres are reportedly aligned in the flow direction, while wider extrusion causes the polymer melt to flow partially in the transverse direction, leading to a larger distribution of angles for the anisotropic fillers in the melt [15]. We hypothesize the same behavior where a larger flow rate induces a perpendicular component into the motion of the fluid, which in turn causes loss of alignment in our LCP samples. In order to shed light on this behavior, the threshold line width beyond which transverse flow occurs can be investigated.

Considering a case where transverse flow, i.e. flow in the y-direction, is absent, the exiting material can only increase the height of the print line through bulging. In this case, the volume conservation equation simplifies to 2D along planes normal to y. In other words, all cross-sectional areas of the melt pool and printed line along the transverse dimension y should be at equilibrium. Using a plug flow assumption inside the nozzle allows us to define the velocity V_N of the melt inside the nozzle before exit as a constant. During one second, a cylindrical volume of height V_N and diameter D_N is extruded. The sectional area of this cylinder along y is $A_{in} = D_{chord}(y) \cdot V_N$ where $D_{chord}(y) = 2\sqrt{(\frac{D_N}{2})^2 - y^2}$. Steady exit of the polymer implies that A_{in} should equal $A_{out} = h \cdot V_{line}(y)$, the area of the printed line deposited without bulging. Consequently, the length deposited per second $V_{line}(y) = \frac{V_N}{h}\sqrt{\frac{D_N}{2}^2 - y^2}$ is only defined within the bounds $y = \pm D_N/2$. The value $W = D_N$ plotted in Figure 3.2c may therefore be considered as a threshold W^* above which transverse flow should occur. Figure 3.2c further indicates that the relationship between elastic modulus and line width follows a trend shifting from linear to power-law with decreasing nozzle diameter. A scaling law was developed using Buckingham's theorem of dimensional analysis [37] with the independent variables D_N and W. For measurements above W^*, the scaling law

$$ E = E_0 \frac{D_N}{L_0} \left(\frac{W}{L_0} + \frac{h}{D_N} \right)^{-\frac{\pi L_0}{4 D_N}} $$

where $E_0 = 25\,\text{GPa}$, and $L_0 = 1\,\text{mm}$, describes the experimental data for the four nozzle diameters that were studied, with R^2 values ranging from 0.80 to 0.93. For all nozzle diameters except 0.25 mm, the data depart from the fitting trend below this value. We hypothesize that elongational flow at low flow rates causes pressure inhomogeneities, which translate into geometrically inconsistent filaments for mechanical testing. The scatter thus becomes higher, in particular for the strength values. In contrast, for the 0.25 mm nozzle, the aspect ratio of the filament is closer to 1 for the thinnest lines ($h = 0.1\,\text{mm}$, $W = 0.17\,\text{mm}$), therefore the extruded melt needs to undergo less strain to fit the expected cross-section. This may facilitate the production of consistent diameters even under extensional flow. As such, the scaling law can be used as a non-linear relationship to predict stiffness from line width beyond the threshold at which transverse flow occurs.

To further understand the influence of transverse flow on mechanical properties, flow behavior can also be conceptually split between elongational flow and shear flow. These two flows coexist during 3D printing since the nozzle is a die geometry with a contraction cone promoting elongational flow, and a straight channel promoting shear flow. Elongational flow is known to be more effective than shear flow in causing molecular orientation in LCPs [38], even more so than other polymers below the threshold of line width W^* where no transverse flow occurs, due to the cooperative nature of the molecules in the nematic phase. The apparent shear rate $\dot{\gamma}$ in the nozzle is computed with the relationship

$$ \dot{\gamma} = \frac{32Q}{\pi (D_N)^3} \tag{3.1} $$

The shear rate imposed at the 0.25 mm diameter nozzle tip spans two orders of magnitude, from $50\,s^{-1}$ to $3500\,s^{-1}$ for line width ranging from 0.15 mm to 0.82 mm. With such a range in the shear rate, the melt behavior can be very different in terms of viscosity, texture, and rheology [32]. The largest apparent shear rate is observed for the most compliant specimens, with a Young's modulus of 3 GPa. In Figure SI 3.1b, Young's modulus is plotted against shear rate for different nozzle diameters. Single lines printed with different nozzle diameters at the same shear rate yield vastly different Young's moduli. These elements indicate that shear inside the nozzle alone cannot explain the discrepancy in alignment. A closer look into the microscopic orientation within the printed lines is needed.

In Figure 3.3, four lines of width ranging between 0.5 mm and 0.6 mm were printed with different nozzle diameters. The lines were polished down to 20-40 μm thickness and imaged with crossed-polarized transmitted light microscopy. A banded texture of horizontal streaks can be observed, whose wavelength λ increases with nozzle diameter until it becomes virtually indistinguishable at $D_N = 0.8$ mm. Such a phenomenon is commonly reported after cessation of shear for a wide range of LCPs, including the thermotropic LCP studied here [32, 39, 40]. Their formation has been linked to elastic energy stored in the nematic texture during flow, which is released through the unwinding of the nematic directors upon flow cessation [32]. This induces a formation of periodic extinctions observable with transmitted light microscopy under crossed-polarizers [41, 42]. The bands can be characterized by their wavelength, which varies with the shear conditions. For $D_N = 0.8$ mm where the banded texture cannot be clearly distinguished, the threshold between elongation and side-way flow W^* is above the line width $W = 0.55$ mm of this specimen. At this line width, the shear rate $\dot{\gamma} = 65\,s^{-1}$ is lowest, and the strong elongational flow imposed at the exit of the nozzle will predominate over existing textures caused by low shear and facilitate molecular re-alignment. To further confirm the nature of these bands, we relate the wavelength of the three visible textures to a texture length-scale l_t, for which extensive theoretical work was conducted. Previous research [43, 44] has demonstrated that in a flow region where the Deborah number De is below unity, the texture of sheared, flow-aligning rigid rod LCP can be related to shear by the following relation $l_t \propto \frac{1}{\sqrt{\dot{\gamma}-\alpha}}$. The agreement between the observed wavelength and this scaling law confirms that these bands are indeed shear bands.

As is the case for the three printed lines with visible textures, the presence of a banded texture has been reported to play a detrimental role in the stiffness along flow direction [45], because the recoil of the nematic directors causes a spatial periodicity of the molecular orientation [41]. At nozzle diameters of 0.25 mm and 0.4 mm, the banded texture is not a straight line but a curve with an angle of approximately 30° on the edges. Such curved banded structures have also been reported for thin sections of injection molded specimens of other thermotropic LCPs [46], where it is suggested that the banded structure runs perpendicular to the flow. In such a case, these curved banded structures are a strong indication of transverse flow behavior.

The strong dependency of line width upon tensile properties for 3D-printed single lines of LCP is caused by the opposing behaviors of transverse flow and extensional flow during the deposition of the melt. Compared to approaches that promote anisotropic re-

arrangement during printing using e.g. nozzle rotation [47, 48], this method relies on nematic self-assembly of the polymer under the different processing pressures to change its resulting stiffness, as shown in Figure SI 3.4. The myriad of routes explored to create stiffness gradients, such as porosity gradients [14, 25] or compositional gradients [49, 50], and their omnipresence in the natural world are indicators of how promising they may be to engineering, should there be an easy approach to manufacture them [8]. For instance, tailoring of such stiffness gradients allows the development of single-material bio-inspired crack-arresters similar to those obtained by alternating stiff and soft polymeric layers [51]. The explored range of stiffness in our work opens new paths for tuning compliance and deformation before failure on the fly, simply by changing the processing conditions of the polymer.

3.2.3. Distance-aware generation of flow-inspired patterns

As illustrated in Figure 3.2, the anisotropy granted by LCP, as well as the wide range of line widths that can be extruded, allow the realization of complex infill patterns. However, typical slicing approaches tend to assign a fixed line width for each printing feature, such as perimeters or infills. They also fill volumes with a fixed geometrical repeat pattern, like gyroid or rectilinear. A versatile method allowing both a freeform distribution of angles and a fully dense coverage of the shape by print paths is therefore needed.

Two main steps are followed to generate streamlines which will form the print paths. The first step involves crafting an angle field corresponding to the target pattern. In the second step, the streamlines are located such that the maximum distance between neighbours does not exceed constraints of manufacturability or desired mechanical behavior. These streamlines are then processed to create manufacturable patterns.

The angle field corresponding to the target pattern can be considered as user input to the streamline generation algorithm. Inspired by fluid dynamics, we propose a facile way of generating patterns by using mathematical functions in the complex domain. We make use of a transformation of the vector space $\mathbb{R}^2$ representing the two-dimensional rectangular design domain into the complex field $\mathbb{C}$. For any given point (x, y) in the domain, we introduce the complex scalar $z = x + iy$. Any complex differentiable function $f : \mathbb{C} \mapsto \mathbb{C}$ can then transform the two-dimensional real space into a complex scalar field. At $z = z_0 = x_0 + iy_0$, the argument of complex number $f(z_0)$ determines the direction followed by a streamline at (x_0, y_0). In fluid dynamics, such a transformation is performed from a real domain to the complex plane to obtain analytical solutions for an irrotational incompressible flow. The scalar function f then represents a complex speed, defined as $f(z) = \frac{\partial p}{\partial z} = u - iv$. The complex potential function p is defined as $p(x, y) = \Phi(x, y) + i\Psi(x, y)$, where Ψ is the stream function and Φ is the velocity potential of an incompressible fluid satisfying Cauchy-Riemann equations [52]. The vertical and horizontal components of the speed (u, v) are by definition $u = \frac{\partial \Phi}{\partial x}$ and $v = \frac{\partial \Phi}{\partial y}$. With knowledge of $f(z)$, the real velocity components (u, v) can be found with $(\text{Re}(f), -\text{Im}(f))$. It is worth noting that here, any complex differentiable function may generate a pattern, regardless whether it represents a physical flow. Three exemplary patterns generated by elementary potential flows are illustrated in Figure 3.4a along with the corresponding

3
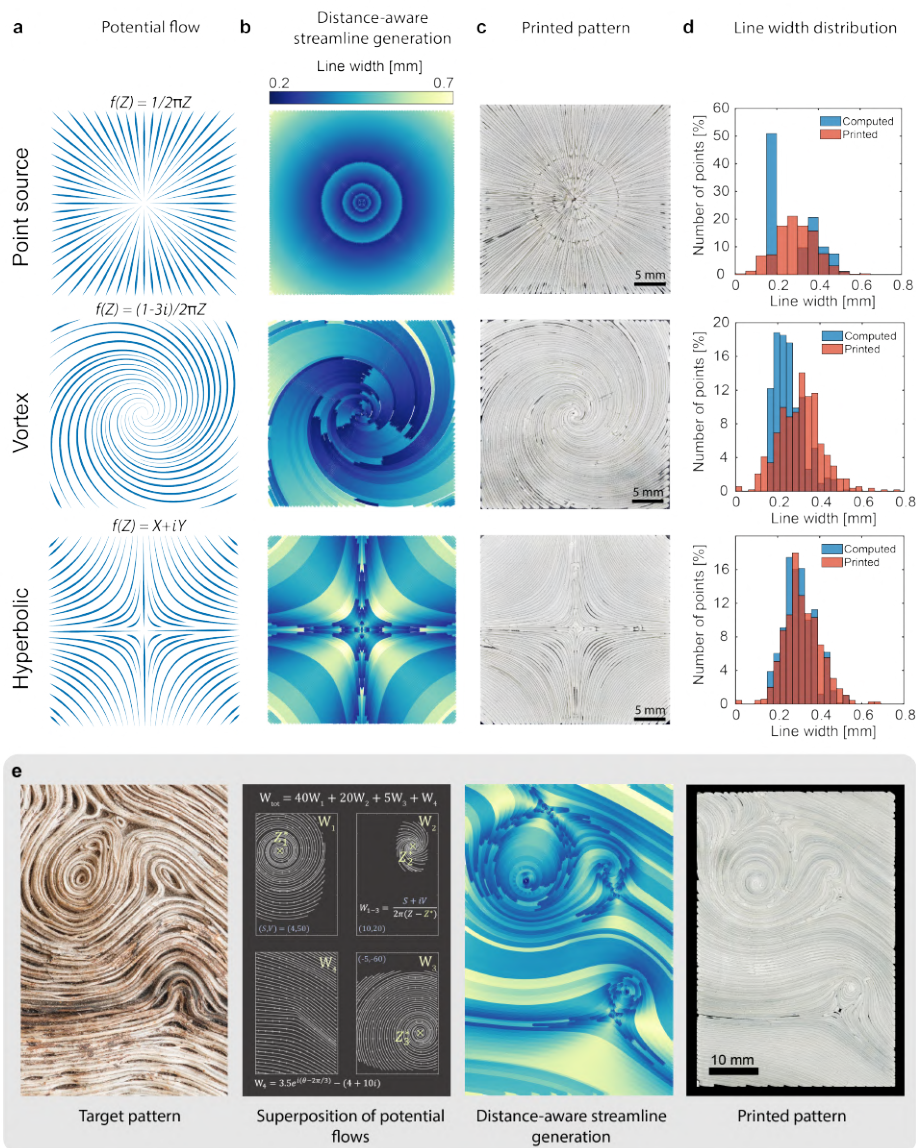
Figure 3.4 – **Complex printable patterns are generated via superposition of elementary potential flows**. **A.** Mathematical expressions describe elementary potential flows in the complex plane, from which an angle field is calculated across the rectangular domain. **B.** Streamlines are computed from the angle field such that the largest distance between neighbouring paths does not exceed $2D_N$. **C.** The paths are transformed into g-code and 3D-printed, covering the area homogeneously. **D.** The distribution of line widths is compared between the planned toolpath (blue) and the image of the printed object (red) along a set of orthogonal "sampling" streamlines, indicating varying levels of accuracy between the response of the polymer and the planned extrusion width depending on the pattern. **E.,** This workflow is successfully applied to a natural pattern such as the weathered wood grain of a maple log (Image credit: ©Mark Windom).

complex velocities [52]: a point source, a vortex, and a right-angle flow. More complex flow fields such as flows through an opening or normal to a flat plate, can also be described analytically with this method [53], and may also be further explored to create relevant patterns for solid mechanics.

After a velocity field has been created, streamlines can be generated. They are defined as a family of curves whose tangent vectors constitute the velocity vector field of the flow. In this work, streamlines are generated to become tool paths for the printer to follow. To achieve this, the algorithm of Mebarki [54] is implemented and adapted such that lines are spaced by manufacturable widths, as illustrated in Figure SI 3.6. At each calculation step, at the location where the largest circle can be fit between two streamlines, a new streamline is inserted until the largest circle that can be fit is smaller than W_{upper}, the largest desired line width. The new streamline is immediately trimmed if it becomes spaced to its neighbours by a distance smaller than W_{lower}, the lowest desired or manufacturable line width. Distances between lines are then extracted to obtain the extrusion amount necessary for each segment of the toolpath. The resulting distribution of line width shown in Figure 3.4b indicates successful replication of the mathematical flow fields. After the streamlines have been generated, simplified, sorted, and transformed into g-code format, they can be 3D-printed, as illustrated for the three elementary flow fields in Figure 3.4c.

To quantitatively assess the ability of the printing method to produce a freeform infill, the image of the printed object in Figure 3.4c is compared to the planned toolpath. Curves that are orthogonal to the planned toolpaths are generated to intersect between 500 and 600 printed paths. Along these intersections, the planned line width is compared to the distance between black pixels in the image. Figure SI 3.6 shows such a comparison along a representative sampling streamline for the three cases represented. The distribution of line widths for planned and printed lines in Figure 3.4d follows a Gaussian pattern in all three cases. The largest deviation to the expected distribution corresponds to the point source case. Due to the radial distribution of distances, the line width along each of the intersecting circles should be constant, which is not the case in the physical printed object. Looking closer at the printed lines in Figure SI 3.7, the deviation can be attributed to both errors in distinction of printed line boundaries and slight overlapping between printed lines. Depending on the fabrication sequence, if a printed line is slightly impinging onto the space of the upcoming one due to local over-extrusion, the distribution of line widths will oscillate between two values whose mean is the target extrusion value. This phenomenon dissipates without intervention but contributes largely to the larger spread of values for printed lines and could impact mechanical performance.

To replicate a more complex pattern, a principle of superposition can be used. Different base patterns can be superimposed with coefficients, as illustrated in Figure 3.4e, using a weathered maple log as source image. The radius of influence on the global angle field can also be restricted simply by the element-wise product of the angle matrix with a masking matrix whose values range from 0 to 1. The impact of upper and lower bounds of line widths on the overall streamline distribution using this pattern, as well as the resulting height profile of this shape, can be seen in Figures SI 3.8, SI 3.9 and SI 3.10. A curve generation method based on phase-fields [24] is compared to our streamline-based

approach in Figure SI 3.12. Instead of one single relatively tortuous path with many U-turns, our approach yields multiple smoother lines. Hence, the workflow proposed here leads to 3D-printing of geometrical patterns ranging from vortices to egg-box shapes, which can easily be superimposed to capture both local and global features.

3.2.4. Tuning mechanical performance via large-curvature patterns

This freedom of path generation, along with the anisotropy of LCP, opens the possibility to explore mechanical features beyond the traditional restricted fibre path of laminated materials such as high-performance continuous fibre composites. This is illustrated in Figure 3.5 both in the elastic region with a buckling optimization (Figure 3.5a) and during fracture to deflect the propagation of a crack (Figure 3.5b).

In Figure 3.5a, the consequences of alleviating the curvature constraints on the mechanical performance are explored in the case of buckling. While we propose a simple mathematical method to generate angle fields, optimization algorithms can also be used as input to the streamline-placement workflow. We demonstrate this with an algorithm that optimizes the fibre angle distribution [6] to maximize the buckling load of 3D-printed LCP plates. In this method, fibre angle retrieval is performed by approximating the structural responses based on the optimal stiffness distribution found for a set of lamination parameters. During the optimization, a steering constraint is introduced to ensure the manufacturability of the material. Such variable stiffness laminates are typically manufactured with AFP of continuous fibre composites. In AFP and continuous carbon-fibre 3D printing, maximum curvatures of around $3\,\text{m}^{-1}$ and $66\,\text{m}^{-1}$, respectively, are conservative limits to the fabrication [6, 56]. At higher curvatures, defects such as wrinkling can be expected due to the intrinsic stiffness of the fibres. In contrast, the maximum curvature that can be explored here is only limited by nozzle diameter, in the range of $1000\,\text{m}^{-1}$ to $2500\,\text{m}^{-1}$. To explore the relationship between curvature and buckling load, four different symmetric and balanced layups were generated by the optimization algorithm with allowed curvature constraints spanning from $0.1\,\text{m}^{-1}$ to $1000\,\text{m}^{-1}$ for $112\,\text{mm} \times 86\,\text{mm}$ samples. To focus on the effect of curvature of the printed paths, the range of line width is restricted such that more than $70\,\%$ of the aggregated length of deposited lines have widths between $0.30\,\text{mm}$ and $0.45\,\text{mm}$, close to the nozzle diameter dimension of $0.4\,\text{mm}$. As shown in Figure SI 3.13, the average Young's modulus across this line width range is $21.4\,\text{GPa}$, with a standard deviation of $1.97\,\text{GPa}$. The angle field and subsequent print paths for a given layer are shown in Figure 3.5a with a coarse line width for visualization purposes. Print paths for other curvatures can be seen in Figure SI 3.14c. The distribution is unidirectional with a $45°$ angle at $0.1\,\text{m}^{-1}$ curvature constraints, but at $100\,\text{m}^{-1}$, two distinct zones start to materialize. Edges where stiffness is maximized appear when the load can be redistributed to the nearby simply-supported fixture clamps in the $0°$ direction, and an oblique central zone emerges to resist buckling. At $1000\,\text{m}^{-1}$, a central transition zone is also clearly observed where the curvature changes abruptly. Samples were tested in compression until failure with the boundary conditions illustrated in Figure SI 3.14a. The quantitative difference between numerical and experimental values was as expected and may be attributed in part to the simplifying assumption chosen in the optimization algorithm that the LCP is an orthotropic material with a constant stiffness, despite a narrow
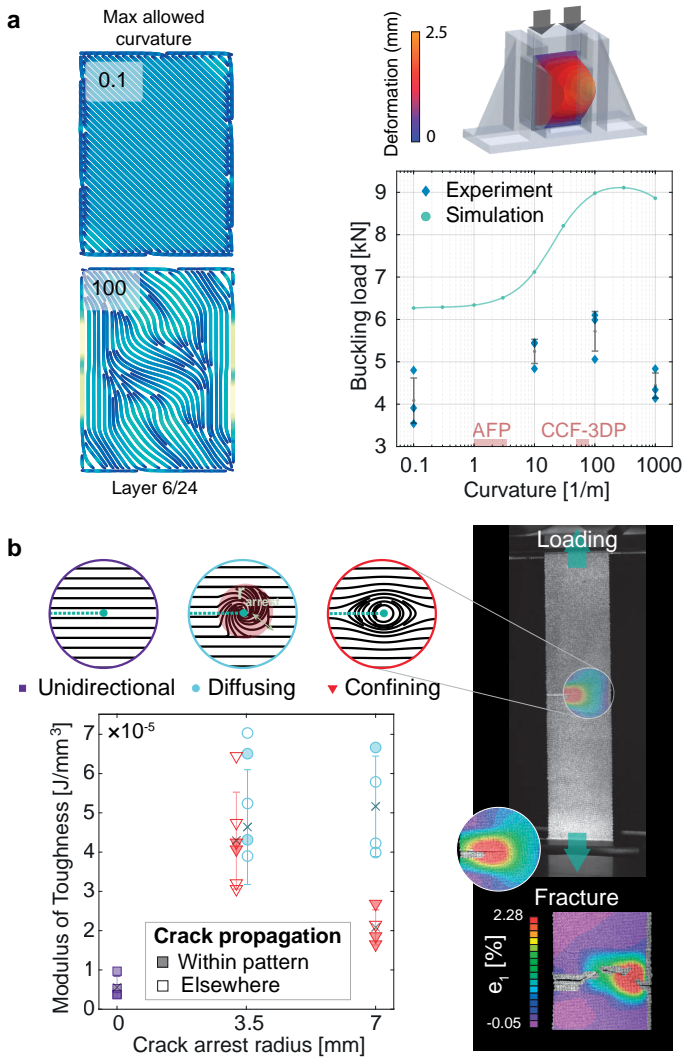
Figure 3.5 – **Patterns can be utilized to enhance mechanical properties. A.** Reducing the curvature constraint in a laminate optimization algorithm [6] leads to an increase in buckling load. **B.** Microstructures that are locally applied to a laminate can enhance the resistance to crack propagation along a cut edge. Error bars represent standard deviation of the data.

3
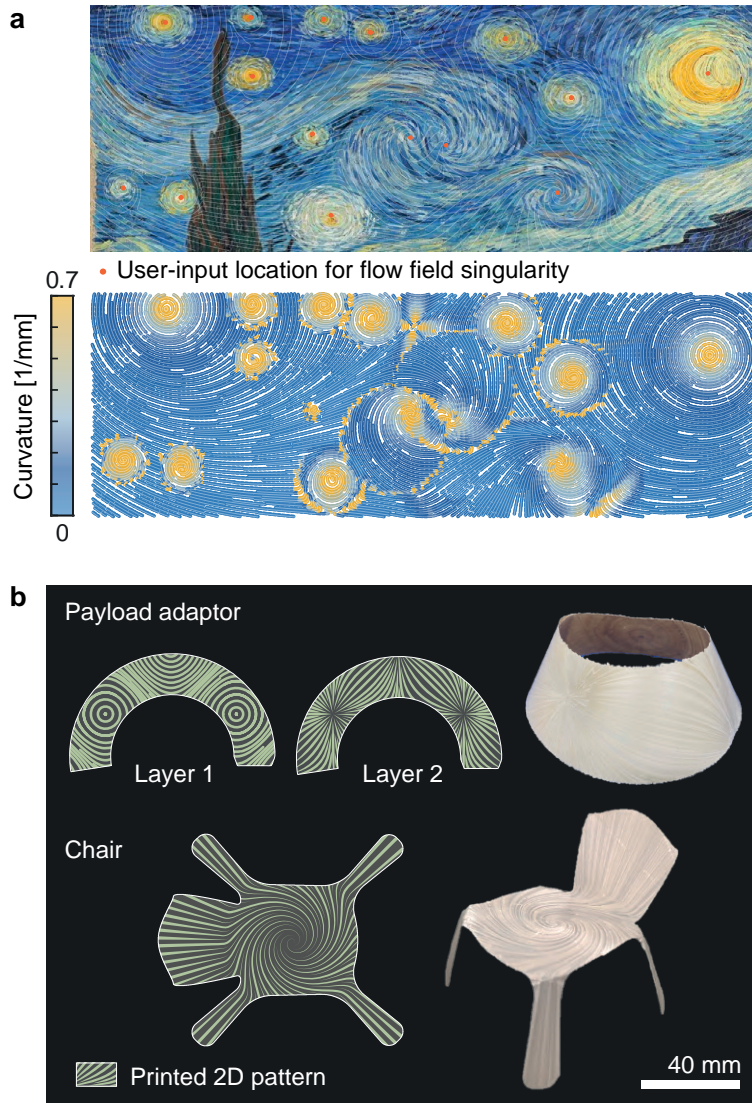
Figure 3.6 – Generated shapes can also be applied to manufacture seldom-seen patterns in solid mechanics such as turbulences, such as **C.** where a detail of the sky of oil painting The Starry Night [55] by van Gogh is reproduced with vortices using the potential flow field method described in Figure 3.4e. ©2023 Digital image, The Museum of Modern Art, New York/Scala, Florence **D.** The generated shapes can also open new design possibilities for functional objects such as a payload adaptor fitting for a launcher, or a chair.

range of line width being used. Further, buckling is strongly affected by experimental perturbations which can be either induced by imperfect clamping, or manufacturing defects that are common in 3D-printing. The deviation to the trend at $1000\,\mathrm{m}^{-1}$ can be explained by the more abrupt changes in angles resulting in a lack of continuity between print lines in this zone (Figure SI 3.14c), as opposed to the smoother pattern at $100\,\mathrm{m}^{-1}$. Despite these discrepancies, a similar behavior is observed for both experiment and theoretical values, with an improvement between $0.1\,\mathrm{m}^{-1}$ and $100\,\mathrm{m}^{-1}$ of 43 % numerically and 40 % experimentally. This concludes that the proposed workflow can explore new pathways in mechanical design, which were previously restricted by manufacturing constraints. Furthermore, since stiffness variation of the material due to line width was minimized, the trend may also be applied to anisotropic printable materials such as fibre-filled polymers with a narrower range of property variation.

Having studied how the design space of an optimization framework can be extended via manufactured gradients of curvature and stiffness, we now explore the possibility of using the patterns described in Figure 3.4 to influence crack propagation. For this purpose, in Figure 3.5b the failure behavior of two-layered Single-edge Notch Tension (SENT) samples is studied. A unidirectional sample perpendicular to the loading direction was taken as a benchmark. The highly-aligned microstructure of 3D-printed LCP inevitably entails a low transverse strength. For the layer height studied here, $h = 0.1\,\mathrm{mm}$, unidirectional tensile strength in the transverse direction and shear strength have been reported as 27.4 MPa and 26 MPa respectively [10].

Correspondingly, the amount of energy needed to propagate the crack along the printed line direction is very low, analogous to the weak fibre interface in wood. This kind of anisotropic biomaterial adapts and grows to attenuate stress concentrations in the transverse direction [57]. In a similar approach aiming to shield sensitive zones, two different configurations were explored to resist crack propagation: a spiraling pattern, which is hypothesized to diffuse the crack course away from the notch zone, called diffusing, and a wood knot pattern, called confining as it could potentially confine the crack within the notch zone. Shown in Figure 3.5b, for each configuration, the radius of the crack arrest feature r_{arrest} was chosen as 3.5 mm or 7 mm to compare the toughness to the feature size. Compared to baseline, the modulus of toughness of samples with the smallest r_{arrest} is 7.7 times higher for the confining pattern on average, and 9.3 times higher for the diffusing pattern. From the strain fields obtained with Digital Image Correlation (DIC), we found that none of the specimens display straight crack propagation. Due to the high toughness developed locally, the crack did not propagate from the notch where the highest stress concentration should be located. Instead, the crack was initiated at much higher loads either at another location inside the patterned zone or at a location away from the notch. The inset strain field shown in Figure 3.5b illustrates a propagation within the crack-arrest zone, for one of the confining samples with $r_{\mathrm{arrest}} = 3.5\,\mathrm{mm}$, immediately after failure. Even though the notch is present at the center of the specimen before failure, the propagating crack avoids the center region and bridges to the opposite edge. The fact that failure takes place at another location than at the notch for 15 specimens out of 23 indicates that the proposed method may be highly successful at shielding sensitive locations, at no added mass cost.

Alternatively, these features could be used as structural fuses to attract cracks to specific locations facilitating monitoring of predictable damage and maintenance for larger engineering systems. Both path directionality and gradient of stiffness may be independently controlled with our method, to influence deformation behavior and favor a specific failure mode. Figure SI 3.15 shows numerically how the maximum curvature of the deflecting shape of a plate subjected to uniform pressure can be influenced by a chosen stiffness distribution, with for instance a more compliant and ductile material configuration along its edges.

To further illustrate the versatile nature of our approach toward the fabrication of natural materials and phenomena, we replicated an artwork well-known for its exquisite ability to capture movement through brushstrokes. In Figure 3.6a, the eddies in the sky of *Starry Night* [55] by painter Vincent van Gogh (1889) are reproduced with vortices of varying radii of influence. The corresponding evenly distributed and printable toolpaths are coloured with absolute curvatures to highlight vortex location. Despite the eddies in the painting not accurately recreating mathematical features of turbulent flow [58], their rapid change in curvature and stroke thickness embodies the motion of turbulence in the eye of many. We find that van Gogh freely exploited a colour scheme of contrasting ultramarine blues to warm yellows which can be related to the curvature of his thick impasto brushstrokes. This link between colour and shape, bridging between style and content, may contribute to convey the striking combination of harmony and turmoil which has fascinated generations [59]. One could even obtain different renderings using our patterning method, with other anisotropic properties such as structural colours [60] or birefringence [22, 61]. Further, integrating the concept of turbulences into solid objects opens routes for materials with new functionalities, such as the shaping of eddy currents [62] via conductive anisotropic polymers.

In Figure 3.6b, proof of concept functional objects which may benefit from complex patterns are presented. A truncated cone was printed in two dimensions and thermally fused at its edges, with a pattern generated from the complex velocity function $f(z) = \sin(x/\lambda) + i \sin(y/\lambda)$. The geometry represents a payload attachment fitting for a space launcher, demonstrating how this method could be used to promote specific buckling modes for non-planar shapes. Next, a chair was formed by overlapping a point source onto a vortex with a diameter of influence equal to half the domain dimension. High-curvature print paths provide out-of-plane compliance at the center of the seat and straighten out gradually to distribute the load to the stiffer, unidirectional legs.

3.3. Conclusions

We discovered that structures can benefit from the high shaping freedom achieved with nematically aligned LCP 3D printing. The wide range of line widths that can be printed with LCP enables the modulation of mechanical behavior within a single material simply by using nozzle pressure. The changing nozzle pressure results in a transverse flow of the nematic domains causing the stiffness to vary from 3 GPa to 30 GPa depending on the deposited line width and nozzle diameter. These variables were used to exploit design freedom by generating evenly distributed print paths within a desired mechanical

property space. Our work enables the flow-inspired design of complex microstructures using ubiquitous inputs such as biological matter, artwork, or fibre angle optimization. In particular, we found that the buckling load could be increased by 40 % by alleviating the curvature constraint in a laminate optimizer. Furthermore, the generated patterns could also effectively arrest or deflect cracks in the presence of a stress concentration. The abundance of patterns that can now be manufactured expands the design space for functional, lightweight objects with gradients of stiffness and curvature, and opens research routes to reproduce and study intricate natural patterns such as turbulence, and biological microstructures such as wood or bone.

Data Availability Statement

The data in this work is available under the repository: `https://doi.org/10.4121/46723f7d-274a-4331-879b-5dacc28b07ce`.

Slith3r, the path-planning algorithm developed for this thesis, is available through GitLab `https://gitlab.tudelft.nl/shapingmatterlab/slith3r`

3

3.4. Materials and Methods

3D-printing

The filament used is the thermotropic random copolymer HBA:HNA with ratio 73:27, supplied by NematX (Switzerland). G-codes are printed on a Prusa i3 MK3S+ 3D-printer, at a nozzle temperature of 330 °C and a bed temperature of 90 °C. The 3D-printer is only modified in hardware and firmware to withstand slightly higher temperatures than its specifications. The PEI bed is coated with a spray (Dimafix, Spain) to maintain good adhesion. Brass nozzles (E3D, England) used in this paper show a L/D ratio of 1.50 for 0.25 mm and 0.4 mm nozzles, and $L/D = 2.0$ for 0.6 mm and 0.8 mm nozzles. Unless otherwise stated, the 0.4 mm nozzle is used. Print speed is 60 mm.s^{-1} for single lines and mechanically-tested parts. For the smaller patterns in Figure 3.4 of size 30 mm × 30 mm, print speed is reduced to 10 mm.s^{-1} such that any viscoelastic response [11] of the material does not affect the effective line width variation. For unidirectional tensile samples, a 0.05 mm layer height is used, with print speed of 35 mm.s^{-1} and temperature of 295 °C.

Optical microscopy

Thin strands of LCP were glued to microscopy glass slides with cyanoacrylate glue. Polishing was carried out manually on a polishing machine (Tegramin-20, Struers) with very short steps mostly in the 45°, 90° and −45° angles with respect to the longitudinal line axis to avoid peeling off the fibrillar structure until translucency was achieved (20-40 μm). An optical microscope (DM100, Leica) was used to image the cross-section with dark-field transmitted light.

SEM

A scanning electron microscope (JSM-7500F, JEOL, The Netherlands) operated with an acceleration voltage of 5 kV was used to visualize the fibrillar and core-shell structures after fracture. A 15-nm gold coating was sputtered (Quorum Q300TD, UK) on their surface prior to imaging.

Toolpath Generation

Evenly-distributed placement of streamlines

Streamlines are generated in MATLAB (MathWorks, USA) from an angle field via a farthest-point seeding method inspired by Mebarki's approach [54]. In the initialization stage, a Delaunay triangulation of the edges of the rectangular design space Ω is performed. The first seeding point is the center of the largest circle circumscribed in any of the triangles inside Ω. This streamline is generated using forward Euler prediction and a trapezoidal rule correction [63]. The integration step used is 10 % of an element size. The current streamline function requires a rectangular grid of evenly-spaced points, however a domain of any shape can be triangulated with the Delaunay method, which imparts robustness to the workflow in case this constraint is alleviated. This approach is illustrated in Figure SI 3.6. The parameter W_{upper} determines the maximum allowable distance between streamlines. Once the first streamline is generated, its waypoints are added to the list of edge points, and a new Delaunay triangulation is performed. While the diameter of the largest circumscribed circle is larger than W_{upper}, a new streamline is generated. A trimming

step is applied directly to make sure that any two streamlines are separated by a distance larger than W_{lower}. Unless otherwise stated, its default value is $W_{lower} = W_{upper}/3.5$. This smaller bound is adapted to respect the desired mechanical boundaries or manufacturable range of line width as illustrated in Figure 3.2. The influence of W_{lower} is illustrated in Figure SI 3.9. Another parameter can be used optionally to further influence distribution of line widths, W_{seed}. As shown in Figure SI 3.8, an initial round of seed points can be spaced by a distance W_{seed} along a specified edge of the domain. This feature is useful for uniform flow fields or to steer the average distribution of line width towards the upper or lower bound. After these initial streamlines are placed, the algorithm described in Figure SI 3.6 takes over to fill the remaining space.

Line width calculation

Once streamlines have been generated, the final distance between all of them should be computed. For each streamline S, a Delaunay triangulation is performed with all way-points P except P_s, the set of vertices belonging to S. We expect for each point p in P_s, two nearest neighbour points to find on either side of S. The first nearest points N_{S1} to P_s are identified with a Nearest-neighbour algorithm. The nearest neighbour algorithm is repeated without N_{S1} in order to find the second-nearest neighbours N_{S2}. The line width to be extruded at each vertex in P_s is set as half the average value of the distance to either two nearest points. This is a simplification due to the impossibility of distributing material asymmetrically on either side of the extrusion direction. These steps are repeated for each layer of the printed object.

Post-processing of toolpaths

Subsequently, a Ramer-Douglas-Peucker algorithm [64, 65] is applied to each streamline in order to reduce the number of way-points with a set tolerance of 0.02 mm as maximal Euclidian distance allowed between the new line and a vertex. Three metrics are taken into account to calculate similarity: x and y coordinates, and line width. This allows the number of points to significantly reduce despite the small iteration step. Overloading the buffer of the 3D-printer would cause inaccurate printing speed. The simplified streamlines are then ordered to minimize the distance between travel moves. The endpoint of the first streamline is connected to the closest among all extremity points of remaining streamlines, until all streamlines are connected. Finally, the g-code is generated. Extrusion amount is calculated by multiplying distance between waypoints, layer height and line width.

Line width comparison

Orthogonal sampling streamlines are computed from the vector field that is orthogonal to the one generating the print path. The seeding points of the N sampling streamlines are the vertices of an N-sided polygon. N is chosen to intercept between 500 and 600 printed lines. In the "point source case", orthogonal streamlines are circles, thus they are chosen with a diameter of 12 mm, 20 mm and 28 mm, as 3D prints are 30 mm wide. Image processing for 3D-printed images is performed via the following steps: first, photographs of the 3D-printed objects are taken with a Keyence VR-5000 wide-angle microscope. Next, a Photocopy filter is applied in Photoshop (Adobe, USA) to enhance the contrast between lines. In MATLAB, the image size is multiplied by four and blurred with a 2-D Gaussian

smoothing kernel of standard deviation of eight. Blurring enables to simplify and increase the accuracy of the central location of the darker zone where two printed lines are in contact, and reduces the false positives linked to the roughness of LCP. The pixel profile along the sampling streamlines is retrieved, and peaks in the intensity values (boundaries between printed lines) are detected when they reach a prominence of 10 %. Finally, the distance between peaks is computed to obtain the printed line width. For the computed line width, each theoretical polyline is checked for intersection with the orthogonal sampling streamlines. If an intersection is found, the line width of the intersecting segment is retrieved. Once the printed and computed line widths at the intersections are found, they can be compared directly in a plot (Figure SI 3.6c) for one sampling streamline, or their distribution can be compared in a histogram (Figure 3.4d). The height of all the bars sums to 100 % as each bar height represents the percentage of intersected points that fall under a given range of line width.

Tensile testing

Single-line testing

For each print batch, 8 to 10 single lines of the same width are deposited in a bidirectional raster pattern, resulting in lines of about 100 mm in length. To prevent edge effects, a gauge length of 20 mm is marked directly on the line at half-length. Images of this portion of the lines are captured on a wide-angle 3D scanner (VR-5000, Keyence, Japan) while still attached to the print bed. This enables to measure width without perspective error. The images are transformed into binary masks in MATLAB, such that white pixels on the transverse axis yield the width continuously along the longitudinal axis. The average width is then calculated. Single lines are individually glued onto paper tabs at their measured gauge-length position. The tensile tests were carried out at a rate of 2 mm.min^{-1} using a 10 kN (Zwick Roell, Germany) universal testing machine equipped with a 100 N load cell (HBM, Germany). Post-processing is performed with a custom MATLAB script.

Unidirectional tensile testing

The unidirectional parts were tested under tension using a Z020 (Zwick, Germany) universal testing machine with a 20 kN capacity load cell. Following ISO 527-5, samples with a nominal width of 5 mm, length of 110 mm and thickness of 2 mm were printed at 0° angle to the tensile direction, varying the line width from 0.2 mm to 0.6 mm with a 0.4 mm nozzle diameter. Bonded glass fibre end tabs supported the clamping region resulting in a gauge length of 65 mm. Five samples were tested per batch, at a displacement rate of 2 mm.min^{-1}.

Single-edge notch tension

Two-layered 3D-printed samples of size 90 mm × 20 mm are tested with a 10 kN (Zwick Roell, Germany) machine equipped with a 100 N load cell. The notch is created with a sharp razor with extra care to avoid any transverse force pulling apart the lines.

DIC

Digital Image Correlation (DIC) was used to measure the local displacements of the SENT specimens. One 9 MP camera (LIMESS, Germany) with a 50 mm-focal length lens is used to acquire images at a rate of 2 Hz. Analysis was performed using Vic-2D 6 (Correlated Solutions), with a subset size and step size of 27 and 7. A speckle pattern size of 0.18 mm was applied with a stamping roll and ink (Correlated Solutions).

Buckling

Laminate optimization code

Theoretical values of buckling loads in Figure 3.5a are computed with the algorithm of Peeters [6] for an orthotropic material similar to LCP, whose stiffness is assumed to not change with line width. The values E_{11} = 15.4 GPa, E_{22} = 2.08 GPa, G_{12} = 1.3 GPa, and v_{12} = 0.57 are used, as reported in [10] for a layer height of 0.1 mm. A frame is padded around the edges of the output angle field such that the laminate optimization describes the design zone, but that enough space is left to apply vertical clamped or lateral pinned boundary conditions.

Compression fixture

3D-printed laminates of 112 mm × 86 mm with 24 layers of a balanced, symmetric layup are subjected to compression. A modified [66] Compression After Impact (CAI) fixture is used to introduce the top compressive load, and keep top and bottom of the plate clamped, and lateral edges simply supported with knife edges. Load is introduced by a 10 kN test bench (Zwick, Germany) with controlled-displacement at a rate of 2 mm.min^{-1}. Buckling load is determined as the first point where the load deviates by 100 N from the linear regression determined in the elastic zone from 500 N onwards.

Shaping of 3D-objects

To fuse flat printed shapes and create a three-dimensional object, the material can be melted again after extrusion. Kapton tape is first applied to protect the material. The hot tip (290 °C) of a soldering iron is applied briefly at the desired location and angle. The position is maintained until solidification.
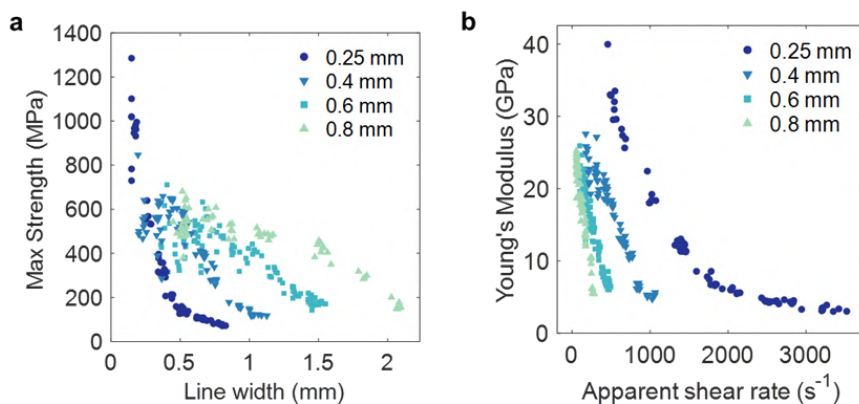
3.5. Supplementary information

Figure SI 3.1 – **A.** Maximum strength against line width for printed lines. **B.** Tensile Young's modulus against apparent shear rate inside the nozzle during printing of with four different nozzle configurations, calculated with Eq. 3.1.
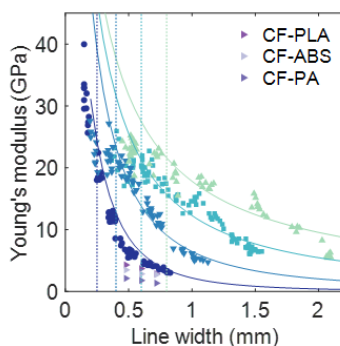

Figure SI 3.2 – 3D-printed lines with varying line widths using LCP and four different nozzle diameters. Other 3D-printed lines of PLA, ABS and PA reinforced by carbon fibres with a 0.4 mm nozzle diameter. Data extracted from Yan *et al.* [15].
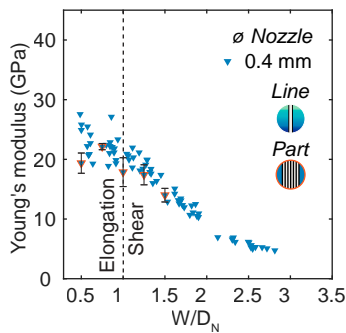
Figure SI 3.3 – Single printed lines and larger unidirectional tensile samples display a similar decrease in Young's modulus with line widths using a 0.4 mm nozzle. Error bars represent standard deviation of the data.

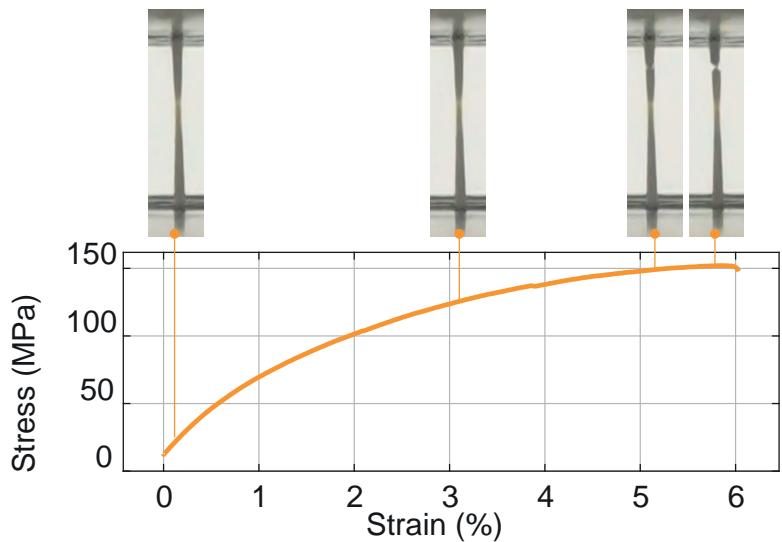Figure SI 3.4 – Stress-strain curve for a varying width sample printed with a 0.4 mm nozzle. Width varies on this line as a sine wave of wavelength 20 mm, corresponding to the gauge length in the test. Video snapshots of the sample during test are located at the corresponding strain percentage. Some necking is observed on the top region leading to fracture, in spite of the thinnest section being 40 % smaller.

As shown in Figure SI 3.4, samples were printed with a pulsating pressure in the nozzle to dynamically vary the line width with a sinusoidal pattern. The test samples are printed with a wavelength of 20 mm, corresponding to the gauge length. Printed width variation could reliably be achieved in print lengths down to 10 mm. Varying-width lines were tested in uniaxial tension, and compared to straight print lines with the same nozzle diameter, with different widths.

A sample with a conventional printable polymer would be expected to fail in the narrowest cross-sectional region of the test sample assuming no defects. Given that the narrow region is a factor 1.4 smaller in area (width, $W = 0.64$ mm) than the actual break location ($W = 0.9$ mm), one may expect failure of the tensile sample to occur there.

Here, the variable width fibres all break close to their widest region. According to data shown in Figure SI 3.2a with straight lines, this reduction in width is associated with an increase of the maximum strength by a factor 2.7. Therefore, failure occurs in the wider region of the sample. This is a useful feature in developing structural fuses, so that in the future, a small region of a structure could be inspected for damage to evaluate a larger complex mechanical system.
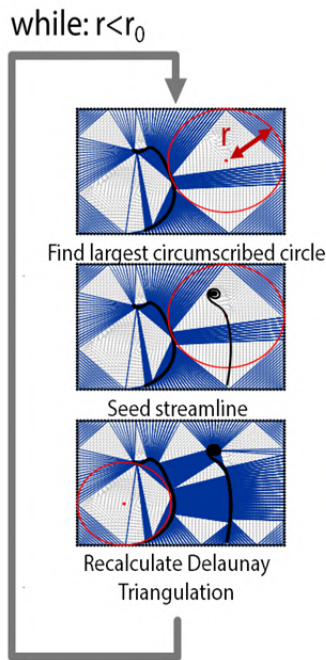
Figure SI 3.5 – Schematics of the core loop of the streamline placement method described by Mebarki [54]. Vertices of the streamlines and edges (black) are used as nodes to the Delaunay Triangulation (blue), from which the largest circumscribed circle of radius r (red) is used as next seeding point, until r becomes smaller than a set value r_0.

3
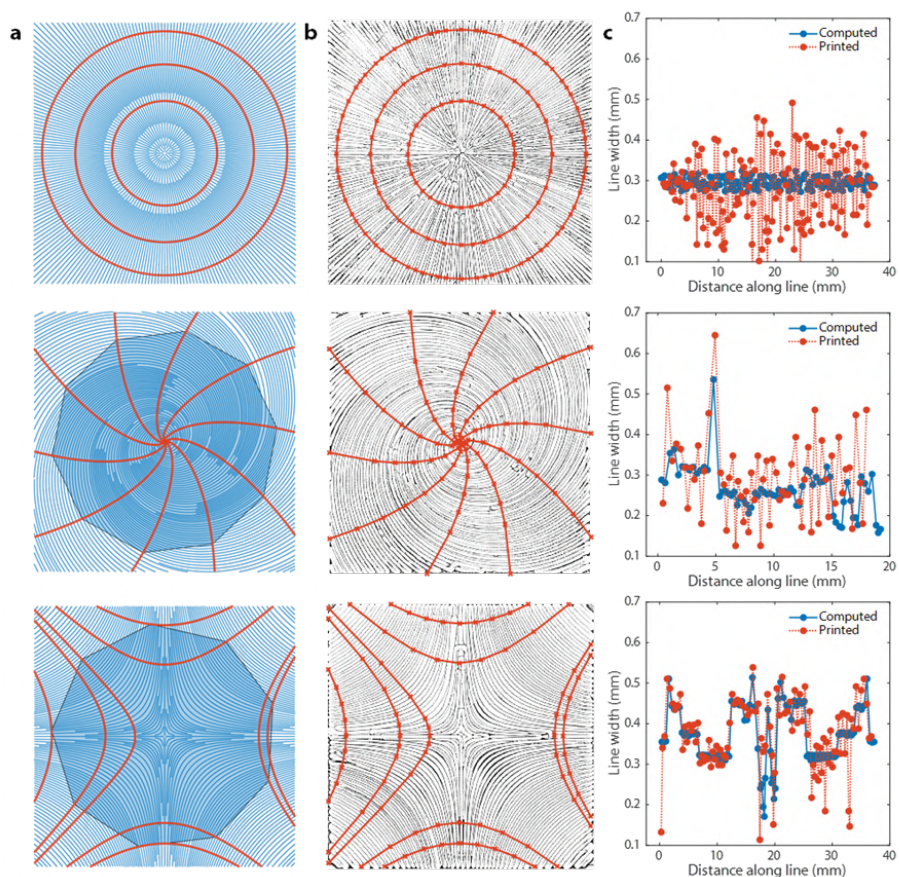
Figure SI 3.6 – Comparison between computed line width and printed line width along orthogonal sampling streamlines (red). **A.** For hyperbolic and vortex flows, the sampling streamlines are generated from the edges of a regular polygon (blue) whose number of vertices creates between 500 and 600 intersecting points. For the radial flow, sampling streamlines are concentric circles. **B.** Pixel intensity along the sampling streamlines is retrieved on the post-processed image of the printed object. **C.** The offset between computed and printed line width can be compared for each sampling streamline.
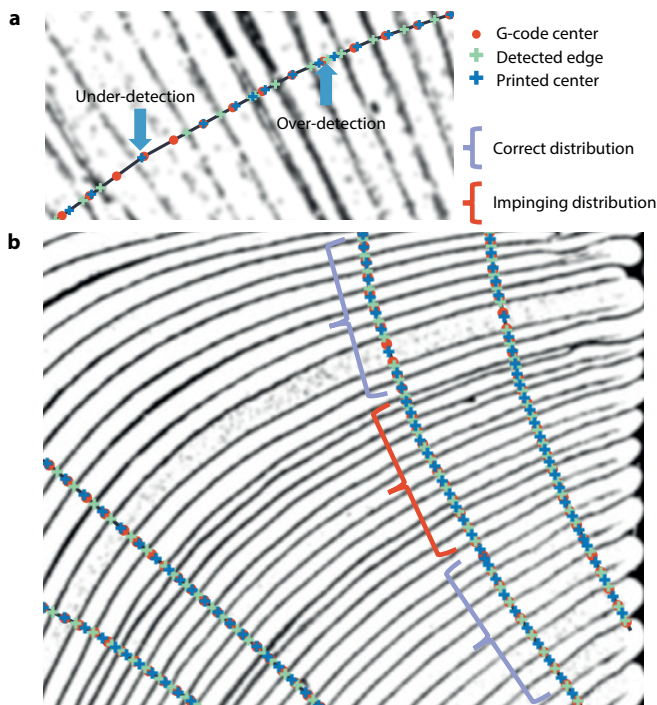
Figure SI 3.7 – Error between computed and printed line width can be attributed to **A.** under or over-detection of the edges between printed lines, or also to **B.** a phenomenon of one line impinging on the space that should be allocated to its neighbour, leading the line width in this zone (red) to oscillate around the target value.

3

Figure SI 3.8 – Distribution of line widths for the wood pattern with different values of (W_{lower}, W_{seed}) with $W_{upper} = 0.7$ mm. **A.** In the absence of preliminary seeding points, the output line widths are subjected to fluctuations especially at zones corresponding to constant flow fields. **B.** When adding seeding points that are evenly spaced along the left edge by the value W_{seed}, line width at such zones becomes more uniform. **C.** This also constitutes a way to influence the average line width.

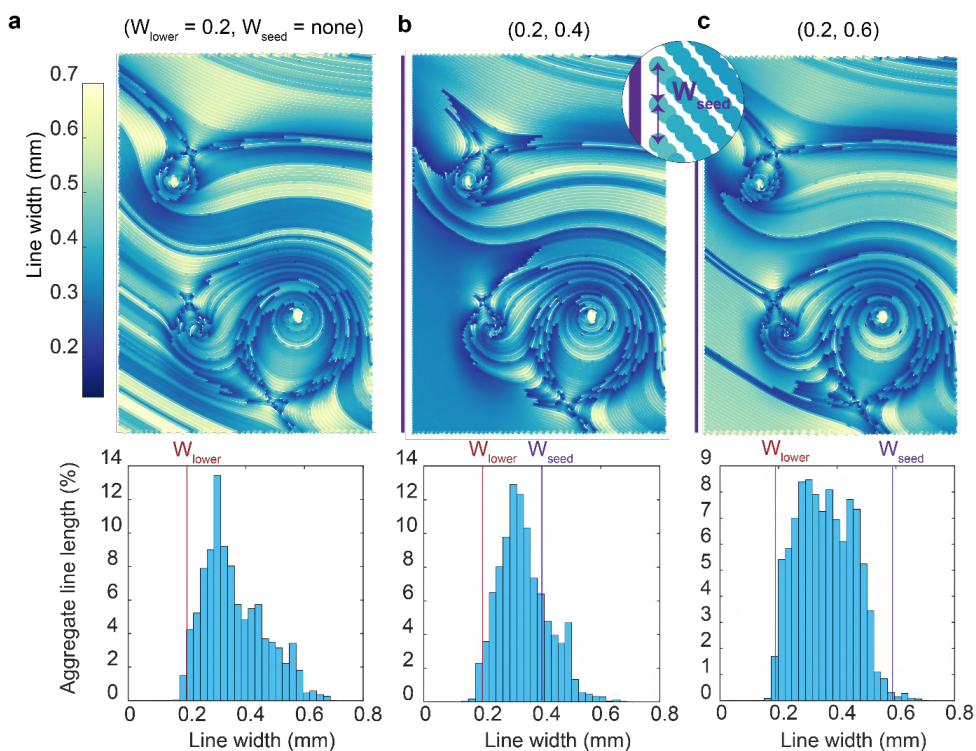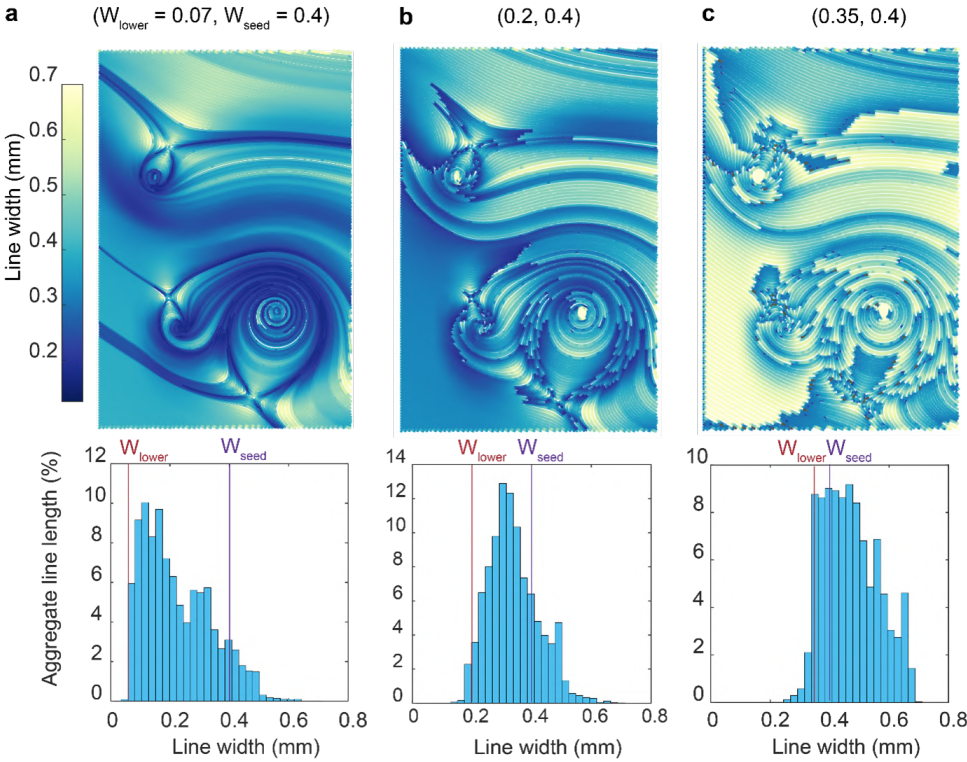Figure SI 3.9 – Distribution of line widths for the wood pattern with different values of (W_{lower}, W_{seed}) with $W_{upper} = 0.7$ mm. While W_{lower} is likely determined by the minimum line width printed with a recommended value of half the nozzle diameter, it may also be used to influence the number of streamlines generated. **A.** A low value for W_{lower} leaves most streamlines uninterrupted, resulting in long, continuous lines with large variations, in contrast to shorter ones, **B.**, **C.** when W_{lower} and W_{seed} are closer.
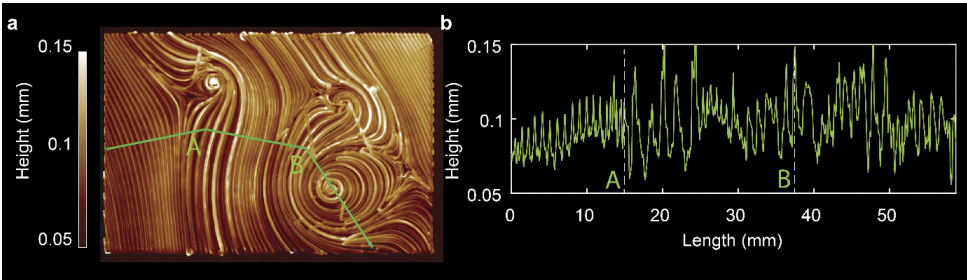
Figure SI 3.10 – **A.** Height map of a sample printed with the wood pattern of Figure 3.4d. **B.** Height profile along green path shown in **A**.
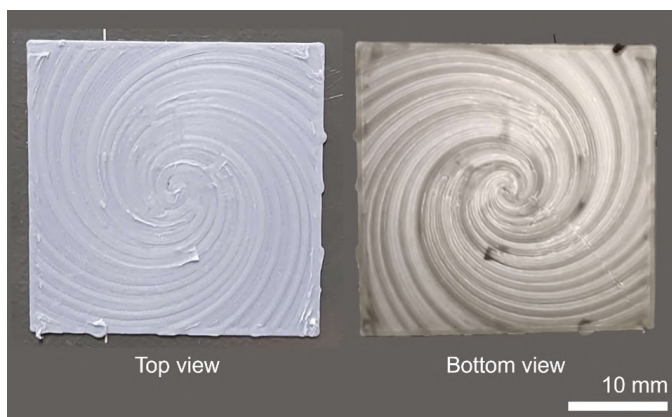
Figure SI 3.11 – White PLA sample printed with vortex pattern, photographed from top on print bed and from bottom with a source of light coming from the opposite side to visualize homogeneity.
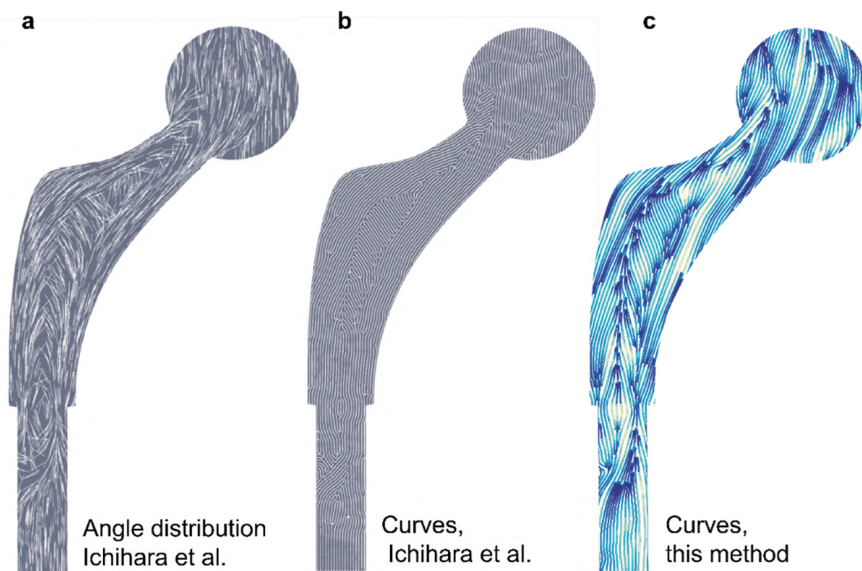
Figure SI 3.12 – **A.** Angle distribution extracted from [24]. **B.** Resulting toolpaths based on phase-field approach of the same work. **C.** Streamlines obtained with our method based on an angle field extracted from **A.**

3
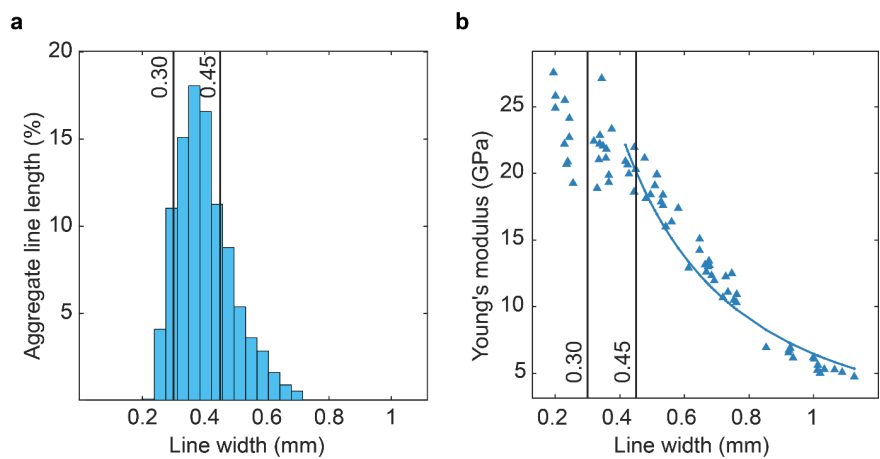
Figure SI 3.13 – **A.** Distribution of line widths for Layer 6 of the plate with $100\,\mathrm{m^{-1}}$ curvature. **B.** Young's modulus for single lines with 0.4 mm nozzle diameter. 70% of the aggregated length of deposited lines have widths between 0.3 mm and 0.45 mm.

3
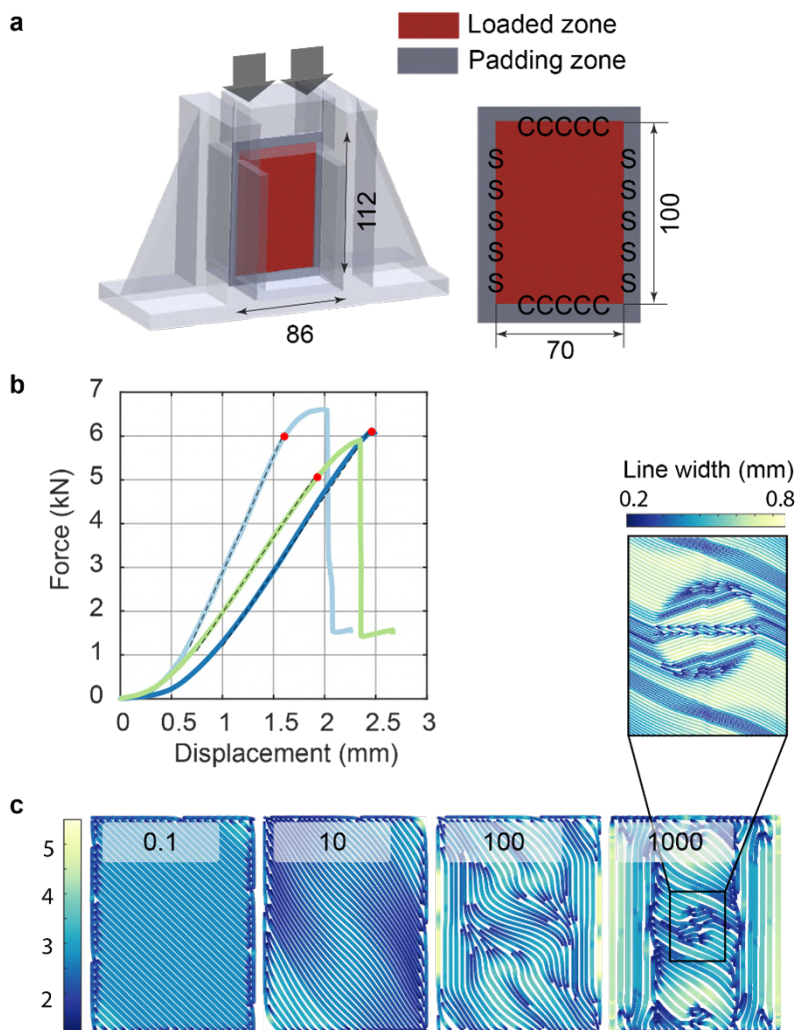
Figure SI 3.14 – **A.** Specimen dimension and load case for the buckling experiment. 24 layers are printed, resulting in a sample thickness of 2.4 mm. C and S indicate clamped and simply-supported zones, respectively. **B.** Force-displacement curve for three samples of $100\,\mathrm{m}^{-1}$ curvature. The first buckling load is obtained at the first point where the load deviates by 100 N from the linear regression determined in the elastic zone from 500 N onwards. **C.** Print paths for a given layer are shown with a coarse line width for visualization purposes. At $1000\,\mathrm{m}^{-1}$, a central transition zone can be observed where the curvature changes abruptly resulting in a lack of continuity between print lines, as opposed to the smoother pattern at $100\,\mathrm{m}^{-1}$.
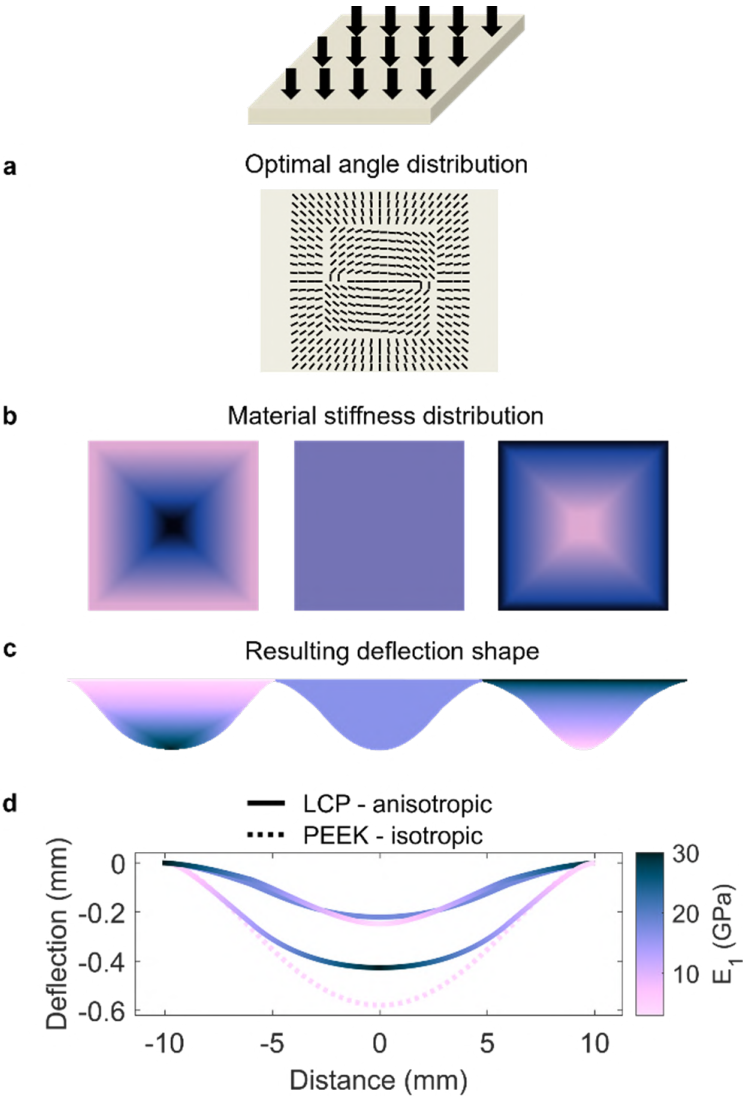
Figure SI 3.15 – **A.** Angle distribution of an orthotropic material which maximizes bending stiffness for a clamped plate subjected to a uniform distributed load, retrieved from [67]. **B.** Three different material gradients are envisioned by varying the line width locally during the 3D-printing of the liquid crystal polymer, from left to right: stiff center and compliant edges, constant stiffness of 18 GPa and compliant center with stiffer edges. **C.** Cross-sections of the deflected shapes obtained for each stiffness case show a different curvature at their extremum. **D** These deflected shapes can be compared to that of an isotropic plate.

We examined a load case scenario of uniform pressure on a clamped flat plate. This configuration has been studied in [67] where the fibre angles that maximize bending stiffness were retrieved for an orthotropic material. Corresponding angles are shown in Figure SI 3.15a. The approach presented in this work allows to vary independently angle orientation and material stiffness between 3 GPa and 30 GPa via varying the line width. Three different configurations of stiffness illustrated in Figure 3.15b are thus modeled: stiff center to compliant edges, no spatial stiffness variation with $E_1 = 18$ GPa and finally, compliant center to stiffer edges.

A comparison is shown in Figure SI 3.15d of the deformation between these configurations following the optimized angle pattern, and a fully isotropic printable material such as PEEK with a Young's modulus of 4 GPa. The three anisotropic configurations resist deflection better than the isotropic material, as expected. The effect of stiffness gradients between the three anisotropic configurations can be observed in Figure SI 3.15c and Figure SI 3.15d. Compared to the constant stiffness case, the "soft center and stiffer edges" configuration displays a pointed tip deflection shape. In contrast, the plate with a stiff center and softer edges shows a blunt, flatter shape at its extremum.

To obtain the results of Figure SI 3.15, a python script is called from ABAQUS which assigns for each element of the 20×20 grid an orthotropic material whose axial direction aligns with the corresponding angle of Figure SI 3.15a. The plate is sectioned by 9 evenly-spaced concentric squares to obtain 10 stiffness zones. The E_1 value of the orthotropic material assigned to each concentric zone is also linearly spaced between 3 GPa and 30 GPa. E_2 is chosen as $E_1/10$ which is a conservative assumption, since we expect the anisotropy ratio E_1/E_2 of the wider lines to be closer to 1. In [10], the transverse Young's modulus E_2 was measured at 2.08 GPa, closer to the value of 3 GPa obtained in this work for the widest lines.

References

1. Färber, J., Lichtenegger, H. C., Reiterer, A., Stanzl-Tschegg, S. & Fratzl, P. Cellulose microfibril angles in a spruce branch and mechanical implications. *Journal of Materials Science* **36,** 5087–5092. ISSN: 00222461 (2001).

2. Sullivan, T. N., Wang, B., Espinosa, H. D. & Meyers, M. A. Extreme lightweight structures: avian feathers and bones. *Materials Today* **20,** 377–391. ISSN: 18734103 (2017).

3. Hu, M., Olsson, A., Hall, S. & Seifert, T. Fibre directions at a branch-stem junction in Norway spruce: a microscale investigation using X-ray computed tomography. *Wood Science and Technology* **56,** 147–169. ISSN: 14325225 (2022).

4. Weinkamer, R. & Fratzl, P. Mechanical adaptation of biological materials - The examples of bone and wood. *Materials Science and Engineering C* **31,** 1164–1173. ISSN: 09284931 (2011).

5. Vincent, J. F., Bogatyreva, O. A., Bogatyrev, N. R., Bowyer, A. & Pahl, A. K. Biomimetics: Its practice and theory. *Journal of the Royal Society Interface* **3,** 471–482. ISSN: 17425662 (2006).

6. Peeters, D. M., Lozano, G. G. & Abdalla, M. M. Effect of steering limit constraints on the performance of variable stiffness laminates. *Computers & Structures* **196,** 94–111. ISSN: 0045-7949 (Feb. 2018).

7. Zucco, G. *et al.* Continuous tow steering around an elliptical cutout in a composite panel. *AIAA Journal* **59,** 5117–5129. ISSN: 1533385X (2021).

8. Chen, J. *et al.* 3D-Printed Anisotropic Polymer Materials for Functional Applications. *Advanced Materials* **34,** 1–33. ISSN: 15214095 (2022).

9. Zhang, H., Chen, J. & Yang, D. Fibre misalignment and breakage in 3D printing of continuous carbon fibre reinforced thermoplastic composites. *Additive Manufacturing* **38,** 101775. ISSN: 22148604 (2021).

10. Gantenbein, S. *et al.* Three-dimensional printing of hierarchical liquid-crystal-polymer structures. *Nature* **561,** 226–230. ISSN: 0028-0836 (Sept. 2018).

11. Gantenbein, S. *et al.* Spin-Printing of Liquid Crystal Polymer into Recyclable and Strong All-Fiber Materials. *Advanced Functional Materials,* 2104574. ISSN: 1616-3028 (Sept. 2021).

12. Hornus, S. *et al.* Variable-width contouring for additive manufacturing. *ACM Transactions on Graphics* **39.** ISSN: 15577368 (2020).

13. Kuipers, T., Doubrovski, E. L., Wu, J. & Wang, C. C. A Framework for Adaptive Width Control of Dense Contour-Parallel Toolpaths in Fused Deposition Modeling. *CAD Computer Aided Design* **128,** 102907. ISSN: 00104485 (2020).

14. Moetazedian, A., Budisuharto, A. S., Silberschmidt, V. V. & Gleadall, A. CONVEX (CONtinuously Varied EXtrusion): A new scale of design for additive manufacturing. *Additive Manufacturing* **37,** 101576. ISSN: 22148604 (2021).

3

15. Yan, J., Demirci, E., Ganesan, A. & Gleadall, A. Extrusion width critically affects fibre orientation in short fibre reinforced material extrusion additive manufacturing. *Additive Manufacturing* **49,** 102496. ISSN: 22148604 (2022).

16. Yan, J., Demirci, E. & Gleadall, A. Controlling anisotropy and brittle-to-ductile transitions by varying extrusion width in short fibre reinforced additive manufacturing. *Rapid Prototyping Journal.* ISSN: 13552546 (2023).

17. Bertevas, E., Férec, J., Khoo, B. C., Ausias, G. & Phan-Thien, N. Smoothed particle hydrodynamics (SPH) modeling of fiber orientation in a 3D printing process. *Physics of Fluids* **30.** ISSN: 10897666 (2018).

18. Šeta, B. *et al. Modelling Fiber Orientation During Additive Manufacturing-Compression Molding Processes* in *International Solid Freeform Fabrication Symposium* (2022).

19. Bedel, A. *et al.* Closed space-filling curves with controlled orientation for 3D printing. *Computer Graphics Forum* **41,** 473–492. ISSN: 14678659 (2022).

20. Boddeti, N., Tang, Y., Maute, K., Rosen, D. W. & Dunn, M. L. Optimal design and manufacture of variable stiffness laminated continuous fiber reinforced composites. *Scientific Reports,* 1–15. ISSN: 2045-2322 (2020).

21. Chen, X., Fang, G., Liao, W.-h. & Wang, C. C. L. Field-Based Toolpath Generation for 3D Printing Continuous Fibre Reinforced Thermoplastic Composites. *Additive Manufacturing* **49,** 102470. ISSN: 2214-8604 (2022).

22. Chermain, X., Zanni, C., Martínez, J., Hugron, P.-A. & Lefebvre, S. Orientable Dense Cyclic Infill for Anisotropic Appearance Fabrication. *ACM Transactions on Graphics* **42** (2023).

23. Tricard, T., Etienne, J., Zanni, C. & Lefebvre, S. A brick in the wall: Staggered orientable infills for additive manufacturing. *Proceedings - SCF 2021: ACM Symposium on Computational Fabrication* **1,** 1–15 (2021).

24. Ichihara, N. & Ueda, M. 3D-print infill generation using the biological phase field of an optimized discrete material orientation vector field. *Composites Part B: Engineering* **232.** ISSN: 13598368 (2022).

25. Ichihara, N. & Ueda, M. 3D-printed high-toughness composite structures by anisotropic topology optimization. *Composites Part B: Engineering* **253,** 110572. ISSN: 13598368 (2023).

26. Murugan, V., Alaimo, G., Auricchio, F. & Marconi, S. An orientation-field based algorithm for free-form material extrusion. *Additive Manufacturing* **59,** 103064. ISSN: 22148604 (2022).

27. Niu, X. J., Yang, T., Du, Y. & Xue, Z. Q. Tensile properties of variable stiffness composite laminates with circular holes based on potential flow functions. *Archive of Applied Mechanics* **86,** 1551–1563. ISSN: 14320681 (2016).

28. Shafighfard, T., Cender, T. A. & Demir, E. Additive manufacturing of compliance optimized variable stiffness composites through short fiber alignment along curvilinear paths. *Additive Manufacturing* **37,** 101728. ISSN: 2214-8604 (Jan. 2021).

29. Malakhov, A. V. *et al.* Three-dimensional printing of biomimetic variable stiffness composites with controlled orientations and volume fraction of fibers. *Composite Structures* **299,** 116091. ISSN: 0263-8223 (2022).

30. Seshadri, B., Hischier, I., Masania, K. & Schlueter, A. 3D Printed Liquid Crystal Polymer Thermosiphon for Heat Transfer under Vacuum. *Advanced Materials Technologies* **2300403,** 1–10. ISSN: 2365709X (2023).

31. Lawrence Chapoy, L., Marcher, B. & Rasmussen, K. H. The morphology of liquid-crystalline polymers and the possible consequences for their rheological behaviour. *Liquid Crystals* **3,** 1611–1636. ISSN: 13665855 (1988).

32. Romo-Uribe, A. & Windle, A. H. A rheo-optical and dynamic X-ray-scattering study of flow-induced textures in main-chain thermotropic liquid-crystalline polymers: the influence of molecular weight. *Proceedings of the Royal Society A: Mathematical, Physical and Engineering Sciences* **455,** 1175–1201. ISSN: 13645021 (1999).

33. Turek, D. E. & Simon, G. P. Processing/property relationships of a thermotropic copolyester: 2. Correlations between tensile properties and orientation. *Polymer* **34,** 2763–2768. ISSN: 00323861 (1993).

34. Reyes-Mayer, A. *et al.* Nanostructure reorganization in a thermotropic copolyester. A simultaneous WAXS and SAXS study. *Polymers for Advanced Technologies* **27,** 748–758. ISSN: 10991581 (2016).

35. Côté, W. A. & Hanna, R. B. Ultrastructural characteristics of wood fracture surfaces. *Wood and Fiber Science* **2,** 135–163 (1983).

36. Maaß, M. C., Saleh, S., Militz, H. & Volkert, C. A. The Structural Origins of Wood Cell Wall Toughness. *Advanced Materials* **32.** ISSN: 15214095 (2020).

37. Gibbings, J. *Dimensional Analysis* 1–297. ISBN: 978-1-84996-317-6 (Springer London, 2011).

38. Peuvrel, E. & Navard, P. Band Textures of Liquid Crystalline Polymers in Elongational Flows. *Macromolecules* **24,** 5683 (1991).

39. Donald, A. M., Viney, C. & Windle, A. H. Banded structures in oriented thermotropic polymers. *Polymer* **24,** 155–159. ISSN: 00323861 (1983).

40. Alderman, N. J. & Mackley, M. R. Optical Textures Observed during the Shearing of Thermotropic Liquid-crystal Polymers. *Faraday Discuss. Chem. Soc* **79,** 149–160 (1985).

41. Ding, J., Feng, J. & Yang, Y. A preliminary morphological evidence for the existence of back-flow effect associated with the formation of band texture after cessation of shear for a polymeric liquid crystal. *Polymer Bulletin* **36,** 773–778 (1996).

42. Vermant, J., Moldenaers, P., Mewis, J. & Picken, S. J. Band formation upon cessation of flow in liquid-crystalline polymers. *Journal of Rheology* **38,** 1571–1589. ISSN: 0148-6055 (1994).

43. Marrucci, G. & Greco, F. in *Advances in chemical physics* 331–404 (1993). ISBN: 0471598453.

44. Grecov, D. & Rey, A. D. Texture control strategies for flow-aligning liquid crystal polymers. *Journal of Non-Newtonian Fluid Mechanics* **139,** 197–208. ISSN: 03770257 (Dec. 2006).

45. Wang, J. & Labes, M. M. Control of the Anisotropic Mechanical Properties of Liquid Crystal Polymer Films by Variations in Their Banded Texture. *Macromolecules* **25,** 5790–5793. ISSN: 15205835 (1992).

46. Plummer, C. J., Zülle, B., Demarmels, A. & Kausch, H. The structure of filled and unfilled thermotropic liquid crystalline polymer injection moldings. *Journal of Applied Polymer Science* **48,** 751–766. ISSN: 10974628 (1993).

47. Larson, N. M. *et al.* Rotational multimaterial printing of filaments with subvoxel control. *Nature* **613,** 682–688. ISSN: 14764687 (2023).

48. Raney, J. R. *et al.* Rotational 3D printing of damage-tolerant composites with programmable mechanics. *Proceedings of the National Academy of Sciences of the United States of America* **115,** 1198–1203. ISSN: 10916490 (2018).

49. Kokkinis, D., Bouville, F. & Studart, A. R. 3D Printing of Materials with Tunable Failure via Bioinspired Mechanical Gradients. *Advanced Materials* **30,** 1–9. ISSN: 15214095 (2018).

50. Giachini, P. A. *et al.* Additive manufacturing of cellulose-based materials with continuous, multidirectional stiffness gradients. *Science Advances* **6,** 1–12. ISSN: 23752548 (2020).

51. Waly, C., Petersmann, S. & Arbeiter, F. Multimaterial Extrusion-Based Additive Manufacturing of Compliant Crack Arrester: Influence of Interlayer Length, Thickness, and Applied Strain Rate. *Advanced Engineering Materials* **25.** ISSN: 15272648 (2023).

52. Chanson, H. *Applied Hydrodynamics - An Introduction to Ideal and Real Fluid Flows* ISBN: 9780429206849 (CRC Press, Taylor & Francis Group, Boca Raton, 2009).

53. Chanson, H. in *Applied hydrodynamics : an introduction* CRC Press, 146 (Taylor & Francis, Boca Raton, 2014). ISBN: 9780203876268.

54. Mebarki, A., Alliez, P. & Devillers, O. Farthest point seeding for efficient placement of streamlines. *Proceedings of the IEEE Visualization Conference,* 61 (2005).

55. Van Gogh, V. *The Starry Night* https://www.moma.org/collection/works/79802 (2023).

56. Iragi, M. *et al.* Design, manufacturing and testing of 3D printed variable-stiffness laminates for improved open-hole tensile behaviour. *Additive Manufacturing* **63.** ISSN: 22148604 (2023).

57. Mattheck, C. *Design in Nature : Learning from Trees* ISBN: 978-3-540-62937-5 (Springer, Berlin, 1998).

58. Finlay, W. H. The midrange wavenumber spectrum of van Gogh's Starry Night does not obey a turbulent inertial range scaling law. *Journal of Turbulence* **21,** 34–38. ISSN: 14685248 (2020).

59. Breunesse, C. & Bluhm, A. Van Gogh Going Global. *Journal of Museum Education* **26,** 10–12. ISSN: 1059-8650 (2001).

60. Patel, B. B. *et al.* Tunable structural color of bottlebrush block copolymers through direct-write 3D printing from solution. *Science Advances* **6,** 1–14. ISSN: 23752548 (2020).

61. Fukuhara, K., Nagano, S., Hara, M. & Seki, T. Free-surface molecular command systems for photoalignment of liquid crystalline materials. *Nature Communications* **5,** 1–8. ISSN: 20411723 (2014).

62. Machado, M. A., Rosado, L. S. & Santos, T. G. Shaping Eddy Currents for Non-Destructive Testing Using Additive Manufactured Magnetic Substrates. *Journal of Nondestructive Evaluation* **41,** 1–11. ISSN: 15734862 (2022).

63. Hanselman, D. *Matlab Central File Exchange: Improved 2-D Streamlines* `https://nl.mathworks.com/matlabcentral/fileexchange/38860-improved-2-d-streamlines?requestedDomain=` (2023).

64. Douglas, D. H. & Peucker, T. K. Algorithms for the reduction of the number of points required to represent a digitized line or its caricature. *The Canadian Cartographer* **10,** 112–122 (1973).

65. Schwanghart, W. *Matlab Central File Exchange: Line Simplification* `https://www.mathworks.com/matlabcentral/fileexchange/21132-line-simplification` (2023).

66. Linke, M., Flügge, F. & Olivares-Ferrer, A. J. Design and validation of a modified compression-after-impact testing device for thin-walled composite plates. *Journal of Composites Science* **4,** 1–16. ISSN: 2504477X (2020).

67. Setoodeh, S., Abdalla, M. M. & Gürdal, Z. Design of variable – stiffness laminates using lamination parameters. *Composites Part B: Engineering* **37,** 301–309 (2006).

3

Chapter 4

Wood-inspired interlocking junctions using 3D-printed LCP

ABSTRACT

Where the trunk of a tree splits into co-dominant branches, wood fibres are highly interlocked. Such an arrangement of fibres has been shown to impart superior strength and toughness to this critical junction. Here, wavy patterns are manufactured with LCPs to evaluate the potential of wood-inspired localized adaptations to improve the robustness of junctions between orthotropic struts. The highly anisotropic, fibrillar microstructure of LCPs can be harnessed by FFF, yielding Young's modulus and tensile strength reaching 30 GPa and 500 MPa respectively. However, unidirectional 3D-prints subjected to normal tensile stresses show weak interfaces, like in wood. To overcome this weakness, sinusoidal, helix and saw-tooth patterns are 3D-printed to create interlocking between layers. A trade-off is established between uniaxial tension and short-beam shear with increasing interlocking angle of the sinusoidal pattern. We find that the work associated with interlaminar crack propagation is increased three-fold compared to a unidirectional pattern, through extrinsic toughening. When applied to a more complex load case in a curved beam in four-point bending, helix-patterning at the junction zone increases the maximum load by 88 %. By locally controlling the level of anisotropy via waviness, this method opens the possibility of improving toughness and transverse properties where the stress state is multi-axial, without adding mass in future recyclable structural materials.

4.1. Introduction

The mechanical anisotropy displayed by biological materials such as wood grants them multi-functionality and adaptability while often making optimal use of scarce resources [1]. Anisotropic materials can also be produced by additive manufacturing, allowing the simultaneous control of topology and orientation. Finding concurrently the optimal topology and directionality for a given load case has also been the purpose of numerical approaches [2–4]. These Topology and Anisotropy Optimisation (TAO) schemes typically output "organic-looking" geometries where struts are smoothly connected at multiple angles to form junctions. Struts tend to be loaded either in compression or tension, similar to conventional truss structures [5]. Junctions, however, are subjected to more complex loads. While for truss configurations, junctions can be treated like pin-joints as the moments transmitted through them are negligible, current topology optimisation schemes do not offer this guarantee. In these designs, as loads are transferred from one strut to its neighbours, the junctions see a combination of tensile, shear and compressive stresses in multiple directions [6]. Optimizing fibre placement accordingly is therefore crucial to the strength of TAO objects, and ultimately to their applicability in demanding scenarios. Several computational works have also introduced the anisotropy level itself as a design variable, along with density and directionality [2, 4, 5, 7]. For instance, in Schmidt *et al.* [2] the algorithm is set to optimize topology and simultaneously choose a material configuration between the bounds $E1 : E2 = 50 : 10$ (orthotropic) and $E1 : E2 = 18 : 18$ (isotropic). The resulting geometry uses orthotropy everywhere except at junctions, where isotropy is deemed more efficient. The work of Kundu *et al.* [5]. has also included the tensile/compressive asymmetry of the failure envelope, highlighting the potential of such a design variable for strength considerations. This illustrates the need for a manufacturing approach where anisotropy levels can be tuned and especially led towards more isotropy at junctions.

To manufacture a part with orthotropic struts and a seamless transition towards isotropic junctions, on-the-fly gradients of material properties are needed. Material properties can be changed with infill type and direction [8], but challenges remain in obtaining continuity between the printed lines and smooth transitions between different anisotropic and isotropic zones. Spinodoids [9, 10] and variable unit cells [11] can be used to obtain smooth anisotropy gradients with a single isotropic printing material. Other manufacturing methods focus on stirring of short-fibre composite via rotational shear [12], or the physical mixing of two materials [13–15].

The scarcity and implementation difficulties of mechanical gradients with synthetic materials are in stark contrast to their prevalence in biological materials [16]. Trees are primary examples of anisotropic structures with complex geometries with multiple junctions [17]. Co-dominant tree forks, in particular, have to sustain two important goals: continued nutrient transport between roots and leaves, and maintain structural integrity [18]. As pointed out by Slater *et al.* [19], the resulting directionality of these junctions shown in Figure 4.1a differs from the simpler 'Engineered' configuration of Figure 4.1b. The main difference takes place at the central apex of the fork (the tip of the 'Y') where axillary wood can be found. This important biomechanical attribute of junctions in trees is a type of reaction wood characterized by its tortuous interlocked grain [20], as shown in Figure 4.1a.

Triggered by thigmo-morphogenesis (mechanical stimulus) [21], it tends to form under the junction bark ridge and is the most developed when the two branches measure approximately the same diameter [18, 20, 22]. The central apex of co-dominant forks has been measured to be five times tougher than side regions, due to both its higher density and the interlocking pattern [23]. Impressively, this reinforced zone was reported to show fracture resistance within the interlaminar plane 1.5 times larger than normal to it. While interlocking is a large contributor to the reinforcement of the apex region, multi-scale toughening mechanisms are numerous on the branch-stem interface of trees. Among others, they include crack-bridging by aggregates of microfibrils, crack tip blunting, and zig-zag crack deflection at cell wall interfaces [24, 25].
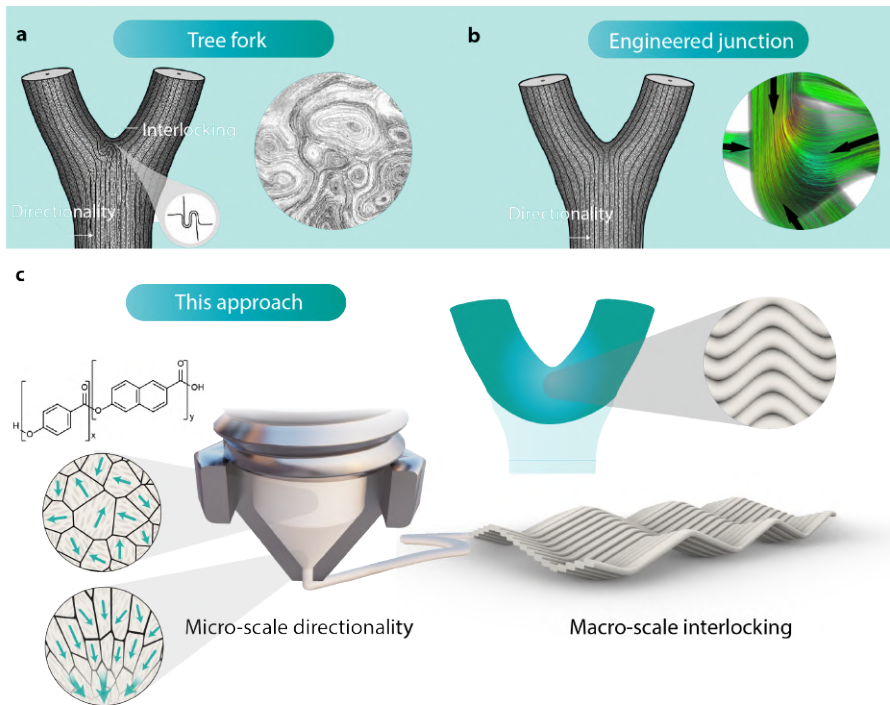
Figure 4.1 – Zones created where multiple mechanical struts are brought together are called junctions. They are found in most topology-optimized geometries, and in natural materials, such as tree branches and forks. For anisotropic materials, the transition from an orthotropic strut with a given orientation to another one can be achieved via multiple routes. **A.** In the "contour-like" engineering route, the simplicity of the toolpath and continuity of the fibres are prioritized, associated with the shortest path between two struts. Reproduced from [19] with permission from Taylor & Francis. **B.** Similar natural structures such as main forks in trees also need to conduct nutrients from root to foliage [20]. At the apex of their junction, denser axillary wood shows a tortuous, interlocking grain. Reproduced from [20] and [2] with permission from Springer. **C.** Approaching isotropy at junctions with an anisotropic material, while keeping continuous toolpaths, is therefore possible for wood by using interlocked patterns. To replicate these biological patterns, LCPs can be readily extruded with Fused Filament Fabrication, allowing the aligned domains to be deposited in the direction of travel. Straight lines can turn into sinusoidal paths with nozzle motion to provide tortuosity at desired locations.

Because of the difficulty and time necessary to shape living wood [17, 26, 27], digital fabrication has been instrumental in integrating desirable wood features into other materials. Sinusoidal-like or tortuous patterns have been also widely studied and reproduced to create interlocking interfaces with 3D-printing [28–31] or composite technologies [32–34], with some studies aiming to reinforce T-joints [35, 36]. 3D-printing wood-like features has also been attempted with helical cylinders to reproduce micro-fibril angles [37, 38]. However, there remains a gap in knowledge in harnessing anisotropy to realise tunable gradients of mechanical properties at junctions.

Here, wavy and helical features, inspired by the characteristic tortuosity of axillary wood, are 3D-printed and studied using liquid crystal polymers. Their main advantage is strong anisotropy with unlimited shaping freedom due to the absence of discrete physical reinforcement such as fibres [39, 40]. Liquid crystallinity is characterized by the presence of local directional order of the molecules in the liquid state at the scale of nematic domains of a few micrometres in size [41]. As the rigid rod-like polymer chains pass through the contracting die of the nozzle, elongational and shear flow align the nematic domain in the same direction [42]. As the 3D-printer nozzle translates, it deposits the molten material which aligns with the extrusion direction, as illustrated in Figure 4.1c. When exposed to ambient temperatures, the material cools down before the relaxation of the directors can take place, resulting in the preservation of this alignment in the solid state [40]. Three routes to tune the anisotropy of this material have been explored: via annealing and changing printing temperature [40], embedding spun fibres as reinforcement to the 3D-printed part [43], or changing the line width [39]. With the last approach, mechanical gradients can be achieved within the same toolpath between 3 GPa and 30 GPa of Young's modulus. Furthermore, the absence of manufacturing constraints like curvature opens the possibility of creating anisotropic patterns seldom seen in engineering materials, such as spirals.

Due to the fibrillar nature of this material, its interlaminar adhesion highly depends on processing conditions and is a point of caution [44, 45]. We hypothesize that the interlocking created by waviness will promote a shear behaviour that dissipates energy through the delamination of fibrils. To explore the potential of such patterns, their properties in tension, short-beam shear, as well as toughness are measured for different planes, with varying wavelengths and amplitudes. Their ability to strengthen parts subjected to a multi-axial stress state is assessed with a curved-beam bending set-up, revealing an 88 %-increase in load bearing capacity with this strategy. By tuning anisotropy and creating interlocking while keeping the toolpath continuous, this research opens new avenues for the manufacturing of TAO parts with complex, robust junctions adapted to complex load cases.

4.2. Results and discussion

4.2.1. Waviness parallel to build plane

To study whether waviness can be used to vary tensile properties and shear properties of 3D-printed LCP, samples with variation along the XY direction, i.e. perpendicular to the build deposition direction are manufactured as shown in Figure 4.2. The parameters studied for these planar infills are shown in Figure 4.2a and b. The infill line is described by the curve $f(x) = A \sin(2\pi x/\lambda)$, where A is the amplitude and λ is the wavelength. The maximum angular deviation to the longitudinal direction is

$$\varphi = \arctan\left(\frac{2\pi A}{\lambda}\right)$$

This angle spans from $\varphi = 17°$ with sample ($A = 0.2$, $\lambda = 4\,\text{mm}$) to $\varphi = 62°$ with sample ($A = 0.6$, $\lambda = 2\,\text{mm}$). For a comparison of surface quality between the six types chosen with varying wavelength and amplitude, the resulting top surface of 3D-printed samples is coloured according to the deviation to its average height within $\pm 100\,\mu\text{m}$ in Figure 4.2c. Their Young's modulus and Ultimate Tensile Strength (UTS) are plotted against amplitude in Figure 4.2d and Figure 4.2e, respectively. The general trend is as expected: the larger the amplitude and the smaller the wavelength, the poorer the performance in tension. Further, the highest stiffness and strength are found in the specimen with the smallest maximum deviation to the 0° angle. For Short-Beam Strength (SBS) in Figure 4.2f, while on average the same trend can be observed, the larger scatter does not allow to draw firm conclusions. This can also be reasoned by the lack of interlocking within the shear plane, located between layers with this type of waviness pattern.

The impact of waviness on tensile properties is further visualized in Figure 4.2g where the average Young's modulus is plotted against φ, and compared to that of LCP printed in the same condition in Gantenbein *et al.* [40], with unidirectional samples of infill angle ranging from 0° to 90°. Classical Laminate Theory describes well both the unidirectional samples, and those printed with waviness when assimilating φ to a ply direction angle. The similarity between both data sets indicates that large deviations to the 0° direction in the wavy patterns make these samples as stiff as if they were unidirectional and oriented at an angle φ. Figure 4.2g also illustrates a scale effect. The samples with $A = 0.2$, $\lambda = 2\,\text{mm}$ and $A = 0.4$, $\lambda = 4\,\text{mm}$ both share the value $\varphi = 32.14°$ yet behave differently. The type with the smallest pattern size outperforms the larger by 33.7 %, 16.7 % and 37.6 % in SBS, Young's modulus and UTS respectively. This may be explained by more numerous interlocking zones for the smallest wavelength which provide a more homogenised stress field. This indicates that both the maximum deviation to the 0° angle and the size of a pattern seem to play a role in the stiffness and strength of parts along the longitudinal direction.

Fracture behaviour can give more insight into the performance of wavy patterns in tension with DIC. In Figure 4.2h, 3D strain fields have been overlaid on photographs of tensile samples before failure. The distribution of the amplitude of the first principal strain (ϵ_1) shows that in all cases, the most strained zones are those where the maximum deviation to the 0° angle (largest slope) is located. This confirms the importance of φ, as already
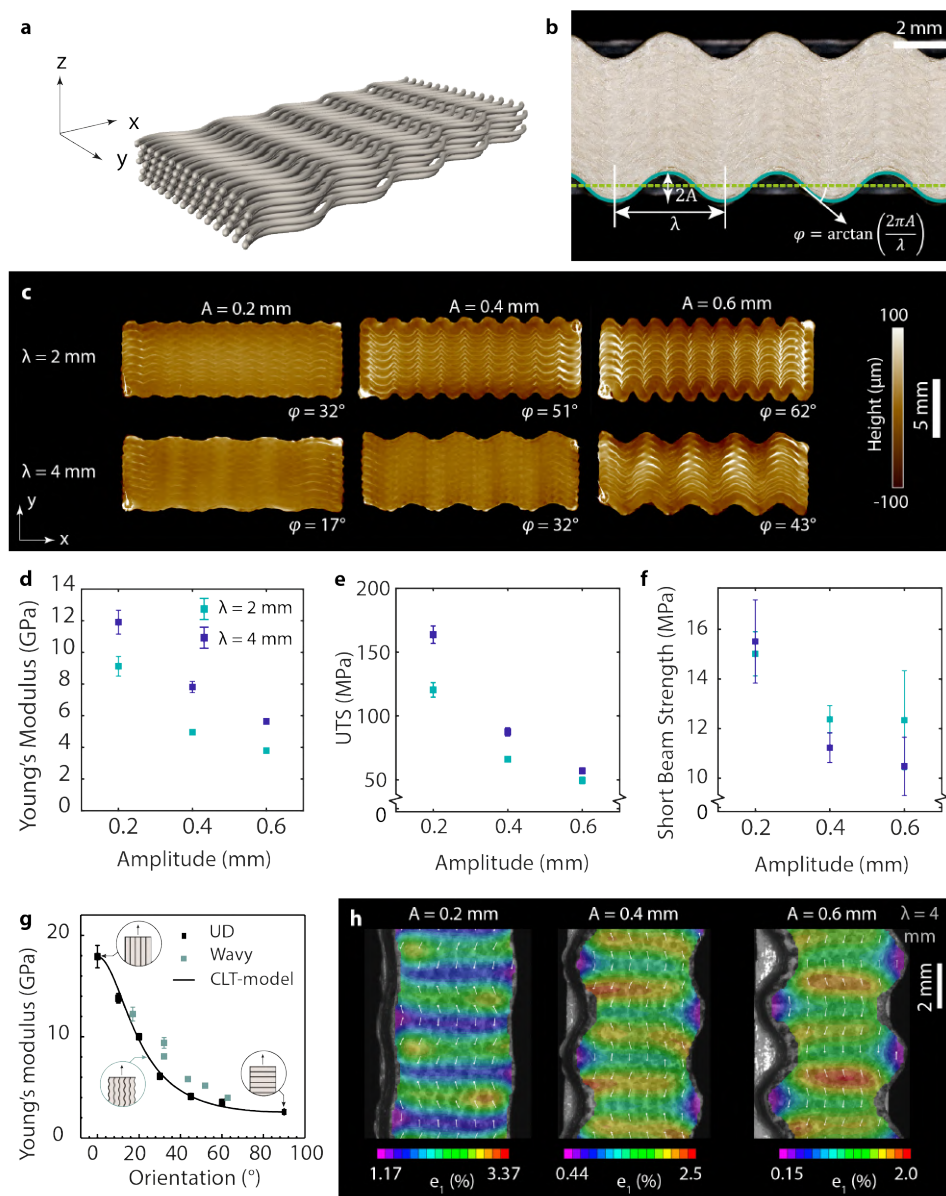
Figure 4.2 – **Liquid crystal polymers 3D-printed with different waviness parameters. A.** The sinusoidal path lies within the build-plane, normal to the Z-direction. **B.** Increasing amplitude A or decreasing wavelength λ results in an increase of φ, the angle between the longitudinal axis X and the steepest slope of the sine. **C.** Height map of the top surface of short-beam shear samples. **D.** Young's modulus (E) and **E.** Ultimate Tensile Strength (UTS) decrease with increasing amplitude and decreasing wavelength. **F.** Increasing amplitude also reduces Short-Beam Strength (SBS). **G.** Young's modulus of the wavy samples is plotted against their maximum angle deviation φ, following the trend obtained from unidirectional parts with different printing angles in Gantenbein *et al.* [40]. The stiffness of the wavy samples corresponds to their unidirectional counterparts oriented at an angle φ. **H.** Digital Image Correlation of typical tensile samples before failure reveals that the strain distribution is highly heterogeneous, with deformations at their maximum at φ. Colours and arrow orientation represent respectively the amplitude and direction of the principal strain ϵ_1.

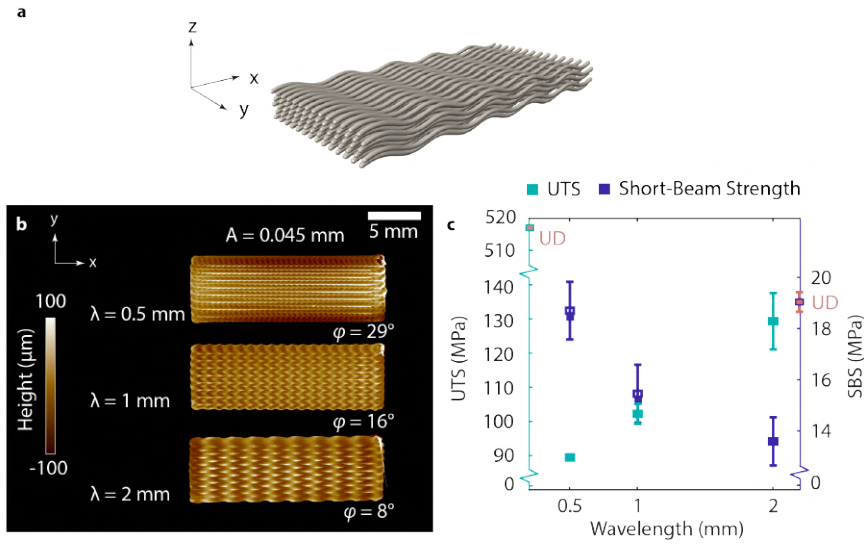Figure 4.3 – **A.** Sinusoidal toolpath located within the XZ plane. **B.** Height map of short-beam shear samples with varying wavelengths showing the waviness pattern. **C.** Samples with different wavelengths show a clear trade-off can be made between ultimate tensile strength and short-beam shear strength.

suggested in Figure 4.2g. Furthermore, another effect explaining the drop in tensile performance with larger amplitudes is revealed with DIC. When the amplitude is large, the effective section width w appears to be $(w - 2A)$, as a width of A is barely strained on either side of the specimen. For instance, for $A = 0.6$ mm, $\epsilon_1 = 0.15\%$ whereas $\epsilon_1 = 2\%$ in the central areas. This corresponds to an effective width reduction of 24 %.

Overall, these elements indicate that increasing angular deviation is detrimental for both tensile and shear properties, with a larger impact on stiffness. The samples behave as compliant as their most compliant link when their waviness is within the loading plane.

4.2.2. Waviness perpendicular to the build plane

In contrast to the samples shown in Figure 4.2, interfaces in wood display features that are oriented perpendicular to the loading plane to create interlocking. As a result, samples with sinusoidal variations along the XZ direction, shown in Figure 4.3a, were also printed. Figure 4.3b presents the parameter values chosen, and height distribution for these samples. The sample surface is also coloured according to the deviation to its average height ± 100 µm to visualize the pattern size. In Figure 4.3c, the experimental test results are shown for ultimate tensile strength, and short-beam shear strength. In contrast to Figure 4.2f, increasing the maximum angle deviation φ, which is achieved here by reducing the wavelength, seems to improve short-beam shear strength for samples with waviness perpendicular to the loading direction. This may also be influenced by the finer scale of the pattern, associated with a larger density of interlocking zones.

Unlike in-plane waviness, out-of-plane waviness triggers a clear trade-off situation between tensile properties and short-beam shear strength. The tensile properties increase with the wavelength, similarly to Figure 4.2d and e, while short beam shear strength decreases. In particular, at $\lambda = 0.5$ mm, short beam shear strength properties are the highest of all sample types and configurations tested with values close to 20 MPa. In terms of pure tension, however, the performance of this pattern drops to 89 MPa, which is close to the literature value of isotropic polymers like PEEK [46, 47]. In comparison, the values attained in ultimate tensile strength of unidirectional samples are (426.8 ± 35.0) MPa for a $0°$ infill and (44.10 ± 2.47) MPa for $90°$ [40] samples. Likewise, the lowest Young's modulus is 5.5 GPa. The Young's modulus is expected to stay within the bounds given by classical laminate theory, i.e. between (2.59 ± 0.23) GPa and (17.91 ± 1.11) GPa. As the lowest bound for stiffness and strength at $90°$ are around the $0°$ values obtained for many engineering polymers without reinforcement [48, 49], focus is placed on shear and toughness properties to locally strengthen junctions.

Because the difference in properties between unidirectional and wavy lines is triggered by the motion of the 3D-printer, the waviness illustrated in Figure 4.3 shows a potential for a continuous transition to be made within one single-printed toolpath between straight, strong orthotropic struts and more compliant but shear-resistant interlocking junctions. In the context of applications in complex three-dimensional loading cases such as those of junctions, this directionality effect may be homogenized by using interlocking patterns on two planes simultaneously.

4.2.3. Waviness in two planes

To create three-dimensional interlocking patterns with waviness, a helix toolpath is investigated in Figure 4.4. This helix pattern follows the curve $A_y \sin(2\pi x/\lambda)$ within the XY plane and $A_z \cos(2\pi x/\lambda)$ within the XZ plane, where A_y and A_z are the amplitudes, as shown in Figure 4.4a. In this case A_z is restricted to 0.045 mm, while two values of A_y and λ are taken. Figure 4.4b shows the parameters chosen and height maps of the four resulting patterns. In Figure 4.4c, the short beam shear strength of these helicoidal samples is plotted against their amplitude in y. To study the effect of superimposing two patterns, the specimen with $(A_y = 0.2, \lambda = 2)$ mm is compared both to its XY and XZ equivalent (i.e. same wavelength and amplitude) shown in Figures 2 and 3. The helix pattern has a 9.7 % lower short-beam strength than its XZ counterpart. A similar decrease in short-beam strength of 7.9 % can also be observed with $(A_y = 0.2, \lambda = 1)$ mm compared to its XZ equivalent, indicating a negative effect of the superimposing of two patterns. In contrast, the short-beam strength of the helix pattern with $(A_y = 0.2, \lambda = 2)$ mm is 9.3 % larger than its XY counterpart. This increase is linked to the interlocking of the layers allowed by the waviness in the Z-direction, perpendicular to the shear plane. It is associated with a 10 % decrease in strength in line with the trade-off between short-beam strength and tensile properties determined in Figure 4.3. It should however be noted that in all these cases, the difference lies within the standard deviation.

In general, Figure 4.4 shows a similar trend to Figure 4.2, with smaller amplitudes and wavelengths beneficial to short-beam strength. Similarly to the XY samples, between the two samples sharing the same value of φ, the smaller pattern size performs best in terms
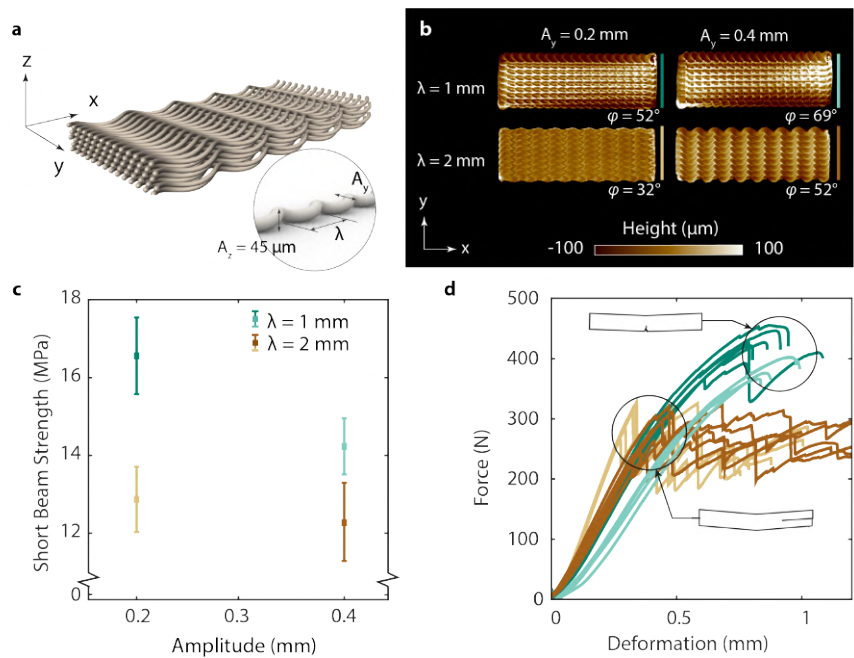
Figure 4.4 – Helicoidal toolpath, with waviness in the XZ and XY plane. A. Different amplitudes are used for the sinusoidal shapes in both planes, with $A_y > A_z$. **B.** Height maps of samples with corresponding parameters (A_y, λ). **C.** The average SBS value is shown against A_y, indicating that smaller pattern sizes are still beneficial for SBS with helical patterns. Error bars correspond to standard deviations. **D.** Force-displacement curves show two kinds of fracture mode: for the lower performing samples with $\lambda = 2\,\text{mm}$, fracture takes place in interlaminar shear, while for the highest ones, tensile fracture takes place, indicating a superior interlocking effect.

Figure 4.5 – **Bi-sinusoidal pattern applied to Compact Tension specimens. A.** Three surfaces are tested, for which $\lambda = 5$ mm and φ makes an angle of 10°, 15° and 20° to the X-axis. **B.** The Compact Tension specimen geometry is printed standing, with a gradual amplitude increase to reach a fully developed pattern throughout the height of the notched region.

of short-beam shear strength. This supports our hypothesis that a smaller pattern size promotes interlocking and increases resistance to interlaminar shear.
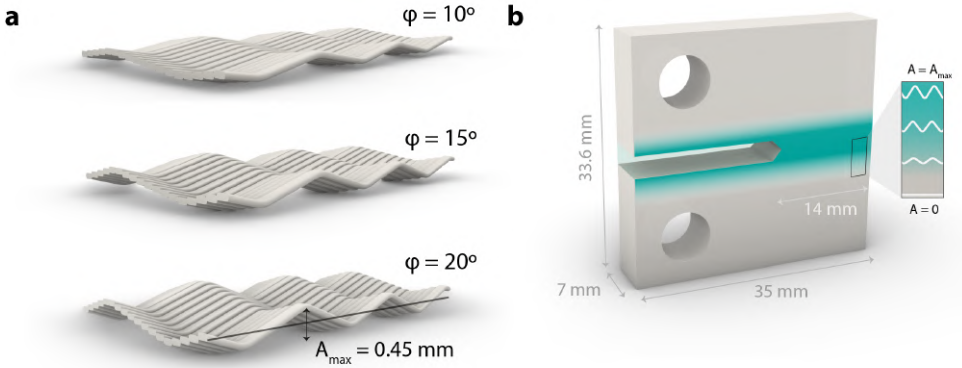
Figure 4.4d, showing force-displacement curves and failure type for all samples, gives further credit to this argument. Within each type, the failure mode is homogeneous and is either interlaminar shear, with successive delamination, or tensile failure on the bottom of the specimen. Both types with $\lambda = 2$ mm, which perform the lowest in short-beam strength, show interlaminar shear fracture. In contrast, the types with $\lambda = 1$ mm fail in tension. This means that the maximum interlayer shear strength has increased to a value above the maximum tensile strength for the smaller pattern size.

A helicoidal pattern has the advantage of creating both intra- and inter-laminar interlocking in shear. However, Mode I loading can be critical for laminar materials such as 3D-printed LCP. In such loading cases, the role of interlocking is less straightforward than in shear. As a result, its impact on Mode-I crack resistance needs to be investigated.

4.2.4. Interlaminar fracture resistance of bi-sinusoidal shapes

The toughness in wood relies on multiple-crack arrest mechanisms, according to a Failsafe strategy that maximises the possibility of healing when damage occurs [25]. The crack front is known to grow along regions of transversally loaded tracheids interwoven with wood rays [25]. On top of the self-healing via resin ducts for hydrophobic and antimicrobial protection, its main features are zig-zag crack deflection which contributes to mechanical closing when the bending moment is decreased, and fibre-bridging by the tracheids [50].

Three configurations of periodic shapes are studied, with $\lambda = 5$ mm and angles φ of 10°, 15° and 20° to the X-axis as shown in Figure 4.5a. The bi-sinusoidal shape is simplified

a

Without fibre bridging

$\varphi = 0°$
$W_{prop} = 19.5$ mJ

$\varphi = 10°$
35.3 mJ

Fibre bridging occurence
- $\varphi = 0°$ 2/5
- $\varphi = 10°$ 0/5
- $\varphi = 15°$ 3/5
- $\varphi = 20°$ 5/5

With fibre bridging

$\varphi = 0°$
$W_{prop} = 89.2$ mJ

$\varphi = 15°$
49.3 mJ

$\varphi = 20°$
175.6 mJ

b   Exp   Area   MM   CR

c

d   -0.25   Height (mm)   0.25   -1   Height (mm)   1   Crack direction
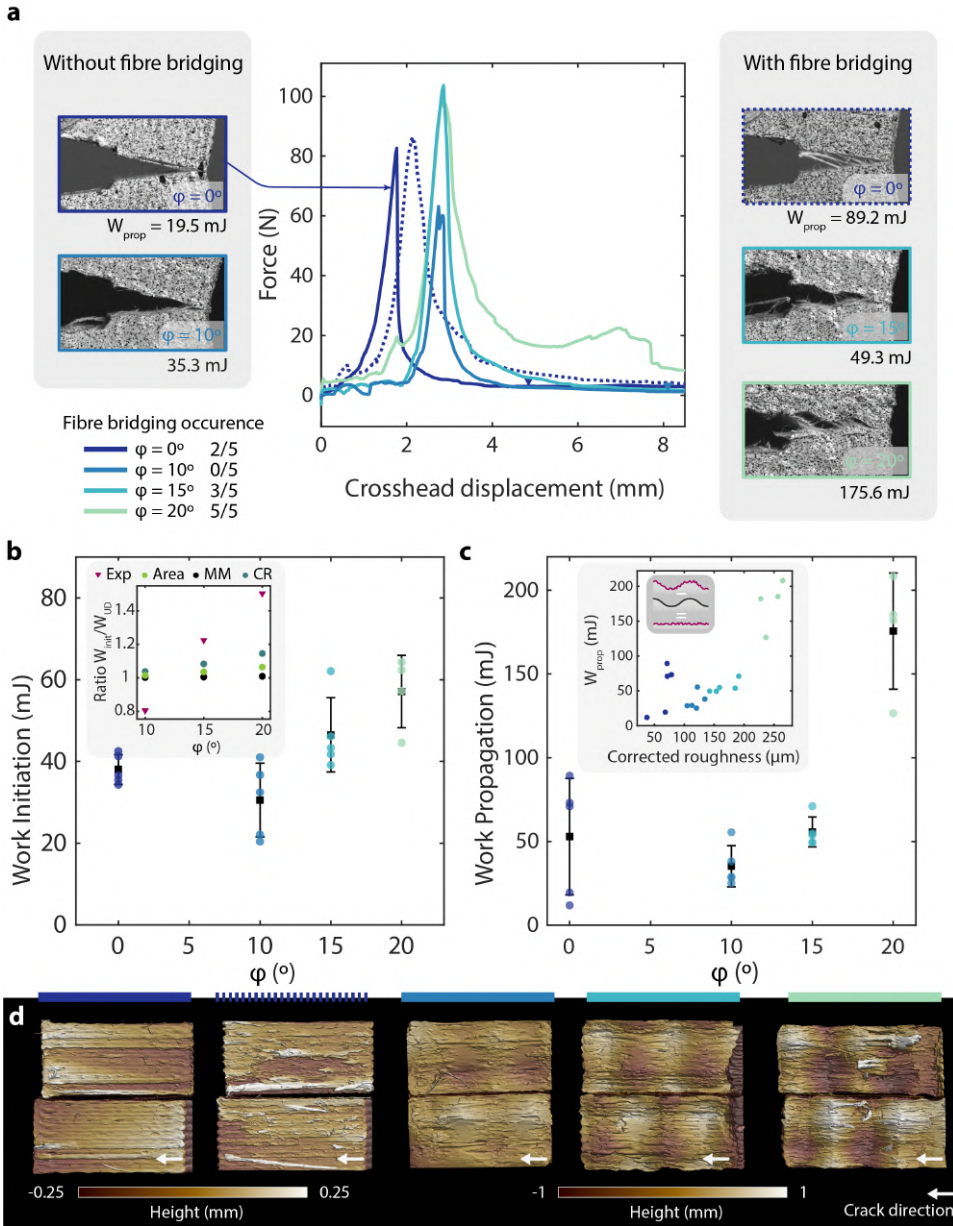
Figure 4.6 – **Bi-sinusoidal patterns tested in Mode I loading show larger crack resistance with increasing angle. A.** Load-displacement curves and imaging during crack-propagation of representative specimen for each configuration illustrate the area under the curve increasing with φ, and in parallel the increasing occurrence of observation of fibres bridging the crack during failure. **B.** Work exerted before max load for crack initiation indicates an initial dip in performance with $\varphi = 10°$, followed by an increase of up to 50 % for $\varphi = 20°$ as shown in the insert. The experimental (legend entry: *exp*) ratio W_{init}/W_{flat} is larger than what is expected from the theoretical increase in area (*Area*), or crack resistance from Mixed-Mode (MM^2), and Cotterell-Rice (CR^2) equations for linear elastic solids. **C.** Work after max load, corresponding to the crack propagation phase, also increases with φ. Insert shows the same data plotted against fracture surface roughness. The surface roughness is corrected to account only for local texture without the height variations linked to geometry itself. This surface roughness is obtained from **D.** height maps of the entire fracture surface, here shown for the samples pictured in **A**, also illustrating the increase in surface roughness with φ.

to a sawtooth pattern to minimize the number of points describing the shape and thus enable faster head movements, especially for the Z-axis. Compact Tension specimens are printed standing as depicted in Figure 4.5b, including supports at the notch region. The zone highlighted in turquoise displays a gradual increase in the amplitude of the periodic path printed, to ensure that throughout the height of the notched region, the maximum amplitude is attained. On the rest of the specimen, flat unidirectional layers are printed to ensure comparable properties everywhere except at the notch region.

Figure 4.6a shows typical load-displacement curves for the four specimen types, tested in Mode I. The area under the curve before and after max peak load is used to obtain a comparative work of fracture for initiation and propagation of the crack. The fracture behaviour differs significantly between samples of different patterns, related to the occurrence of a fibre-bridging phenomenon. fibre-bridging seems to be more frequent as φ increases: from no occurrence at all for the five specimens tested at $\varphi = 10°$, to all five specimens showing a larger quantity of fibres pulled out at $\varphi = 20°$, as seen in the inserts. Within the group of unidirectional samples ($\varphi = 0°$), fibre-bridging is also observed in two out of the five specimens. On the load-displacement curve, this translates into a larger area under the curve after peak load. For the exemplary samples shown in the inserts, it is measured at 89 mJ with fibre-bridging (shown by blue dashed lines), compared to 19 mJ without (blue full lines). Fibre-bridging at the scale of printed lines detaching seems to be related to an increase in area under the curve after peak load, which can be expected as this is a typical extrinsic toughening mechanism, in wood [50] and other fibrous materials [51]. However, another qualitative effect other than fibre-bridging that influences the area under the curve after peak load should also be noted. A secondary bump well after maximum peak load can be noticed at the load-displacement curve of the $\varphi = 20°$ example. This bump is present for four out of the five $\varphi = 20°$ samples. It is absent in some samples where fibre-bridging was also observed. The presence of these qualitative effects translate directly into toughness performance.

In Figure 4.6b, work exerted for the initiation of the crack is shown for the straight and three wavy configurations. In theory, increasing φ is indeed expected to improve performance in toughness via several geometrical contributions. Three of these are considered here. First, Cotterell and Rice [52] have for instance developed a ratio of stress-intensity factors at the tip of a slightly curved crack. This ratio has been shown by Zavattieri *et al.* [53] to characterize well a sine crack between linear elastic solids with $A/\lambda < 0.25$. Our maximum A/λ is well below this value, with 0.091. The equation describing the ratio of the stress-intensity factor of a curved crack over the flat equivalent is:

$$CR = \frac{K_{IC}}{K_0} = \frac{2}{1 + \left[1 + 4\pi^2 \left(\frac{A}{2} \right)^2 \right]^{-\frac{1}{2}}}$$

This value is plotted for the different patterns in the insert of Figure 4.6b under the legend entry CR.

Again in the Linear Elastic Fracture Mechanics (LEFM) framework, Hutchinson and Suo [54] have calculated a similar ratio focusing on mixed mode cracking,

$$MM = \frac{R}{R1} = \left(1 + (\eta - 1)\sin^2 \Psi\right)^{-1},$$

where $\eta = 0.7$ for a rather ductile material and $\Psi = \arctan\left(\frac{K_{IIeff}}{K_{Ieff}}\right)$. The ratio $\frac{K_{IIeff}}{K_{Ieff}}$ is a function of φ only. Since the maximum calculated Ψ in our case is 10°, this ratio stays very close to 1, as shown with the legend entry MM in the same graph.

Finally, the increase in surface area of a sinusoidal pattern over a planar version can also be considered, with a corresponding ratio $Area = 1/\cos\varphi$. For $\varphi = 10°$, $\varphi = 15°$ and $\varphi = 20°$, this area increase is 2.0 %, 5.0 % and 9.2 % respectively, compared to the flat zone.

These theoretical ratios are all compared in the insert of Figure 4.6b to the experimental ratio measured between work to initiate the crack in the patterned and unidirectional surfaces. Both CR and MM are ratios of fracture toughness K_{ic}. In LEFM under plane strain, the relationship between G, the energy release rate, and K_{ic} is quadratic. In order to be comparable to the experimental ratio of work, these ratios are squared on the graph. While they are derived for LEFM which does not apply here, they can shed light on the theoretical contribution of the geometry, versus that of LCP's characteristics such as its fibrillar microstructure.

The general trend of experiments does show an increase in W_{init} with φ. However, the average value at $\varphi = 10°$ is smaller than the average for unidirectional samples. The value should not be below 1 in theory, and is here close to 0.8, indicating poor adhesion between layers. The total absence of fibre-bridging noticed at $\varphi = 10°$ is another symptom of lower adhesion. This may be explained by manufacturing differences, such as the influence of speed: it is indeed much slower to print one layer with waviness, which may decrease interlayer adhesion as the time elapsed between the deposition of two neighbouring lines, and consequently layers, is larger. Due to the large movements in the Z-direction, which is a slower, threaded axis on our 3D printer, the printing duration is 34 s for one flat layer, and 64.5 s, 68.9 s and 75.6 s respectively for one layer at $\varphi = 10°$, $\varphi = 15°$ and $\varphi = 20°$. It is possible that the smaller interlocking seen at $\varphi = 10°$ does not counterbalance the change in manufacturing conditions such as lower speeds. A systematic study on the influence of speed on the adhesion of LCP should therefore be carried out in future work.

Furthermore, the increase in W_{init} with $\varphi = 15°$ and $\varphi = 20°$ over unidirectional samples is noticeable. If the three theoretical contributions are combined (CR: increase due to crack tip deviation, MM mixed mode loading, and $Area$ as crack surface increases), a 42 % increase is expected for $\varphi = 20°$, while the experimental improvement is closer to 50 %. For $\varphi = 15°$, the theoretical ratio of 1.227 matches with the experimental value of 1.222.

A similar trend as that seen for W_{init} is noticed for W_{prop}, the work measured after maximum load, which is related to the propagation of the crack. It is in fact even more marked, as shown in Figure 4.6c. The increase with φ is in this case up to three-fold larger than that of the average unidirectional specimen for $\varphi = 20°$. Another more pronounced trend

is the lower performance of W_{prop} for $\varphi = 10°$ compared to the unidirectional samples, with $\frac{W_{prop,\varphi=10°}}{W_{prop,flat}} = 0.66$ compared to the previous ratio $\frac{W_{init,\varphi=10°}}{W_{init,flat}} = 0.80$. Again, this could be attributed to lower adhesion combined with a lack of interlocking for this sample geometry. As an indication of the importance of fibre-bridging, a distinction of the performance of specimens with and without its occurrence can be made using unidirectional specimens. Three specimens which display fibre-bridging have an average W_{prop} of 78 mJ. The other two which do not show bridging and have an average W_{prop} of 16 mJ. The average increase with $\varphi = 10°$ is 76 % compared to the lower baseline value for flat samples without fibre-bridging. However, the occurrence of fibre-bridging in flat samples may be stochastic as it is not triggered by printing parameters. Therefore, for all other purposes, comparisons should use the total range of samples, with and without bridging.

To further investigate the toughening role of the different patterns, fracture surface roughness is measured on fractured surfaces. It is plotted as an insert in Figure 4.6c against W_{prop}. One may first observe that roughness seems consistent within each specimen type and an average increase with φ is noticed. Moreover, specimens with the largest surface roughness seem to also display the largest W_{prop}. Surface roughness quantifies distributed damage such as the pull-out of short fibrils, and even cohesive fracture zones within a layer, whose areas are seen to increase with φ in Figure 4.6d. However, local damage due to individual, macroscopic fibre-bridging is less readily captured with surface roughness. Again, this can be observed with the two distinct unidirectional sample behaviours, with and without fibre-bridging. The two leftmost height maps of Figure 4.6d show an exemplary unidirectional sample displaying fibre-bridging and another one without. The Surface roughness (Sa) of the sample displaying fibre-bridging is 71.4, compared to 68.4 for the specimen for which the crack has propagated between two layers, but without any pulled-out fibre observed. Sa quantifies the average difference in height of each point compared to the arithmetical mean of the idealized smooth surface. A single fibre bridging the crack and pulling out until total fracture may contribute significantly to enhance W_{prop} but will not be captured with Sa, illustrating the limits of fracture surface roughness as a metric to quantify this phenomenon.

On the fracture surfaces, one may also note that the smoother areas tend to be those located at the crests and troughs of the bi-sinusoidal shape. These smooth regions represent a large proportion of the total area for $\varphi = 10°$. They decrease in size for $\varphi = 15°$ and are non-existent for $\varphi = 20°$. Instead of smooth surfaces, one can distinguish between individual torn printed paths. In Figure SI 4.1, the fracture surface areas of three samples are observed with scanning electron microscopy (SEM). The two flat samples, with and without macro-scale fibre-bridging, display relatively little plasticity at micro-scale, in contrast to the sample with $\varphi = 20°$, showing a rougher fracture surface with many pulled out fibres and fibrils. This may indicate that the relatively higher shear forces favoured by a steeper φ are very effective at provoking plastic deformation such as local fibril pull-out, and larger fibre-bridging. Being loaded in tension, they can simultaneously shield the crack and also dissipate energy in LCP better than what may theoretically expected from geometrical arguments and LEFM.

In summary, these elements suggest that the combination of bridging and deviation are the main mechanisms responsible for the increasing fracture energy with increasing φ. At most, increasing crack area of 9.2 % with the largest φ may play a role, but cannot explain the average increase in work after fracture from 53 mJ to 176 mJ, i.e. more than three-fold increase from the straight specimen. This improvement may be attributed to the more tortuous crack geometry and the plasticity induced by the increased mode-mixity effect in LCP. We hypothesize that the shear stresses introduced at the steepest locations of the bi-sinusoidal shapes become large enough at $\varphi = 15°$ and $\varphi = 20°$ to provoke a widespread pull-out of the fibrils involved at the interface, thereby promoting a more tortuous crack growth and increased energy dissipation, in a similar fashion to wood fracture.

In future designs, the study of crack propagation should include high-resolution imaging to quantify the influence of micro- and macroscopic fibre-bridging. It should also relate to recent modelling efforts, especially using cohesive fracture models similar to those developed for wood [50]. Moreover, because of the similarities with wood, in particular the highly fibrillar structure of this anisotropic material, it could also be used to replicate and study such bio-materials, which are often influenced during their growth by external factors.

4.2.5. Junctions with helix patterns

Interlaminar toughness is an important component of the robustness of materials, however, the loading configuration of a junction is often more complex. To represent a junction, the geometry shown in Figure 4.7a is chosen for its ability to produce a tensile stress normal to the fibre direction in a confined zone. The geometry replicates a two-strut junction, or a three-strut junction without external loading on the last strut, subjected to a worse-case loading scenario. The stress state of such a shape in four-point bending consists of the following components: circumferential tensile stresses along the inner surface, circumferential compressive stresses along the outer surface, radial tensile stresses, from 0 at the inner and outermost surfaces with a peak in the middle third of the thickness [55, 56]. The potential reinforcing effect of waviness is assessed with a helix toolpath shown in Figure SI 4.2 and compared to a unidirectional pattern, in which print paths follow the contour of the curved beam. The helix pattern is only applied to the curved zone, while the struts are printed unidirectional for both types to provide a consistent strut arm stiffness between the two sample types. The parameters of the helix are chosen to summarize previous learnings. A small pattern size with a wavelength of 1 mm is chosen. The maximum deviation angle φ drives the trade-off between toughness and tensile properties. In this case, a value of $\varphi_{max} = 27°$ is chosen to maximize toughness and interlocking. The corresponding sinusoidal amplitude in the Z-axis is 0.08 mm, for a printed layer of 0.1 mm. Height maps of the printed unidirectional and helix junctions are shown in Figure SI 4.2.

The load displacement curve of the specimen subjected to four-point bending are shown in Figure 4.7b. A clear distinction in overall performance and fracture behaviour can be made between the unidirectional and the helix samples. With (645 ± 29) N, the helix samples attain a max load P_{max} on average 88 % larger than the unidirectional samples reach-
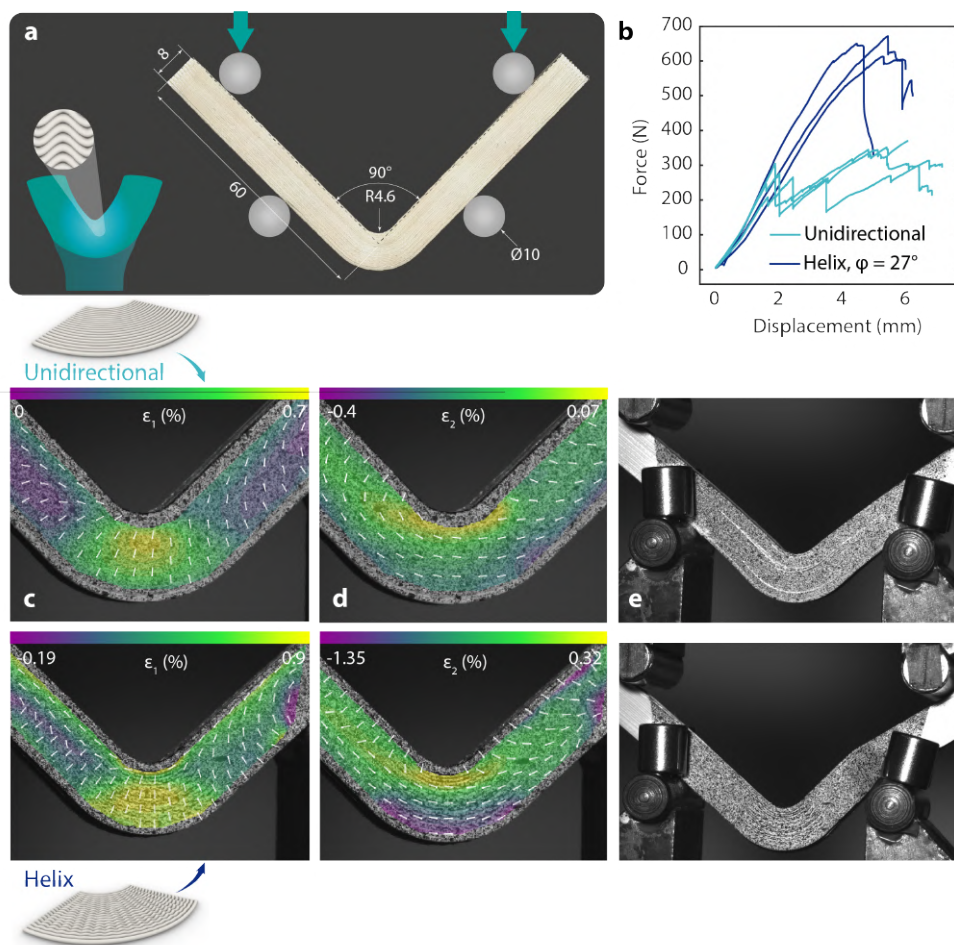
4

Figure 4.7 – **Four-point bending of an elbow-like junction compares the behaviour of a contour-like pattern to a helical pattern. A.** Dimensions of the curved beam and test set-up. The thickness of the beam is 10 mm **B.** Force-displacement curves show that the unidirectional samples reach about half the load of the Helix samples. Digital Image correlation of unidirectional (top) and Helix (bottom) samples gives further insight into their fracture mechanisms. Colours and arrow orientation represent respectively the amplitude and direction of the principal strain ϵ_1 in **C.** and the second principal strain ϵ_2 in **D.** Photographs of the same specimen after final fracture illustrate the two different behaviours in **E.** The unidirectional specimens all delaminate early, and continue deforming with successive propagation of delaminations. In contrast, the helix specimens show close to a three-times larger strain before the first failure. Furthermore, failure also does not occur at the junction zone but in the indentation point of a strut, indicating superior resistance of the Helix zone compared to unidirectional samples.

ing (342 ± 28) N. The strain attained at max failure is also 2.96 times larger for the helix samples, without any significant increase in mass, as shown in Table SI 4.1. In Figure 4.7c, the amplitude and direction of first principal strain ϵ_1 obtained by DIC are overlaid onto the two configurations just before the onset of their first load drop. In both cases, ϵ_1 in the curved zone is a tensile radial strain as indicated by the arrows and positive value. However, the distribution of maximum amplitude is more concentrated on the unidirectional specimen than on the helix one. This zone is the one where the first delamination takes place in the unidirectional pattern, corresponding to the middle third of the sample width, as expected. In contrast, for the helix specimen, the maximum ϵ_1 is seen on the entire patterned zone, indicating a more even distribution of strain which contributes to delay the onset of fracture. The second principal stresses are shown in Figure 4.7d, with the expected tensile and compressive circumferential stresses.

Both configurations before the test arrest, set to not exceed 7 mm of cross-head displacement, are illustrated in Figure 4.7e. The fracture behaviour differs between the two types. The unidirectional samples crack earlier but can carry a load close to P_{max} via the continued onset and propagation of delamination until the test is interrupted. In contrast, the helix samples break catastrophically at P_{max} via strut failure at a contact point to the fixture. As a result, the junction zone was not tested to its fullest potential and may be capable of carrying even more load in this configuration if the struts are stiffened by doublers. Since the struts are the same unidirectional LCP in both types, these elements indicate that wherever the unidirectional configuration is prone to early failure upon radial tensile loading, the helix pattern can indeed be implemented to impart robustness.

To illustrate the potential of this method at reinforcing junctions in TAO parts, a sinusoidal pattern is applied for illustration purposes to a three-strut junction in Figure 4.8. In a TAO part such as the one printed with LCP in Figure 4.8a, an optimal load transfer can be ensured by continuous printed lines across the different struts. Such a part possesses many kinds of junction configurations, including two- and three-strut junctions. Three two-strut junctions similar to those tested in Figure 4.7 can be rotated and adapted to create a three-strut junction, as shown in Figure 4.8a and Figure 4.8c. The 3D-printed junction with interlocked continuous toolpaths between all struts is shown in Figure 4.8d.
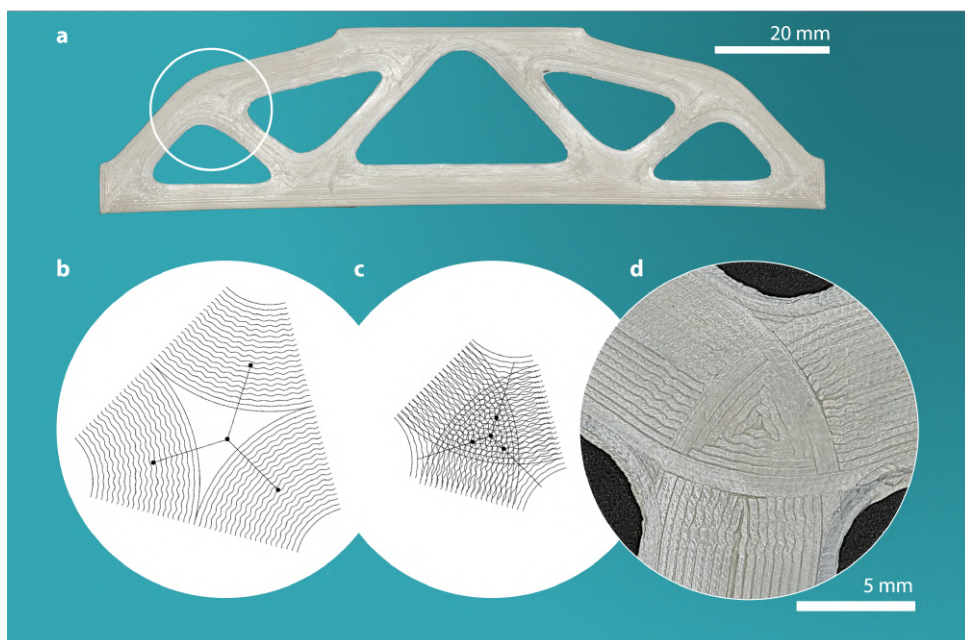
4

4

Figure 4.8 – **The sinusoidal pattern can also be applied on a three-strut junction. A.** A typical bridge-like topology optimized part contains sets of two-strut, three-strut and four-strut junctions. This part is printed with LCP using a fully dense concentric infill without waviness. **B.** A three-strut junction can be made of three sets of continuous paths with waviness, each of them being a two-strut junction. **C.** These paths can be overlapped, and **D.** 3D-printed, creating interlocking within the junction while remaining continuous to transfer the loads from one strut to the next.

4.3. Conclusions

For a 2D sinewave pattern lying within the build plane, larger amplitude and smaller wavelength are detrimental to performance in tension. The maximum angle of deviation between the sinewave and the X-axis, named φ, is shown to play an important role. In general, the samples behave as stiff as if they were unidirectional but oriented at the angle φ, following the corresponding expected behaviour from Classical Laminate Theory. While a similar trend can be noticed in tension for a sinusoidal pattern lying perpendicular to the build plane creating non-planar layers, short-beam shear performance increases due to layer interlocking.

Bi-sinusoidal patterns studied in interlaminar fracture resistance with the largest φ show a 50 % increase in work exerted before peak load, and a three-fold increase in work exerted for crack propagation. An increase of the surface roughness and macroscopic fibre-bridging is observed with increasing φ. These elements may indicate that the rising ratio of Mode-II loading introduced with larger φ leads to enough shear stresses being applied to the interface to pull out the fibrillar microstructure, thus dissipating more energy and slowing the crack propagation, similar to fibres in wood.

To test a junction zone, a helical pattern of a curved beam was loaded under four-point bending. Compared to the same geometry without the pattern, the failure load is improved by 88 % without additional mass. Strain-to-failure is also close to three-fold larger since the unidirectional specimens delaminate when exposed to radial tensile stresses. Combined with the development of new topology optimisation schemes, this approach opens avenues for higher structural performance with only marginal extra energy or material consumption. By utilizing the synergy between anisotropic materials and geometric patterns, designers can blend material properties to tune compliance, strengthen weak regions or redistribute loads, with the frugality and elegance of natural materials produced by living organisms.

4.4. Data availability

The data in this work is available under the repository: `https://doi.org/10.4121/46723f7d-274a-4331-879b-5dacc28b07ce`.

4.5. Materials and methods

Toolpath generation

Custom toolpaths are created using Rhino 7 (MacNeel, USA) with the visual programming platform Grasshopper.

3D-printing

The thermotropic random copolyester HBA:HNA (4-hydroxy-benzoic acid and 6:hydroxy-naphthalene-2-carboxylic acid) with ratio 73 : 27, is supplied as filament by NematX AG (Switzerland). The filament is printed on a Prusa MK3S+ 3D-printer, modified to withstand slightly larger temperatures than its specification. Printing temperature is 295 °C except in Figure 4.5 where 330 °C is chosen to facilitate manufacturing of the standing compact-tension specimen in an enclosure. Layer height is fixed to 0.05 mm for Figures 4.2 and 4.3, and to 0.1 mm from Figure 4.4 to Figure 4.8. Print speed is set to 35 mm/s and linewidth is 0.35 mm for a nozzle (E3D V6, England) diameter of 0.4 mm.

Microscopy

A VR-5000 wide-area 3D microscope (Keyence, Japan) was used to measure the surface profile of representative samples for each pattern and calculate the arithmetic average Surface roughness (Sa) of fractured surfaces of compact-tension specimens, with $Sa = \frac{1}{A} \iint_A |Z(x,y)| \, dx \, dy$. A correction is applied by removing the roughness value of a perfectly smooth bi-sinusoidal shape, to only consider local, "textural" roughness.

Mechanical testing

Tension

Unidirectional samples of 110 mm × 5 mm × 2 mm are 3D-printed and tested with a 10 kN universal testing machine (Zwick-Roell, Germany) equipped with a 10 kN load cell, at a rate of 2 mm/min following ISO 527-5. The specimens are bonded to glass-fibre end tabs with DP160 adhesive (3M, USA) for consistent load introduction. A hydraulic grip system is used to prevent slippage of the specimen. Five to seven specimens are tested per batch. Ultimate Tensile Strength is calculated by P_{max}/A where P_{max} is the maximum load recorded, and A is the specimen cross-section at the gauge length. The Young's modulus is calculated by the slope of the linear fit of the stress-strain curve in between DIC-measured strain values of 0.1% and 0.3%.

Short-beam shear

Samples of dimensions 18 mm × 6 mm × 3 mm are tested in three-point bending. The span length is adjusted according to the standard ASTM D2344 to four times the specimen thickness with a tolerance of 0.3 mm. The load is introduced by a three-point bending fixture with side supports diameters of 3 mm, and a centered load introduction head of 6 mm in diameter. Deformation is measured by the displacement of the central pin with respect to its initial position after a pre-load of 5 N. The test is performed on a 10 kN universal testing machine (Zwick-Roell, Germany) with a 1 kN load cell at a speed of 1 mm/min. Short-beam shear strength is calculated by the formula $\sigma_{SBS} = 0.75 P_{max}/(bh)$ where b and h are the width and thickness of the specimen, respectively, and P_{max} is the maximum load recorded. A minimum of seven specimens are tested per batch. Unless otherwise mentioned in Figure 4.4, the samples failed in interlaminar shear.

Mode-I fracture with compact tension
Samples of dimensions 35 mm×33.6 mm×7 mm are 3D-printed following ASTM standard D5045, with the holes for the loading pins and the notch integrated in the geometry. The notch is further sharpened by a razor drawing with gentle pressure to create a starter crack. A 10 kN universal testing machine (Zwick-Roell, Germany) is used with a 1 kN load cell and a strain rate of 10 mm/min. A minimum of five specimens are tested per batch. Load-displacement values are recorded until complete dissociation of the specimen, but data is considered until the slope reaches a value of 0.02 consistently for 100 data points.

Four-point bending
Curved-beam specimens are tested in four-point bending with a top span length of 60 mm and a bottom span length of 50 mm, with a diameter of 10 mm for the support rods and loading rods. Since the geometry is beam-like with a 10 mm × 8 mm cross-section that may show instability in the out-of-plane direction during loading, strong cylindrical magnets are placed on the support rods to secure the specimen in a vertical position during load introduction.

4

DIC
Digital Image Correlation is used to measure the deformation of tensile specimens. Two 9 MP cameras (LIMESS, Germany) with a 50 mm-focal length lens were used to acquire images at a rate of 2 Hz. The analysis is performed using Vic-3D 8 (Correlated Solutions), with a subset size and step size of 27 and 7. This enables the use of a digital extensometer to obtain strain values for Young's modulus calculations.
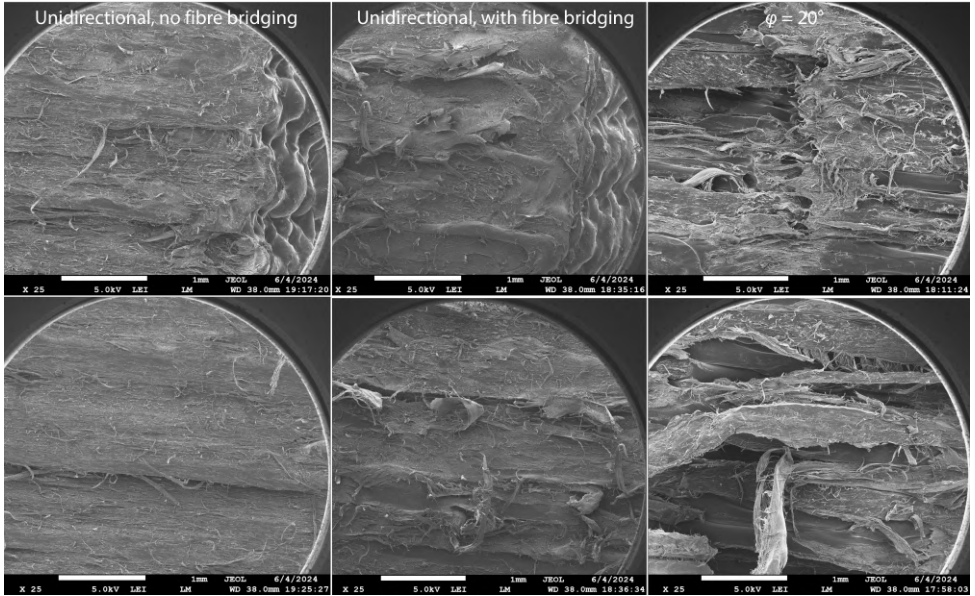
4.6. Supplementary Information

Figure SI 4.1 – **Scanning electron microscopy of the fracture surfaces of Compact-Tension specimen.** Top row shows the zone of onset of crack propagation. Bottom row shows an area on the sample deemed the roughest by visual comparison. The fracture surface is relatively smooth for the flat specimen without fibre-bridging (left) compared to the flat specimen displaying fibre-bridging (middle). The extent of plasticity is however superior on the sample with $\varphi = 20°$, with a multi-scale structure characteristic of LCPs, visible on multiple pulled out fibres.
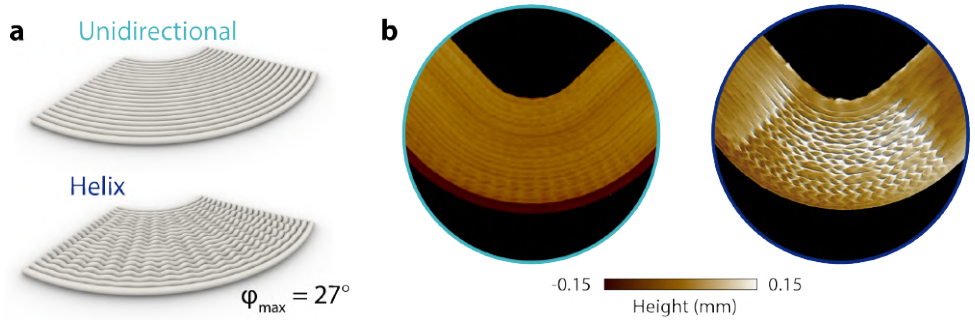

Figure SI 4.2 – **A.** Detail of the two junction zones. Both geometries are printed with the face shown on all images corresponding to that normal to the build plane. In the unidirectional (UD) configuration, printed lines follow the curvature of the beam, while in the Helix configuration, a pattern of amplitude of 0.08 mm and $\varphi_{max} = 27°$ is added. Outside of the junction zone, the printed struts are identical. **B.** Height map of the unidirectional (right) and helix (left) patterns. Oscillations localized to the outer radius region of about 10 µm can also be noticed in the unidirectional specimen and are attributed to vibrations from the 3D-printer.

Type	Sample ID	Mass (g)	Max Force (N)	Deformation at first peak (mm)
Unidirectional	U1	7.6	343.9	5.26
	U2	7.7	370.3	5.43
	U3	7.9	313.3	4.44
Helix	H1	7.5	613.2	1.64
	H2	7.3	672.0	1.87
	H3	8.0	649.8	1.59

Table SI 4.1 – Curved beam sample mass versus maximum loading and deformation at the first peak.

4

References

1. Weinkamer, R. & Fratzl, P. Mechanical adaptation of biological materials - The examples of bone and wood. *Materials Science and Engineering C* **31,** 1164–1173. ISSN: 09284931 (2011).

2. Schmidt, M. P., Couret, L., Gout, C. & Pedersen, C. B. Structural topology optimization with smoothly varying fiber orientations. *Structural and Multidisciplinary Optimization* **62,** 3105–3126. ISSN: 16151488 (Dec. 2020).

3. Jantos, D. R., Hackl, K. & Junker, P. Topology optimization with anisotropic materials, including a filter to smooth fiber pathways. *Structural and Multidisciplinary Optimization* **61,** 2135–2154. ISSN: 16151488 (2020).

4. Vertonghen, L., Irisarri, F. X., Bettebghor, D. & Desmorat, B. Gradient-based concurrent topology and anisotropy optimization for mechanical structures. *Computer Methods in Applied Mechanics and Engineering* **412,** 116069. ISSN: 00457825 (2023).

5. Kundu, R. D. & Zhang, X. S. Stress-based topology optimization for fiber composites with improved stiffness and strength: Integrating anisotropic and isotropic materials. *Composite Structures* **320,** 117041. ISSN: 02638223 (2023).

6. Hmeidat, N. S., Brown, B., Jia, X., Vermaak, N. & Compton, B. Effects of infill patterns on the strength and stiffness of 3D printed topologically optimized geometries. *Rapid Prototyping Journal* **27,** 1467–1479. ISSN: 13552546 (2021).

7. Ranaivomiarana, N., Bettebghor, D. & Desmorat, B. Advances in Structural and Multidisciplinary Optimization. *Advances in Structural and Multidisciplinary Optimization* (2018).

8. Kundu, R. D. & Zhang, X. S. Additive manufacturing of stiff and strong structures by leveraging printing-induced strength anisotropy in topology optimization. *Additive Manufacturing* **75,** 103730. ISSN: 22148604 (2023).

9. Kumar, S., Tan, S., Zheng, L. & Kochmann, D. M. Inverse-designed spinodoid metamaterials. *npj Computational Materials* **6,** 1–10. ISSN: 20573960 (2020).

10. Wang, Z., Dabaja, R., Chen, L. & Banu, M. Machine learning unifies flexibility and efficiency of spinodal structure generation for stochastic biomaterial design. *Scientific Reports* **13,** 1–14. ISSN: 20452322 (2023).

11. Di Rienzo, A., Duriez, E., Charlotte, M. & Morlier, J. Lightweighting structures using an explicit microarchitectured material framework. *Mechanics and Industry* **25.** ISSN: 22577750 (2024).

12. Raney, J. R. *et al.* Rotational 3D printing of damage-tolerant composites with programmable mechanics. *Proceedings of the National Academy of Sciences of the United States of America* **115,** 1198–1203. ISSN: 10916490 (2018).

13. Giachini, P. A. *et al.* Additive manufacturing of cellulose-based materials with continuous, multidirectional stiffness gradients. *Science Advances* **6,** 1–12. ISSN: 23752548 (2020).

14. Kokkinis, D., Bouville, F. & Studart, A. R. 3D Printing of Materials with Tunable Failure via Bioinspired Mechanical Gradients. *Advanced Materials* **30,** 1–9. ISSN: 15214095 (2018).

15. Larson, N. M. *et al.* Rotational multimaterial printing of filaments with subvoxel control. *Nature* **613,** 682–688. ISSN: 14764687 (2023).

16. Ren, L. *et al.* Graded biological materials and additive manufacturing technologies for producing bioinspired graded materials: An overview. *Composites Part B: Engineering* **242,** 110086. ISSN: 13598368 (2022).

17. Wang, X. *Build with nature: Biomechanical properties and performance of self-growing connections in interconnected trees* PhD thesis (2024), 289. ISBN: 9789055841745.

18. Drénou, C., Restrepo, D. & Slater, D. Demystifying Tree Forks: Vices and Virtues of Forks in Arboriculture. *Journal of Botany Research* **3,** 100–113 (2020).

19. Slater, D. & Ennos, R. Interlocking wood grain patterns provide improved wood strength properties in forks of hazel (Corylus avellana L.) *Arboricultural Journal* **37,** 21–32. ISSN: 21681074 (2015).

20. Slater, D., Bradley, R. S., Withers, P. J. & Roland Ennos, A. The anatomy and grain pattern in forks of hazel (Corylus avellana L.) and other tree species. *Trees - Structure and Function* **28,** 1437–1448. ISSN: 09311890 (2014).

21. Jaffe, M. J. & Forbes, S. Thigmomorphogenesis: the effect of mechanical perturbation on plants. *Plant Growth Regulation* **12,** 313–324 (1993).

22. Slater, D. The mechanical effects of bulges developed around bark-included branch junctions of hazel (Corylus avellana L.) and other trees. *Trees* **35,** 513–526. ISSN: 09311890 (2021).

23. Özden, S., Slater, D. & Ennos, R. Fracture properties of green wood formed within the forks of hazel (Corylus avellana L.) *Trees - Structure and Function* **31,** 903–917. ISSN: 09311890 (2017).

24. Maaß, M. C., Saleh, S., Militz, H. & Volkert, C. A. The Structural Origins of Wood Cell Wall Toughness. *Advanced Materials* **32.** ISSN: 15214095 (2020).

25. Müller, U., Gindl-Altmutter, W., Konnerth, J., Maier, G. A. & Keckes, J. Synergy of multi-scale toughening and protective mechanisms at hierarchical branch-stem interfaces. *Scientific Reports* **5,** 1–9. ISSN: 20452322 (2015).

26. Duhamel du Monceau, H. L. *De l'exploitation des bois : seconde partie* (ed Guérin, L.) (Paris, 1764).

27. Wang, X., Gard, W., Borska, H., Ursem, B. & van de Kuilen, J. W. Vertical greenery systems: from plants to trees with self-growing interconnections. *European Journal of Wood and Wood Products* **78,** 1031–1043. ISSN: 1436736X (2020).

28. Liu, Z., Zhang, Z. & Ritchie, R. O. Interfacial toughening effect of suture structures. *Acta Biomaterialia* **102,** 75–82. ISSN: 18787568 (2020).

29. Allum, J., Kitzinger, J., Li, Y., Silberschmidt, V. V. & Gleadall, A. ZigZagZ: Improving mechanical performance in extrusion additive manufacturing by nonplanar toolpaths. *Additive Manufacturing* **38,** 101715. ISSN: 22148604 (Feb. 2021).

30. Jia, Z. & Wang, L. 3D printing of biomimetic composites with improved fracture toughness. *Acta Materialia* **173,** 61–73. ISSN: 1359-6454 (July 2019).

31. Malik, I. A., Mirkhalaf, M. & Barthelat, F. Bio-inspired "jigsaw"-like interlocking sutures: Modeling, optimization, 3D printing and testing. *Journal of the Mechanics and Physics of Solids* **102,** 224–238. ISSN: 00225096 (2017).

32. Mencattelli, L. & Pinho, S. T. Herringbone-Bouligand CFRP structures: A new tailorable damage-tolerant solution for damage containment and reduced delaminations. *Composites Science and Technology* **190,** 108047. ISSN: 02663538 (Apr. 2020).

33. Damodaran, V., Castellanos, A. G., Milostan, M. & Prabhakar, P. Improving the Mode-II interlaminar fracture toughness of polymeric matrix composites through additive manufacturing. *Materials and Design* **157,** 60–73. ISSN: 18734197 (Nov. 2018).

34. Zhang, M. *et al.* Improved interlayer performance of short carbon fiber reinforced composites with bio-inspired structured interfaces. *Additive Manufacturing* **79,** 103936. ISSN: 22148604 (2024).

35. Selvam, A., Mayilswamy, S. & Whenish, R. Strength Improvement of Additive Manufacturing Components by Reinforcing Carbon Fiber and by Employing Bioinspired Interlock Sutures. *Journal of Vinyl and Additive Technology* **26,** 511–523. ISSN: 15480585 (2020).

36. Burns, L. A., Mouritz, A. P., Pook, D. & Feih, S. Bio-inspired design of aerospace composite joints for improved damage tolerance. *Composite Structures* **94,** 995–1004. ISSN: 02638223 (Feb. 2012).

37. Zorzetto, L. & Ruffoni, D. Wood-Inspired 3D-Printed Helical Composites with Tunable and Enhanced Mechanical Performance. *Advanced Functional Materials* **29,** 1–9. ISSN: 16163028 (2019).

38. Liu, H. *et al.* Interlocked wood-like composites with tunable mechanical properties. *Journal of the Mechanics and Physics of Solids* **188,** 105679. ISSN: 00225096 (2024).

4

4

39. Houriet, C. *et al.* 3D Printing of Flow-Inspired Anisotropic Patterns with Liquid Crystalline Polymers. *Advanced Materials* **2307444,** 1–12. ISSN: 15214095 (2023).

40. Gantenbein, S. *et al.* Three-dimensional printing of hierarchical liquid-crystal-polymer structures. *Nature* **561,** 226–230. ISSN: 0028-0836 (Sept. 2018).

41. Hudson, S. D. & Lovinger, A. J. Transmission electron microscopic investigation of the morphology of a poly(hydroxybenzoate-co-hydroxynaphthoate) liquid crystal polymer. *Polymer* **34,** 1123–1129. ISSN: 00323861 (1993).

42. Ide, Y. & Ophir, Z. Orientation development in thermotropic liquid crystal polymers. *Polymer Engineering & Science* **23,** 261–265. ISSN: 15482634 (1983).

43. Gantenbein, S. *et al.* Spin-Printing of Liquid Crystal Polymer into Recyclable and Strong All-Fiber Materials. *Advanced Functional Materials,* 2104574. ISSN: 1616-3028 (Sept. 2021).

44. Lefèvre, J. *et al.* "Foil spintrusion" of high-performance polymer films. *Journal of Polymer Science, Part B: Polymer Physics* **50,** 1713–1727 (Dec. 2012).

45. Peijs, T. & Tervoort, T. A. High-performance liquid-crystalline polymer films for monolithic "composites". *Composites Part A: Applied Science and Manufacturing* **81,** 296–304. ISSN: 1359835X (2016).

46. Vindokurov, I., Pirogova, Y., Tashkinov, M. & Silberschmidt, V. V. Effect of Heat Treatment on Elastic Properties and Fracture Toughness of Fused Filament Fabricated PEEK for Biomedical Applications. *Polymers* **14,** 1–19. ISSN: 20734360 (2022).

47. Xu, Q. *et al.* Enhanced interlayer strength in 3D printed poly (ether ether ketone) parts. *Additive Manufacturing* **55.** ISSN: 22148604 (2022).

48. Zhang, G. *et al.* A systematic investigation on the minimum tensile strengths and size effects of 3D printing polymers. *Polymer Testing* **117,** 107845. ISSN: 01429418 (2023).

49. Nelson, J. W. *et al.* Generalized models for unidirectional anisotropic properties of 3D printed polymers. *Rapid Prototyping Journal* **26,** 1453–1462. ISSN: 13552546 (2020).

50. Mirzaei, B., Sinha, A. & Nairn, J. A. Measuring and modeling fiber bridging: Application to wood and wood composites exposed to moisture cycling. *Composites Science and Technology* **128,** 65–74. ISSN: 02663538 (2016).

51. Khan, R. Fiber bridging in composite laminates: A literature review. *Composite Structures* **229.** ISSN: 02638223 (2019).

52. Cotterell, B. & Rice, J. Slightly curved or kinked cracks. *International Journal of Fracture* **16,** 155–169 (1980).

53. Zavattieri, P. D., Hector, L. G. & Bower, A. F. Determination of the effective mode-I toughness of a sinusoidal interface between two elastic solids. *International Journal of Fracture* **145,** 167–180. ISSN: 15732673 (2007).

54. Hutchinson, J. W. & Suo, Z. *Mixed Mode Cracking in Layered Materials* 63. ISBN: 0120020297 (1976).

55. Kress, G., Roos, R., Barbezat, M., Dransfeld, C. & Ermanni, P. Model for interlaminar normal stress in singly curved laminates. *Composite Structures* **69,** 458–469. ISSN: 02638223 (2005).

56. Süsler, S. & Kazancı, Z. Delamination Strength Comparison of Additively Manufactured Composite Curved Beams Using Continuous Fibers. *Polymers* **15.** ISSN: 20734360 (2023).

4

Chapter 5

3D-printing of liquid crystal polymers for space applications

ABSTRACT

Fused Filament Fabrication is a promising manufacturing technique for the improvement of circularity in space missions. Potential scenarios include in-orbit applications to maximize mission life and to support long-term exploration missions with in-situ manufacturing and recycling. However, its adoption is restricted by the availability of engineering polymers displaying high mechanical performance combined with resistance to space conditions. Here, a thermotropic Liquid Crystal Polymers (LCP) is studied as a candidate material with extrusion 3D printing. To expand its scope of applicability to structural parts for space applications, four different exposure conditions are studied: thermal cycling under vacuum, atomic oxygen, UV, and electron irradiation. While 1 MeV-electron irradiation leads to a green coloration due to annealable color centers, the mechanical performance is only slightly decreased in dynamic mode but not significantly in quasi-static mode. Increased printing temperature affects tensile stiffness and strength negatively but improves transverse strength and resistance to thermal cycling. Samples exposed to thermal cycling and the highest irradiation dose at lower printing temperatures still display an average Young's modulus of 30 GPa and 503 MPa of tensile strength which is exceptionally high for a 3D-printed polymer. For the types of exposure studied, overall, our results indicate that LCP 3D-printed parts can be used for space applications.

5.1. Introduction

The European Space Agency (ESA) aims to implement a circular economy in space by 2050 [1]. While in the 20th century, space was strictly limited to a very small number of governmental actors, in the 21st century, a "New Space" economy is developing. It is characterized by a diverse collection of actors such as private enterprises, startups, and universities [2]. The global reduction in satellite size has also coincided with a seven-fold increase in the number of satellites orbiting Earth in 10 years, with constellations of small satellites now representing their majority. Within the same time frame, the number of CubeSats has also been multiplied by 25 [3]. In this context, to avoid the piling up of space debris, mitigate the threat they pose on operational satellites, and make the industry sustainable, new aspects start to be considered in mission designs. In-orbit servicing, in-orbit assembly, in-orbit manufacturing, and eventually in-orbit recycling projects are envisioned in future developments [4]. Given its extensive design freedom, strong automation capabilities, and versatility in raw material selection, AM is a key technology to facilitate Out-of-Earth manufacturing, compared to traditional manufacturing methods for satellite structures, such as composite layup or machining of metal alloys [5]. Fused Filament Fabrication (FFF) works well in micro-gravity due to its reliance on a pressure difference to extrude, as demonstrated by 3D printers already functional on the ISS, as well as the MELT 3D printer [6] and the IMPERIAL 3D printer [7, 8], developed in collaboration with ESA. FFF has also the advantages of high customizability of components and high shaping freedom. However, the use of FFF for space applications has been restricted by the moderate mechanical properties of available materials compared to traditional ones, such as aluminum, titanium or composite structures, especially when it comes to withstanding the extensive loads during launch [5, 9]. Within the selection of polymers that are suitable for the extreme space environment, few have demonstrated compatibility with FFF such as PEEK [10, 11], or PEI [12–14]. In particular, the MakerSat-1 CubeSat, deployed in orbit in 2020, was the first satellite to use a fully 3D-printed frame. It embedded material durability experiments on 3D-printed polymers. After four months of exposure, the PEI/PC (Ultem) blend showed a 20.9 % mass loss, which was attributed to space environmental degradation and especially to the effect of atomic oxygen erosion [14].

The emergence of thermotropic liquid crystal polymers as printable material could prove to be disruptive for space applications. Indeed, the thermotropic liquid crystal polymer HBA:HNA with a ratio 73:27 has been used under a fibre form in the space environment, often referred to by its commercial tradename Vectran. Being non-polar and with an aromatic backbone, it possesses high thermal and chemical resistance properties combined with high mechanical performance [15–17].

As a fabric, its good fold characteristics have resulted in its use for safety and protection such as for parachutes and the Pathfinder airbags [18]. It is also one of the structural components of the restraint layer of the Bigelow Expandable Activity Module currently deployed on the ISS [19]. More recently, it has been selected for the LIFE habitat of Sierra Space for its mechanical performance for the same purpose. A full-size test unit of 300 m^3 using Vectran fibres woven into straps, or webbings, was recently tested to failure, exceeding NASA safety levels by 27 % [20]. Furthermore, it has been used as a highly cut-resistant
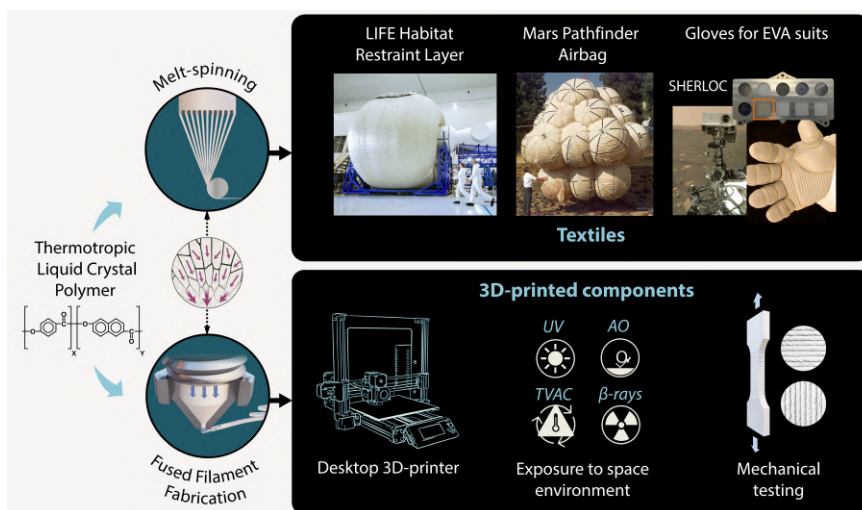
Figure 5.1 – **Overview of the Vectra 3D-printing process as opposed to melt-spinning of Vectran.** During melt-spinning, alignment is obtained via elongational flow. During 3D printing, the nematic domains in the liquid crystal state also align as they undergo elongational flow, as well as shear flow inside the nozzle. To evaluate the space-worthiness of the 3D-printed polymers, it is exposed to four different components of the space environment; UV-irradiation, atomic oxygen, thermal cycling, and high-energy electron irradiations (known as beta-rays). Subsequently, it is evaluated for its optical, chemical, and mechanical changes. Image credits: NASA, Sierra Space.

material for the palms and fingers of astronaut gloves during EVAs [21, 22]. Its properties are currently further investigated in situ on Mars with the SHERLOC module, integrated into the Perseverance rover [23]. SHERLOC is capable of periodically analyzing the composition of Martian rocks and four fabrics considered for future space suits, including Vectran. The results of their exposure to the Martian atmosphere, radiations, dust, and thermal cycling will guide the design of future Mars-specific spacesuits [23]. Overall its usefulness as a space material under its melt-spun form is undoubtedly present and has attracted great interest as shown in Figure 5.1.

Recently, Fused Filament Fabrication (FFF) was employed to process this polymer, instead of melt-spinning [24–27]. A parallel can be drawn between the contraction die geometry inside the 3D-printer nozzle, and the spinneret during the melt-spinning process which both enable the alignment of the nematic domains during extrusion, granting the polymer its remarkably high mechanical properties compared to injection-molding. Due to the large temperature difference between the nozzle ($T = 295\,°C$ or higher) and the ambient environment, the polymer is solidified before full relaxation of the nematic domains can take place, leading to a strong molecular anisotropy in the printing direction [24].

In contrast to other approaches where anisotropy is obtained by the top-down combination of a matrix and a fibre, this method utilizes the bottom-up capability of rigid-rod polymer chains to self-align along a favored orientation of shear and elongational

flow. Similarly, while natural materials, such as wood, bone, or nacre, are made of weak building blocks, the strength and toughness they possess are granted by their hierarchical arrangement and anisotropy [28]. In LCP, this molecular anisotropy is controllable with printed line width, leading to tailorable stiffness and strength on the fly [26]. Spatial gradients of mechanical behavior can be embedded within one part, between high-stiffness (30 GPa) associated to low-strain regions, and lower stiffness (3 GPa) with large-deformation regions. Furthermore, lines can also be spun by the 3D printer itself, akin to the melt-spinning manufacturing of Vectran fibres, thus creating reinforcement and matrix made of the same material [25]. To our knowledge, such a palette of deposition methods and available mechanical properties with one single material and a desktop printer is unprecedented.

The three-dimensional printing of LCP therefore indicates a complementary scope of uses to the traditional melt-spinning method, for various structural and functional objects. For instance, the highly packed chains in the nematic state also grant the material a low free volume, giving rise to good gas-barrier properties as well as mechanical strength. As such, its low permeability [27] may prove useful for applications in liquid or gas retention in space. An extensive material selection survey was performed by Slejko *et al.* [9] across 3D-printable polymers and metals, considering structural requirements like specific stiffness (using injection-moulding values for polymers) and heat for demise during atmospheric re-entry for debris mitigation purposes. This survey indicated that LCP was the only polymer approaching the performance of the best metal choices according to this metric. In the context of out-of-Earth manufacturing and future permanent human settlement on the Moon or Mars, the potential capability of this polymer to be reprocessed after its first life as Vectran fabric, and especially reused as FFF-feedstock should be further noted.

However, while the polymer backbone is the same between the 3D-printed LCP (3DP-LCP) and the melt-spun LCP (MS-LCP), the strong influence of processing parameters and methods on most material properties is a well-known feature of this kind of thermotropic LCPs [29–31]. FFF is also known to create inhomogeneities inside parts, such as voids [32, 33]. These may pose a concern as Low Earth Orbit (LEO) and Geostationary Earth Orbit (GEO) orbits expose the spacecraft to a harsh environment consisting of atomic oxygen (for LEO), solar UV photons, heavy ions, solar flare protons, as well as protons and electrons trapped in belts by the Earth's magnetic field [34]. The exact application of such a material for space hardware does also depend on its durability in the respective space environment. Therefore, there is a need to assess the space-relevant characteristics of 3D-printed LCP to evaluate its potential as a structural bus for CubeSats, or other applications in orbit and on planetary settlements.

To establish whether 3DP-LCP possesses similar resistance to the space environment to MS-LCP, four different types of exposure were selected: thermal vacuum cycling (TVAC), Vacuum UV, high energy electron irradiation, and lastly exposure to Atomic Oxygen (AO) via the Euro Material Ageing campaign carried out by ESA and CNES [35]. Further characteristics studied here are outgassing and change in thermo-optical properties after exposure. Mechanical response is measured after thermal vacuum cycling, for two dif-

ferent printing configurations, four printing temperatures, and with the highest dose of electron irradiation. DMA and FTIR were also used to gain insight into potential polymer degradation. The polymer performance was compared to data available for melt-spun LCP and 3D-printable candidates such as PEEK and PEI. We show that 3D-printed LCP retains its pre-exposure mechanical properties, despite some drastic appearance changes under UV and electron irradiation.

5.2. Results and Discussion

5.2.1. Exposure of LCP to simulated space environment

Vacuum

Quantifying the magnitude of outgassing is crucial to assess the space-worthiness of polymers, to avoid contamination of optics and other critical surfaces by the Volatile Organic Compounds (VOC) released under exposure to vacuum at elevated temperatures [36, 37]. These chemicals, which are impurities, space environmental degradation products, or left over from chemical reaction or cleaning steps, migrate and escape via diffusion and desorption, respectively [36]. Potential contaminants may increase the outgassing phenomenon in the 3D-printed LCP compared to the melt-spun form Vectran because the polymer is extruded twice after being received in the form of pellets: First to be spooled as a 3D-printing filament and second through the nozzle of a 3D printer during manufacturing.

Figure 5.2 shows the outgassing performance of 3DP-LCP compared to literature values for Vectran [38] and PEEK [11]. In Figure 5.2a, results for total mass loss after exposure to vacuum are almost identical for Vectran and 3DP-LCP. Residual Mass Loss (RML) is the mass loss after water reabsorption during post-conditioning, thus it represents the total mass loss of the specimen without the absorbed water. The lower RML for 3D-printed LCP indicates that it is more prone to absorbing moisture than the Vectran rope. For both metrics, the 3D-printed LCP shows less outgassing than 3D printed PEEK. However, in all cases, values are below 1 % RML, the maximum threshold according to ECSS standards [39]. The testing apparatus, a Micro Volatile Condensable Measurement facility could not collect any Collectible Volatile Condensable Material (CVCM). A Residual Gas analysis was therefore carried out on 3D-printed LCP to analyze released gases in high vacuum. Figure 5.2b shows the chemical composition of outgassed compounds for two types of samples exposed to vacuum during 48 h: with and without 24 h of prior bake-out at 150 °C. A small amount of hydrocarbon can be observed on the pristine sample, but not when bake-out has occurred. Figure 5.2c indicates that after bake-out, the outgassing rate has reached a level close to the high vacuum limit (1.0×10^{-10} mbar.L.s^{-1}.cm^{-2}). The sample without bake-out shows an outgassing rate two orders of magnitude lower than 3D-printed PEEK.

Meeting outgassing requirements is a necessary condition for space applications, which both melt-spun and 3D-printed LCP fulfill. However, contamination can still arise from the reaction of the material through space environmental exposure. For example, in LEO, Atomic Oxygen (AO) can be damaging to the external materials of a spacecraft [34]. The oxygen atom, which is a result of the photodissociation of dioxygen with UV irradiation,
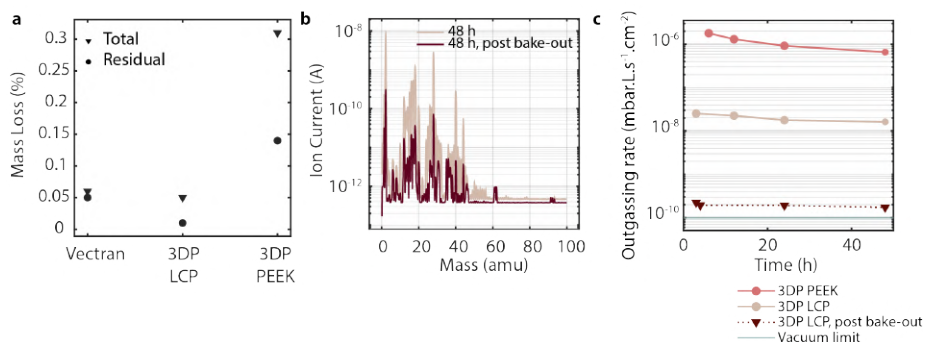
Figure 5.2 – **Pristine 3D-printed LCP (3DP-LCP) outgassing properties compared to another polymer (PEEK) and Mlet-Spun LCP (MS-LCP), known as Vectran. A.** Total Mass Loss and Residual Mass Loss indicate lower values for the Vectran fibre rope [38] and 3DP-LCP than for 3DP-PEEK [11]. In all cases, values are acceptable per ECSS standards [39]. A residual gas analysis enables to obtain **B.** indications of the molecular composition of the outgassed compounds and **C.** outgassing rate over time, showing two orders of magnitude decrease in outgassing rate when the polymer has been baked out for 24 h at 150 °C.

5

has one unpaired valence electron and is therefore highly reactive. With the orbital velocity of a spacecraft, the energy of an atomic oxygen impacting the surface is ca. 4.5 eV, sufficiently high to break chemical bonds. It is however not reaching a sputter threshold of ca. 30 eV, and thus materials degradation follows an oxidative erosion mechanism [40]. Therefore, exposed organic surfaces in particular tend to erode gradually. On top of the gradual reduction in thickness, low mass volatile reaction by-products can be emitted, increasing the risk of further contamination of critical surfaces.

Atomic Oxygen

In LEO, such as the altitude of ISS (400 km), Atomic Oxygen (AO) constitutes one of the most important contributors to material degradation, as it tends to impact the surface of exposed structures [34]. Moreover, it is the most abundant species found between altitudes of 180 km to 650 km. During a pre-flight qualification step of the Euro Material Ageing study organized by ESA, 3DP-LCP was exposed to 2.0×10^{21} atoms.cm^{-2} in a space environment simulation facility, under high vacuum and 15 °C to 40 °C temperature range. AO damage can often be seen with a change in the color or dullness of the material. In Figure 5.3a, the 3D-printed samples were compared to reference and did not sustain visible changes. Solar absorptance and thermal emittance were measured as they help determine the thermo-optical characteristics of the spacecraft. Solar absorptance increased slightly from 0.27 ± 0.03 to 0.32 ± 0.03 after exposure. The thermal emittance coefficient increased from 0.87 ± 0.05 to 0.93 ± 0.05. This change in properties is usually linked to the erosion and formation of roughness of the surface of the samples due to AO [34]. To assess the extent of damage, the specimens are observed in SEM and compared to pristine counterparts in Figure 5.3b. The microstructure of 3D-printed LCP exposed to AO is typical for organic materials with a carpet-like microstructure caused by oxygen etching away and then penetrating inside the formed holes [47]. Vectran fibres of
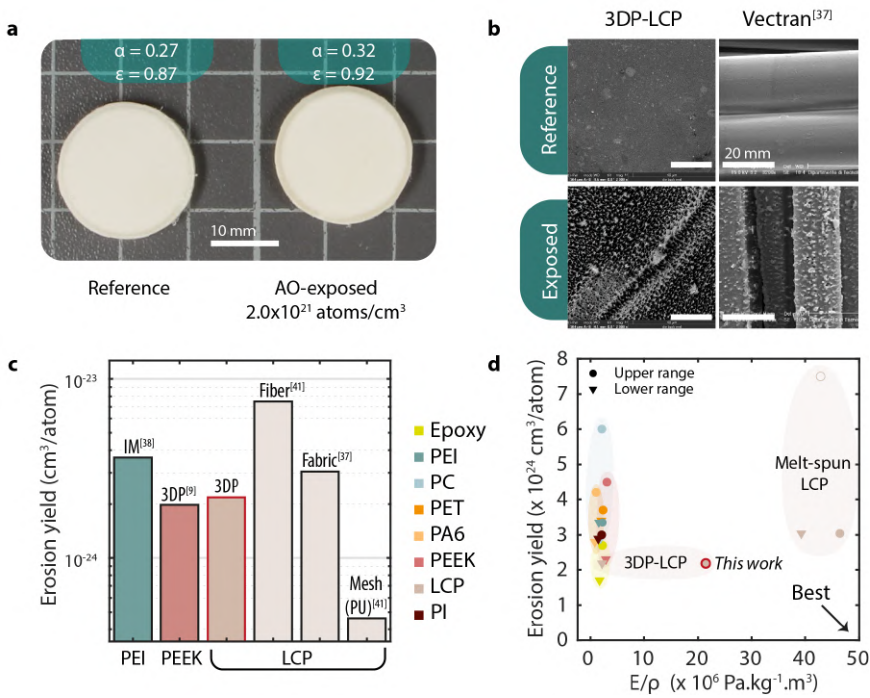
Figure 5.3 – **Exposure of 3DP-LCP to Atomic Oxygen (AO). A.** No visible change can be spotted after exposure. **B.** Surface damage becomes noticeable in SEM micrographs, with a typical 'carpet-like' pitted pattern. This behavior is comparable to that of Vectran fibres (MS-LCP) [41]. **C.** Erosion yield is compared to 3DP-LCP and MS-LCP under different forms. 3DP-LCP behaves in the range of other 3D-printable polymers, such as 3D-printed PEEK [11] and PEI [42]. On a flown Vectran mesh (Mission MISSE-7 [43]), a polyurethane coating imparts further resistance to AO. **D.** An Ashby diagram compares erosion yield to specific tensile stiffness for different polymers, including 3D-printable ones. Polymers: PEI - polyetherimide (ULTEM), PC – polycarbonate, PET - polyethylene terephthalate (Mylar), PA6 – Polyamide-6 (Nylon), PEEK – polyether ether ketone (Victrex), LCP – liquid crystal polymer (Vectran), PI – polyimide (Kapton). The dot circled in red corresponds to the average specific tensile stiffness obtained for 3DP-LCP between printing temperatures of 295 °C and 310 °C. Erosion yield is extracted from NASA-flown missions [44, 45], stiffness-density ranges from Ansys Granta Selector database [46] and from [12, 26].

a fabric exposed to AO, with a fluence of 2.2×10^{20} atoms.cm^{-2}) at 200 °C [41] also show this microstructure.

The erosion damage of 3DP-LCP can be quantified by measuring the erosion yield, which is the volume of material removed per incident impacting atom. It is compared in Figure 5.3c against high-performance 3D-printable thermoplastics (PEEK and PEI) and MS-LCPs under different forms. All data except that of the fabric [41] and the 3D-printed samples come from flight missions such as NASA MISSE-7 where specimens are attached to ISS (ram or wake) and brought back to Earth for analysis. The erosion yield of the 3D-printed LCP is 2.18×10^{-24} cm^3.atom^{-1}. In a previous study, 3D-printed conductive PEEK was also measured with 1.98×10^{-24} cm^3.atom^{-1} [11]. This is in a typical range of thermoplastic polymers. The expected thickness loss of the 3D-printed LCP is estimated to be 0.1 mm per year in the context of the Euro Material Ageing study where samples will be exposed to a LEO environment within the Bartolomeo module of the International Space Station. In real use for long-term missions in low orbits, protective coatings are being used [34]. For instance, a Vectran mesh coated with polyurethane [44] was shown to limit Atomic Oxygen (AO) damage by an order of magnitude.

In Figure 5.3d, an Ashby chart compares erosion yield to specific stiffness, i.e. the ratio of Young's modulus to density, for typical 3D-printable polymers, as well as Vectran, epoxy resins, and polyimide (Kapton). 3DP-LCP has the advantage of a very high specific stiffness that can be tailored via line width as shown in Chapter 3. This possibility is illustrated by the large span in specific stiffness on the graph. The interaction of AO with metals is different: Non-volatile metal oxides are typically produced as a result of their oxidation. These oxides tend in most cases to shield the surface below and reduce any further damage. Therefore the metric of erosion yield is not meaningful and they do not appear on this graph. While erosion resistance is a great advantage for metals, as pointed out in [9], LCPs with the addition of protective coatings should still be considered when metrics such as shaping freedom are valued in the case of a CubeSat structure.

One can notice a large variation in erosion yield with the melt-spun LCP. The highest erosion yield has been reported at 7.5×10^{-24} cm^3.atom^{-1} for a yarn [48], while in MISSE-2 [45] a Vectran fabric displays an erosion yield of 1.08×10^{-25} cm^3.atom^{-1}. This order of magnitude difference was attributed in [45] to the presence of of an oil-based T150 weaving finish, absent in the non-woven yarns. Moreover, other factors may play an important role as well. Variability in erosion yields during different MISSE missions has been related to the variation in solar exposure. AO has a synergetic effect with UVs, which can cause the photoaging of polymers [49].
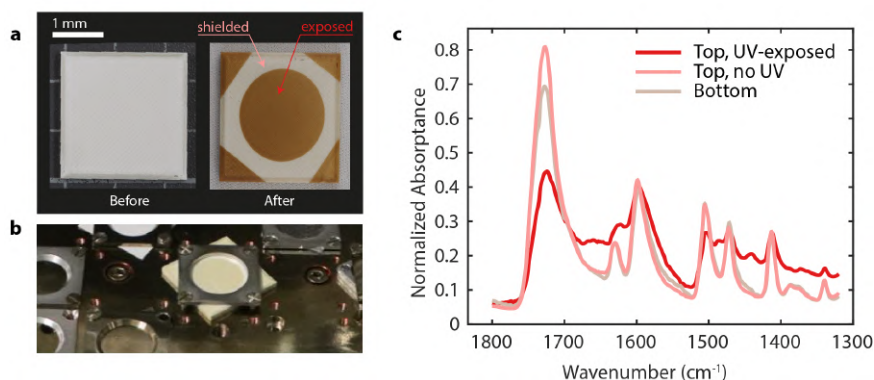
Figure 5.4 – **Exposure of 3D-printed LCP to VUV/UV irradiation. A.** The specimen shows significant discoloration in the exposed locations which can be compared to the ones shielded by **B.** the sample holder. **C.** Fourier-Transform Infrared Spectroscopy (FTIR) is performed to evaluate changes in the chemical nature of the surface. The top surface is evaluated at two different points (central zone exposed in red, and edge zone sheltered in pink) and compared to the center of the bottom surface (beige).

UV irradiation

Spacecraft outside of Earth's atmosphere are subjected to the full solar spectrum of the Sun. Relevant wavelengths are the Vacuum UV (VUV) and Near UV (NUV) spectra, between 100 nm and 400 nm. UV-irradiation is known to be extremely damaging to most polymers, as it is energetic enough to cause the breakage of organic bonds, such as $C=C, C=O, C-C$ [50].

Vectran fibres in particular contain ester groups, which are known to undergo photochemical reactions, leading to chain scission and thus decrease in mechanical properties. A ten-fold decrease in mean strength is for instance reported between no exposure and 336 hours of exposure under a Xenon lamp by Liu *et al.* [51]. Such exposure also typically shows a transition from a smooth, defect-free structure, to the occurrence of roughness, delamination, and fissures. The degree of fibre structure ordering is also decreased. The mechanism of photo-aging has been studied for Vectran in the N_2 environment [51] and involves the scission of the $C-O$ bond within the ester group ($C=O-O$).

In Figure 5.4, a 3D-printed LCP sample was exposed to VUV/UV conditions with an acceleration factor of 6.7 suns in a high vacuum environment for 432 hours between 65 °C and 100 °C. This amounts to approximately 2900 solar hours. The UV damage can be assessed visually in Figure 5.4a thanks to the shadowing effect of the sample holder shown in Figure 5.4b. Significant yellowing can be noticed with exposure. This results in a significant increase in the solar absorptance from 0.27 to 0.52. However, thermal emittance stayed constant at 0.87. Further investigation was conducted with FTIR in Figure 5.4c to understand the chemical nature of the damage. Spectra at three locations were obtained: First, two un-exposed locations at the top and the bottom of the part. Bottom refers to the side in contact with the bed during printing, and to the cold plate during exposure. Another location corresponds to the center of the top surface, with UV damage. The spec-

tra were normalized by their highest peak at a higher wavenumber. The intensity of the $1600\,cm^{-1}$ peak is almost identical between all measurement locations, which can be attributed to the aromatic ring stretching of HBA [51]. The most prominent peak for the unexposed location is associated with the carbonyl group (C=O) stretching out-of-plane at $1727\,cm^{-1}$. Its drop in intensity from 0.80 to 0.40 between the two upper locations may indicate that the ester group has been undergoing a photochemical reaction as suggested in [51]. At the UV-exposed location, a peak at $1440\,cm^{-1}$ is present, contrary to the unexposed locations. This peak can be attributed to the O−H bending of the carboxylic acid. This may indicate breakage of the polymer chains and a higher number of terminations of the chains or radicals. These elements indicate that chain scission also occurs in photo-aged 3DP-LCP, like many aromatic copolyesters [15].

In essence, while the chemical consequences of photoaging between 3DP-LCP and MS-LCP for UV resistance are similar, the difference lies more in their respective scale of use: the diameter of Vectran fibres is approximately $20\,\mu m$ [15]. In contrast, a 3D-printed functional piece displays a layer height of $100\,\mu m$ and is composed of dozens to hundreds of layers, leading to a typical size in the order of centimeters. Approximately 95 % of incident radiation below 250 nm is absorbed within a depth of $0.3\,\mu m$ for most polymers [52]. Therefore, the bulk of the 3D-printed components is not exposed, as shown in the cross-section of the exposed sample in Figure SI 5.1. Furthermore, in light of the low penetration depth of the UV photons, coatings are also effective in shielding the polymer. For example, titanium dioxide coatings have been studied specifically to reduce superficial UV damage in Vectran fibres [53, 54].

Both UV and AO are related to superficial damage. However, other types of radiation can penetrate much deeper into materials because of their higher energy, such as protons, electrons, heavier ions, and energetic photons such as X-rays and gamma rays [34]. These fall under the category of ionizing radiation, as they can ionize atoms as they move through matter. Degradation caused by radiations in polymers is based on the same mechanisms that those occurring during UV exposure, linked to either chain scission or cross-linking depending on the type of polymer [55].

Beta irradiation

Several types of charged particle radiations occur in space: galactic cosmic rays, solar proton events, and trapped particles in radiation belts. In LEO below the radiation belts, damage from particle radiations may be overshadowed by degradation caused by UV and AO for the duration of a mission. Particle radiation damage becomes important to consider in GEO and deep space mission environments. Solar Particle Events strong enough to endanger astronaut health are rare, on the occurrence of one per decade [56]. Nevertheless, long transit times involved with deep-space missions call for a better understanding of these phenomena on materials. Furthermore, the solar wind can penetrate the Martian atmosphere, giving rise to dose rates of low-energy protons and electrons similar to those encountered inside the ISS [57]. Depending on mission type, cumulative doses on optical elements have been estimated to range between 1 krad and 500 krad when non-directly exposed to the space environment, and 1 Mrad to 180 Mrad, respectively for LEO and GEO, when exposed [58].
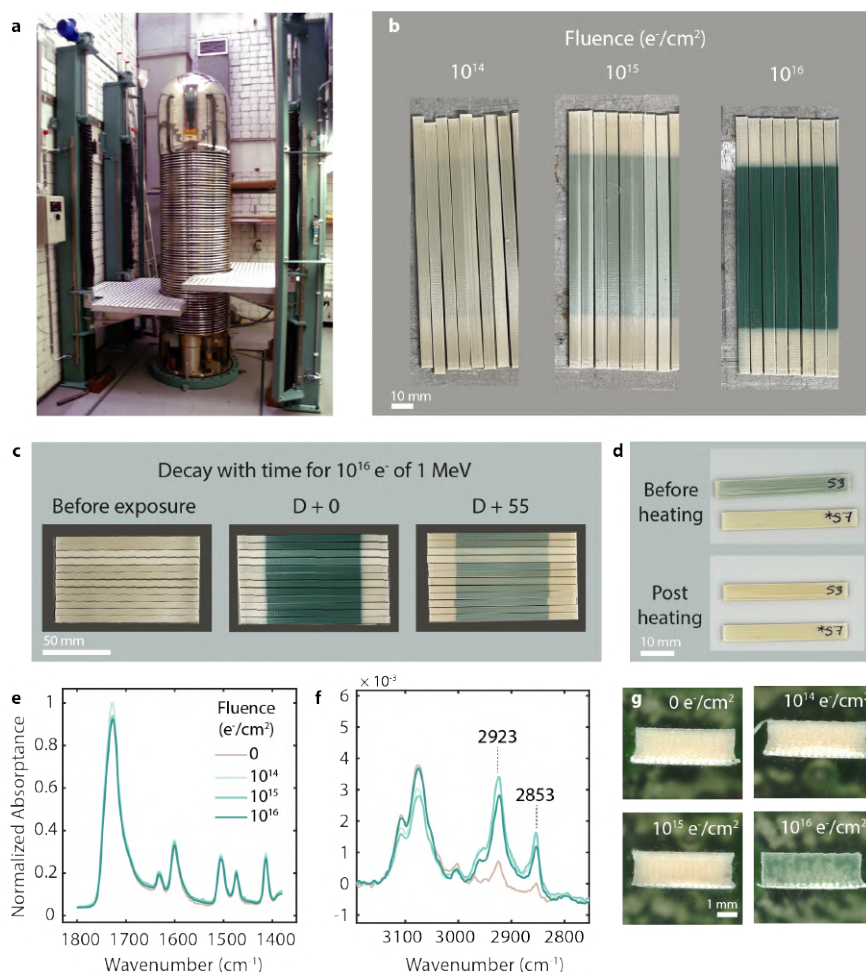
Figure 5.5 – **Exposure of 3DP-LCP to beta irradiation. A.** A Van der Graaf accelerator is used to send 1 MeV electrons onto 3D-printed specimens. **B.** Three different fluences are applied (10^{14} e^-.cm^{-2}, 10^{15} e^-.cm^{-2} and 10^{16} e^-.cm^{-2}), resulting in an important change in coloration from almost none to a vibrant green. **C.** This color change can be attributed to trapped electrons inside the polymer matrix (color centers). The specimen coloration fades away with time, and and stabilizes between 20 to 55 days. **D.** The non-permanent nature of the color center is evidenced by annealing samples for 1 hour under 200 °C. While the pristine specimen (bottom) does not display any visible color change, the specimen with the highest fluence has lost its coloration. **E.** FTIR spectra do not show any significant difference between pristine samples and the three irradiation doses at low frequencies. **F.** However, a difference is noticed at around 2923 cm^{-1} and 2853 cm^{-1}. These absorption peaks are typically attributed to the stretching of the C-H bonds. **G.** Micrographs of cross-sections indicate that the color centers are present uniformly throughout the depth of the highest-dose sample. In contrast, color centers cannot be seen for the lower fluences six months after irradiation.

The penetration depth of a particle increases with its energy [59]. To maximize possible damage within the bulk of the material, LCP samples are irradiated with high-energy electrons (1 MeV) in a Van de Graaf accelerator shown in Figure 5.5a. Even though the synergistic effect of different radiation types (protons, heavy ions, electrons) cannot be reproduced, cumulative doses are chosen to compare to those of LEO and GEO missions. Three different doses are selected: 10^{14} e^-.cm^{-2}, 10^{15} e^-.cm^{-2} and 10^{16} e^-.cm^{-2}. This is equivalent to accumulated doses of 2.92 Mrad, 29.2 Mrad and 291 Mrad, assuming linearity as detailed in Table SI 5.1. Three different batches of tensile samples are exposed corresponding to these different doses. Figure 5.5b shows photographs obtained directly after exposure. Sample color can be compared between sample extremities, which are unexposed thanks to lead shields, and center. A change to dark green can be noticed, with intensity increasing with the fluence. The origin of the color change is attributed to so-called color centers, first observed in single crystals in the late 19th century [60]. For polymers, the work of Wallace and Clough *et al.* [61, 62] have led to the classification of radiation-induced color centers between two types: annealable and permanent. Anneal-able color centers have been associated with free radicals trapped within rigid polymer matrices, such as cyclohexadienyl or benzyl [62]. The annihilation of free radicals happens via diffusion of O_2 (oxygen quenching), or the combination of one color center with another (self-quenching). The process is typically accelerated by heating above the glass transition, which facilitates molecular motion [63].

Color centers caused by irradiations have already been reported for many optical polymers [61, 64], polycarbonate [65], and polystyrene [66], which tend to turn from transparent to shades of yellow or dark brown with gamma irradiations. Some epoxy glasses were also reported to display a greenish color after electron irradiation [67, 68]. However, to our knowledge this is the first time that a liquid crystal polymer, or a 3D-printed polymer, is reported to display color centers.

The intensity of the color with the largest fluence fades away rapidly before stabilizing after 20 days, as shown in Figure SI 5.2. Furthermore, the hue completely disappears with exposure to 200 °C for 1 h, as shown in Figure 5.5d. These elements suggest that the color centers created by the electron beam are of the annealing kind. A relationship between the increasing proportion of annealable centers and lower permeability has been previously noted [63], which is in line with the low gas permeability of the LCP studied here [27]. The temporal and reversible nature of this color change indicates that the polymer network has not been dramatically changed by radiation. This is also supported by the FTIR spectra of pristine samples compared to radiated specimens of 3 different doses in Figure 5.5e. In contrast to the UV-exposed specimen in Figure 5.4c, the spectra are rather similar. A difference can however be noted between the pristine sample and irradiated ones in Figure 5.5f, where two absorption peaks at 2923 cm^{-1} and 2853 cm^{-1} are noted. These absorption peaks are typically attributed to the C — H bonds stretching [69]. In the work of Hou *et al.* [68], an epoxy was exposed to 170 keV electrons at the same fluence range as this work. A similar green coloration was observed after irradiation. This was associated with a decrease in the 2923 cm^{-1} peak with increasing fluence. In this case, the diamino- diphenylmethane (DDM) structure present in this epoxy, contained a methylene group linking two phenyl groups, which was shown to transform into
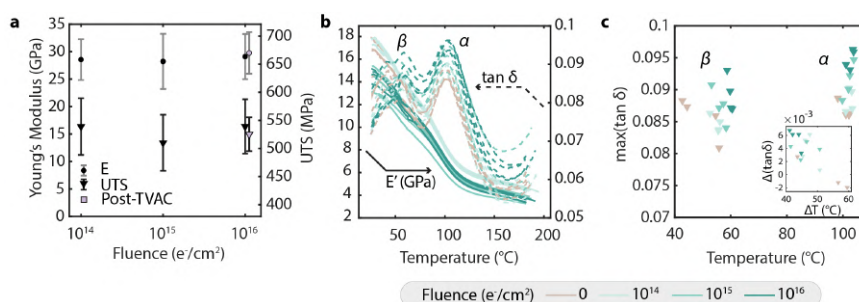
Figure 5.6 – **Impact of electron irradiation on quasi-static and dynamic mechanical properties. A.** Young's modulus and Ultimate Tensile Strength (UTS) of exposed samples do not show a significant difference with increasing fluence, even after Thermal Vacuum Cycling (TVAC). Error bars represent standard deviation. **B.** Three-point bending Dynamic Mechanical Analysis at 10 Hz and 0.1 % strain indicates a gradual softening in the storage modulus with increased irradiation dose. **C.** This softening is further noticed in the evolution of the damping factor $\tan\delta$. The first relaxation increases in magnitude and temperature with increasing dose, while the second relaxation only increases in magnitude. The insert indicates the difference in amplitude and temperature between the α- and β-peaks.

a quinone-type radical upon irradiation. It is hypothesized that a similar mechanism should occur within this polymer, with further study needed to identify its precise origin.

Unlike previous exposure types, the relatively high energy of the irradiated electrons was chosen to enable the 2 mm-thick specimens to be affected throughout their depth. The experimental relative dose versus penetration depth in water of 1 MeV with the Van der Graaf accelerator used in this study is shown in Figure SI 5.3. The dose is at its maximum (147 % of surface dose) at a depth of 1.8 mm. While the media is different, the order of magnitude of penetration in the polymer is similar. Cross-sections of samples with the three increasing fluences are shown in Figure 5.5g, compared to a non-exposed specimen, six months after exposure. For samples with fluences of 10^{14} e^-.cm^{-2} and 10^{15} e^-.cm^{-2}, no visible difference to the pristine sample can be noticed. In contrast, the specimen with 10^{16} e^-.cm^{-2} fluence is still marked after six months with a green shade throughout its depth. The uniform presence of color centers indicates that the electrons have penetrated the bulk of the polymer. Any alteration to the polymeric network should therefore have consequences on the mechanical properties of these specimens, which are discussed next.

5.2.2. Mechanical properties of exposed materials
Influence of radiation and thermal cycling on mechanical properties

Dawes *et al.* [55] report that the dominant effect of high-energy irradiation on polyesters is chain scission, although both chain scission and cross-linking can occur. Since the LCP studied here is of the class polyester-arylate, one should investigate which of the two occurs. The important change in appearance and the indication of methylene group appearing with irradiation in FTIR spectroscopy indicate that some damage may be expected at these doses.

To study the impact of electron irradiation on mechanical properties, two types of specimen are therefore studied, respectively for tensile test under quasi-static load and flexural bending under dynamic loading using Dynamic Mechanical Analysis (DMA). In both cases, the direction of printing (0°) is aligned with the longitudinal dimension. Some of the specimens with the largest irradiation dose are also subjected to Thermal Vacuum Cycling (TVAC) (thermal vacuum cycling for 25 cycles between $-100\,°C$ and $100\,°C$), and their properties are compared to non-cycled counterparts. Indeed, a synergistic effect of thermal cycling and irradiation occurs in the space environment [70]. When irradiated and un-irradiated composites were thermally cycled between $-157\,°C$ and $121\,°C$, higher microcrack density and mechanical property change were found for irradiated composites.

The Young's modulus and Ultimate Tensile Strength (UTS) are plotted in Figure 5.6a for tensile specimens exposed to different conditions. Several observations can be made: first, despite the strong difference in coloration and differences noticed in FTIR in Figure 5.5f, the three different fluences, $10^{14}\,e^-.cm^{-2}$, $10^{15}\,e^-.cm^{-2}$ and $10^{16}\,e^-.cm^{-2}$, do not show any difference in stiffness or UTS. Second, the impact of TVAC on the irradiated sample cannot be seen. The samples exposed with the highest dose, which belong to the same printing batch, behave the same whether they have been exposed to 25 thermal cycles in vacuum or not. Furthermore, the samples that are tested as closest to exposure to the space environment (TVAC'd and radiated with the highest dose estimated at 292 Mrad) still show an average Young's modulus of $(29.8 \pm 3.8)\,GPa$ and $(525.0 \pm 30.1)\,MPa$ of UTS. As shown in Figure SI 5.5, the samples fail in a catastrophic fashion typical of composites with strong anisotropy. The fibres revealed from the inside of the fractured sample also show a characteristic green color due to penetration of the β-radiations.

Dynamic Mechanical Analysis allows a finer description of the sample behavior with temperature and usually indicates molecular changes in the material. Figure 5.6b shows the effect of temperature on storage modulus and damping factor $\tan\delta$ for the three irradiation doses. Two relaxations are noticed, as previously reported in [29, 71, 72]. The lowest relaxation, termed β, taking place at approximately $60\,°C$, corresponds to the motion of the HNA moiety. The other relaxation, named α, is associated with cooperative motions of both HNA and HBA, akin to a glass transition, taking place close to $100\,°C$. Typically before any exposure, the β-relaxation is more intense than the α-relaxation. This is reported to change after 5 hours of annealing [29]. In our case, the α-relaxation is higher even for the pristine sample. One should however note that what we considered "pristine" has already been processed twice: first into a filament and second to be 3D-printed.

Across the temperature range, two distinct groups are noticed. The storage modulus of pristine and $10^{14}\,e^-.cm^{-2}$ specimens is higher than that of the specimen with higher doses ($10^{15}\,e^-.cm^{-2}$ and $10^{16}\,e^-.cm^{-2}$). This is also noticed in Figure 5.6c, where the amplitudes of the relaxation peaks are plotted against the temperature at which they occur. The insert shows the corresponding difference in amplitude and temperature between α- and β-peaks. Both low-irradiation and the pristine specimens display similar magnitude for their α-and β-peaks. For the most irradiated specimen, the α-peak has a higher

magnitude than the β-peak (positive value). Interestingly, the temperature of the β-peak increases with fluence, but the values for higher fluence are closer to those of literature ($\approx 60\,^\circ$C). The fact that storage modulus is lower throughout the range for the specimen irradiated with $10^{15}\,e^-.\text{cm}^{-2}$ and $10^{16}\,e^-.\text{cm}^{-2}$, supports the hypothesis of degradation of the samples with high exposure rate, and possible chain modification, as suggested in Figure 5.5f. However, the plausible degradation at this high dose does not enable us to notice statistically significant changes in unidirectional tensile performance in quasi-static testing at room temperature.

Influence of printing temperature

In the space environment, temperatures can vary rapidly from either extreme, for instance $-160\,^\circ$C in the Earth's shadow and $120\,^\circ$C in direct sunlight in low earth orbit [73]. Extremes can even coexist within the same exposed piece. This thermal cycling present throughout the mission life can be an important contributor to material damage. Thermal expansion can cause critical thermal stresses leading to thermal fatigue [74].

In the case of LCP, the Coefficient of Thermal Expansion (CTE) depends on processing conditions and the state of anisotropy of the material. The melt-spun LCP displays an axial CTE of $-5.78\,\mu\text{m/(m.K)}$ [75]. This can be explained by the fact that when the stiff chain vibrates as temperature rises, its projection becomes shorter along the longitudinal axis [76]. The CTE of 3D-printed LCP in the X-direction is also slightly negative ($-2.4\,\mu\text{m/(m.K)}$), as shown in Figure SI 5.4. The anisotropy of the 3D-printed object makes the value differ from injection-molded or melt-spun LCP, especially in the Z-direction, with a value of $198\,\mu\text{m.m}^{-1}.\text{K}^{-1}$. The particularly high anisotropy of CTE has been observed before in 3D-printed carbon-fibre polycarbonate, for which a CTE of $210\,\mu\text{m/(m.K)}$ was reported [77]. Graphite is another example of a layered material where the layered direction is much weaker than the planar one [78, 79]. Such a discrepancy compared to the X-axis is linked to the fact that the chains tend to vibrate along the direction where interchain interactions are weaker [76].

Since high discrepancies in expansion upon heating are observed depending on the printing direction, thermal cycling may also be more harmful to the polymer in the interlaminar direction. To test this hypothesis, two types of specimens were manufactured. Unidirectional samples, with the printing direction aligned with the loading direction, are shown in Figure 5.7a. Dog-bone-shaped samples with the loading direction aligned with the Z-direction are shown in Figure 5.7b. A batch was printed and tested directly while another batch was first subjected to 25 cycles of TVAC between $-100\,^\circ$C and $100\,^\circ$C, with a heating rate of $5\,^\circ$C/min.

As processing conditions are known to strongly affect the mechanical performance of LCPs [80], four different printing temperatures T_{print} were tested, from $295\,^\circ$C to $340\,^\circ$C. In Figure 5.7a, specimens tested in their axial direction show a decrease in Young's modulus with printing temperature. This trend is more apparent for pristine samples than TVAC samples. The span ranges from $35\,$GPa at $T_{print} = 295\,^\circ$C to $17\,$GPa at $T_{print} = 340\,^\circ$C for pristine samples, while it ranges from $25\,$GPa to $15\,$GPa for the same printing temperatures, exposed to TVAC. UTS is also similarly affected by printing temperature. However
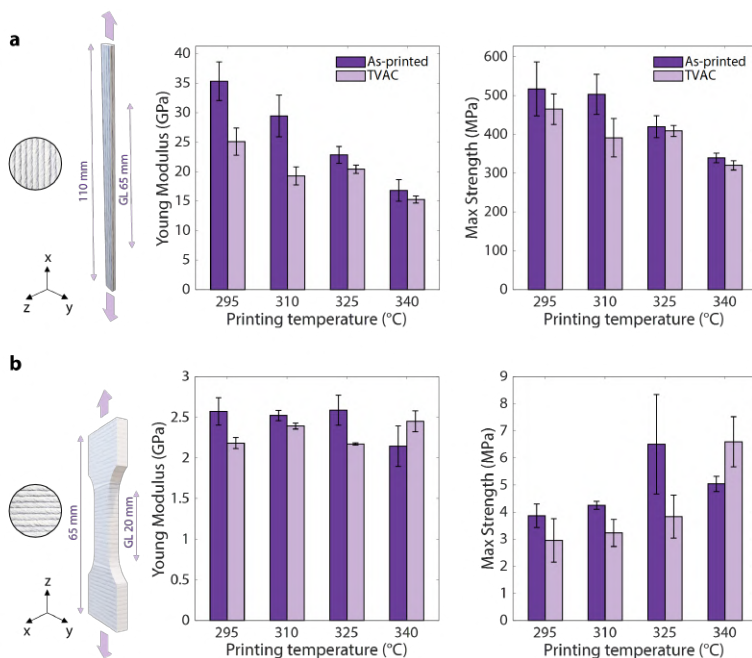
Figure 5.7 – Mechanical testing of samples tested in **A.** longitudinal direction, coinciding with the printing direction, and **B.** normal to the printing plane. Two different batches are compared, with and without exposure to TVAC, for different printing temperatures, illustrating the strong influence of processing conditions. The printing direction is represented in inserts with the unit vector Z. The specimen geometry is shown with its longitudinal dimension and gauge length (GL). Error bars represent standard deviation

here the same range (300 MPa to 500 MPa) is covered by both pristine and TVAC samples. This decrease in performance with printing temperature is in line with previous findings and was attributed to the longer time available for the nematic domains to relax into a lesser-ordered state after extrusion, before reaching solidification temperature [25].

For each printing temperature, thermal cycling appears to impact Young's modulus more than UTS. Even if UTS values are on average slightly smaller for TVAC samples than non-exposed, the scatter does not allow us to conclude on the impact of thermal cycling on strength, except at $T_{print} = 310°C$ where the discrepancy is significantly larger ((503 ± 51) MPa vs (312 ± 49) MPa). In contrast, the impact of TVAC on Young's modulus of samples is statistically significant at low printing temperatures. One should however take this result with caution, as these data were issued from two different batches. Even if care was spent on using the same g-code, same filament spool, and same printer, experience indicates that the parts produced at lower printing temperatures tend to also inevitably display higher variability in appearance and susceptibility to printing environment from one batch to another. At higher printing temperatures, in a similar manner to the ultimate tensile strength, a discrepancy between non-exposed and exposed samples is still present on average but becomes less statistically significant.

While loading in the X-direction seems to show a larger performance drop on Young's modulus than on UTS with increasing printing temperatures, this behavior changes when loading in the Z-direction. Figure 5.7b indicates that Young's modulus is not affected by printing temperature while strength improves with printing temperature, both for exposed and non-exposed samples. The improvement in strength, both for TVAC samples (from (2.9 ± 0.8) MPa to (6.6 ± 0.9) MPa) and for non-exposed samples (from (3.9 ± 0.4) MPa to (5.0 ± 0.3) MPa), is expected from past experiments with unidirectional samples tested 90° from their printing direction, still in the printing plane [24, 25]. This series of experiments, normal to the printing plane, confirms the trend. While printing at low temperatures is beneficial to axial properties as shown in Figure 5.7a, it is detrimental to bonding strength. As a result, printing temperature may be leveraged for a trade-off between strength in the axial and transverse direction at different locations in the objects.

Results shown in Figure 5.7 indicate that there may be a drop in performance when exposing samples to TVAC, which seems more important at lower printing temperatures for the longitudinally-loaded specimen. This trend seems to decrease and even reverse for the transversally loaded samples with higher temperatures, for which TVAC appears to improve bonding.

These results also indicate that the variability of processing conditions plays a key role. The UTS of LCP is about 400 MPa for the XY loading direction (in-plane, along the printed line direction) compared to about 4 MPa in the XZ direction (normal to the printing plane). In comparison, these values are 95 MPa to 13.4 MPa for PEEK [81] and 74 MPa to 32 MPa for PEI [12] due to its amorphous nature. The highly anisotropic nature of 3D-printed LCPs inevitably implies that the polymer chains, which are stiff and rigid in one direction, cannot engage with other layers in the same manner as flexible-chain polymers and result in the same level of adhesion [81]. This calls for the design of 3D-
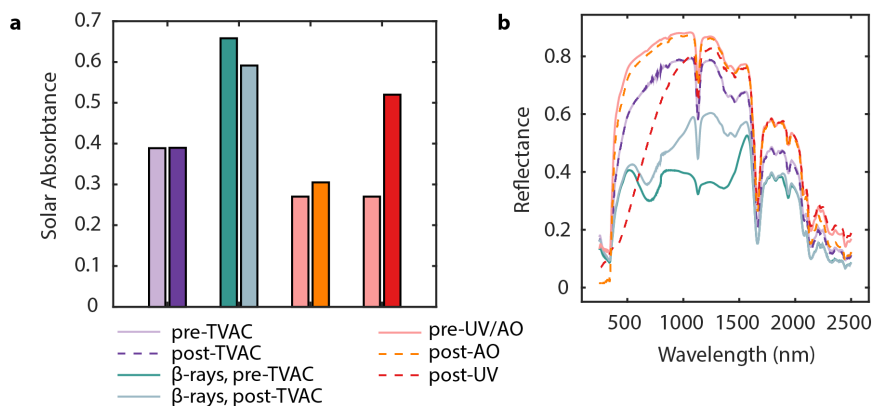
Figure 5.8 – **Change of optical properties of 3DP-LCP with different exposure types. A.** Solar absorptance before and after exposure indicates that UVs have the largest impact among all exposure types due to its darkening effect. **B.** The reflectance spectrum of selected samples also indicates that a significant difference can be observed for samples exposed to β-rays.

printed objects where loading perpendicular to the printing plane should be avoided, in a similar fashion to the adaptive growth of wood [82]

Comparison of optical properties

Among all samples printed and exposed, not all samples could be mechanically tested due to restrictions in sample size, and availability of the exposure facility. However, all exposed specimens could be tested for space-relevant optical properties, namely solar absorptance in Figure 5.8a and UV/Vis/Near-Infrared reflectance spectra in Figure 5.8b before and after exposure. Solar absorptance represents the fraction of incident solar radiation that is absorbed by the material. Tracking its evolution with exposure is valuable, as the absorbed solar radiation is often the predominant external heat input to the spacecraft [34].

Reference spectra are taken for each sample type before exposure. Indeed, the AO and UV-exposed samples are printed with a 0.05 mm layer height, while all other samples are printed at 0.1 mm layer height. Therefore their reflectance spectra even before exposure differ. As can be expected from Figure 5.5, the most significant difference in optical properties occurs with the high-dose irradiated specimen, shown with the full green line in Figure 5.8b. After TVAC, while no significant changes have been visually observed (in contrast to Figure 5.5d where color centers visibly disappear after just 1 hour of exposure at 200 °C), the full spectrum reveals a partial degree of recovery towards the pre-TVAC reference represented by the lilac-dashed line, in the near-Infrared. Overall, the beige color of the 3D-printed LCP before exposure grants the specimens a relatively low value of solar absorptance. The impact of UV is however considerable by this metric, due to darkening shown in Figure 5.4a. This change of color and the resulting increasing absorptance should be carefully assessed depending on the mission scenario. The ratio between absorptance and emissivity controls the temperature of the part's surface. An increasing ratio over time results in exposed surfaces becoming warmer than expected. If the ma-
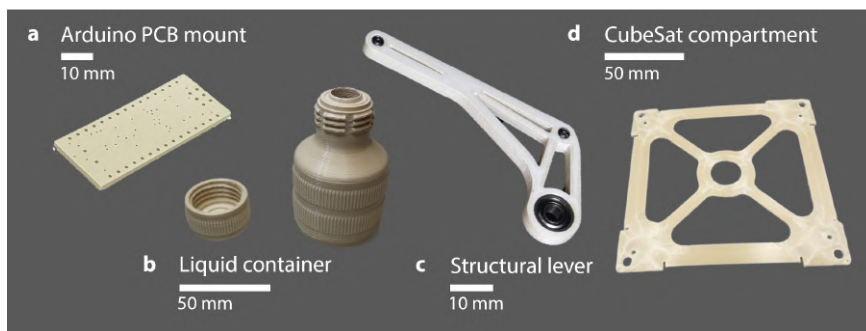
Figure 5.9 – **Possible use cases of 3D-printed LCP in space.** Different scales of application from left to right, manufactured with different 3D printers: **A.** an Arduino PCB mount, **B.** a screw-cap liquid container, **C.** a structural lever with bearings, and **D.** a compartment panel for a CubeSat.

terial is directly exposed to the space radiative environment, a common practice is to apply protective coatings with long-lasting flight heritage to maintain such properties in time when thermo-optical performance is a key driver for spacecraft operability. Several potential applications of 3D-printed LCPs are gathered in Figure 5.9. A PCB mount which requires high precision and modularity, and can also be thinned for wearable electronics, is printed with a micron-resolution NEX01 3D-printer (NematX AG). The MELT zero-gravity 3D-printer from ESA was used to fabricate a screw-cap liquid container. A structural lever is also printed by an Ultimaker 2+, with inserted bearings for use in a larger assembly. Finally, part of a CubeSat bus was printed with a Prusa MK3S+ 3D-printer, as was suggested in [9]. The diversity of printers used and geometries possible illustrates the versatility of applicability of LCP for structural use cases.

5.3. Conclusion

The space-worthiness of 3D-printed LCP was evaluated. Specimens were exposed to four different simulated space environments: AO, Vacuum UV, electron irradiation, and thermal cycling. Surface damage caused by Atomic Oxygen has been quantified and results in surface erosion comparable to other high-performance polymers such as PEEK and PEI. The effect of 6.7 solar constant worth of Vacuum UV is significant, indicating that like many other polymeric surfaces, its exposed use in space requires protection coatings to prevent surface damage, discoloration, and chain scission. Furthermore, bulk damage was targeted by choosing 1 MeV electrons, with three different doses. This has led to the observation of annealable color centers, for the first time, with 3D-printed polymers or liquid crystal polymers. The consequent coloring of the polymers with a green hue was recoverable after 1 h of exposure to 200 °C. The large change in optical appearance coincides with the increase in amplitude of peaks corresponding to $C-H$ stretching in FTIR. This indicates a degree of structural change to the polymeric backbone. DMA also indicates a slight decrease in storage modulus with increasing fluence across the temperature range studied, which is in line with the hypothesis of chain scission.

Nevertheless, the quasi-static tensile mechanical properties do not vary significantly with increasing dose.

The influence of thermal cycling across four different printing temperatures and two build orientations was also studied. Thermal cycling may cause a decrease in mechanical performance, especially at lower printing temperatures. This effect attenuates with increased printing temperature, as does the scatter in values. This can be explained by a higher sensitivity to small manufacturing errors and environmental fluctuations when the printing temperature is closer to the polymer solidification threshold. This result also illustrates the high anisotropy of LCP, with a hundred-fold difference in strength between loading conditions longitudinal and normal to the printing planes, as opposed to a seven-fold or two-fold difference for PEEK and PEI, respectively. Samples that are exposed to the maximum dose, 292 Mrad and then thermally-cycled under vacuum between $-100\,°C$ and $100\,°C$ still display an average Young's modulus of 30 GPa and 503 MPa of UTS. The maximum ultimate tensile strength of 503 MPa of LCP is also more than five times larger than PEI.

We have concluded that akin to its melt-spun version which is already used in space, 3D-printed LCP remains a suitable material to consider for in-orbit applications or out-of-Earth manufacturing, and a great alternative to engineering polymers like PEEK or PEI. In an out-of-Earth mission scenario, several features of an anisotropic and recyclable material like LCP become useful throughout the life of a part: during the design phase, its anisotropy can help minimize material use by using concurrent topology and anisotropy optimization [83, 84]. During manufacturing, its relative ease of printing with a desktop printer compared to approaches needing an enclosure and drastic thermal control such as PEEK or PEI can be associated with low energy consumption. During its use, its high mechanical performance and resistance to space exposure can maximize its service duration. Finally, the lack of additives or other materials such as fibres or compounds, facilitates its recyclability after end-of-life [24].

5.4. Materials and Methods

Specimen preparation

Feedstock material

The 3D-printing filament of LCP is supplied by NematX AG (Switzerland). Vectra A950 is the trademark for the thermotropic random copolymer HBA:HNA with a ratio 73 : 27.

3D-printer

Two 3D-printers were used for this study: a Ultimaker 2+ (Ultimaker, The Netherlands) which was modified with a direct-drive Hemera (E3D, England) printhead and a PT100 temperature sensor. A Prusa MK3S+ printer (Prusa, Czech Republic) was also modified to print up to $340\,°C$ by changing the factory printhead to higher-temperature polycarbonate parts, adding a PT100 temperature sensor, and altering the firmware correspondingly. Figure 5.9 also contains a PCB mount produced with a NEX01 high-accuracy 3D-printer (NematX AG, Switzerland) and a liquid container produced by the MELT zero-gravity 3D-printer (ESA).

Specimen geometry and printing parameters

Constant printing parameters in this study are bed temperature of 90 °C, 35 mm/s deposition speed, 0.35 mm line width, and 0% printing fan speed. The slicing was performed in Cura (Ultimaker, The Netherlands). The printing bed was coated with an adhesive (Dimafix, Spain) to maintain good adhesion. A brass nozzle with a diameter of 0.4 mm (E3D, England), was also used.

Specimen that were prepared for outgassing, AO and for UV exposure in Figure 5.2, 5.3, and 5.4 were printed at a temperature of 295 °C on the Ultimaker 2+, with a layer height of 50 μm. The sample geometries (25.4 mm × 25.4 mm × 2 mm rectangle for outgassing and UV, and cylinder of 20 mm diameter and 2 mm thickness for AO, corresponding to available sample holders) were printed with a rectilinear 100% infill, a stacking sequence of ±45°, 3 perimeter walls and a printing temperature of 295 °C.

All the specimen prepared for mechanical testing in Figure 5.5, 5.6, and 5.7 were printed on the Prusa MK3S+ printer at a printing temperature of 295 °C unless otherwise stated, with a layer height of 100 μm. For in-plane testing in Figures 6a and 7a (printing direction aligned with loading direction), specimen dimensions of 110 mm × 5 mm × 2 mm were used. Slicing parameters chosen were 100% rectilinear (unidirectional) infill without perimeter. GFRP tabs were used to ensure a gauge length of 65 mm. These tabs were beveled at 45° to introduce the load gradually to the test section according to ISO 527-5 [85]. The LCP specimen were sanded and cleaned at the tabbing zone, and then glued to the GFRP tabs with a strong adhesive (DP460, 3M). A minimum of five specimen were printed per batch.

The dogbone samples, illustrated in Figure 7b, is 20 mm wide, and 65 mm tall, with a constant gauge length of dimensions 20 mm × 10 mm × 4 mm according to ISO 527-2 [86]. A concentric 100% infill was used to print the specimen. Specimen were also sanded lightly on both faces before applying the speckle pattern for DIC in order to smoothen the layered effect caused by the additive manufacturing process, and reduce potential stress concentrations. Four specimen were printed per batch.

Exposure to space environment

Outgassing

Outgassing was performed with the μVCM vacuum chamber in ESTEC according to ECSS-Q-ST-70-02C [87]. Samples were conditioned for 24 hours at (22 ± 3) °C and (55 ± 10) %RH. During the test for 24 h, the sample was subjected to a temperature of 125 °C. The condensable material was collected by a collector plate, kept at 25 °C, while the test vacuum pressure was kept below 10^{-5} mbar. Post-test conditioning of the sample was 24 hours at (22 ± 3) °C and (55 ± 10) %RH.

A bake-out step was performed before the Residual Gas Analysis (RGA) study at 150 °C for 24 hours. The RGA was performed both for baked-out and pristine samples.

Atomic Oxygen

Atomic Oxygen exposure was performed in the LEOX facility of ESTEC [88], where a pulsed CO_2 laser dissociates molecular O_2. The location of the sample holder led to a flux of 6.96×10^{15} atoms.cm^{-2}.s^{-1}, with a typical atomic oxygen energy of 5.5 eV. The mass of the sample before (M_{BOT}) and after the test (M_{EOT}) is measured to calculate the erosion yield E via the relationship

$$E = \frac{M_{BOT} - M_{EOT}}{A_s \rho_s F},$$

where A_s is the exposure area, ρ_s is the sample density and F is the total atomic oxygen fluence, equal to 1.98×10^{21} atoms.cm^{-2} in this experiment.

UV irradiation

Vacuum-UV irradiation was carried out in the Cross I facility of ESTEC [89]. The UV housing consists of high-pressure discharge UV lamps with an air fan and process water cooling. The UV source produces UV, visible, and IR radiation. The lamp unit is positioned outside the vacuum chamber. The radiation down to 200 nm is transmitted to the sample plate through the fused silica window. The lamps are powered by stabilized power supplies, which can be operated at a variable wattage from 270 W to 600 W. The sample plate is radiated under an angle of approximately 45°. UV intensity is measured with a calibrated UV detector, inside the facility before and after the test. It is then compared to the solar spectrum and averaged to obtain an acceleration factor, expressed in solar constants. The value of 6.7 solar constant was obtained.

Sample temperature was maintained between 65 °C and 100 °C. The pressure was kept below 1×10^{-5} mbar for a total test duration of 432 h, amounting to 2900 equivalent sun hours.

Beta Irradiation

A Van der Graaf accelerator (Radiation Institute, TU Delft) was used to accelerate electrons at 1 MV with a beam current varying between 64.4 μA and 67.5 μA. During irradiation, table temperature was monitored and did not exceed 22 °C. The specimens were flushed with nitrogen throughout the exposure time, varying from 3 minutes to 5 hours. Currents used, exposure time and dose rates obtained are specified in Table SI 5.1.

Thermal Cycling

Thermal vacuum cycling was performed in a specific chamber for 25 cycles from −100 °C to 100 °C with a vacuum level between 10^{-6} mbar and 10^{-7} mbar using a 5 K/min heating rate and 30 min dwell time according to ECSS-Q-ST-70-04C [90].

Post-exposure characterization
FTIR
Fourier-Transform Infrared Spectroscopy (FTIR) was performed with a Spectrum 100 FTIR Spectrophotometer (PerkinElmer, USA), equipped with a universal ATR sampling accessory and Diamond/ZnSe crystal. Spectra were collected over a wavenumber range from $4000\,cm^{-1}$ to $600\,cm^{-1}$, with $2\,cm^{-1}$ resolution, and were signal averaged over 8 scans.

Mechanical testing
Quasi-Static tests were performed for two kinds of unidirectional samples in tension using an universal testing machine (Zwick-Roell, Germany). The 0° samples in Figure 5.6a and Figure 5.7a were clamped with hydraulic grips to avoid slippage of the samples from the tabs. Specimen were loaded at a strain rate of $2\,mm.min^{-1}$ and force was measured by a 10 kN Zwick load-cell. Fracture occurred by catastrophic splitting as shown in Figure SI 5.5.

For the dogbone specimen in Figure 5.7b, rubber grips were used to load the specimen at a strain-rate of $0.5\,mm.min^{-1}$. Force was recorded with a 1 kN load cell. No necking was observed before failure, which happened within the gauge length, in the interface between layers.

For the two specimen types, DIC was used to measure strain. Two 9 MP cameras are used (LIMESS, Germany) with a 50 mm focal length are used to acquire images at a rate of 2 Hz. Extraction of strain values was performed with the Vic 3D-8 (Correlated Solutions, USA) software.

DMA was performed with a RSA G2 DMA bench (TA Instruments) equipped with a furnace. Samples of size 30 mm × 5 mm × 2 mm were tested under three-point bending, at a frequency of 10 Hz between 22 °C and 200 °C, with a span length of 25 mm.

CTE measurements
Coefficient of Thermal Expansion (CTE) values for different printing directions of 3D-printed LCPs were extrapolated from TMA measurements, using a TMA Q400 (TA Instruments, USA). Samples were 3D printed with a size of 50 mm × 50 mm × 5 mm, then cut for TMA into cubes of side 5 mm with a diamond saw. Specimens were heated up from 40 °C to 240 °C, with a heat rate of 2 °C/min. Each specimen underwent 3 heating cycles, and the average of the CTEs given at each round was taken.

Optical Measurements

A Cary 5000A UV/VIS/NIR spectrophotometer (Agilent, USA) fitted with an internal integrating sphere was used to acquire the total reflectance of the samples between 2500 nm to 250 nm under ambient conditions. Reflectance measurements were corrected against a calibrated Spectralon diffuse standard. For the determination of the Solar absorptance (α), total reflectance spectra were weighted against the Sun spectrum according to ESA ECSS-Q-70-09C and ASTM E490. The uncertainty of the solar absorptance determination through this method is ± 0.03 (confidence factor = 2). Thermal emittance (ϵ) was measured using a TESA 2000B portable reflectometer/emissometer (AZ Technology, USA). The IR emittance was obtained by integrating over the spectral range from $3\,\mu m$ to $30\,\mu m$ and weighting it with the spectrum of a 300 K blackbody. The uncertainty for the IR emittance measured with the portable equipment is ± 0.05 (confidence factor = 2).

5.5. Data availability

The data in this work is available under the repository: https://doi.org/10.4121/46723f7d-274a-4331-879b-5dacc28b07ce.
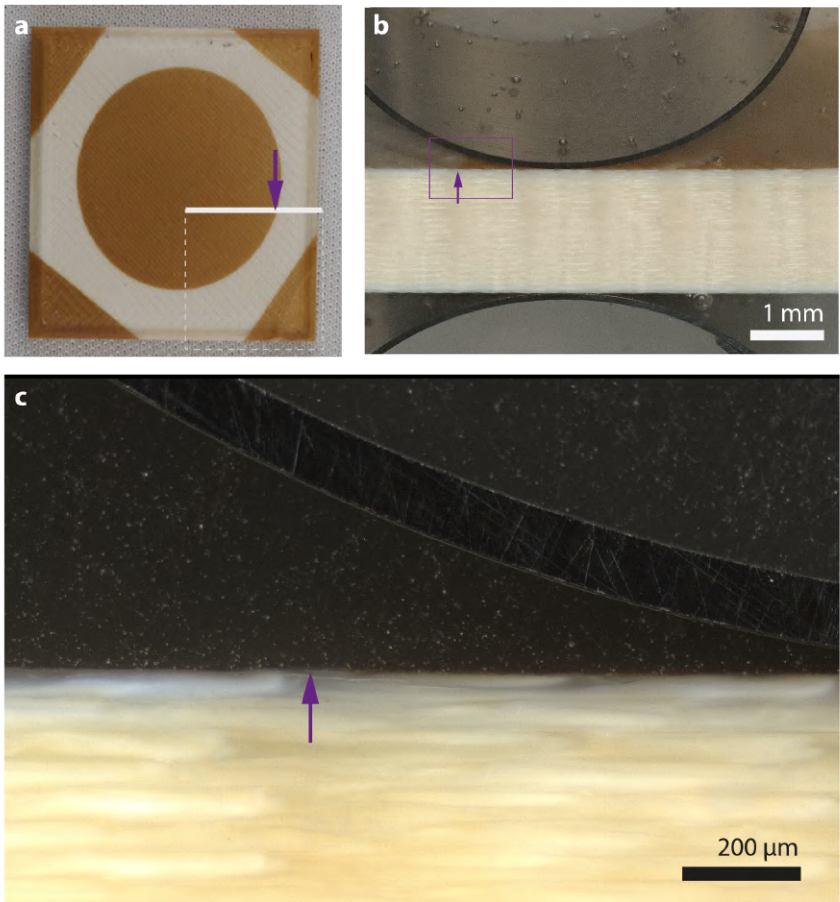
5.6. Supplementary information

Figure SI 5.1 – Penetration depth of UVs into the 3DP-LCP sample. **A.** Cut section with purple arrow indicating boundary between exposed and non-exposed area. **B.** Photograph of the same boundary, which can be located in the depth of the sample thanks to the transparent resin. **C.** This boundary on the surface is not visible in the cross-section under optical microscopy, indicating that UVs do not damage the bulk of the 3D-printed specimen, as expected.
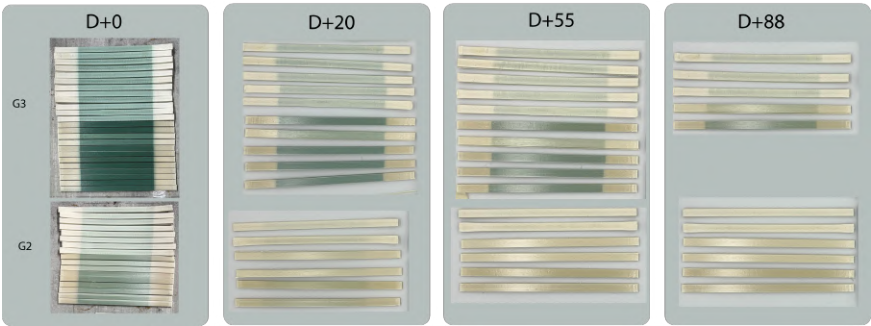
Figure SI 5.2 – Decay of the visible component of color centers at different time stamps, in days.
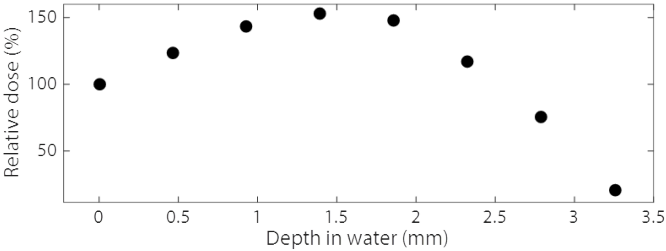

Figure SI 5.3 – Experimental calibration of the Van der Graaf accelerator for penetration depth of 1 MeV electrons into water.

Current	Time	Dose rate	Dose	Dose
(µA)	(s)	$e^-/(s.cm^2)$	e^-/cm^2	Mrad
64.8	193	5.20×10^{11}	1×10^{14}	2.92
64.4	1935	5.17×10^{11}	1×10^{15}	29.2
67.5	18461	5.42×10^{11}	1×10^{16}	292

Table SI 5.1 – Irradiation parameters and dose calculations based on current intensity on the Van der Graaf Accelerator.
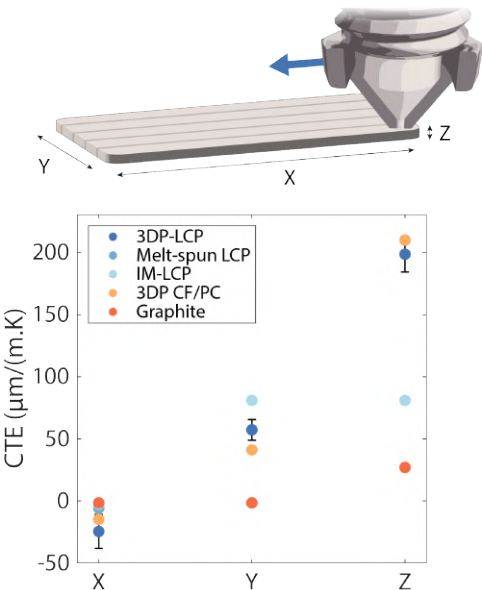
Figure SI 5.4 – Coefficient of Thermal Expansion for different 3D-printed and non-3D-printed anisotropic polymers depending on measurement direction. References: Melt-spun LCP [75], Injection-moulded LCP [91], 3D-printed carbon fibre-reinforced polycarbonate [77], graphite [78]
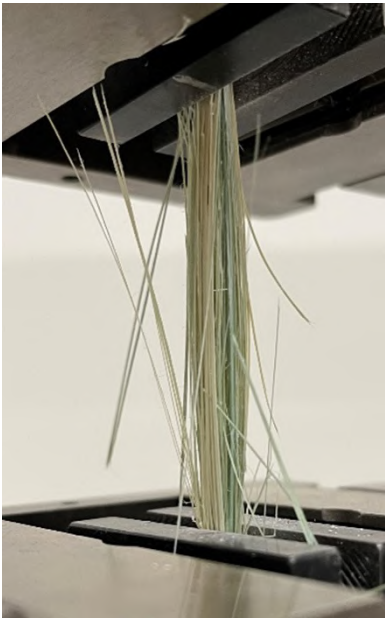

Figure SI 5.5 – Irradiated tensile specimen post-fracture (maximum fluence). Green coloration is visible on the inner fibres now exposed after failure.

References

1. European Space Agency. *Help ESA pave the way for a space circular economy* https://www.esa.int/Enabling_Support/Preparing_for_the_Future/Discovery_and_Preparation/Help_ESA_pave_the_way_for_a_space_circular_economy (2024).

2. Denis, G. *et al.* From new space to big space: How commercial space dream is becoming a reality. *Acta Astronautica* **166,** 431–443. ISSN: 00945765 (2020).

3. Kulu, E. *Nanosatellite Launch Forecasts - Track Record and Latest Prediction* in *36th Annual Small Satellite Conference* (2022).

4. El-Shawa, S., Cattani, B. M., Innocenti, L. & Delaval, J. From Cradle to Grave: ESA Clean Space's Approach to Space Sustainability. *72nd International Astronautical Congress,* 1–12 (2021).

5. Makaya, A. *et al.* Towards out of earth manufacturing: overview of the ESA materials and processes activities on manufacturing in space. *CEAS Space Journal* **15,** 69–75. ISSN: 18682510 (2023).

6. Daurskikh, A. *et al. Influence of spatial orientation on properties of 3D printed PEEK parts and their design adaptation* in *Proceedings of the 69th International Astronautical Congress, Bremen, Germany* (2018), 1–5.

7. Sertoglu, K. *ESA consortium develops high-temperature FFF 3D printer for the ISS* https://3dprintingindustry.com/news/esa-consortium-develops-high-temperature-fff-3d-printer-for-the-iss-187388/ (2024).

8. Ortega Varela de Seijas, M. *et al.* Closing the loop in space 3D printing: Effect of vacuum, recycling, and UV aging on high performance thermoplastics produced via filament extrusion additive manufacturing. *Acta Astronautica* **219,** 164–176. ISSN: 00945765 (2024).

9. Slejko, E. A., Gregorio, A. & Lughi, V. Material selection for a CubeSat structural bus complying with debris mitigation. *Advances in Space Research* **67,** 1468–1476. ISSN: 0273-1177 (2021).

10. Gonçalves, J. *et al.* Electrically conductive polyetheretherketone nanocomposite filaments: From production to fused deposition modeling. *Polymers* **10,** 1–20. ISSN: 20734360 (2018).

11. Lafont, U. *et al.* 3D printing of multifunctional polymer for space application. *9th European Conference for Aeronautics and Space Sciences (EUCASS)* (2022).

12. Zhang, Y. *et al.* Additive manufacturing of ULTEM 9085: Weak interface-enriched multi-toughening mechanisms and fracture resistance optimization. *Engineering Fracture Mechanics* **297,** 109885. ISSN: 00137944 (2024).

13. Yilmaz, M., Yilmaz, N. F. & Kalkan, M. F. Rheology, Crystallinity, and Mechanical Investigation of Interlayer Adhesion Strength by Thermal Annealing of Polyetherimide (PEI/ULTEM 1010) Parts Produced by 3D Printing. *Journal of Materials Engineering and Performance* **31,** 9900–9909. ISSN: 15441024 (2022).

14. Campbell, B. *et al. On-Orbit Polymer Degradation Results from MakerSat-1 : First Satellite Designed to be Additively Manufactured in Space* in (2020).

15. Sloan, F. in *Structure and Properties of High-Performance Fibers* 113–140 (Elsevier Ltd, 2017). ISBN: 9780081005514.

16. Guerriero, G., Alderliesten, R., Dingemans, T. & Benedictus, R. Thermotropic liquid crystalline polymers as protective coatings for aerospace. *Progress in Organic Coatings* **70,** 245–251. ISSN: 03009440 (Apr. 2011).

17. Wissbrun, K. F., Kiss, G. & Cogswell, F. Flow behavior of a thermotropic liquid crystal aromatic copolyester. *Chemical Engineering Communications* **53,** 149–173 (1987).

18. Cadogan, D., Sandy, C. & Grahne, M. Development and Evaluation of the Mars Pathfinder Inflatable Airbag Landing System. *Acta Astronautica* **50,** 633–640 (2002).

19. Kenner, W. S., Jones, T. C. & Le Boffe, V. M. *Controlled Environmental Effects on Creep Test Data of Woven Fabric Webbings for Inflatable Space Modules (NASA/TM2020-220561)* tech. rep. (NASA, 2020).

20. Sierra Space. *Sierra Space Sets the Stage for Pioneering Full-Scale "Burst Test" of Expandable Space Station Module* https://www.sierraspace.com/newsroom/press-releases/sierra-space-sets-the-stage-for-pioneering-full-scale-burst-test-of-expandable-space-station-module/ (2024).

21. Mousavi, M. M. S. *et al. Spacesuits and EVA gloves evolution and future trends of extravehicular activity gloves* in *41st International Conference on Environmental Systems 2011, ICES 2011* (2011), 1–10. ISBN: 9781600869488.

22. Weiss, P. *et al.* Advanced Materials for Future Lunar Extravehicular Activity Space Suit. *Advanced Science News* **5,** 1–30 (2020).

23. Fries, M. D. *et al.* The SHERLOC Calibration Target on the Mars 2020 Perseverance Rover: Design, Operations, Outreach, and Future Human Exploration Functions. *Space Science Reviews* **218,** 1–33. ISSN: 15729672 (2022).

24. Gantenbein, S. *et al.* Three-dimensional printing of hierarchical liquid-crystal-polymer structures. *Nature* **561,** 226–230. ISSN: 0028-0836 (Sept. 2018).

25. Gantenbein, S. *et al.* Spin-Printing of Liquid Crystal Polymer into Recyclable and Strong All-Fiber Materials. *Advanced Functional Materials,* 2104574. ISSN: 1616-3028 (Sept. 2021).

26. Houriet, C. *et al.* 3D Printing of Flow-Inspired Anisotropic Patterns with Liquid Crystalline Polymers. *Advanced Materials* **2307444,** 1–12. ISSN: 15214095 (2023).

27. Seshadri, B., Hischier, I., Masania, K. & Schlueter, A. 3D Printed Liquid Crystal Polymer Thermosiphon for Heat Transfer under Vacuum. *Advanced Materials Technologies* **2300403,** 1–10. ISSN: 2365709X (2023).

28. Dunlop, J. W., Weinkamer, R. & Fratzl, P. Artful interfaces within biological materials. *Materials Today* **14,** 70–78. ISSN: 13697021 (2011).

5

29. Romo-Uribe, A., Reyes-Mayer, A., Calixto Rodriguez, M. & Sarmiento-Bustos, E. On the influence of thermal annealing on molecular relaxations and structure in thermotropic liquid crystalline polymer. *Polymer* **240,** 124506. ISSN: 00323861 (2022).

30. Turek, D. E. & Simon, G. P. Processing/property relationships of a thermotropic copolyester: 2. Correlations between tensile properties and orientation. *Polymer* **34,** 2763–2768. ISSN: 00323861 (1993).

31. Wiberg, G., Hillborg, H. & Gedde, U. W. Assessment of development and relaxation of orientation in a sheared thermotropic liquid crystalline copolyester. *Polymer Engineering and Science* **38,** 1278–1285. ISSN: 00323888 (1998).

32. Allum, J., Moetazedian, A., Gleadall, A. & Silberschmidt, V. V. Discussion on the microscale geometry as the dominant factor for strength anisotropy in material extrusion additive manufacturing. *Additive Manufacturing* **48.** ISSN: 22148604 (2021).

33. Das, A., Gilmer, E. L., Biria, S. & Bortner, M. J. Importance of Polymer Rheology on Material Extrusion Additive Manufacturing: Correlating Process Physics to Print Properties. *Applied Polymer Materials* **3,** 1218–1249 (2021).

34. De Groh, K. K., Banks, B. A., Miller, S. K. R. & Dever, J. A. in *Handbook of Environmental Degradationof Materials* Elsevier, 601–645 (Elsevier Inc., 2018). ISBN: 9780323524728.

35. Suliga, A. *et al.* Euro Material Ageing – Ground-based testing and selection of the ESA flight candidate materials. *IOP Conference Series: Materials Science and Engineering* **1287,** 012026. ISSN: 1757-8981 (2023).

36. Suliga, A., Ergincan, O. & Rampini, R. *A new dynamic outgassing procedure to predict reemission and deposition values of contaminants* in *Systems Contamination: Prediction, Control, and Performance* (SPIE, 2020), 50–60. ISBN: 9781510637825.

37. Yang, J. & de Groh, K. Materials Issues in the Space Environment Introduction and Background. *MRS bulletin* **35,** 12–20 (2010).

38. NASA (Goddard Space Flight Center). *Outgassing Properties of Vectran - Data Base* https://outgassing.nasa.gov/outgassing-data-table?field_material_value_op=contains&field_material_value=Vectran&field_application_value_op=contains&field_application_value=&field_data_ref_value_op=contains&field_data_ref_value=&field_cvcm_value_op=%3C%3D& (2024).

39. *ECSS-Q-ST-70-02C: Thermal vacuum outgassing test for the screening of space materials* tech. rep. (European Cooperation For Space Standardization, 2008).

40. Stidham, C. R., Stueber, T. J., Banks, B. A., Dever, J. A. & Rutledge, S. K. *Low Earth orbital atomic oxygen environmental simulation facility for space materials evaluation (NASA TM 106128)* tech. rep. 1 (1993), 649–663.

41. Bitetti, G., Mileti, S., Marchetti, M. & Miccichè, P. *Space environment effects on flexible materials in LEO orbits* in *Proceedings - 10th ISMSE* **2006** (2006), 19–23. ISBN: 9290929278.

42. De Groh, K. K. & Banks, B. A. *Atomic Oxygen Erosion Data From the MISSE 2-8 Missions* tech. rep. May (NASA, 2019).

43. Yi, G. T. *et al. Overview of the MISSE 7 polymers and zenith polymers experiments after 1.5 years of space exposure* in *International Symposium on Materials in the Space Environment (ISMSE-12)* (2013).

44. Banks, B. A., De Groh, K. K. & Miller, S. K. *Low earth orbital atomic oxygen interactions with spacecraft materials* in *MRS Online Proceedings Library* (2004), 426–437.

45. Finckenor, M. M. & Marshall, G. C. *Comparison of High-Performance Fiber Materials Properties in Simulated and Actual Space Environments (NASA/TM—2017–219634)* tech. rep. July (NASA, 2017), 1–48.

46. ANSYS Inc. *Ansys Granta EduPack Database* www.ansys.com/materials (2024).

47. Cool, G. R. *Atomic Oxygen Erosion Resistance of Organic Polymers for Low Earth Orbit Spacecraft* PhD thesis (University of Toronto, 1996).

48. Finckenor, M. M., Vaughn, J. A. & Watts, E. *Changes in Polymeric tether properties due to Atomic Oxygen* in *42nd AIAA Aerospace Sciences Meeting and Exhibit* (2004), 322. ISBN: 9781451184723.

49. Groh, K. K. D., Banks, B. A., Asmar, O. C. & Sechkar, E. A. *Erosion Results of the MISSE 8 Polymers Experiment After 2 Years of Space Exposure on the International Space Station (NASA/TM—2017-219445)* tech. rep. (NASA, 2017).

50. Dever, J. A. *Low earth orbital atomic oxygen and ultraviolet radiation effects on polymers (NASA-TM-103711)* tech. rep. (NASA, 1991).

51. Liu, Y. *et al.* Structural evolution and degradation mechanism of Vectran® fibers upon exposure to UV-radiation. *Polymer Degradation and Stability* **98,** 1744–1753. ISSN: 01413910 (2013).

52. Adams, M. *The degradation of polymeric spacecraft materials by far-UV radiation and atomic oxygen* PhD thesis (University of Connecticut, 1993). ISBN: 0315880678.

53. Liu, Y. *et al.* Hyperbranched polyester-stabilized nanotitania-coated vectran fibers with improved UV-Blocking performance. *Macromolecular Materials and Engineering* **300,** 64–69. ISSN: 14392054 (2015).

54. He, J., Liu, Z., Zhang, W., He, C. & Li, W. Atomic layer deposition of TiO2 nanolayer coated Vectran fabrics with enhanced UV-blocking performance and structural colors. *Surfaces and Interfaces* **42,** 103477. ISSN: 24680230 (2023).

55. Dawes, K., Glover, L. C. & Vroom, D. A. in *Physical properties of polymers handbook* 867–887 (2007).

56. Dietze, G. *et al.* ICRP publication 123: Assessment of radiation exposure of astronauts in space. *Annals of the ICRP* **42,** 1–339. ISSN: 1872969X (2013).

57. Matthiä, D. *et al.* The radiation environment on the surface of Mars - Summary of model calculations and comparison to RAD data. *Life Sciences in Space Research* **14,** 18–28. ISSN: 22145532 (2017).

5

58. Fruit, M., Berghmans, F., Ulbrich, G., Gussarov, A. & Doyle, D. *Radiation impact on the characteristics of optical glasses test results on a selected set of materials* in *Proceedings - International Conference on Space Optics* **10569** (2017), 56. ISBN: 9781510616271.

59. Nikezic, D., Beni, M. S., Krstic, D. & Yu, K. N. Characteristics of protons exiting from a polyethylene converter irradiated by neutrons with energies between 1 keV and 10 MeV. *PLoS ONE* **11.** ISSN: 19326203 (2016).

60. Seitz, F. Color centers in alkali halide crystals. *Reviews of Modern Physics* **18,** 384–408. ISSN: 00346861 (1946).

61. Clough, R. L., Gillen, K. T., Malone, G. M. & Wallace, J. S. Color formation in irradiated polymers. *Radiation Physics and Chemistry* **48,** 583–594. ISSN: 0969806X (1996).

62. Wallace, J. S., Sinclair, M. B., Gillen, K. T. & Clough, R. L. Color center annealing in γ - irradiated polystyrene, under vacuum and air atmospheres. *Radiation Physics and Chemistry* **41,** 85–100. ISSN: 0969806X (1993).

63. Harmon, J., Gaynor, J. & Taylor, A. Approaches to optimize scintillator polymers for optical radiation hardness. *Radiation Physics and Chemistry* **41,** 153–164 (1993).

64. Nouh, S. A. & Bahareth, R. A. Color changes in some irradiated polymers. *Radiation Effects and Defects in Solids* **167,** 766–773. ISSN: 10420150 (2012).

65. Peng, J., Hsu, C., Yeh, S. & Lee, S. Annihilation Kinetics of Color Center in Polycarbonate Irradiated with Gamma Ray at Elevated Temperatures. *Polymer Engineering and Science* **52,** 2391–2395 (2012).

66. Liu, C. K., Tsai, C. J., Hu, C. T. & Lee, S. Annihilation kinetics of color center in irradiated syndiotactic polystyrene at elevated temperatures. *Polymer* **46,** 5645–5655. ISSN: 00323861 (2005).

67. Fulton, M. I., Pomery, P. J., St. John, N. A. & George, G. A. Colour development and luminescence phenomena in epoxy glasses. *Polymers for Advanced Technologies* **9,** 75–83. ISSN: 10427147 (1998).

68. Hou, L., Wu, Y., Xiao, J., Guo, B. & Zong, Y. Colored effects and mechanism in DDM-cured epoxy after 170keV vacuum electron irradiation. *Nuclear Instruments and Methods in Physics Research, Section B: Beam Interactions with Materials and Atoms* **439,** 1–6. ISSN: 0168583X (2019).

69. Socrates, G. *Infrared and Raman Characteristic Group Frequencies: Tables and Charts* pp 18–- (John Wiley and Sons Inc, 2004).

70. Funk, J. G. & Sykes, G. F. *Effects of simulated space environmental parameters on six commercially available composite materials (NASA/TM-1989-2906)* tech. rep. (NASA, 1989).

71. Blundell, D. J. & Buckingham, K. A. The b-loss process in liquid crystal polyesters containing 2,6-naphthyl groups. *Polymer* **26,** 1623–1627. ISSN: 00323861 (1985).

72. Troughton, M. J., Davies, G. R. & Ward, I. M. Dynamic mechanical properties of random copolyesters of 4-hydroxybenzoic acid and 2-hydroxy 6-naphthoic acid. *Polymer* **30,** 58–62. ISSN: 00323861 (1989).

73. Williams, J.-P., Paige, D., Greenhagen, B. & Sefton-Nash, E. The global surface temperatures of the Moon as measured by the Diviner Lunar Radiometer Experiment. *Icarus* **283,** 300–325. ISSN: 0019-1035 (Feb. 2017).

74. Anvari, A. Thermomechanical Fatigue of Unidirectional Carbon Fiber/Epoxy Composite in Space. *Journal of Engineering* **2020,** 1–5. ISSN: 2314-4904 (2020).

75. Fette, R. B. & Sovinski, M. F. *Vectran Fiber Time-Dependent Behavior and Additional Static Loading Properties (NASA/TM—2004-212773)* tech. rep. (NASA, 2004).

76. Green, D. I., Orchard, G. A., Davies, G. R. & Ward, I. M. Thermal expansion of oriented liquid crystal copolyesters. *Journal of Polymer Science Part B: Polymer Physics* **28,** 2225–2231. ISSN: 10990488 (1990).

77. Colón Quintana, J. L. *et al.* Effects of Fiber Orientation on the Coefficient of Thermal Expansion of Fiber-Filled Polymer Systems in Large Format Polymer Extrusion-Based Additive Manufacturing. *Materials* **15,** 1–27. ISSN: 19961944 (2022).

78. Nelson, J. B. & Riley, D. P. The thermal expansion of graphite from 15°c. to 800°c.: Part I. Experimental. *Proceedings of the Physical Society* **57,** 477–486. ISSN: 09595309 (1945).

79. Zhao, L., Tang, J., Zhou, M. & Shen, K. A review of the coefficient of thermal expansion and thermal conductivity of graphite. *Xinxing Tan Cailiao/New Carbon Materials* **37,** 544–555. ISSN: 18725805 (2022).

80. Turek, D. E. On the tensile testing of high modulus polymers and the compliance correction. *Polymer Engineering & Science* **33,** 328–333. ISSN: 15482634 (1993).

81. Xu, Q. *et al.* Enhanced interlayer strength in 3D printed poly (ether ether ketone) parts. *Additive Manufacturing* **55.** ISSN: 22148604 (2022).

82. Weinkamer, R. & Fratzl, P. Mechanical adaptation of biological materials - The examples of bone and wood. *Materials Science and Engineering C* **31,** 1164–1173. ISSN: 09284931 (2011).

83. Schmidt, M. P., Couret, L., Gout, C. & Pedersen, C. B. Structural topology optimization with smoothly varying fiber orientations. *Structural and Multidisciplinary Optimization* **62,** 3105–3126. ISSN: 16151488 (Dec. 2020).

84. Kundu, R. D. & Zhang, X. S. Additive manufacturing of stiff and strong structures by leveraging printing-induced strength anisotropy in topology optimization. *Additive Manufacturing* **75,** 103730. ISSN: 22148604 (2023).

85. ISO. *ISO 527-5:2009 Plastics—Determination of Tensile Properties — Part 5: Test conditions for unidirectional fibre-reinforced plastic composites* tech. rep. (International Organization of Standardization, 2009).

86. ISO. *ISO 527-2:2012 Plastics—Determination of Tensile Properties — Part 2: Test conditions for moulding and extrusion plastics* tech. rep. (International Organization of Standardization, 2012).

87. ECSS. *ECSS-Q-ST-70-02C - Space product assurance, thermal vacuum outgassing test for the screening of space materials* tech. rep. (ESA-ESTEC Requirements Standards, 2008).

5

88. Tighe, A. *European Space Agency: Overview of the LEOX Test facility* https://esamultimedia.esa.int/multimedia/industry/ESA_TECQE_AO_013375.pdf (2024).

89. Heltzel, S., Semprimoschnig, C., Moser, M. & van Eesbeek, M. *Overview of ground-based environmental testing facilities in the ESTEC TEC-QMC laboratories* in *Spacecraft Structures, Materials and Mechanical Testing Conference* (2005).

90. ECSS. *ECSS-Q-ST-70-04C – Thermal testing for the evaluation of space materials, processes, mechanical parts and assemblies* tech. rep. (ESA-ESTEC Requirements Standards, 2008).

91. Campus Plastics - Celanese. *Vectra A950 LCP Datasheet* https://www.campusplastics.com/material/pdf/190204/VECTRAA950?sLg=en (2024).

5

Chapter 6

Conclusions

Despite the excellent mechanical properties of fibre-reinforced polymers, only relatively simple patterns with low curvature have been attainable with traditional manufacturing techniques. Furthermore, their level of anisotropy is Boolean: directionality is either absent in the isotropic matrix or present within the oriented fibre. This "black-or-white" landscape contrasts with the subtle shades of grey used by the majority of biological materials. For them, anisotropy can be a continuum, with smooth spatial gradients within a range of properties. To improve the mechanical performance of man-made structures while minimizing resource utilisation, the following question has been considered:

Does a manufacturing method that can control the directionality of a material and locally tune its level of anisotropy, improve structural performance?

Two sub-questions arise from it: the first one is "What manufacturing methods can be developed to obtain control of directionality and level of anisotropy?". The second one is "How can they improve structural performance?". To tackle these questions, two different approaches to manufacturing these gradients have been proposed in Chapter 3 and Chapter 4, and the resulting material properties and structural performance in specific use cases have been studied.

In Chapter 3, the high sensitivity of LCPs to flow conditions was harnessed to create gradients of properties on the fly during the printing process. By varying the width of the printed lines, a large range of Young's modulus between 3 and 30 GPa was obtained. Furthermore, a scaling law using nozzle diameter and line width as input to describe the stiffness of printed lines was established. Slith3r, an open-source toolpath placement

method was developed to construct and 3D print complex patterns with small curvature radii within a set range of line widths. This combination of material and path-planning approach can be used for any application where increasing shaping freedom or anisotropy gradients may improve performance or functionality. This was shown for the first buckling load, which increases by 40 % when the curvature constraint is relaxed, or to shelter sensitive locations from cracks.

In Chapter 4, a route to create gradients of properties via sinusoidal and helical patterns with LCP was proposed. Inspired by the tortuous wood fibres found at regions where two branches meet, 3D-printing offers the possibility to integrate localized interlocking patterns to multi-axis loaded regions of anisotropic engineering parts. The importance of a maximum angle of deviation φ, and of the scale of the pattern, were established as parameters driving the tensile and interlocking performance of the different configurations tested. Adding local waviness decreases stiffness in tension according to Classical Laminate Theory, and drastically improves toughness, due to the fibrillar nature of LCP. The potential of this method is illustrated by a simplified junction between two angles. Compared to the contour-like unidirectional patterns which delaminates between printed lines at the junction zone in four-point bending, the samples reinforced with a helix pattern are able to carry 88% more load, and can sustain a three-times larger cross-head deformation before showing failure at another location.

Two manufacturing methods that are able to locally tune stiffness properties in the longitudinal direction have thus been developed. In the first one using line width, a Young's modulus range of 3 to 30 GPa is attained, with a smooth transition in failure behaviour from ductile to brittle. In the second one, it is capped by the straight orientations parallel and perpendicular to the print plane, i.e. 2.6 and 18 GPa respectively, but additional interlocking and Mode-I toughening are provided.

To assess whether the strategies developed in previous chapters can apply to space structures, the ability of 3D-printed LCP to resist the harsh space environment has been studied in Chapter 5. Future long-duration space exploration missions will need to maximize the mechanical performance of structures with a constraint on resource utilisation. The substantial flight heritage of the LCP studied in this thesis in its woven form, as well as its potential at recyclability, make it an attractive 3D-printing candidate material for Out-of-Earth manufacturing. 3D-printed samples were subjected to four different space exposure types. High-energy electrons, which penetrate the bulk of the material, created colour-centres, causing a greener coloration with increasing irradiation dose. No difference in mechanical performance was noted at the scale of static tests, in spite of a possible degree of chain scission indicated by FTIR. Samples that were thermally-cycled and irradiated with the largest dose of electrons still retained a maximum tensile strength of 503 MPa. Higher printing temperatures, combined with thermal cycling, were also shown to decrease longitudinal tensile stiffness and strength but increase the interlayer strength, which can also constitute another way to tune levels of anisotropy depending on the load case.

Outlook

The manufacturing approaches proposed in this thesis enable to tune material properties on-the-fly with a desktop 3D-printer. To further explore this dimension of the design space and assess whether it could benefit man-made structures as it does biological materials, many possibilities arise. Three main avenues are open: finding different approaches, improving the existing ones, and exploiting them in engineering.

Exploring other approaches to manufacture anisotropy gradients

Other approaches to control anisotropy levels could utilize the shear induced by ironing. Preliminary results indicate that ironing could for instance improve the transverse strength of the material locally. This could also be combined with the sheltering patterns developed in Chapter 3 to improve further the crack resistance of the material in sensitive zones.

Improving existing approaches

To improve existing approaches, research on adhesion of LCP should be conducted, as the typical reptation mechanisms expected in flexible chain polymers can less readily happen. These studies could be combined with rheological and thermal in-situ measurements during printing. This could have two benefits: increase manufacturing reliability to build closed-loop control, and feed numerical models of the flow of nematic LCPs.

Exploration of the design space

The manufacturing approaches proposed in this thesis contrast with the way we have studied and engineered anisotropic materials for decades. Most existing frameworks are made for composites, where two materials have distinct properties. In this case the same material shows smooth gradients of properties. Metaphorically, we have introduced water into ink, and we now need to master shade.

The potential of 3D-printed LCP should therefore be leveraged by a topology- and anisotropy- optimization scheme able to take into account strong asymmetry between tension and compression, and handle mechanical property gradients. The scaling law found in Chapter 3 can be utilized to translate the desired distribution of properties into a distribution of line widths. The resulting line width and optimized angle fields could then be transformed by the path-planning algorithm Slith3r into manufacturable toolpaths.

Furthermore, the high shaping freedom enabled by Slith3r could also benefit other fields. For instance, tailored eddy currents could be created by shaping anisotropic conductive material into complex patterns. The approach could also be used to study deeper how bio-materials, such as wood, shape their anisotropy.

List of Publications

Journal Articles

Pertaining to this thesis:

- Houriet, C., Damodaran, V.,Mascolo, C., Gantenbein, S., Peeters, D., and Masania, K. (2024). "3D Printing of Flow-Inspired Anisotropic Patterns with Liquid Crystalline Polymers". Advanced Materials, 36(11), 2307444. `https://doi.org/10.1002/adma.202307444` - Chapter 3

- Houriet, C., Ulyanov, B., Pascoe, J. and Masania, K. (2024). "Wood-inspired interlocking junctions using 3D-printed liquid crystal polymers". *Under review* - Chapter 4

- Houriet, C., Claassen, E., Mascolo, C., Jöhri, H., Brieva, A., Szmolka, S., Vincent-Bonnieu, S., Suliga, A., Heeb, R., Gantenbein, S., Lafont, U., Rohr, T., and Masania, K. (2024). "Three-dimensional printing of liquid crystal polymers for space applications". Advanced Manufacturing Technologies, 2400571. `https://doi.org/10.1002/admt.202400571` - Chapter 5

Not pertaining to this thesis:

- Cinefra, M., de Miguel, A. G., Filippi, M., Houriet, C., Pagani, A., & Carrera, E. (2019). Homogenization and free-vibration analysis of elastic metamaterial plates by Carrera Unified Formulation finite elements. Mechanics of Advanced Materials and Structures, 28(5), 476–485. `https://doi.org/10.1080/15376494.2019.1578005`

- Gantenbein, S., Mascolo, C., Houriet, C., Zboray, R., Neels, A., Masania, K., & Studart, A. R. (2021). Spin-Printing of Liquid Crystal Polymer into Recyclable and Strong All-Fiber Materials. Advanced Functional Materials, 31(52), 2104574. `https://doi.org/10.1002/adfm.202104574`

Others

- **Conference presentation** - Houriet, C., Damodaran, V., Gantenbein, S., Peeters, D., and Masania, K., "3D-Printing Liquid Crystal Polymers to replicate the Anisotropic Complexity of Wood", 17th International Conference on Advances in Experimental Mechanics, 30/08-01/09/2023, Glasgow, UK.

- **Poster** - Houriet, C., Gantenbein, S., Mascolo, C., Zboray, R., Neels, A., Studart, A. R. and Masania, K., "Bioinspired spin-printing of recyclable self-reinforced composites", 07/07/2022, Delft BioDay 2022. *Best Poster award*

Contributions to results

Chapter 3

For Chapter 3, design of the experiments and conceptualization were done by Caroline Houriet, Vinay Damodaran and Kunal Masania. Silvan Gantenbein, Kunal Masania and Daniël Peeters developed the initial idea of using LCPs for variable stiffness laminates and carried the initial investigations. The experimental data in this chapter was obtained and post-processed by Caroline Houriet, apart from unidirectional parts in Figure SI 3.3 provided by Chiara Mascolo. The laminate optimization code was written by Daniel Peeters. The author built the tool-path generation algorithm with contributions from Vinay Damodaran. Vinay Damodaran also wrote an ABAQUS routine that calculated the deflection shape data in Figure SI 3.15. The original draft was written by Caroline Houriet, and reviewed by Kunal Masania who also supervised the research.

Chapter 4

In Chapter 4, conceptualization and design of experiments were done by Caroline Houriet and Kunal Masania. All the experimental data was acquired by C.H., apart from data shown in Figure 4.6 gathered by Boris Ulyanov. He designed, manufactured and tested the Compact Tension specimen for interlaminar fracture resistance for his master thesis under the supervision of C.H. and Kunal Masania. All the data was post-processed and analyzed by C.H., who also wrote the manuscript with helpful comments and review from Kunal Masania and John-Alan Pascoe. John-Alan Pascoe was involved with reviewing the manuscript and helpful discussions on interpretation of the toughness data.

Chapter 5

Chapter 5 is the outcome of the support of the European Space Agency to this PhD (Open Science Innovation Platform grant No. 4000131850). Ugo Lafont and Thomas Rohr contributed with Kunal Masania to the supervision of Caroline Houriet for this project, funding acquisition as well as design of experiments. Abel Brieva, Haimo Jöhri and Raphael Heeb contributed to collecting data for outgassing and RGA in Figure 5.2. AO and UV samples were prepared by Chiara Mascolo, Silvan Gantenbein and Raphael Heeb, as part of the Euro-Material Aging programme supervised by Sébastien Vincent-Bonnieu. AO and UV data was collected by Agnieszka Suliga, and post-processed and analyzed by C.H.. Data related to exposure to electron irradiation and thermal cycling were obtained by C.H. and Evelien Claassen as part of her master thesis, supervised by Kunal Masania and C.H.; Szilvia Szmolka, Agnieszka Suliga and C.H. obtained the spectroscopy data shown in Figure 5.8. Chiara Mascolo, Silvan Gantenbein, Ugo Lafont and C.H. printed the samples presented in Figure 5.9. All the data was post-processed and analyzed by C.H., who also wrote the manuscript with input from Kunal Masania. All co-authors cited were also involved in reviewing the manuscript.

Biographical note

Caroline Houriet was born on 17th of June 1995 in Calais, France. As she grew up, she never really knew whether she liked more science or art, and has been very admirative of how they always meet in nature. She started higher education in the French system of 'Grandes Écoles' in 2013. Following a two-year preparatory class in Lycée Louis-le-Grand in Paris focused on physics, mathematics and chemistry, she entered ENSTA Paris where she studied mechanics of fluids and solids. In 2017, a research placement in Politecnico di Torino led her to study homogenization of metamaterials for acoustic applications. Since she could not decide either between materials or structures but was certain that she wanted to touch them with her hands, she joined TU Delft the same year to follow a MSc in the Aerospace Structures and Materials department.

During her master thesis under the supervision of Dr. Calvin Rans and Prof. Clemens Dransfeld, she focused on interlayer features that could be observed during additive manufacturing of liquid crystal polymers. She graduated cum laude in 2019. She found the topic so interesting that she started working as a PhD student in 2020 on the same material, under the supervision of Dr. Kunal Masania, supported by the European Space Agency via Dr. Ugo Lafont and Dr. Thomas Rohr. She received the Zonta Amelia Earheart fellowship in 2020. Besides her PhD, she began offering Climate Fresk workshops at TU Delft in 2023 with Dr. Irene Fernandez-Villegas. These workshops educate participants on the mechanisms and systemic scale of climate change, empowering them to take meaningful action.

In the future, Caroline strives to combine her passion for natural materials and sustainability into her work, to contribute both scientific knowledge and societal well-being.

Acknowledgements

"Dernière ligne droite" I heard often these days from supportive friends and family... the final stretch, especially as I'm writing these lines concluding my PhD journey. But has it *ever been* a straight line? The path of a dreaming child in awe with Chladni patterns, NASA pictures, science-fiction, and tree silhouettes, leading now to the completion of this thesis, has been definitely wavy, interlaced with many topics, enriched by many people.

I would first like to express my gratitude to my supervisor Dr. Kunal Masania, for his guidance throughout my PhD journey. It would be hard to summarize, so among others: thank you Kunal for always making time for advice and feedback, leading by example, your constant good mood, encouraging enthusiasm and unstoppable flow of wild ideas. I wish anyone the freedom that I had in my thesis to explore the fields that I felt drawn to.

My thanks also go to Prof. Clemens Dransfeld, for his continuous support as I evolved from MSc student on my journey as an independent researcher to PhD. I also wish to thank Dr. Ugo Lafont, whose enthusiasm since we started discussing about LCP in space many moons ago, and dedication to space printing has left a big mark on me. I am also grateful to the other committee members, Prof. Stephen Picken, Prof. Jan Willem van de Kuilen, Dr. Joseph Morlier and Dr. Flavia Libonati for their time and effort in reviewing my work. I would also like to thank Dr. Thomas Rohr from ESA, as well as Dr. Silvan Gantenbein, Dr. Raphael Heeb, Yannick Nagel and the whole NematX team, with a special mention to Chiara Mascolo, for their support and always very helpful discussions.

In March 2020, my PhD started strangely with a pandemic. "Shaping Matter Lab" (which didn't exist yet) consisted of Kunal and I, joined by Chiara who soon had to show her resourcefulness by doing tensile testing with bags of pasta, and a couple of months later also by Satya. Satya, thank you for sharing the OG status with me for better or for worse, for your kindness and for knowing, always, that "it's gonna be fine". Vinay, the OG post-doc as well: thank you for your support and great scientific insights in all our discussions, and thanks to both Taylor and you for the nice dinners, random Saturday discussions on trusses and so on. Thanks Mu, for your humour, bringing the fancy tech to us, and I still keep a few of the saffron black tea bags in case of emergency breakdown. Then SML was growing so much, attracting so many enthusiastic talents, that group meetings started to happen in lecture rooms. Thank you to everyone at SML for the nice working atmosphere you contribute to, full of kindness, creativity and bouncing ideas: Natalia, Deniz, Ingo, Mark, Yaren, Chris, Jasper, Alex, Swaliha, Zhiyuan, Poorva, Derin, Wouter, Momo, Sarah, Saurav, Chintan, Sourav, the ones I haven't even met yet, and the ones we proudly saw graduate, off to new adventures: Guille, Sander, Shishi, Sian, Kevin, Sungi, Lars... I would also like to acknowledge the great work of the students I have had the pleasure to work with on LCPs: Nick, Berend, Ranjan, Boris, Antoine, Lucas, Evelien, Harold, Stefan, and Lorenzo.

Thank you to my office mates of 2 different offices for being so cool (and putting up with my plants): Sasan, Mariana, Giovanna, Swaliha, Chizoba, Sofia. Thanks to the other PhDs and post-docs in ASM, for being great colleagues as well: Billy, Clément, Davide, Eva, Rose, Mary, Mirko, Onur, Silvia, Wenjie, and everyone else. A massive thank you is also due to the technicians in DASML: Dave, Alexander, Chantal, Roy, Victor, Johan, Pietro, Durga. Thank you for your patience, sharing your knowledge with us, and reducing the inevitable friction that makes the π-rule a reality ("if x is the time you think you need for an experiment, then you will really need πx"), with small and big things. I would also like to mention Dr. Calvin Rans. Thank you for really caring about my well-being, for dropping by regularly, and for discussions about the PhD or the end of our civilization. Thanks also for bringing me in touch with Dr. Irene Fernandez-Villegas so that we could actually try to do something about it, via the Climate Fresk. Irene, I'm so happy and proud to see it take off at TU Delft thanks to your dedication. Thank you both for being so inspiring.

And thank you, all of you, for your help and our great, enriching conversations.

A strange thanks but a thanks anyways also goes to Moebius, Frida Kahlo and Mondrian, faithful 3D printers. Considering the time we spent together, the love-hate relationship was rather healthy. Thank you to Prusa for building open-source printers with safety margins allowing us tinkerers to get away with a lot of things.

Finally, this brings me to people outside of TU Delft and the world of research.

At this stage of writing the last words of this thesis, I would like to thank all my professors, from the elementary school till master. I remember each one of you. Thank you for blowing on the sparks, for your enthusiasm and sharing your passion to the next generations.

This journey would not have been quite the same without my friends: Alba and Robert, who, since Day 1 of our life at TU Delft, by their kindness and generosity, slowly became like our family in the Netherlands. Thanks as well to the members of the "Raclette-ski club" for the great time together too. And, last but not least, Merci les Meilleurs, for spicing up my life for a good 10 years as well now, with exorcisms, stair races, 120% slopes, reveaaals, exploding batteries, rappelling down castles, sailing cart flips, glitter outfits and birthday salads.

I want to also acknowledge my parents who fostered my curiosity, but also taught me to always try my best with everything. Thank you mum for bringing us to the library every Wednesday, thank you dad for always trying to answer questions. Thank you both and Nicolas for your overall support, for allowing me to pursue my studies even abroad and be happy. Special thanks also to the Bouchan family, for your great support and love during the last 10 years.

And finally, I would like to thank Thomas, for his continuous support during all this time, and for simply being an amazing life partner.

<div align="right">- Caroline, 10/10/24, Delft</div>

Acronyms

165